Collisional and Photoexcitation of Transition Metal Clusters

A thesis submitted for the
degree of Doctor of Philosophy

Imogen Parry

Michaelmas Term, 2014

Supervisor: Professor Stuart Mackenzie

Department of Chemistry
University of Oxford

Collisional and Photoexcitation of Transition Metal Clusters

Imogen Parry, Exeter College

A thesis submitted for the degree of Doctor of Philosophy

Michaelmas Term, 2014

The properties of transition metal clusters differ from those of both atomic and bulk size regimes. Such clusters are incompletely understood and potentially useful, making them attractive targets for further study.

The very smallest clusters studied in this thesis (CuO, Cu_2 and Cu_3) have been investigated with velocity map imaging. 1+1′ photodissociation of CuO X $^2\Pi_{3/2}$ was observed, via the C, D, E, F and H states of CuO. CuO* was photodissociated to form Cu($^2D_{3/2}$) + O($^1D_2$). D_0(CuO) was determined to be 3.041±0.030 cm^{-1}. Non-resonant three-photon Cu_2 photodissociation occurred throughout the energy range studied to produce one ground-state and one highly-excited copper atom, Cu*. Cu* was ionised by a single additional visible photon. Nearly all Cu* atoms with internal energies between 41000 and 53000 cm^{-1} were observed. $D_0(Cu_2)$ has been calculated to be 1.992±0.037 eV.

Features arising from photodissociation of Cu_3 were observed in the Cu^+ and Cu_2^+ ion yield spectra and images. Their structure was ill-resolved due to uncertainties in the internal energy of both parent Cu_3 and product Cu_2. These features correspond to single-photon dissociation of Cu_3 to produce metastable D-states of the copper atom and vibrationally excited Cu_2. One series of features implies a previously-unobserved state of either Cu_2 or Cu_3.

$Rh_nN_2O^+$ and $Rh_nON_2O^+$ (n=5, 6) were collisionally activated in collision-induced dissociation (CID) experiments with Ar and ^{13}CO. These experiments were carried out in a Fourier Transform Ion Cyclotron Resonance (FT-ICR) spectrometer. Argon collisions induced both N_2O desorption and N_2O reduction. The branching ratios observed reproduced those seen in prior IR-MPD experiments. ^{13}CO was observed to chemisorb to the cluster upon collision, activating not only N_2O desorption and reduction but also CO oxidation. Formation of CO_2 was noted to be particularly rapid on the n=5 cluster compared to the n=6 cluster.

Reactions of $Rh_nN_2O^+$ (n=4-6) clusters were also activated by black body radiation. This technique is known as BIRD - black-body induced infrared radiative dissociation. These studies revealed that the N_2O desorption barrier exceeds the N_2O reduction barrier on all clusters studied, but that the entropic favourability of desorption increases its rate relative to reduction with increasing cluster

internal energy. The BIRD rate was much reduced upon cooling the ICR cell to 100 K. A further test of the BIRD mechanism increased the number of N_2O ligands and hence the absorption rate. An approximately linear increase in the dissociation rate of $Rh_n(N_2O)_m^+$ was observed with index m. Deviations from linearity were caused by variations in the N_2O desorption rate. In the case of $Rh_5(N_2O)_m^+$, desorption rates corresponded closely to N_2O binding energies calculated by density functional theory. The system was modelled using a master equation approach.

Acknowledgements

I would like to thank my supervisor, Professor Stuart Mackenzie, for the use of his lab and for all the time that he has so generously invested in me over the past four years. I would also like to thank Professor Dr. Martin Beyer for allowing me to use his lab in Kiel, in 2011 and 2012, and for all the assistance he has given us in writing up the experiments afterwards. Additionally, I am very grateful to the NSCCS for hours of computing time on their machines.

I am also most grateful to Dr. Petru Ovidiu-Balaj for teaching us how to use the FT-ICR equipment in Kiel and for overseeing the experiments every step of the way. I would like to thank Dr. Scott Hopkins, who taught me how to use the Oxford lab, and Dr. Aras Kartouzian for setting up the copper experiments. I would like to thank Dr. Suzanne Hamilton and Dr. Alexander Hermes for teaching me how to run calculations, and for all the technical advice and help they gave me during their time in Oxford.

I would also like to thank Paul Mitchell, Lab Services, workshops and the electronics team in Oxford for the innumerable hours they have spent ensuring that our lab runs as smoothly as possible.

Finally, I would like to thank Stephen Bedford for teaching me LaTeX and C, and for his assistance in writing and debugging all the code used herein.

List of publications

1. I. S. Parry, A. Kartouzian, S. M. Hamilton, O. P. Balaj, M. K. Beyer and S. R. Mackenzie, *Collisional activation of N_2O decomposition and CO oxidation reactions on isolated rhodium clusters,* J. Phys. Chem. A, **117,** 8855-8863 (2013).

2. I. S. Parry, A. C. Hermes, A. Kartouzian and S. R. Mackenzie, *Imaging the photodissociation dynamics of neutral metal clusters: copper dimer, Cu_2, and copper oxide, CuO,* Phys. Chem. Chem. Phys., **16,** 458-466 (2014).

3. I. S. Parry, A. Kartouzian, S. M. Hamilton, O. P. Balaj, M. K. Beyer and S. R. Mackenzie, *Chemical reactivity on gas-phase metal clusters driven by black body infrared radiation,* accepted by Angew. Chem. Int. Ed.; DOI: 10.1002/anie.201409483.

Contents

1 Introduction **9**

1.1 The definition of a metal cluster 9

1.2 Origin of interest in metal clusters 9

1.3 Generation of metal clusters 14

1.4 Experimental studies of metal clusters 17

1.4.1 Detection methods at low number density 17

1.4.2 Experiments on clusters directly from the source 17

1.4.3 Photoionisation 19

1.4.4 Electron detachment 20

1.4.5 Photodissociation 22

1.4.6 Collision-induced dissociation 25

1.4.7 Reactive collisions 26

1.5 Theoretical treatment of metal clusters 28

1.6 Thesis overview 31

2 Velocity Map Imaging of Copper Oxide Photofragments **33**

2.1 Experimental Technique 33

2.1.1 Development of Velocity Map Imaging 33

2.2 Applications of Velocity Map Imaging 36

2.2.1 Our apparatus 37

2.2.2 Image processing 39

2.2.3 Errors 43

2.3 Previous Work on CuO 43

2.4 Two-colour spectroscopy 47

2.5 CuO Images 50

2.5.1 Determination of $D_0(CuO)$ . . . 50
2.5.2 Proof of the 1+1' mechanism . . . 53
2.5.3 Anisotropies . . . 55
2.6 Concluding remarks . . . 58

3 VMI of Copper Clusters **59**
3.1 Previous work on Copper Clusters . . . 59
3.1.1 Copper Dimer . . . 59
3.1.2 Copper Trimer . . . 63
3.2 One Colour Spectroscopy . . . 66
3.2.1 The origin of features in the high-intensity photoion spectra . . . 69
3.2.2 Spectral evidence for the trimer . . . 73
3.3 Cu Images . . . 76
3.3.1 Three photon dimer dissociation . . . 77
3.3.2 Testing the three-photon assigment . . . 81
3.3.3 Low-TKER peaks in the 21000-24000 cm^{-1} region . . . 81
3.3.4 Calculation of $D_0(Cu_2)$ . . . 83
3.3.5 Low-energy Cu^+ images . . . 84
3.4 Cu_2 Images . . . 87
3.4.1 Comparison with the atom channel . . . 87
3.4.2 The mechanism of formation of Cu_2 images . . . 90
3.4.3 Calculation of $D_0(Cu_3)$ . . . 91
3.5 Conclusions . . . 94

4 Collisional activation of stored rhodium clusters **95**
4.1 Experimental Technique . . . 96
4.1.1 Development of FT-ICR . . . 96
4.2 Principles of FT-ICR . . . 97
4.2.1 Ions in magnetic fields . . . 97
4.2.2 Resonant excitation . . . 98
4.2.3 Ion motion parallel to the field axis . . . 100
4.2.4 Developments . . . 102
4.2.5 Sources of uncertainty . . . 103

4.3 Applications of FT-ICR . . . 104
4.3.1 Uses of FT-ICR . . . 104
4.3.2 The Kiel apparatus . . . 105
4.4 Previous work on rhodium clusters . . . 106
4.5 CID with argon . . . 110
4.5.1 Experimental Results . . . 110
4.5.2 Calculating the energy transferred on collision . . . 113
4.6 CID with carbon monoxide . . . 115
4.6.1 Calculated binding energies . . . 116
4.6.2 ^{13}CO collisions with $Rh_nN_2O^+$ . . . 119
4.6.3 ^{13}CO collisions with $Rh_nON_2O^+$ . . . 123
4.7 Calculation of collision rates . . . 126
4.7.1 Concluding remarks . . . 129

5 Black Body Infrared Radiative Dissociation of $Rh_n(N_2O)_m^+$ 131
5.1 Development of BIRD . . . 132
5.1.1 History and development . . . 132
5.1.2 Master equation modelling . . . 135
5.1.3 Applications . . . 140
5.1.4 Errors . . . 142
5.2 Relevant Previous Work . . . 143
5.3 $Rh_nN_2O^+$ BIRD . . . 145
5.3.1 Experiments at 300 K . . . 145
5.3.2 Experiments at 100 K . . . 147
5.3.3 Barriers to reaction . . . 149
5.3.4 Effect of additional O atoms . . . 150
5.4 $Rh_n(N_2O)_m^+$ BIRD . . . 150
5.4.1 Calculation of structures and spectra . . . 150
5.4.2 Dissociation rates of the parent ion . . . 155
5.4.3 $Rh_5(N_2O)_m^+$ products . . . 158
5.4.4 Master equation modelling of $Rh_5(N_2O)_m^+$ . . . 161
5.5 Concluding remarks . . . 165

6 Conclusions and outlook **166**

A Eigenvalues of the transport matrix **173**

B Code used in thesis **175**

B.1 Full transport matrix 175

B.2 Truncated Boltzmann method 188

Bibliography **197**

Chapter 1

Introduction

1.1 The definition of a metal cluster

A metal cluster is generally recognised as a particle containing anywhere between two and several hundred thousand metal atoms [1]. At the top end of this size range, the characteristics of metal clusters begin to become bulk-like [2]. The bonding in very large clusters is metallic, and their structures usually correspond to the close-packed structure of the bulk metal. However, in smaller clusters, a significant fraction of the atoms sit at the cluster surface, and such clusters often do not behave like small pieces of metal [3]. Neither do they conform to the covalent molecular orbital structure of organic molecules, wherein molecular structure is defined by the directional nature of the bonds. Instead, their bonding is somewhere in between localised and delocalised, varying greatly between metals and as a function of size [3]. This gives rise to unusual and interesting properties specific to the cluster size range.

1.2 Origin of interest in metal clusters

The unusual and size-specific properties of metal clusters may be employed in the creation of new materials with properties not typically exhibited by bulk metals and alloys [4]. Optical [5], magnetic [6], and catalytic [7] properties of clusters may be tuned with their size, as may their electronic band structure [8]. The properties of cluster-based materials may, in theory, be finely controlled. Deposited clusters have already been shown to exhibit unusual catalytic, magnetic, optical, electronic and even mechanical properties [8, 9]. Such materials may be useful in, for instance, catalytic converters, magnetic data storage and sensing devices [10]. Deposition of clusters is a field of research in itself;

this thesis will focus instead on the fundamental properties of the cluster building blocks used.

A key property of clusters is their ability to model catalytic sites on extended surfaces [11]. Active sites in homogeneous catalysis are generally surface defect sites such as steps or holes [12]. This is illustrated by the adsorption of NO on rhodium surfaces [13]. The (111) Rh surface favours end-on NO binding, but the (331) surface has a high concentration of step defects which preferentially bind NO in a 'bent' orientation. This orientation weakens the NO bond and favours dissociation, promoting reaction with other surface species. The structural similarity between surface defects and isolated clusters is illustrated in figure 1.1, which shows the binding sites of small molecules to a vanadium oxide surface and to gas phase $V_xO_y^+$ clusters [14].

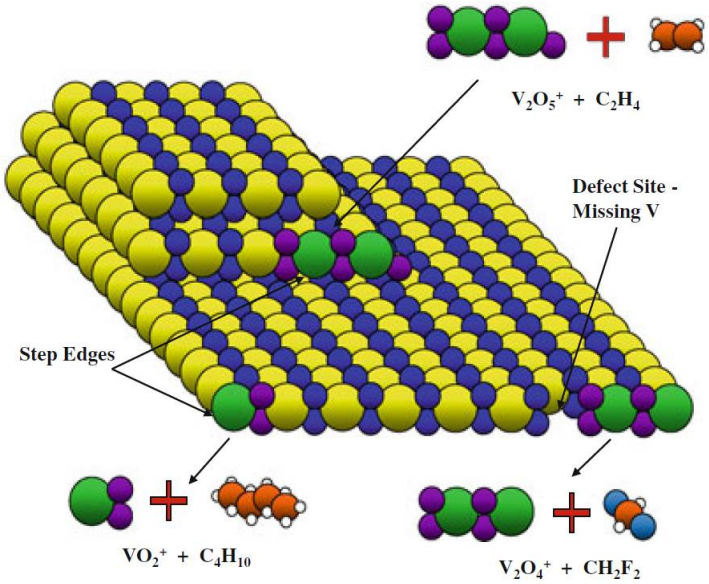

Figure 1.1: The analogy between vanadium oxide surface defect sites (shown in green and purple) such as steps, ledges, corners and holes, and isolated $V_xO_y^+$ clusters is illustrated. Small molecules bind preferentially at such defect sites on the bulk oxide. Reproduced from Catalysis Letters, Volume 141 (2011) p1243, "Cluster Structure and Reactions: Gaining Insights into Catalytic Processes", A. W. Castleman Jr, Fig. 1, with kind permission from Springer Science and Business Media.

There are significant advantages to the study of catalytic processes in the gas phase as opposed to the bulk. A high concentration of defect sites of known structure is achieved using very little metal. Solvent effects, and the interference of the rest of the metal surface, are removed, which simplifies the study of catalytic cycles. For instance, in a particularly elegant demonstration of the catalytic ability of gas-phase clusters, Pt_7^+ has been shown to perform a full catalytic cycle under controlled conditions, catalysing the reaction of N_2O with CO [15]. The poisoning effect of multiple CO adsorption was identified. Similar demonstrations have been performed for large rhodium clusters [16].

Precise control of defects and minimal usage of metal is desirable in all heterogeneous catalysis due to the cost of the elements involved. Much work has therefore been done to 'bridge the gap' between gas- and condensed-phase work in order to understand the origin of cluster catalytic activity. A common approach is to deposit clusters on supports and study their reactivity. Many examples exist for gold, which is inert in bulk but highly catalytically active on the nanoscale [17]. In one such experiment, Häkkinen *et al.* deposited very small gold clusters on a MgO surface and examined their ability to oxidise CO with O_2. They found the clusters' structural flexibility to be key in their ability to dissociate O_2. The role of electronic structure in cluster catalysis was emphasised by Valden *et al.*, who found that gold nanoparticles exactly two atoms thick deposited on TiO_2 are enormously reactive towards CO+O_2, forming CO_2. Single gold layers have atom-like band gaps and three-atom layers are metallic, but two-atom layers have band gaps which are strongly suited to sticking CO [18].

Some research groups have gone beyond attempts to understand the fundamental principles behind cluster catalytic activity, and are attempting to make functional heterogeneous catalysts using clusters [19]. One particularly interesting example involves the CO methanation reaction,

$$CO + 3H_2 \rightarrow H_2O + CH_4, \tag{1.1}$$

which removes unwanted CO from gas mixtures. Having found that small ruthenium oxide clusters catalyse this process very efficiently, the researchers propose to deposit Ru_nO_m clusters into zeolites to create a workable catalyst for reaction (1.1) [20].

Catalytic ability is not the only interesting cluster property. The non-catalytic reactivity of transition metal clusters is observed, in some cases, to vary by several orders of magnitude between adjacent cluster sizes. Rates of reaction of Rh_n^+ with N_2O are shown as filled squares in figure 1.2 and illustrate this effect [21]. Size-dependent reactivity is not limited to rhodium cations' reactions with N_2O; it has been observed in numerous cases, and emphasises that, in small transition metal clusters, every atom counts [22, 23, 24]. Not all reactions of clusters are size-dependent. The reaction of Rh_n^- with N_2O, shown as open circles in figure 1.2, varies very little with cluster size. Where a reaction has strict geometric requirements (for instance, the dehydrogenation of alkanes [23]) changes in cluster geometry with each additional atom can greatly alter the rate at which suitable cluster-molecule binding can be achieved. Where long-range electronic interactions such as charge transfer govern the reaction, differences in cluster geometry have little effect on rate [25, 26, 27].

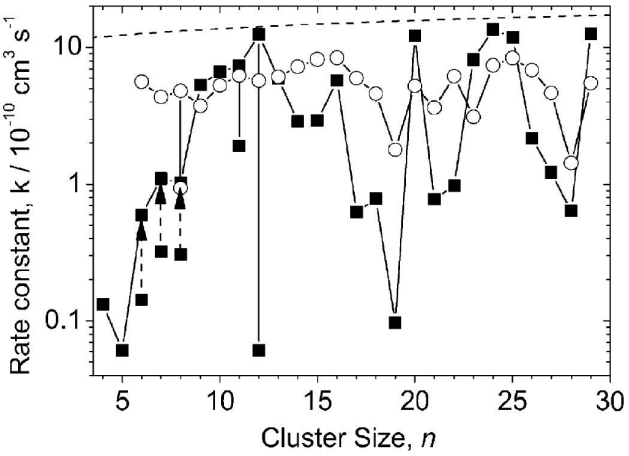

Figure 1.2: Rate of reaction of $Rh_n^{+/-}$ with N_2O. Anions are shown by open circles, cations by filled squares. Multiple rates indicate complex kinetics interpreted as resulting from multiple isomers. Reproduced from PCCP Vol. 9 (2007) p2130, "Dramatic size effects and evidence of structural isomers in the reactions of rhodium clusters, $Rh_n^{\pm}$, with nitrous oxide" D. Harding, M. S. Ford, T. R. Walsh and S. R. Mackenzie. Reproduced by permission of the PCCP owner societies.

The changes in cluster geometry with size can be very marked. For instance, small Fe_n^+ adopt face-centered cubic, body-centered cubic and possibly also icosahedral-type structures [28]. Electronic properties also vary non-monotonically with increasing cluster size and can affect reaction rates. Ionisation potentials are a prime example of this. Alkali and coinage metal clusters' valence electrons occupy hydrogen-like orbitals extended over the whole cluster (these 'superatoms' will be discussed later on). They have stability associated with electronic shell-closings at certain sizes, analogous to the shell-fillings across the periodic table, and show corresponding enhancements and dips in their ionisation energies and electron affinities (figure 1.3) [29]. Odd-even fluctuations are observed in the ionisation potentials and electron affinities of such one-valence-electron clusters, due to the difference in energy associated with an electron entering a low-energy occupied orbital as opposed to the higher unoccupied molecular orbitals [30]. The odd-even alternation is overlaid upon the electron shell-closing pattern. Non-monotonic changes in ionization energy are observed for all metal clusters, not just those forming superatoms [31, 32].

Variation in geometry and electronic structure affects the magnetic moment of small metal clusters. Metals which are magnetic in the bulk, namely iron, cobalt and nickel, can form clusters with large temperature-dependent magnetic moments [33, 34]. More surprisingly, metals which are not magnetic in the bulk can also exhibit magnetic moments in cluster form [6]. Magnetic moments were originally predicted for high-symmetry clusters of the 4d metals Ru, Rh and Pd [35]. When Rh_n^+ were

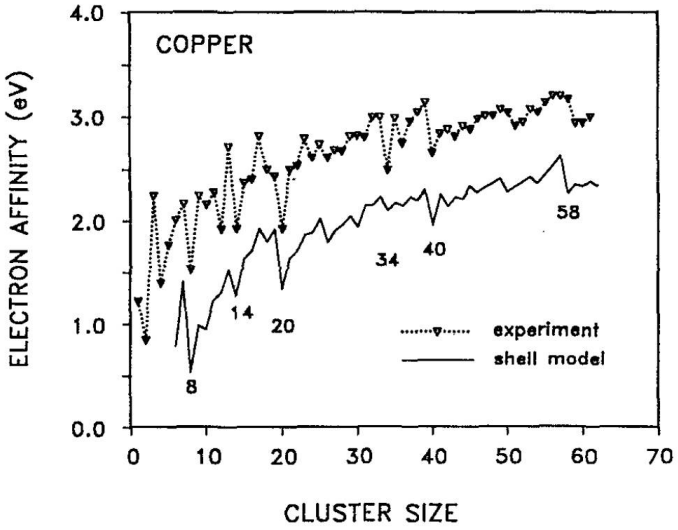

Figure 1.3: Experimental and theoretical electron affinities of $Cu_{1\text{-}61}$. Predicted shell closings at 8, 14, 20, 34, 40 and 58 are observed. Reprinted with permission from J. Chem. Phys. Vol 96 (1992) p3319, "Ultraviolet photoelectron spectra of coinage metal clusters". K. J. Taylor, C. L. Pettiette-Hall, O. Cheshnovsky and R. E. Smalley. Copyright 1992, AIP Publishing LLC.

examined, giant magnetic moments were indeed found for the n=15, 16 and 19 clusters, although the high-symmetry icosahedral Rh_{13}^{+} cluster did not show such a marked magnetic moment [6]. Once again, the properties of small transition metal clusters are proven to be highly non-monotonic.

Other tunable, size-specific cluster properties are band structure [36] and optical properties [5]. An example of the latter is the emission of red light from silicon microcrystals embedded in silicon oxide. The wavelength distribution varies with crystallite size. Quite apart from being of scientific interest, these cluster properties are key to their potential utility in, for instance, electronic components and have motivated much research [18, 37].

In addition to having size-specific and possibly useful properties, transition metal clusters are of interest as a testing-ground for theoretical methods [38]. Transition metal clusters have large numbers of electrons, high spin states, relativistic and spin-orbit coupling effects, all of which are very demanding to treat theoretically [39]. To simplify matters, the coinage metals (whose d-orbitals are filled) are preferred subjects of study [40]. The wealth of theoretical and experimental data available for Cu_2 and Cu_3 means that they are among the best-studied of all transition metal clusters [3].

1.3 Generation of metal clusters

The investigation of metal clusters has been largely directed by the methods available to make them; transferring metal into the gas phase is not an easy task. The earliest cluster sources were ovens, which produced metal vapour [41]. The hot vapour was condensed into metal clusters by collision and supersonic expansion. The principles of supersonic expansion are illustrated in figure 1.4. When a high-pressure gas expands through a hole whose diameter is larger than its mean free path, escaping particles undergo many collisions, causing adiabatic cooling and creating a rotationally and vibrationally cold molecular beam. The cold centre of the beam is selected by a skimmer [42].

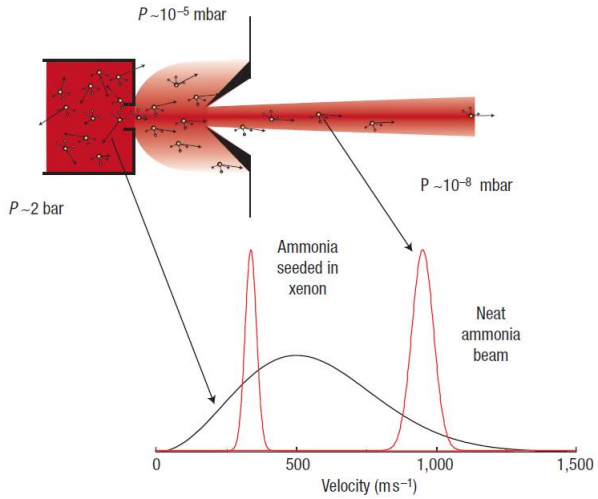

Figure 1.4: Supersonic expansion. Particles escaping a high-pressure region undergo collisions in the nozzle region, creating rotationally and vibrationally cold particles. A seed gas increases the number of collisions, narrowing the velocity distribution of the escaped beam. A skimmer selects the coldest part of the beam. Reprinted by permission from Macmillan Publishers Ltd Nature Physics, from ref. [42], copyright 2008.

The earliest studies of metal clusters were therefore restricted to alkali metals which form vapour at comparatively low temperatures. Improved engineering of oven sources increased the range of metals accessible to the technique. Small copper clusters were made in this way [43]. An improvement to the method introduced an inert collision gas to mix with the vapour, also known as 'seeding' [44]. A seed gas promotes condensation of clusters out of the metal vapour by increasing the number of three-body collisions. Three-body collisions are required to initiate condensation because, when small clusters form, the binding energy released will cause them to dissociate immediately unless it is removed by a cooling collision. A seed gas also influences the width and centre of the molecular beam's velocity distribution in its direction of travel [45].

Later incarnations of the oven source are gas aggregation sources, which mix hot metal vapour with a flow of cold inert gas [46]. They can produce clusters of tens of thousands of metal atoms, whereas early oven sources were limited mainly to dimers and trimers [10, 43]. Despite their differences, all oven sources produce a *thermodynamic* distribution of clusters as the initial distribution tends to be hot, and therefore clusters cool by evaporation until they reach a particularly stable size [1]. In a thermodynamic distribution, clusters' relative abundance reflects their relative stability.

An alternative method for producing larger clusters from molten metal is the liquid cluster source, analogous to an electrospray source. Liquid metal enters a needle with a very high electric field at its tip, producing a fine spray of multiply-charged droplets which cool by evaporation and fragmentation to species of lower charge [47].

Newer sources rely on local heating of the target rather than melting it. One example is the sputtering source [48]. The method 'sputters' a target metal cathode by accelerating rare gas ions towards it. When ions strike the cathode surface, their impact heats it to a sufficient extent to dislodge material. Coinage metals sputter particularly efficiently [49]. The method is most efficient using heavy rare gas ions, which create the greatest impact. Clusters are formed initially hot and cool by evaporation, producing a thermodynamic distribution; consequently, sputtering is not very good at producing large clusters [1]. Magnetron sputtering is a modification of the sputtering technique, which ignites a plasma at the surface of the metal target and maintains it there with a magnetic field [4, 50]. Magnetron sputtering can vaporise a lot of material and produce very large clusters compared to a regular sputtering source. This ability means that sputtering has found uses in the growth of thin films by deposition of clusters (molecular beam epitaxy) [4].

The Pulsed-Arc Cluster Ion Source (PACIS) uses an electric discharge to vaporise a metal surface [51, 52]. The technique works by producing an arc discharge between two electrodes which burns away the cathode. The discharge coincides with a gas pulse which carries away the vaporised material, promoting cooling and cluster formation. PACIS can produce both neutral and charged species in large quantities and at a high repetition rate; the disadvantage of the technique is that it uses a lot of material. As with all previous methods, one of the first metals tested with PACIS was copper [51, 53]. Copper is an ideal test material due to its simple isotopic distribution (70:30 ^{63}Cu:^{65}Cu), the ease with which it may be handled and its relative cheapness.

Most widely used is the laser vaporisation source (fig. 1.5), developed almost simultaneously in 1981 by Smalley and Bondybey [54, 55]. Local heating of the target surface is performed by a high peak

power pulsed laser, typically a Nd:YAG laser. The plasma produced by ablation is swept up by a pulse of carrier gas to assist cluster formation. Larger clusters are promoted using a growth channel, which contains the plasma/gas mixture for a longer distance and forces additional collisions. After cluster formation, the gas mixture expands supersonically into a vacuum and the beam is skimmed. Developments in the laser ablation cluster source have recently been reviewed by Duncan [56].

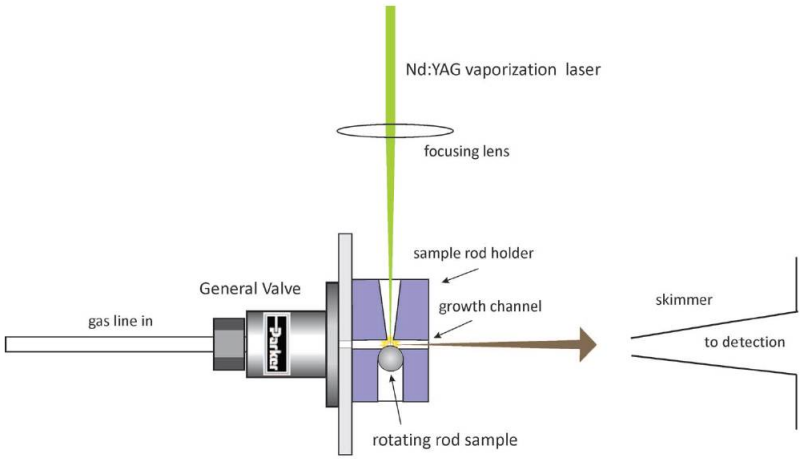

Figure 1.5: Smalley/Bondybey-type source, described in the text. Reprinted with permission from Rev. Sci. Instrum. Vol. 83 (2012) 041101, "Invited review: laser vaporization cluster sources", M. A. Duncan. Copyright 2012, AIP Publishing LLC.

Any solid material can be vaporised, although different laser sources are more efficient for different materials, dependent on their ability to reflect or absorb each laser wavelength [56]. Targets are typically rods or discs, which are slowly rotated so as to continually present a fresh surface to the ablation laser. Mixed-metal clusters may be formed using an alloy target or two separately-ablated target rods in the source region [57]. Non-metal targets have been used; some of the earliest work using the source considered semiconductors such as silicon [58]. The source typically produces very cold clusters, allowing the study of weakly-bound ligands such as argon, which are not accessible to the hot sources [59]. The cluster distribution is kinetically controlled by the collision dynamics in the source. The relative abundance of each cluster size therefore represents its rate of formation in the source rather than its relative thermodynamic stability [60]. The most abundant cluster sizes produced by laser ablation are not necessarily the most thermodynamically preferable species. A final advantage of laser ablation is that it can produce large clusters, again because evaporative cooling does not occur. The laser ablation source can favour charged clusters or neutral simply by varying the plasma conditions [61].

1.4 Experimental studies of metal clusters

1.4.1 Detection methods at low number density

Experiments examining the reactivity and structure of metal clusters are desirable. However, the low number density of clusters produced by the sources described above makes their detection difficult. Laser ablation typically produces at most only 10^5 clusters of a particular size ($\approx 10^{-19}$ mol) per shot [62]. This must be accounted for in designing experiments for their study.

Emission experiments are essentially background-free, making them extremely sensitive and therefore suitable for the study of metal clusters. For instance, Preuss *et al.* performed laser-induced fluorescence experiments on Cu_2 [43]. Absorption experiments produce signal intensities according to the Beer-Lambert law, wherein absorbance is directly proportional to the concentration of absorbing species. Low number densities of clusters from laser ablation sources make absorption experiments difficult but not impossible. Saykally's group used the cavity ringdown technique, which passes a light pulse through a sample very many times to increase sensitivity, to detect vibronic absorption bands in Cu_2 and Cu_3 [63]. However, many spectroscopic methods struggle with the small dipole changes and correspondingly small infrared absorbance of many metal clusters upon vibration.

Cluster number densities may be increased by accumulation in a trap, although this is only possible for charged species [64, 65]. A number of experiments described in this introduction will involve trapped ions [66, 67, 68]. A more common solution is to rely on a highly sensitive detection technique: mass spectrometry. Clusters are generated in molecular beams which makes them particularly suitable for time-of-flight (TOF) detection as heavier species travel slower (see section 1.4.5 below). The pulsed nature of laser ablation sources provides a well-defined 't_0' from which different species' times of flight to the detector may be measured. Almost all ions are detected by micro-channel plates (MCPs) [69]. This does impose the requirement that neutral species be ionised before detection.

1.4.2 Experiments on clusters directly from the source

It is possible to examine metal clusters without modifying them at all after they emerge from the source. Giant magnetism in rhodium clusters was detected with a method analogous to Stern and Gerlach's famous experiment, [6] with neutral rhodium clusters supersonically expanded from a laser ablation source into an inhomogeneous magnetic field. The cluster's magnetic moment determines the magnitude of its deflection from the beam path. A narrow ionisation laser beam scans the width of

the cluster distribution just before the time-of-flight detector. A similar probe of electronic structure was performed by Knight *et al.*, who passed neutral alkali metal clusters from the source through an inhomogeneous electric field to measure electric polarisability [70]. Both rhodium magnetism and sodium polarizability were large in small clusters, dropping towards bulk values in a non-monotonic manner as cluster size increased.

Ion mobility experiments are used to investigate the geometric structure of metal clusters straight from the source. Clusters enter a drift cell filled with inert gas *via* a mass gate. Different isomers of clusters of the selected mass adopt differing shapes. The larger the collision cross section an isomer presents, the slower its progress through the cell due to collisions with the inert gas. The isomers are therefore detected at differing times by a mass spectrometer after the cell. Comparison of experimental drift times with theoretical predictions distinguishes cluster geometries [71]. The technique was first applied to metal clusters in 1993 [72]. This work found the most compact Al cluster structures to coincide with electronic shell closings, as open-shell clusters undergo Jahn-Teller structural distortions. Ion mobility studies of Cu_n^+ and Ag_n^+ show marked transitions from planar to 3D structures at M_6^+ (figure 1.6). Au_n^+ remain planar up to n=8, and gold anions up to and including Au_{12}^-. Gold clusters behave differently as relativistic effects lower the energy of the 6s orbital and increase sp hybridisation. Gold clusters have also proven interesting as multiple isomers are observed in Au_9^+, which disappear at high temperature as the clusters become fluxional [73].

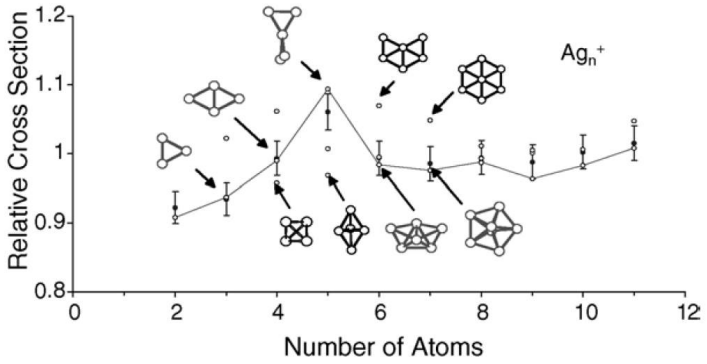

Figure 1.6: Relative collision cross-sections of Ag_n^+ clusters. Experimental results are filled circles, theoretical predictions hollow circles. The observed cross section drops sharply between n=5, 6 as the cluster changes from a 2D to a 3D structure. Reprinted from Int. J. Mass Spec. Vol 245/1, P. Weis, "Structure determination of gaseous metal and semi-metal cluster ions by ion mobility spectrometry", 1-13 (2005), with permission from Elsevier.

Cluster ions from the source may be collected in a Penning trap and studied using trapped ion electron

diffraction, TIED [66]. An electron beam is passed through the trap and diffracted electrons are detected by a phosphor screen and CCD camera assembly [74]. Cluster structures are elucidated by performing density-functional theory calculations (see later) and comparing predicted diffraction patterns with the experimentally-observed one. Structures of Au_{14}^--Au_{19}^- were found in this way. In general, experiment and theory find the same minima, although neglect of spin-orbit coupling in the calculations causes occasional disagreement [75]. A particularly notable example of a gold anion cluster whose structure was elucidated by TIED is Au_{34}^-, which is found to have a chiral, helical structure, which is interesting in the context of chiral catalysis [76].

1.4.3 Photoionisation

Another experimental method which studies clusters without modifying the source distribution is photoionisation spectroscopy (as opposed to photofragmentation spectroscopy, section 1.4.5).

Some of the earliest work on metal clusters was the abundance spectroscopy of sodium clusters [77]. A thermodynamic distribution of sodium clusters was produced from an oven source seeded with argon, and all clusters were ionised with a 1 kW Hg-Xe lamp. Clusters with 2, 8, 18, 20, 34, 40, 58 and 92 atoms were observed to have enhanced intensities in the mass spectrum. A simple Jellium model can explain their stabilities. This model treats the s-electrons as a delocalised homogeneous gas in a uniform positive potential created by the Na_n core. Solving the Schrödinger equation for this system predicts that the s-electrons occupy orbitals similar to those of a hydrogen atom, but delocalised over the whole cluster [78]. Special stabilities arise due to the presence of filled shells: $1s^2$, $1s^21p^6$, $1s^21p^61d^{10}$, $1s^21p^61d^{10}2s^2$, $1s^21p^61d^{10}1f^{14}2s^2$ and so on. The thermodynamic stability of these cluster sizes was further emphasised by later abundance experiments using a laser ablation source. Laser ablation produces a kinetically-controlled distribution of Na_n clusters which do not show the same magic number peaks with enhanced intensities [60].

This simple model works well for both alkali and coinage metal clusters, predicting patterns in their ionisation energies and electron affinities [29]. Low ionisation energies are seen where a closed shell is formed by electron loss (3, 9, 21, 41 etc, shown in figure 1.7). These trends are not visible for larger clusters which may adopt more rigid, less spherical cores. Also visible in figure 1.7 is an odd-even alternation arising from the relatively lower energy of a doubly-occupied HOMO compared to a singly-occupied HOMO [30, 79, 1]. Early attempts at determining ionisation energies generally used fixed-frequency lasers; they showed that metal clusters which do not obey the Jellium model do have

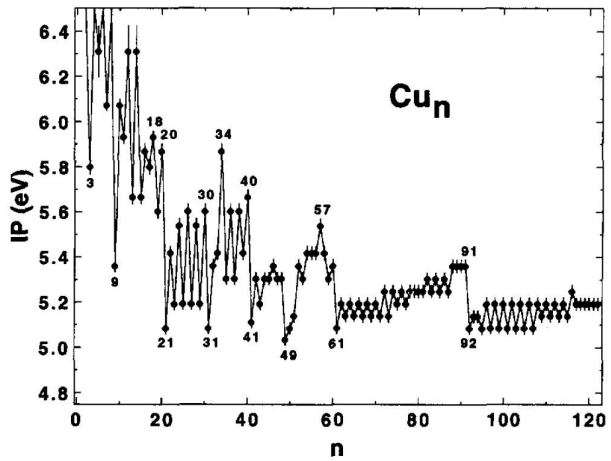

Figure 1.7: Copper cluster ionisation potentials. Odd-even oscillations are observed, along with a pattern reflecting the electronic shell-closings in Cu_n. Reprinted from Chem. Phys. Lett., Vol 192/1, M. B. Knickelbein, "Electronic shell structure in the ionization potentials of copper clusters", 129-134, Copyright (1992), with permission from Elsevier.

size-related variations in their ionisation energies [80, 31]. In general, clusters' ionisation potentials decrease slowly towards the work function of the bulk metal as cluster size increases [32]. Knickelbein explains the decrease as being due to the atomic electronic energy levels gradually coalescing into a continuous band structure.

Photoionisation through a resonance is much more efficient than non-resonant ionisation, so monitoring enhancements in ion signal as a function of a tunable laser's wavelength can be used to investigate electronic transitions. This is resonance-enhanced multiphoton ionisation spectroscopy, or REMPI. The electronic transitions of the copper dimer and trimer have been examined with vibrational resolution using REMPI [80, 81]. Some metal dimers' vibronic transitions have even been studied with rotational resolution, for example Ni_2 [82]. Many more examples of cluster studies performed with REMPI appear in Morse's 1986 review [3].

1.4.4 Electron detachment

Photoionisation can equally be monitored by electron detection. Two techniques using this approach have been applied to metal clusters: zero electron kinetic energy (ZEKE) spectroscopy and photoelectron spectroscopy (PES).

Briefly, the principle of ZEKE is that when an ionisation laser's energy exactly matches the transition energy from the parent species to its ionised product, the ejected electron will have no kinetic energy. After a delay (in which non-resonantly produced electrons with non-zero kinetic energies are lost) an

electric field is applied to extract zero-energy electrons. The electron need not be detached before the field is applied; it may be ionised from a high-n Rydberg state by the field itself. The application of pulsed-field ionisation ZEKE (PFI-ZEKE) to metal clusters was reviewed in 2000 [83]. Detection of ZEKE electrons can identify cluster resonances with extremely high resolution, which is a most attractive quality for the study of metal clusters. Clusters may have a large number of low-lying isomers with similar structures and so precise determination of their rovibronic characteristics is imperative in order to determine their true structures (figure 1.8). The technique has proved extremely useful in determining the geometric (and, in some cases, electronic) structure of V, Y, Nb and Zr clusters and their oxides, nitrides and carbides [83].

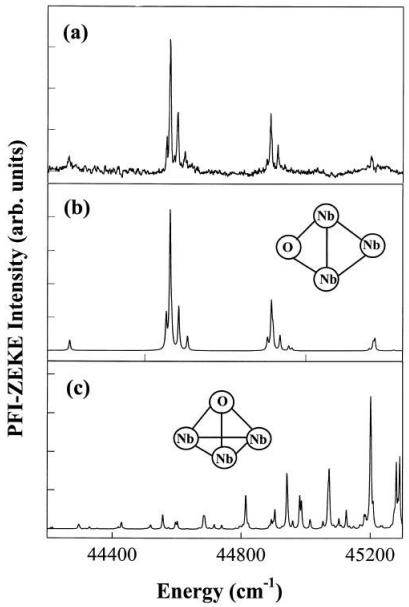

Figure 1.8: Experimental Nb_3O PFI-ZEKE spectrum, (a), and theoretically-predicted spectra for two potential structures, (b) and (c). (b) is clearly dominant. Reprinted from J. Elec. Spec. and Relat. Phenom., Vol 106/2, D. Yang and P. A. Hackett, "ZEKE spectroscopy of free transition metal clusters", p153-169, Copyright (2000), with permission from Elsevier.

A disadvantage of electron detection is that electrons originating from clusters of different masses are not distinguishable. The different times of flight of the parent ions cause 'mass slippage' (a difference in the time at which ejected electrons are detected) which allows some distinction [84]. A better alternative is to detect the parent clusters after electron detachment, as they may be distingushed by their mass. Mass-analysed threshold ionisation (MATI) was first applied to a metal-containing cluster, AlAr, in 1993 [85]. MATI retains the rotational resolution of ZEKE, and has been used to determine the geometry of the V_3 and V_3^+ ground states [86].

PES measures the kinetic energy of detached electrons after photoionisation. It is a lower-resolution technique than ZEKE, but probes the deeper electronic band structure of the clusters. Copper was one of the first metal anions studied by photoelectron spectroscopy [48, 87]. PES has been used to determine the electron affinities of neutral coinage metal clusters. The electron affinities show odd-even alternation and increase towards the bulk value. This reflects the fall in clusters' ionisation potentials towards the bulk value as cluster size increases [30, 88]. Coinage metal clusters' electron affinities agree quite well with the Jellium model, confirming previous suggestions that they behave as perfectly conducting spheres with delocalised s-electrons [49]. Good agreement of the measured HOMO-LUMO gap with Jellium model predictions has also been noted [30, 88].

Vibrationally-resolved photoionisation spectroscopy yielded geometric and electronic information on the clusters studied. Similarly, the detailed band structure of the PES spectra of Cu_3^- and Ag_3^- has been used to deduce linear geometry of both the parent anion and the excited neutral product [48]. Gold anions decay in a dissociative photoionisation process and so their structures cannot be elucidated in the same way. Structural information has been obtained by anion PES on many other metal clusters, such as oxides [37]. The work of Lai-Sheng Wang in this area has been recently reviewed [36]. He has uncovered much unusual electronic band structure not seen in the bulk. A novel example is the observation of aromaticity in Ta_2O_3.

1.4.5 Photodissociation

Absorption of sufficient photon energy can break bonds in the cluster. Cluster dissociation upon absorption of a resonant photon depletes its intensity in the beam. While one photon may not be enough to break cluster bonds, multiple absorptions may occur. After absorption, internal vibrational relaxation redistributes the absorbed photon energy and the cluster mode resonant with the laser is rapidly 'freed up' to absorb again. Products of fragmentation appear in lower mass channels. The method of performing spectroscopy by monitoring photodepletion as a function of irradiating wavelength is known as an *action spectroscopy*. Photodepletion caused by multiple absorptions of infrared photons is infrared multiple photon dissociation, or IR-MPD.

Metal cluster vibrational spectroscopy has been greatly facilitated by the development of tunable infrared light sources FELIX and CLIO. [68] These sources can access the vibrational modes of metal clusters in the 500-2500 cm^{-1} region and are sufficiently intense (tens of mJ per micropulse) to allow multiple photon absorption. They can also ionise neutral clusters by multiple-photon non-resonant

ionisation. However, neutral species' intensities (and neutral fragments) may also be monitored using an ionisation laser of fixed frequency to avoid wavelength-dependent photoionisation efficiency.

Metal clusters may be 'tagged' with weakly-bound messenger species which are easily lost by photodissociation. Weakly-bound species do not significantly disturb the cluster's electronic or geometric structure. Argon is commonly used for this purpose, as it is monoisotopic and binds more weakly than Kr or Xe while still being 'sticky'. Kappes proved that argon tagging of gold clusters did not affect their structures in a combined vibrational spectroscopy and DFT study of $Au_4Ar_n^+$ [89]. The same conclusion was also reached by Gregoire and Duncan, who found that addition of one argon atom slightly changes the spectrum of $Fe(CO_2)_m^+$, but the shift is small and successive argon atoms do not have much further effect [90]. As a result, photodissociation studies of clusters with weakly-bound tagging atoms using infrared cluster sources reveal the vibrational structure of the parent cluster. Examples include work on vanadium, [59] rhodium (figure 1.9) [91] and gold clusters [92]. All of these examples compare experimental vibrational spectra with those calculated by DFT.

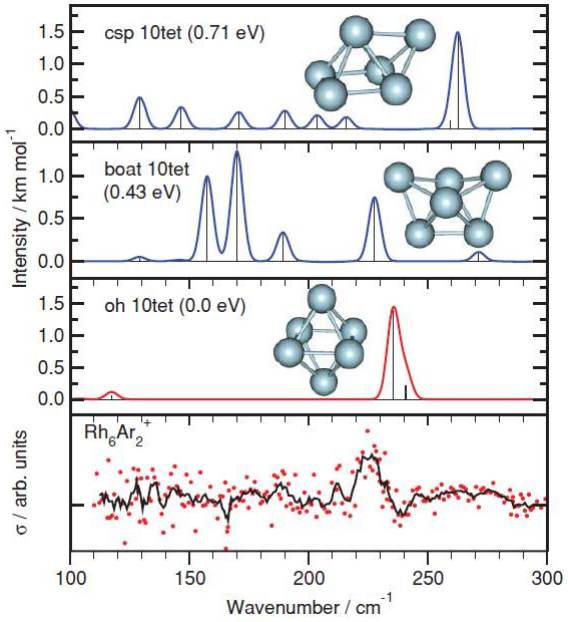

Figure 1.9: Vibrational spectrum of $Rh_6Ar_2^+$ and predicted spectra for various Rh_6^+ geometries from DFT. The octahedron is the best match. Reprinted with permission from J. Chem. Phys. Vol. 133 (2010), 214304, "Probing the structures of gas-phase rhodium clusters by far-infrared vibrational spectroscopy." Harding *et al.*. Copyright 2010 AIP Publishing LLC.

More strongly-bound small molecules such as CO can also act as tags which are lost upon multiple photon absorption [93]. Strongly-bound adsorbates perturb the electronic and geometric structure of the cluster [94]. However, the perturbed spectra are still useful. For instance, Fielicke *et al.* have

examined the C-O stretching frequency of CO adsorbed on $Rh_n^{+/0/-}$ clusters as a function of size. They determined that CO almost exclusively binds on atop (η^1) sites, and observed the convergence of the C-O stretch towards its bulk value [93, 95]. If the adsorbed tagging molecule is a strong chromophore, the light source used for photodissociation need not be a laser. Black-body-induced photodissociation will be discussed later; here it is mentioned in passing as another method of examining the binding of ligands to metal clusters. For instance, changes in the bond strength of water molecules to metal atoms have been used to determine the solvent shell structure around metal ions [96, 97, 98].

Before the free electron lasers FELIX and CLIO, the most convenient tunable light sources for photodissociation of metal clusters were lasers in the visible and UV regions. These energies excite electronic rather than vibrational transitions in the metal cluster and are sufficiently energetic to break metal-metal bonds. Small molecule tags are not needed. Small clusters' electronic transitions have been studied with vibrational resolution, for example Cu_3 [99]. Larger copper clusters have also been studied by photodissociation, although the spectral features broaden with increasing cluster size due to increasing densities of states [100]. Other clusters studied by photodissociation include Fe, Nb and Ni [62]. Photofragmentation processes yield geometric and electronic information, as well as product channels. Laser fluence studies can reveal the number of photons required for photodissociation at individual wavelengths. However, the method does not provide accurate dissociation energies [100].

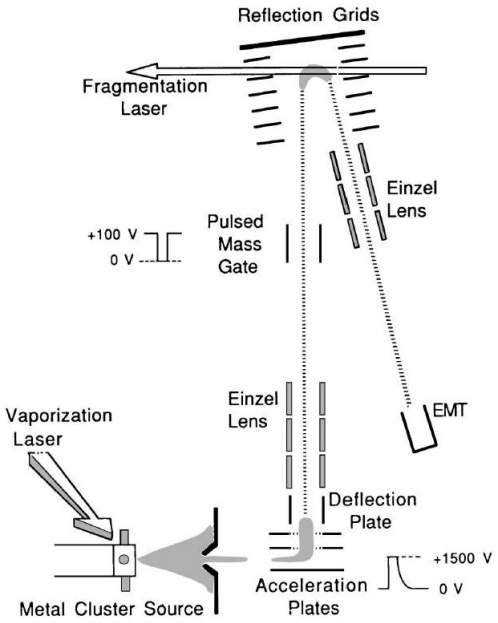

Figure 1.10: Reflectron TOF mass spectrometer, such as that employed by Duncan, described in text. Reproduced from reference [101] with permission of The Royal Society of Chemistry.

Mass selection is desirable in photofragmentation experiments as, without it, the cascade of mass from heavy into lighter channels can be difficult to disentangle. One solution to this problem is mass separation using a reflectron time-of-flight mass spectrometer (figure 1.10) [101]. Charged clusters are accelerated by a Wiley-McLaren electrode arrangement. A pulsed mass gate in the beam path deflects unwanted masses. Mass-selected clusters proceed to a reflectron, an electrode arrangement which acts as an electrostatic mirror. At the point of reflection, the ions are bunched and the packet intercepted by a fragmentation laser. The parent ion and its fragments are then detected by mass spectrometry [102]. The apparatus is suited to REMPI as well as photodissociation experiments. Size selection may alternatively be performed by selective ejection of ions from a trap [103]. For instance, size-selected gold cluster cations in a Penning trap have been photodissociated with various harmonics of a Nd:YAG laser. The timescale of photodissociation is found to depend on the laser wavelength [64].

Position-sensitive detection of fragments will be touched on only briefly here, as it will be discussed in more detail in the velocity map imaging (VMI) section. Position-sensitive detection gives information about the exit channel of a dissociation process; either ionic fragments or electrons may be detected [104, 105]. VMI has been used to image the transition from atomic to bulk properties in clusters by observing photoelectrons from anionic tungsten clusters [106]. A transition from anisotropic photoelectron ejection from states with well-defined electronic symmetries gives way to homogeneous thermionic emission with increasing cluster size.

1.4.6 Collision-induced dissociation

Clusters may be dissociated by collision rather than by irradiation. Ions may be trapped with a collision gas in an ion cyclotron resonance (ICR) cell, Penning trap, or ion guide; [38, 107, 108] neutrals are instead studied in fast flow reactors [109]. Charged species are particularly amenable to CID studies as their collision energy may be gradually varied by excitation, and the cluster's dissociation threshold may be extracted from the extent of dissociation as a function of collision energy [110].

Armentrout and coworkers have performed CID studies on metal clusters using a guided ion beam. Charged clusters are mass-selected and then passed through an octopole ion beam guide containing collision gas. The ion's speed is varied with the injection voltage. Undissociated parent and fragment ions are detected as they exit the octopole by scanning the ejected masses with a quadrupole mass filter [111]. Mass filtering is used as fragmentation products have velocities in all directions, rendering

them unsuitable for time-of-flight detection. Many of Armentrout's studies of cationic clusters of the first and third row transition metals have been reviewed [38]. Ervin and coworkers have examined anions using much the same method [112]. Fragmentations performed in a Penning trap control the fragments' velocity so time-of-flight detection may be used [108]. CID in a Fourier-transform ion cyclotron resonance spectrometer will be discussed later, and detects fragments using their cyclotron resonance frequencies [107].

Dissociation energies are indicative of a cluster's stability and structure. For instance, the dissociation energy of Fe_{13}^+ is large compared to that of neighbouring Fe_n^+ clusters, confirming the stable closed-polyhedron icosahedral geometry of Fe_{13}^+ [28]. Coinage metal clusters' dissociation energies follow a pattern dictated by the Jellium model. Close-packed spherical core geometries occur at electronic shell closings while open electron shells allow Jahn-Teller distortion of the core, allowing ions to be "chipped off" it more easily [72]. Certain patterns in the dissociation energy are therefore indicative of certain geometric cluster shapes. For instance, icosahedral structures are stable at 7, 13 and 19 atoms. On this basis, nickel cations are believed to adopt icosahedron-based structures [113]. Cluster sizes with multiple apparent dissociation thresholds have multiple isomers [28].

Kinetic products are formed by CID. Most metals 'prefer' atom loss as a decay route (Ti, Fe, Co and Ta do so exclusively) [38] even if a more extensive rearrangement of bonds is thermodynamically preferable. The exceptions to the rule are coinage metal clusters which undergo substantial dimer loss, particularly for odd-sized anions [112, 114, 115]. The odd-even size variations in the decay pathways coincide with a thermodynamic preference for dimer generation influenced by bond energies, ionisation potentials and electron affinities.

1.4.7 Reactive collisions

CID experiments rely on a collision gas which does not stick to the cluster surface, such as argon. Molecules like CO, O_2 or CH_4 are sticky and may adsorb or react upon collision. Reactivity is dependent on a cluster's size and charge, and very difficult to predict. As in CID, charged clusters may be stored in a Penning trap, ICR cell or ion guide; neutral clusters react in a fast flow reactor.

Riley and coworkers suggested that the number of molecules adsorbed to a cluster are indicative of the cluster's binding sites and hence geometry [116, 117]. The average number of probe gas molecules adsorbed by each Ni_n^+ cluster size was recorded in a fast flow reactor (figure 1.11). Minima in this plot indicate saturation of successive types of binding site, which are in turn compared to possible

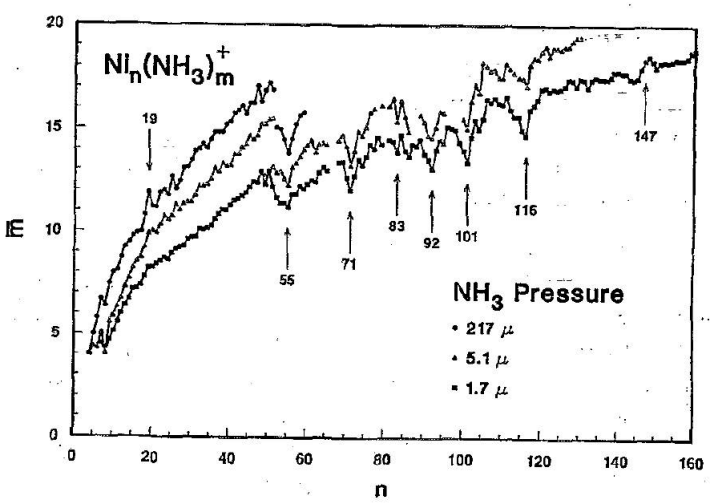

Figure 1.11: Mean number of molecules, $\bar{m}$, adsorbed on Ni_n^+. Dips indicate particularly stable, unreactive clusters. Reprinted with permission from J. Chem. Phys. Vol. 94 (1991) 1882, "The structure of nickel clusters", Parks, Winter, Klots and Riley. Copyright 1991 AIP Publishing LLC.

cluster geometries. The technique has been used to infer the structure of nickel [116], iron [118] and niobium clusters [22]. As the number of adsorbed species grows, the metal skeleton beneath becomes likely to distort, limiting the usefulness of the technique for large clusters [116].

Metal clusters exhibit much more complex reactivity than simple adsorption. For instance, Irion and coworkers observed the special ability of Fe_4^+ to synthesise benzene from ethylene or cyclopropane [7]. Cationic rhodium clusters in the size range $Rh_{9\text{-}18}^+$ are able to fully dehydrogenate benzene with varying efficiency [119], and have a similar effect on small alkanes [23]. Small ruthenium oxide clusters can make CH_4 and H_2O from CO + H_2 while discriminating against reaction with CO_2 [20]. Gold and rhodium clusters can oxidise CO to CO_2 in the presence of O_2 and N_2O respectively [16, 18]. Very many more examples may be found in the literature. All come with restrictions on the charge and size of cluster which can undergo these reactions.

Enormous variations can be seen in the rate of reaction of metal clusters, even clusters of the same charge with the same reactant (figure 1.2). The reactions of metal clusters with D_2 are a useful example. Neutral iron clusters $Fe_{6\text{-}68}$ show rates of reaction with D_2 in a fast flow reactor which vary by five orders of magnitude [109]. However, rhodium clusters in a fast-flow reactor show a fairly smooth increase in their rate of uptake of D_2 with cluster size, proving that reaction rates cannot be predicted from the cluster's reaction partner [120]. Even so, clusters' reactivity with oxygen appears to be generally independent of cluster size [38]. Similarly, the case cannot be made that certain metal clusters are more reactive than others. For instance, rhodium cations show great variation in their

rate of reaction with N_2O, in some cases reacting very slowly indeed, but all Rh_n^+ react with CO approximately at collision rate [21, 121].

Variations in reactivity are rooted in variations in the clusters' electronic and geometric structure. For instance, coinage metal cluster anions show strong odd-even oscillations in their rates of reaction with O_2. This is explicable in terms of the frontier orbitals involved. The cluster cores adopt structures which minimise the electronic energy. The HOMO of odd-numbered cluster anions is full, meaning that donated electrons from O_2 must enter the antibonding LUMO, which is high in energy. Even-numbered cluster anions can accept an electron into the HOMO, which is much more energetically favourable, and these clusters react faster [122]. Correlation of reaction rate with molecular orbital energy is seen elsewhere [120]. Similarly, charge transfer is the key step in reaction of Nb clusters with H_2 and so the rate of reaction is determined by the (strongly cluster size-dependent) ionisation potentials [27]. However, reaction rate is not always attributable to electronic factors.

Reactions with requirements for, say, a particular type of binding site, have rates which are particularly sensitive to a cluster's geometric structure [123]. If a cluster exhibits the same reactivity pattern with a number of different small molecules, geometric factors rather than electronic factors are likely to be controlling the rate. For example, iron clusters show the same pattern in reactivity with H_2 and D_2O [118]. Dehydrogenation of alkanes and reduction of N_2O by Rh_n^+ show minima at the same cluster sizes [21, 23]. Similarly, observation of the same pattern of reactivity regardless of a cluster's charge state indicates a geometrically-controlled rate. Cationic and neutral niobium clusters have minima in their reactivity towards H_2 at the same cluster sizes [22]. Minima also appear at the same cluster sizes in the rate of benzene physisorption on $Nb_n^{+/-}$ [124].

1.5 Theoretical treatment of metal clusters

Small metal clusters are interesting precisely because they do not behave like the bulk. Their bonding is neither metallic nor covalent, and multiple low-lying geometric isomers are often observed at some cluster sizes [26, 91, 113]. Theoretical models must be sought to describe these clusters.

In 1984, a very simple theoretical model was proposed to account for the 'magic number' abundances of certain alkali metal clusters [77]. The model neglects the ionic core's structure entirely, treating it simply as a spherical positive potential. The electrons are treated as a homogeneous electron gas, or 'Jellium', and hereafter this simple model will be referred to as the 'Jellium model'. The potential

used is of the form [77]:

$$U = -\frac{U_0}{e^{(r-r_0)/\epsilon} + 1}, \tag{1.2}$$

where U_0 is the sum of the Fermi energy and the work function of the bulk, r_0 is the radius of the cluster calculated from bulk parameters and ϵ is a fitted parameter describing the potential at the edge of the sphere. The Schrödinger equation may be solved self-consistently within these assumptions to give a series of atomic-like orbitals. [78] The relative energy ordering of each of these orbitals has been calculated to be: 1s < 1p < 1d < 2s < 1f and so on [77]. As a result of electronic shell-closing, clusters with 2, 8, 18, 20, 34 electrons (and so on) are expected to have special stability.

These predictions agree strikingly well with experimental 'magic number' abundances, ionisation potentials and electron affinities of coinage and alkali metal clusters [1, 29, 30]. Many of these experiments have been discussed in the preceding sections. The similarity of the electronic structures of alkali and coinage metal clusters to atomic electron shell structure has led to their being called 'superatoms'. Clusters with an s^1 atomic electron configuration obey the modelling assumption of a perfectly-conducting cluster remarkably well. These clusters' ionic cores are able to respond to ionisation or electron attachment and maintain the perfectly smooth potential well required by the Jellium model [125]. The model has some limited success for metals other than those in groups I and XI [72].

Even in groups I and XI, agreement between the Jellium model and experimental data is imperfect [1]. It was improved by Clemenger, who adapted the Nilsson model of nuclear structure to allow for core distortions [126]. Distortion of the positive cluster potential can alter level ordering and spacing, so its precise shape is important. The Clemenger-Nilsson model explains the 'substructure' in abundance spectra by accounting for Jahn-Teller distortions in the spherical potential of open-shell clusters. However, it does not work well for n≤12 clusters whose distortions do not create perfect ellipsoidal potentials [1].

Replacing the electron cloud with an electron gas is also the first step towards a more rigorous theoretical treatment of clusters: density functional theory (DFT) [78]. The electron density has x, y, z and spin coordinates. It is therefore a more tractable description of the electron cloud than one which uses all the valence electrons, each having x, y, z and spin coordinates. The Jellium model simplifies the electron density by assuming it is a perfectly uniform function, while DFT allows for the treatment of an *inhomogeneous* electron density function. DFT is more sophisticated than the Jellium model, not

only in treating inhomogeneities in the density function, but also in abandoning the spherical positive potential. The core's potential may be constructed from individual atomic potentials.

The first treatment of an inhomogeneous electron gas was proposed by Hohenberg and Kohn [127]. They showed that a functional (a function of a function) existed which could extract the ground state energy of the system from the electron density function. However, although they did not have the exact functional. This density functional could be expressed 'in terms of the correlation energy and linear and higher order polarizability of a uniform electron gas'. This formulation only covered closed-shell systems; Kohn and Sham extended it to cover open-shell systems in which the number of spin-up and spin-down electrons differed [128]. Kohn and Sham proposed a set of one-electron orbitals which could be solved in a self-consistent field [128]. The electron density is then found by summing the squares of the occupied orbitals [129]. The electrons' kinetic and Coulomb energies are calculable directly from this density function. The exchange-correlation energy, however, is not; it must be extracted from the density function using a functional and its exact value depends on the functional used. Although the exchange-correlation energy is a small fraction of the total, it is key to the system's physical and chemical properties [130].

Many different functionals are available, and have been visualised according to their increasing complexities as a ladder [129]. On the lowest rung is the local density approximation (LDA). The LDA calculates the local spin density of an inhomogenous electron gas by using the known analytical form of the electron density of a homogenous electron gas [129, 131]. The next level of complexity (or 'rung on the ladder') includes the gradient of the spin density as a parameter. These functionals are generalised gradient approximations (GGAs) [132]. Further rungs include meta-GGAs which also include the second derivative of the spin density, and are described in reference [129]. Corrections to the functional do not all rely on derivatives of the spin density. Another kind of correction altogether is the use of a 'hybrid functional' which includes a fraction, eg 10%, of Hartree-Fock exchange. DFT calculations performed in this thesis use the hybrid meta-GGA functional TPSSh. TPSS or Tao-Perdew-Staroverov-Scuseria is a meta-GGA functional [133]; its hybrid version, TPSSh, includes 10% Hartree-Fock exchange [134].

Although an improvement on the Jellium model, DFT is not a perfect theory and has known failings [135]. Examples include the inability of a single functional to perform well for many systems, and the fact that it does not properly account for dispersion forces. Despite its inaccuracy, DFT is often used for metal clusters as its computational cost scales slowly with system size [39]. It has been used for

comparison with experimental results to determine cluster structure in many of the studies mentioned thus far (figure 1.9, for example). To address the failings of DFT, many different density functionals have been optimised for different purposes and none emerges as best in an extensive review [39].

Small coinage metal clusters have relatively simple electronic structures and thus are accessible to better-quality calculations than DFT. Small copper clusters have been particularly well-examined [3]. In the early 1980's, the best calculations available on small copper clusters were all-electron self-consistent field calculations [136, 137]. In 1986, *ab initio* calculations were performed by Langhoff and coworkers on Cu_3 [138]. More recently, time-dependent DFT calculations have been performed to examine the excited states of copper clusters [139]. Theoretical studies of small copper clusters have been summarised elsewhere [140, 141].

1.6 Thesis overview

Two very different experimental techniques have been used to study transition metal clusters during this project. Velocity map imaging (VMI) is a method of examining the exit channels of photodissociation. For CuO, it leads to determination of the products' electronic states and accurate dissociation energies. Unique assignment of product states is only possible where the options are relatively limited. This is particularly important in our experiments, in which the neutral parent species cannot be mass-selected and so the photodissociation cofragment must also be deduced. Small coinage metal clusters with a limited number of possible dissociation pathways, and sparse electronic states, are best suited to VMI. However, even Cu_3 photodissociation is difficult to unravel using VMI. To study larger clusters, we turn to Fourier-Transform Ion Cyclotron Resonance (FT-ICR). Charged clusters may be mass-selected, allowing their individual decay processes to be isolated from all others. FT-ICR monitors only the masses of ionic products, not their electronic states.

Chapter 2 describes spectroscopic and VMI studies of CuO. Across the whole energy range studied, 18000 to 24000 cm^{-1}, CuO appears to dissociate into a single channel, enabling a very precise determination of its dissociation energy, D_0(CuO). Examination of the anisotropies leads us to concur with previous workers: spin-orbit coupling in CuO is strong enough to make Hund's case (a) an inadequate description of the system.

Chapter 3 gives the results into an extensive investigation of the photodissociation of Cu_2 and Cu_3 in the visible region. At low light intensities, a simple spectrum is observed in the Cu_2^+ channel

arising from resonant ionisation of Cu_2 via its B and C electronic states. At high laser intensities, much additional structure is observed in both Cu^+ and $Cu_2{}^+$ channels. A combination of spectrum and image fitting in both channels suggests that the structure arises from single-photon dissociation of Cu_3. The Cu_2 product is vibrationally excited, and resonant photoionisation and photodissociation from this multitude of vibrational states produces complex spectral structure. Ground-state Cu_2 from the beam also dissociates, producing a series of very sharp rings in the Cu^+ images and permitting a very accurate determination of $D_0(Cu_2)$.

Chapter 4 documents collision experiments performed on $Rh_nO_mN_2O^+$ (n=5, 6; m=0, 1). Two products are observed: $Rh_nO_m{}^+$, arising from N_2O desorption, and $Rh_nO_{m+1}{}^+$, due to N_2O reduction and N_2 desorption. Upon collision with argon, N_2O reduction is the preferred channel and $Rh_nO_{m+1}{}^+$ is the major product. $Rh_5N_2O^+$ is an exception to this rule. The energy transferred upon argon collision is difficult to quantify, and ^{13}CO is used as an alternative collision gas as it chemisorbs, depositing a fixed, calculable amount of energy into the cluster. Upon collision, the same reactions as mentioned above may occur. Surface oxidation of CO with loss of CO_2 is seen in addition, and is particularly fast on the $Rh_5{}^+$ surface.

Chapter 5 describes black-body infrared radiative dissociation (BIRD) experiments on $Rh_n(N_2O)_m{}^+$. This method is a valuable, complementary alternative to the collision experiments in chapter 4 as the rate of energy deposition into the cluster is approximately calculable and the system remains unperturbed. It also forms a useful contrast with previous IR-MPD experiments as the slow absorption regime prevents entropic factors from determining the rates, giving a better understanding of the relative barriers to the various decay channels. The BIRD mechanism is proven in two ways: by repeating the experiment at low temperature, and by observing the change in dissociation rate with the number of adsorbed chromophores. The $Rh_5(N_2O)_m{}^+$ (m=1-5) rates are simulated using a master equation, and surprisingly good agreement is obtained with reaction barriers calculated by density functional theory.

Chapter 6 summarises the conclusions drawn from chapters 2-5, and discusses the further work suggested by this thesis. In particular, additional simulations might aid understanding of the experimental results contained in chapters 4 and 5.

Chapter 2

Velocity Map Imaging of Copper Oxide Photofragments

Copper oxide, CuO, has been investigated spectroscopically by 1+1′ photodissociation. An OPO in the visible region is used to excite ground state X $^2\Pi_i$ CuO present in our molecular beam to some of its many known electronic excited states. Absorption of a UV photon dissociates the CuO* thus formed, and absorption of subsequent UV photons ionises the copper atoms formed by dissociation. This process has been studied by velocity map imaging (VMI), which reveals that all observed excited states of CuO dissociate into the same channel, Cu*($^2D_{3/2}$) + O*(^1D). Extrapolation of the total kinetic energy release (TKER) upon dissociation to zero kinetic energy allows us to calculate the ground-state dissociation energy, D_0(CuO), of CuO. It is found that D_0(CuO)=3.041±0.030 eV. Our assignment of the system is tested by tuning the UV laser to a resonant transition in the Cu* produced, $3d^{10}5p\ ^2P_J{}^0 \leftarrow 3d^9 4s^2\ ^2D_{3/2}$, whereupon significant enhancement in the Cu^+ signal is observed in the presence of the visible laser. This work has been published in Physical Chemistry and Chemical Physics [142].

2.1 Experimental Technique

2.1.1 Development of Velocity Map Imaging

Velocity map imaging (VMI) was developed by Eppink and Parker in 1997 [143] and has since become a popular technique for ion imaging in the gas phase. VMI represents a high-resolution version of an ion imaging technique first reported by Chandler and Houston in 1987 [144]. Their setup consisted of a repeller plate followed by a pair of grounded grids, as shown in fig 2.1 (a). The grids

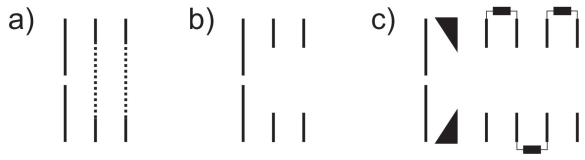

Figure 2.1: Electrodes typically used in ion imaging. a) consists of a repeller plate and two grounded grids, and is the type originally used by Chandler and Houston. [144] b) has open repeller, extractor and ground plates as built by Eppink and Parker. [143] c) is a repeller, conically-shaped extractor and a stack of electrodes linked by resistors stepping the potential down to ground.

were used to ensure a uniform electric field between each of the plates, but their presence was not wholly advantageous: their presence in the ions' path blurred the image and reduced the ion transmission. In the original study, a neutral beam of CH_3I passed through a hole in the repeller, where it was photodissociated and the CH_3 fragment ionised by Nd:YAG and dye laser pulses respectively. Upon photodissociation, any 'spare' energy left over after breaking the CH_3-I bond and populating the fragments' internal energy states must be conserved and so becomes kinetic energy:

$$h\nu_{\text{diss}} = D_0(\text{CH}_3 - \text{I}) + E_{\text{int}}(\text{CH}_3) + E_{\text{int}}(\text{I}) + E_{\text{kin}}. \tag{2.1}$$

In equation (2.1), $h\nu_{\text{diss}}$ is the energy of the dissociating photon (the fourth harmonic of a Nd:YAG laser), $E_{\text{int}}(\text{CH}_3, \text{I})$ are the internal energies of the CH_3 and I products and E_{kin} is the kinetic energy released. Momentum is also conserved upon dissociation:

$$m_{CH_3} v_{CH_3} = m_I v_I, \tag{2.2}$$

where m_i and v_i are, respectively, the mass and velocity of species i. Once formed, the CH_3 fragments were ionised before passing through the grids and were recorded by a spatially-sensitive detector.

Eppink and Parker were the first to realise that the grids could be removed, and developed an asymmetric inversion lens consisting of three open lens electrodes: a repeller, an extractor and a ground plate (see fig. 2.1 (b)). Although the field lines between the plates are now bent, their curvature can be controlled by varying the potentials applied to the repeller and extractor. Eppink and Parker found that, with appropriate potentials, ions passing through this setup could be 'space-focussed'. A three-plate electrode setup is typically operated in a Wiley-McLaren arrangement such that ions with the same mass (and hence the same velocity in the molecular beam) travelling through the electrodes are accelerated in order to arrive at the detector at the same time. This is a temporal focus. Space focussing means that ions passing through the electrodes are accelerated such that *ions with the same*

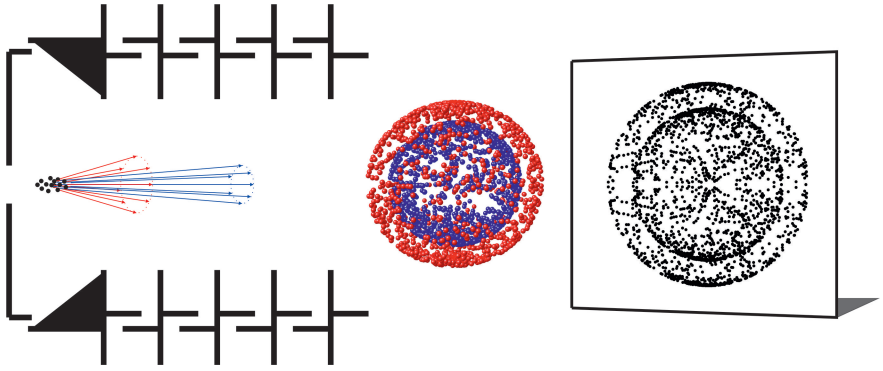

Figure 2.2: Ion trajectories in an imaging setup. Neutral species enter the electrode setup and are photodissociated, and ionised, between the repeller and extractor plates. Each fragment has some kinetic energy and accelerates away from its cofragment. Although the fragment's kinetic energy may be well-defined, its direction of recoil is not and each fragment species collectively forms a so-called 'Newton sphere' which travels along the electrode setup. Two nested spheres are shown by way of example. At the detector, the Newton spheres are crushed into a 2D image.

off-axis velocity are mapped to the same point on the position-sensitive detector. Temporal focussing adjusts ions' velocities in the direction of the molecular beam to ensure a specific time of arrival at the detector, whereas space focussing adjusts the off-axis velocity to ensure a specific arrival location. Using open-lens electrodes with voltages tuned for space focussing of ions, Eppink and Parker produced much sharper images than had been seen previously. They were able to resolve the different dissociation channels following photodissociation of O_2 around 225 nm, corresponding to different electronic states of the atomic products [143, Fig. 5].

The ions' journey from inception to detection is drawn in figure 2.2. The Oxford electrode setup is depicted here, but the principle is general. Ionic fragments are created by photodissociation and photoionisation of neutral species between the repeller and extractor plates. A specific kinetic energy is released upon fragmentation, which, together with the mass of the dissociation partner (cofragment hereafter), determines the magnitude of the ion's initial recoil velocity from its cofragment. The direction of the ion's velocity is less well-defined and so collectively each dissociation channel creates an expanding sphere of ions, called a Newton sphere. As the Newton spheres pass through the electrode setup, they expand. In the absence of any electric field, ions with the same initial off-axis velocity appear at larger radii if they are produced on the side of the sphere further away from the detector rather than the side of the sphere close to the detector. This is because ions on the 'rear half' of the Newton sphere have more time to expand outwards from the beam. The electric field created by the electrode stack is tuned to reduce the off-axis velocity of ions which travel more slowly towards the detector. Consequently, ions with the same initial off-axis velocity hit the same point on the detector

(spatial focussing). This creates a sharp 2D image.

2.2 Applications of Velocity Map Imaging

Thus far, VMI has been described as a technique whereby the ionised fragments of a photodissociated neutral molecule may be imaged. In reality, VMI is more generally applicable [104]. At its inception, VMI was used to image the photoelectrons, as well as the oxygen cations, produced by three-photon excitation of ground-state oxygen at around 225 nm. [145] An electron has such a low mass that small differences in the kinetic energies of photoelectrons manifest themselves as large differences in the initial off-axis velocities:

$$v_e = \sqrt{\frac{2E_{kin}}{m_e}}. \tag{2.3}$$

Photoelectron imaging is therefore sensitive to small differences in kinetic energy release and may be used to image different vibrational states of a molecule after photoionisation [146]. The principles of VMI are explained in section 2.2.2.

Introduction of a second molecular beam to the setup allows the study of interaction between molecular species by VMI (as opposed to the study of one species' interaction with a photon, as above). In this case, the detector is moved from an in-line position to one perpedicular to the crossed beams. Non-reactive and reactive collisions may be studied in such a setup. As an example of the former, Lorenz, *et al.* used VMI to study inelastic scattering in the HCl-Ar system. HCl and Ar molecular beams were crossed such that their point of intersection fell between the repeller and extractor plates of the electrodes. Rotational states of the scattered HCl product were selectively resonantly ionised and extracted through the electrode stack to the detector [147]. The size of the ring showed how much collision energy was converted to kinetic energy, and the angular distribution of HCl^+ allowed differentiation between forward- and back-scattering collisions (*i.e.* collisions probing the attractive and repulsive parts of the Ar+HCl potential). Attractive collisions result in forward scattering.

Reactive interactions may also be studied by VMI in a crossed molecular beam experiment [148]. For instance, Ahmed, Peterka and Suits studied the abstraction of a hydrogen atom from methanol by a chlorine atom [149]. Again, the detection of products with spatial resolution allowed these workers to extract more than just the branching ratio between the two H-abstraction positions from their experiments. The collision energy was known, and examining the size of the rings produced by the CH_3O^+/CH_2OH^+ fragments yielded the fraction of that energy that was converted to kinetic energy.

The internal energy of the fragments was thus deduced. Additionally, the angular distribution of products gave some information about the dynamics of the process. Strong side- and back-scattering indicated a direct process rather than formation of a long-lived CH_3OH-Cl complex.

While the applications of VMI have proliferated, its methodology has also been developed. One of the major difficulties associated with VMI is the mathematical reconstruction of the Newton spheres and their associated kinetic energies from the 2D projection recorded experimentally. This will be dealt with fully in section 2.2.2. Experimental approaches designed to remove the need for such post hoc processing by selectively detecting only the central portion of the Newton sphere are called slice imaging. When only the central cross-section of the sphere is present in the image, the need to reverse the 'pancaking' effect of crushing the sphere into a flat image is removed. Slice imaging has been effected by selectively ionising only the central portion of the sphere using sheet ionisation [150] and by time gating the detection over a very narrow window [151]. Slice imaging has since been used to investigate variation in a time-resolved ion signal [152, 153, 154].

2.2.1 Our apparatus

Our setup is somewhat different from that used by Eppink and Parker. Our molecular beam is produced not from a gas bottle but from a Smalley/Bondybey-type laser ablation source [56] as described in the introduction and shown in fig. 2.3. The system operates at 10 Hz. A disc-shaped copper target is ablated by a pulsed 532 nm Nd:YAG source (Litron Nano, 10-12 mJ/pulse) which is focussed at

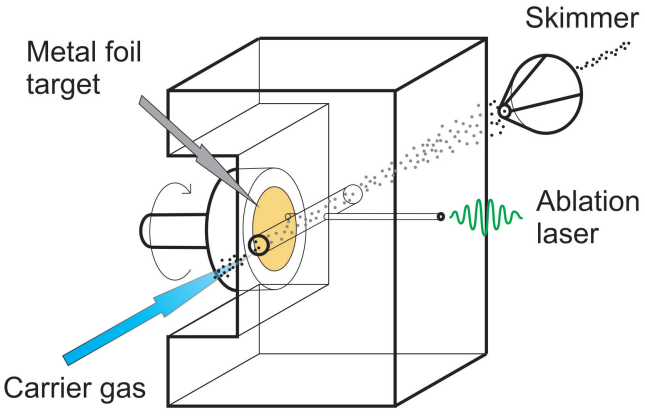

Figure 2.3: The cluster source. The disc-shaped metal target is continuously rotated so as to present a fresh surface to the ablation laser. Carrier gas is pulsed into the system and entrains the plasma produced at the metal surface, facilitating collisions and therefore cluster formation. The beam emerges from the clustering block and undergoes a supersonic expansion. It is then skimmed to form a collimated, cold beam.

or near the target's surface to a beam waist of less than 1 mm. The target is constantly rotated so as to provide a fresh surface for ablation. A pulse of helium gas containing approximately 10% N_2O is produced by a Jordan valve with a backing pressure of 4 bar and timed to entrain the copper plasma produced by ablation. The gas mixture travels a further 18 mm through a 3 mm diameter channel in the ablation block, during which time some three-body collisions occur allowing clusters to form. The mixture then expands supersonically into a vacuum, and is skimmed to form a cold, collimated beam.

The skimmed beam enters an electrode array, shown schematically in fig. 2.1 (c); the electrode array differs from those previously discussed in that it contains a series of electrodes joined by resistors stepping down to ground, rather than a single ground electrode. This minimises the penetration of the electric field between the extractor and ground plate into the VMI region. The electrodes also differ from a conventional stack in that the extractor plate is cone-shaped rather than being a flat ring electrode. Its shape is illustrated in the cut-through of the stack shown in figure 2.2. The unusual extractor shape was implemented by the Mackenzie group because simulations suggested that it would minimise the setup's magnification factor, a correction factor required to account for distortion of the ions' path by the electric field. This is indeed the case; we find our magnification factor to be very close to 1, whereas Eppink and Parker's magnification factor varied between 1.3 and 1.4, depending on the details of their electrode arrangement [143].

Neutral molecules are photodissociated and ionised between the repeller and extractor plates by either visible or UV photons from 10 ns pulsed laser systems. The visible light is the output of a 355 nm-pumped optical parametric oscillator (Continuum Panther), producing typically 8-12 mJ/pulse in the ionisation region, depending on output wavelength. The UV laser is the frequency-doubled output of a dye laser (Sirah Cobra Stretch). The dye used was a Coumarin, C540a (also known as C153) in ethanol, and the doubled output was typically around 2 mJ/pulse in the 260-280 nm region. Any positive ions produced are then focussed by the VMI lens onto the detector, which is a commercial system (Photek) and consists of a pair of MCP plates coupled to a phosphor screen. Cascades of electrons are liberated each time an ion hits the MCPs, which in turn cause the screen to phosphoresce. Each flash of light is recorded, along with its position, by a 580x776 pixel CCD camera. The whole system is kept under vacuum by differential pumping using turbomolecular pumps. During operation, the source region reaches a pressure of approximately 10^{-5} mbar due to the high gas load from the Jordan valve, while the VMI region stays at 10^{-7} mbar. The detection region's operating pressure is

very slightly lower, around 10^{-8} mbar. The whole system is illustrated in fig. 2.4. This figure also shows a pair of retractable MCP plates preceding the VMI detection region. When these plates are lowered into the molecular beam, the voltages across the repeller and extractor are adjusted to form a Wiley-McLaren-type arrangement in order to achieve a temporal focus of ions with the same mass, rather than a spatial one, at these MCP plates. Their output is recorded on an oscilloscope (Lecroy Waverunner) and enables us to record mass spectra as a function of time-of-flight; mass spectra are processed by a custom-built LabView routine.

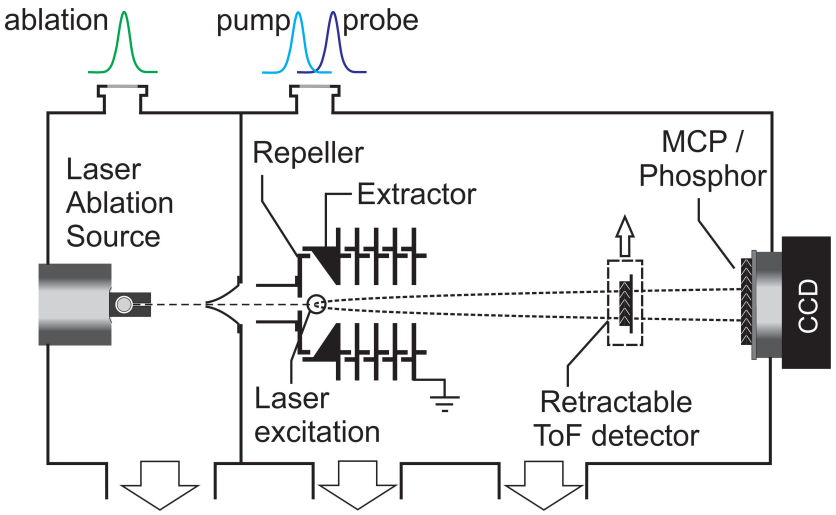

Figure 2.4: A diagram of our VMI instrument. After being produced in a Smalley/Bondybey-type source, clusters enter the VMI region of the instrument. They are photodissociated and ionised between the repeller and custom-shaped extractor plates, and the charged fragments are then focussed onto a pair of MCPs coupled to a phosphor screen and a CCD camera.

2.2.2 Image processing

Images recorded by the CCD camera do not directly yield information about dissociation processes. They are 2D projections of the 3D spheres of ions created when photodissociated species fly apart from each other in all directions. As the fragments approach the detector, each sphere (representing a pair of ion fragments in specific quantum states) expands perpendicular to the TOF axis. Upon striking the detector, the spheres are compressed along the TOF axis, forming a 2D 'pancake'. Fortunately, if the photodissociating laser's electric vector is parallel to the detection plates, the image will be cylindrically symmetric about the laser polarisation vector. It is possible to reconstruct the spheres from the 2D image by virtue of their cylindrical symmetry. Indeed, a method of doing so is well-established; the Abel transform (and its inverse) is used in many areas of science and engineering and

was used to analyse ion images before VMI was developed [155]. The Abel transform calculates the projection of a sphere onto a plane, and its inverse describes a sphere given its 2D projection [156].

The inverse Abel transform can fail or create artificial structure in the reconstructed image, particularly in noisy conditions; it is therefore desirable to modify the calculation [157]. One method, pBasex, uses a basis set of Gaussian functions to create a 3D sphere and then performs a forward Abel transform (a "well-behaved operation") to fit the 2D projection data [158, 159]. Methods have been developed to numerically simulate the image, making no use of the Abel transformation at all [160, 161]. The onion-peeling algorithm is another alternative; it divides the 2D image into a series of thin concentric rings (limited by the CCD camera's pixel size) [162]. From the intensity and radius of the outermost ring, the initial velocity vector of the contributing ions can be deduced; the contribution made by those ions to all other points on the detector can therefore be subtracted. Each ring is considered in turn, from large to small radii, fitting its ion sphere contribution and then subtracting its intensity from the image.

Our method, implemented in a custom-built LabView routine, uses the onion-peeling algorithm. However, instead of constructing each 3D sphere in the iteration from scratch, they are constructed from Legendre polynomials, which greatly speeds up the peeling process [160, 163]. The raw 2D image is described by two variables: radial distance from the image centre, r, and the angle subtended by that radius from the vertical (α). We formulate the image as consisting of a finite number of component images, each having a radius less than the maximum radius R:

$$G(R,\alpha) = \int_0^R g(r \leq R, \alpha) dr. \tag{2.4}$$

$G(R,\alpha)$ is easier to deal with in polar coordinates, so each of the Cartesion coordinates is mapped to its polar location, such that $G(R,\alpha) \rightarrow H(R,\theta)$ [160]. The process is illustrated in figure 2.5. Just as the total image G is construed as a number of summed smaller images g, in polar coordinates the raw image $H(R,\theta)$ is described as a sum of smaller images in polar coordinates, $h(r \leq R, \theta)$. The

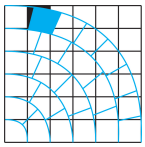

Figure 2.5: An illustration of Cartesian to polar coordinate mapping, after *Rev. Sci. Instrum.* 80(5):76-87, 2003. Each pixel in the Cartesian array is mapped to the pixel in the polar grid that best overlaps it. In this example, the black-shaded square maps to the blue-shaded arc.

function describing the constituent image which extends out to the largest ring, $h(r = R, \theta)$ is fitted to a Legendre polynomial in a process analogous to the numerical fitting of basis sets to an image. The fitted polynomial is transformed back into Cartesian coordinates to $g_{fit}(r \leq R, \alpha)$ which is subtracted from the original image:

$$G^{\ddagger}(R, \alpha) = G(R, \alpha) - g_{fit}(R, \alpha). \tag{2.5}$$

The fitting procedure iterates over r, subtracting $g_{fit}(R, \alpha)$ and then successive $g_{fit}(r < R, \alpha)$ from $G^{\ddagger}$ ($G^{\ddagger}$ being the remainder of the original image after previous subtractions) until r=0, at which point the image is said to have been deconvoluted.

Having deconvoluted the image, the variation in signal intensity with radial distance from the image centre is known. To calculate the kinetic energy of ions creating a peak at radius r in this distribution, the program requires a number of inputs, namely: t, the ions' time of flight from photodissociation to the detector; N, a magnification factor which accounts for the distortion of the ions' path due to the electrode stack; and m, the ions' mass. The off-axis velocity, $v_{\perp}$ is determined from r, t and N:

$$v_{\perp} = \frac{r}{Nt}, \tag{2.6}$$

and the kinetic energy release (KER) may be determined from $v_{\perp}$:

$$KER = \frac{1}{2} m v_{\perp}^2. \tag{2.7}$$

In the present experiments, N could be determined internally, because the photon orders of the observed dissociation processes were known. N was therefore calculated from the correction factor needed to extract these photon orders. N thus obtained was consistent with the N found by examination of our group's previous 'standard' system, Au_2 [105].

The kinetic energy carried by a single fragment is not enough to describe the energetics of the system; for that purpose, the total kinetic energy release or TKER must be calculated, according to:

$$TKER = KER(1) + KER(2) = \frac{1}{2} m_1 v_{\perp,1}^2 + \frac{1}{2} m_2 v_{\perp,2}^2. \tag{2.8}$$

Fortunately, if the KER of one fragment is known from equations (2.6) and (2.7) then the TKER can

be calculated from this and the masses of both fragments by conservation of momentum:

$$TKER = KER(1)\left(\frac{m_1 + m_2}{m_2}\right). \tag{2.9}$$

Thus the energy of the photodissociation process can be fully described in terms of the number of photons absorbed, $nh\nu$, the dissociation energy of the parent, D_0, the internal energy of the fragments, E_{int} and the TKER.

$$nh\nu = D_0 + E_{int}(1) + E_{int}(2) + TKER. \tag{2.10}$$

Equation (2.10) shows that, for a particular pair of quantum state products, a plot of TKER vs $h\nu$ will have a gradient n. If the fragments' internal energy can be determined, D_0 may be calculated.

The steps described above, from experimental data to TKER spectrum, are illustrated in figure 2.6. Ion Newton spheres, each sphere generated by a different photodissociation pathway, are shown in panel (i). The example spheres of (i) are shown with vertical anisotropy in order to illustrate how the spheres are contained within one another. Anisotropy is a non-uniform angular distribution of the fragments and will be discussed more fully in section 2.5.3. At the detector, the spheres of (i)

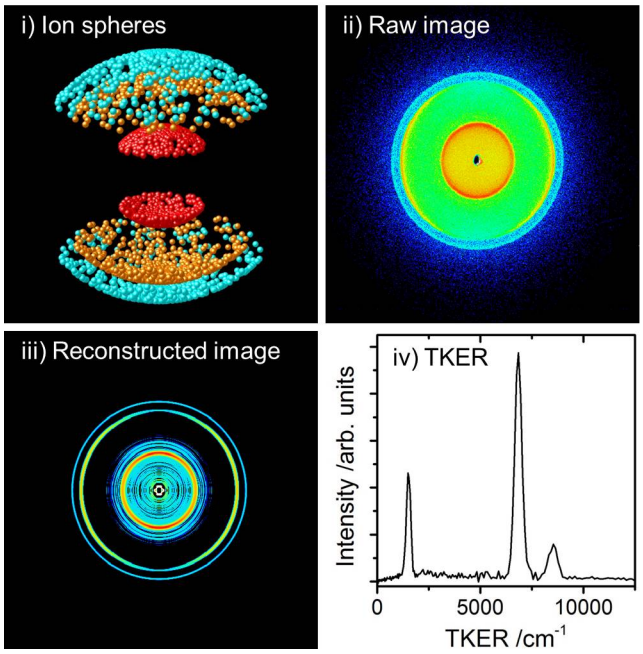

Figure 2.6: Conversion of ion intensity to TKER spectra. (i) The ion spheres. Three nested spheres are shown with vertical anisotropy; this is merely to allow the reader to see all three spheres and is *not* representative of the anisotropy in the images. (ii) Raw data. (iii) A reconstructed image, obtained by the onion peeling algorithm from the raw data. (iv) A TKER spectrum obtained from the reconstructed image, showing the three peaks arising from the three spheres in (i).

are crushed into a 2D image. The raw image is shown in (ii). An onion-peeling algorithm is used to reconstruct the spheres from the raw image, and thus to create a reconstructed image consisting only of the central slice through the spheres. The reconstructed image is shown in (iii). A common pitfall of the onion peeling program is that it can create structure out of noise; the blue background at the centre of (iii) arises from the peeling algorithm creating imaginary ion spheres from noise at the image's centre. Finally, using the information from the reconstructed image, signal intensity is plotted as a function of distance from the image centre. This distance is converted into a kinetic energy using equations (2.6) to (2.9), yielding the TKER plot in (iv). The central pixel is the one which creates the TKER plot with the narrowest peaks.

2.2.3 Errors

The uncertainty in a VMI measurement for a single fragmentation pathway manifests itself in the width of the peaks in the kinetic energy release spectrum. This is limited experimentally by the accuracy to which the position of ion impacts on the detector can be measured, and is determined by pixel density on a top-grade CCD array to around 0.1% [104]. Additional variations in the fragments' off-axis velocity may be caused by variations in the parent ion's energy. We see vibrationally cold clusters in our beam, but a number of rotational states may well be populated. The spread in the parent ions' kinetic energy is generally small and must be considered only in the case of crossed molecular beam imaging. Inhomogeneities in the electric field and 'space charge' effects (repulsion of like-charged ions in the same small voltage) also contribute to uncertainties in the off-axis velocity. The observed limiting resolution is therefore of the order of a few percent [104]. Additionally, our onion peeling procedure introduces some small errors when mapping Cartesian to polar coordinates [163]. Vibrational resolution is therefore only achievable in the case where a light atom is observed recoiling from a heavy one.

2.3 Previous Work on CuO

Among the transition metal oxides, copper monoxide has been particularly well-studied. This is due, in part, to interest in its industrial uses. Copper- and oxygen-containing catalysts $Cu/ZnO/Al_2O_3$ are used to synthesise methanol from a CO, CO_2 and H_2 feedstock [164]. High-temperature superconducting materials based around copper oxides doped with varying quantities of lanthanides, rare earth metals and other heavy atoms have been developed [165, 166, 167]. Understanding the bonding in

simple copper monoxide is key to understanding these more exotic materials. Interest in CuO is not limited to the bulk perovskite structures; at the molecular level, copper-oxygen binding is relevant to the study of copper-containing proteins.

The comparatively simple electronic structure of copper makes it an attractive target for spectroscopic studies [168]. $Cu^+(3d^{10})O^-(2p^5)$ has a closed d-shell and hence no complications due to the involvement of d-electrons in bonding. For similar reasons, coinage metal dimers and trimers are among the most thoroughly studied transition metal clusters [3, 169]. The wealth of experimental data available on these species makes them ideal candidates with which to calibrate theoretical methods, leading to a significant body of theoretical work on these species [139]. Reviews of theoretical and experimental work on the transition metal monoxides have appeared periodically, and discuss the relevance of such species to a broad range of fields including astrophysics, catalysis, corrosion and biological processes [170, 171, 172].

Early work on CuO has been fully surveyed by Appelblad *et al.* [173]. The molecule was first observed in 1893 by Hartley, and its rich emission spectrum was the subject of a number of incorrect analyses until Lagerqvist and Uhler studied the $M^2\Pi_i \leftarrow X^2\Pi_i$ transition in 1967 [174]. This study turned out to be the key to the spectrum. Appelblad in Stockholm, and Pinchemel and Lefebvre in Lille, systematically examined the emission spectrum using variations on a conventional hollow copper cathode filled with an oxygen-containing gas mixture [175]. Arc discharges between copper electrodes [176], nitrogen-cooled composite wall hollow cathode lamps [177, 178, 179] and electrodeless discharge through bulbs containing copper and oxygen [174] have all been used as light sources. The cooled cathode is advantageous as it ensures low rotational temperatures. They explored alternative techniques, such as forming CuO in an oven and using a dye laser to excite laser-induced fluorescence [173, 180]. Some fluorescing states are populated efficiently by collisional transfer from higher states that can be laser-excited, so a reasonable pressure of carrier gas is required [181]. As a result, over 15 bands in the visible were characterised by these groups [173, 175, 176, 177, 178, 179, 181, 182, 183, 184]. An extremely helpful diagrammatic summary is given in reference [185] and is reproduced here as figure 2.7.

One particularly interesting aspect of this work is that it emphasises the importance of theory in directing experimental work. *Ab initio* calculations on CuO predicted a low-lying $^2\Sigma$ state, which prompted a search in the infrared part of the CuO emission spectrum. This region had not previously been examined in the gas phase, and the Y state was indeed located [181]. Prior evidence for a new

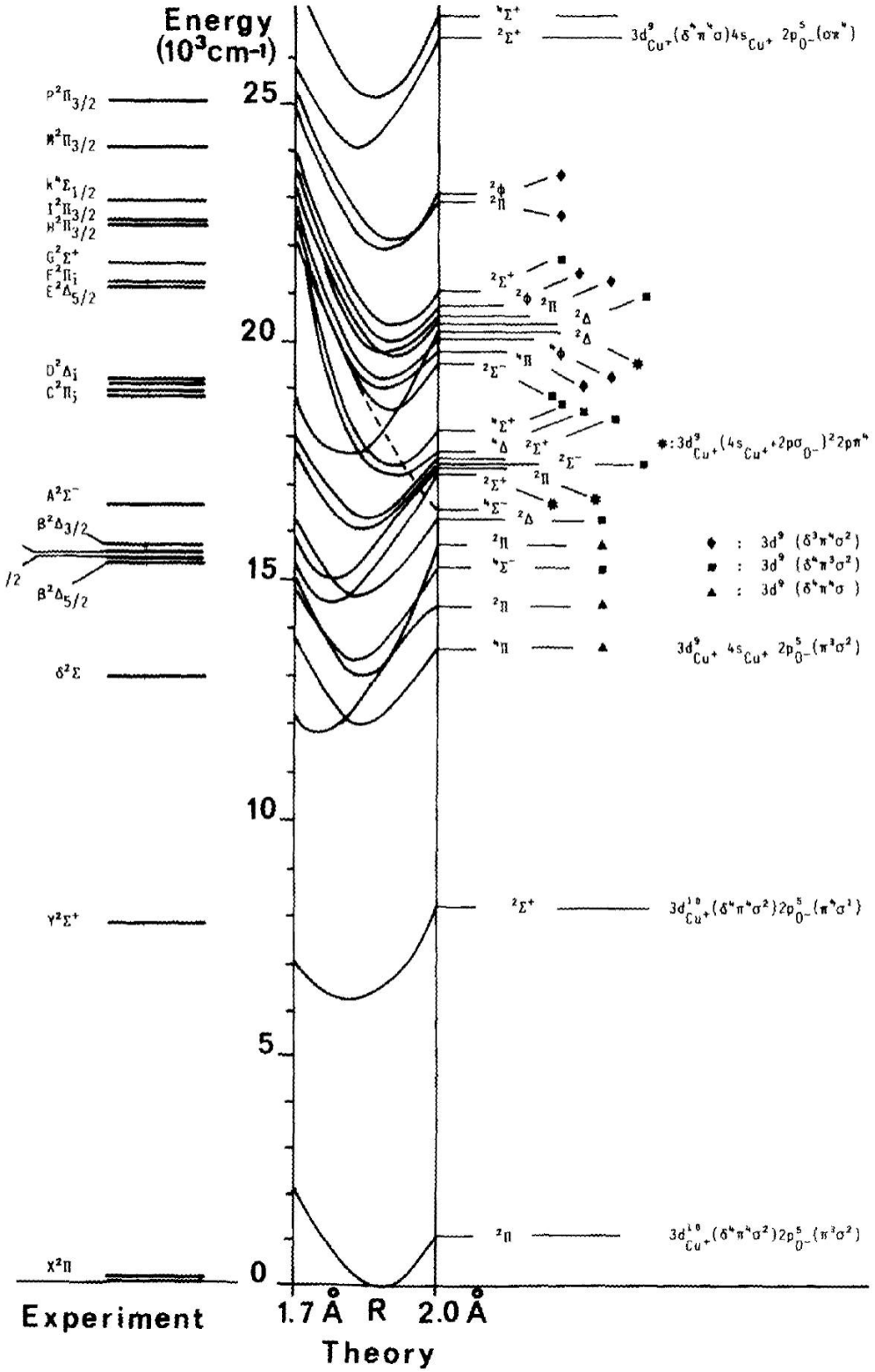

Figure 2.7: Energy level diagram of CuO featuring experimentally-observed (left) and theoretically-predicted states (right). Reprinted from J. Mol. Spec., 101(2), J. Schamps, B. Pinchemel, Y. Lefebvre, and G. Raseev, The electronic valence states of CuO: An energy level diagram, 344-357, Copyright(1983), with permission from Elsevier.

state had also come from matrix studies on CuO, which suggested a state approximately 0.5 eV above or below the $^2\Pi$ state subsequently found to be the ground state [186]. Matrix isolation also provided some of the first evidence for the Π splitting of the ground state [187, 188].

More recent work has been directed toward spectroscopic determination of the electronic structure of the excited states, in order to compare them more directly with theoretical predictions. This includes determination of nuclear hyperfine structure [180], lifetimes [189] and permanent electric dipole moments [190]. Steimle's sub-Doppler measurements of rotational transitions have yielded magnetic and electric hyperfine splittings and Fermi contact parameters [190, 191, 192, 193]. Other more recent developments include the application of Fourier-transform spectroscopy to study vibronic transitions in high resolution [194] and the use of anion photoelectron spectroscopy to probe electronic configuration [195, 196].

Of particular interest here is the dissociation energy of CuO. Most determinations thus far have not distinguished the differing dissociation energies of the spin-orbit components of the ground state. The equilibria between Cu and O_2, NiO/Ni and CuO/Cu were studied in 1972 and yielded D_0(CuO)=2.76±0.22eV [197]. However, subsequent authors concluded that these equilibria were not sufficiently established to provide an accurate value for D_0. [198] In 1974, Appelblad used a Birge-Sponer extrapolation to estimate D_0(CuO $^2\Pi_{3/2}$)=2.83 eV, but concluded, without argument, that this was an overestimate and that 2.48 eV would be more reasonable [176]. In 1991, preliminary results were published by Clemmer on the reaction between Cu^+ and NO_2 which suggested D_0(CuO))=2.85±0.15 eV [199]. In 1994, the observation by Vinckier *et al* that the reaction of Cu with NO_2 was thermoneutral over a significant temperature range implied that D_0(CuO)≈D_0(O-NO)=3.116±0.008 eV [200]. Collision-induced dissociation results gave 2.94±0.12 eV [201].

This thesis is not explicitly concerned with theoretical treatments of copper monoxide and so for a full summary of theoretical work on CuO the reader is directed to Gong's 2009 review of transition metal oxides and references therein [172]. However, a few theoretical papers will be mentioned. In 1983, Bagus *et al.* classified the theoretically-predicted states in manifolds according to the nominal electronic configurations of the constituent atoms [202]. Since these manifolds occupy different energy ranges, this is a particularly useful system of classification. The first good agreement between experiment and theory for ground-state properties was obtained by Langhoff and Bauschlicher in 1986 using configuration interaction and the coupled-pair formalism [203]. Madhavan and Newton made the first substantial efforts to correlate theoretically-predicted with experimentally-known states in 1985; the

enormous number of predicted states means that there are several options for each experimental state [204]. Recently, DFT has been used to calculate spectroscopic properties [205, 206, 207, 208].

2.4 Two-colour spectroscopy

The two-colour ion yield spectrum of our cluster beam was recorded from 410 to 550 nm (approximately 18000 to 24400 cm^{-1}) and is shown in figure 2.8. The general term 'ion yield' is used as no single descriptor covers the numerous processes occurring to produce the spectrum. The visible laser fires approximately 30 ns before the UV laser, the latter being fixed at 267.05 nm, resonant with the Cu_2 J←X($^1\Sigma_g^+$) transition. Both enhancements and depletions are visible in the atom channel, while only depletions are seen in the dimer channel. Depletions in both channels are found to coincide with energies of known electronic transitions in Cu_2: A $^1\Sigma_u^+(\nu)$←X $^1\Sigma_g^+(0)$, B $^1\Sigma_u^+(\nu)$←X $^1\Sigma_g^+(0)$ and C $^1\Pi_u(\nu)$←X $^1\Sigma_g^+(0)$ [209]. Two dips at 20100 cm^{-1} and 21569 cm^{-1} are tentatively assigned as hot bands arising from transitions out of X(ν=1), but given the lack of further hot progressions, this interpretation is not well-founded.

Depletions are due to an 'ion-dip' mechanism illustrated in figure 2.9 (a). In the absence of the visible laser, UV photons (resonant with the Cu_2 J←X transition) are the sole source of excitation of Cu_2. Resonant two-photon ionisation (R2PI) of Cu_2 leaves Cu_2^+ in either its ground state or one of two known excited states [210]. Absorption of a further UV photon dissociates Cu_2^+, making Cu^+. When the visible laser comes into resonance with an electronic excitation of Cu_2 $X^1\Sigma^+_g$, the ground state population is depleted. Consequently R2PI from ground state Cu_2 to form Cu^+ and Cu_2^+ is diminished. Previous work on the copper dimer is discussed in more detail in the next chapter.

The enhancements in the atom channel correspond to vibronic transitions of CuO, and the strongest are labelled in fig. 2.8 [185]. The linewidth of our visible laser is 5 cm^{-1}, which is insufficient to allow rotational resolution of these transitions. However, we see virtually all the lines we might expect in this energy region originating from CuO $X^2\Pi_{3/2}(\nu=0)$, $^2\Pi_{3/2}$ being the lower spin-orbit component of the ground state. Starting at low energy, we see what appears to be a repeated set of three intense peaks. They are indeed connected; the first three are, respectively, C $^2\Pi_{3/2}(\nu=0)$←X $^2\Pi_{3/2}(\nu=0)$, C $^2\Pi_{1/2}(0)$←X $^2\Pi_{3/2}(\nu=0)$ and D $^2\Delta_{5/2}(\nu=0)$←X $^2\Pi_{3/2}(\nu=0)$ while the second three are the transitions to ν=1 in the same three upper electronic states. If the D $^2\Delta_{3/2}$←X $^2\Pi_{3/2}$ transition is present, it is probably obscured by the C $^2\Pi_{3/2}$←X $^2\Pi_{3/2}$ transition; however, it was not observed by Appelblad in

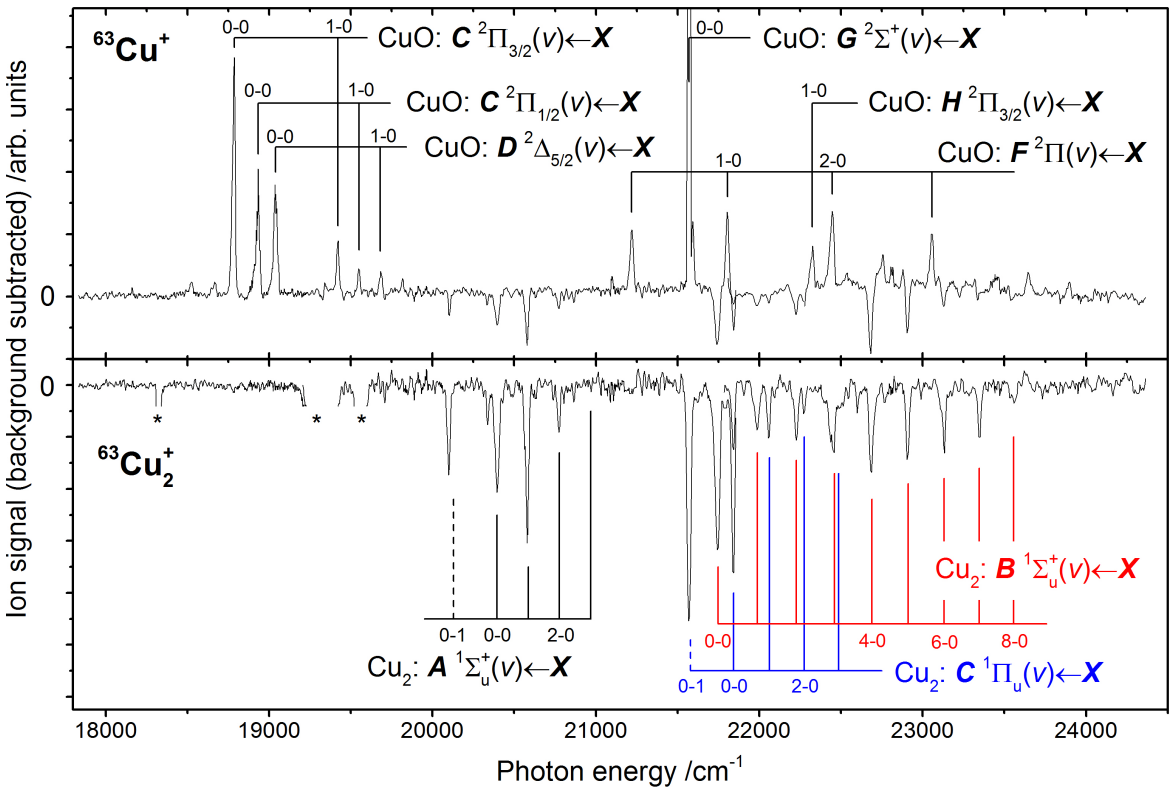

Figure 2.8: Two-colour ion yield spectrum recorded in the $^{63}Cu^+$ and $^{63}Cu_2{}^+$ channels. Depletions in both channels are due to depletion of the X $^1\Sigma_g{}^+$ Cu_2 ground state by the visible laser. This reduces resonant 2-photon ionisation of Cu_2 via its J state. Enhancements in the atom channel arise from dissociation of CuO and ionisation of the Cu fragment. Starred peaks in the dimer channel are artefacts caused by the visible laser creating extremely strong Cu^+ signals, and have been removed.

his study of the C and D states [177]. There is little evidence for any significant population of the upper spin-orbit component of the ground state in our beam. However, the two very small peaks to the red of the previously-discussed C and D transitions are probably the transitions from X $^2\Pi_{1/2}(v{=}0)$ to C $^2\Pi_i(v{=}0)$.

The next line we might expect is for the E $^2\Delta_{5/2}(v{=}0)\leftarrow$X $^2\Pi_{3/2}(v{=}0)$ transition at 21104 cm^{-1}. A very small peak is indeed present at this position. As in the D$\leftarrow$X band, E $^2\Delta_{3/2}\leftarrow$X $^2\Pi_{3/2}$ has never been observed [182]. Again, we do not expect to see E $^2\Delta_{3/2}(v{=}0)\leftarrow$X $^2\Pi_{1/2}(v{=}0)$, as the population of the upper spin-orbit component of X in our molecular beam appears to be low. It is unclear why the E $^2\Delta_{5/2}(v{=}0)\leftarrow$X $^2\Pi_{3/2}(v{=}0)$ transition should be so much weaker than the D $^2\Delta_{5/2}(v{=}0)\leftarrow$X $^2\Pi_{3/2}(v{=}0)$ transition; it may be more forbidden - the Δ state configurations are unknown. The ground state electron configuration of CuO is believed to be $Cu^+(3d^{10})O^-(2p^5)$ [196]. Most of the configurations contributing to the excited states of CuO are believed to have a single hole in the 3d orbital; the

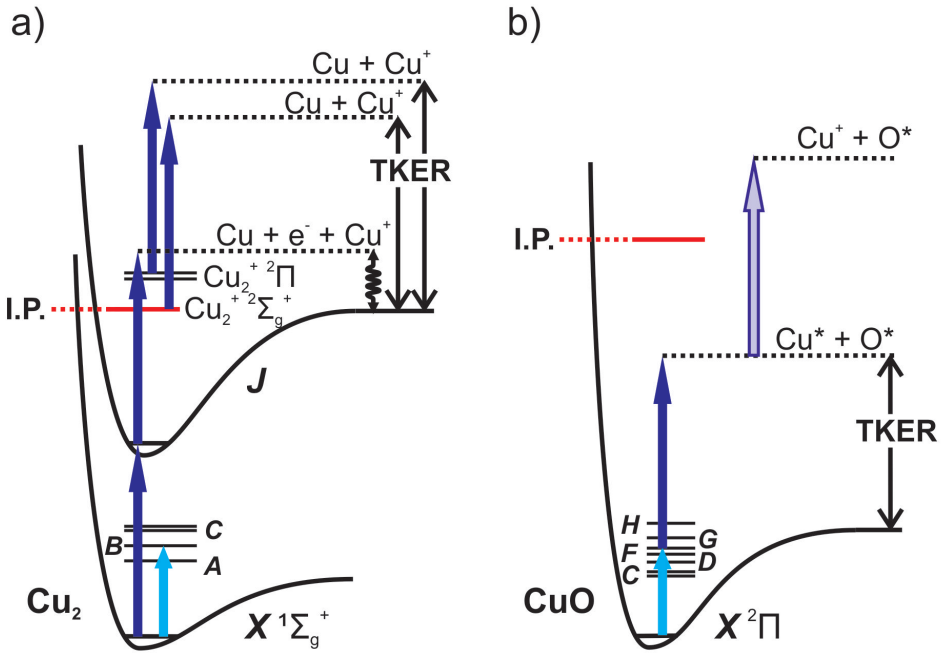

Figure 2.9: Dissociation mechanisms for a) Cu_2 and b) CuO. In a), the visible laser excites Cu_2 to a low-lying electronic state and depletes its ground state population. The resulting decrease in R2PI of Cu_2 via its J state causes dips in the Cu_2^+ signal. Enhancements in the atom channel are due to resonant excitation of the electronic states of CuO by the UV laser. Subsequent UV absorption photodissociates CuO* to create excited Cu atoms which are ionised by the UV laser.

symmetry of the 3d orbital which lacks an electron determines the electronic state's symmetry and energy among other parameters. Madhavan attempted to correlate experimental states with theoretical ones, and suggested that the electron configurations of the D and E states may differ, with D having the 3d-hole in a π-type orbital while E has the hole in a δ-type orbital [204]. However, particularly at high energies, there is much confusion about state assignment; those with the same Ω value are known to mix heavily and it has been observed that more $^2\Pi_{3/2}$ states have been assigned than can exist; some of them could be the $^4\Sigma_{3/2}$ states calculated to be close in energy [170].

Returning to the spectrum, a fairly long progression is seen to the F state: F $^2\Pi_i(v)\leftarrow$X $^2\Pi_{3/2}(v=0)$ where v=0-4. The spin-orbit splitting in the F state is less than our laser linewidth [182], so we cannot distinguish its components with certainty. However, given that Appelblad only observed $\Delta(\Lambda)=0$ F$\leftarrow$X transitions, it is likely that we are forming F $^2\Pi_{3/2}$ [176]. Within this progression, we also see G $^2\Sigma^+(v=0)\leftarrow$X $^2\Pi_{3/2}(v=0)$ and H $^2\Pi_{3/2}(v=1)\leftarrow$X $^2\Pi_{3/2}(v=0)$ transitions. The H(v=0)$\leftarrow$X(v=0) transition has never been observed; Appelblad speculates that this is due to predissociation [182]. Finally, a weak peak at 22818 cm^{-1} is attributable to the k $^4\Sigma_{1/2}(v=0)\leftarrow$X $^2\Pi_{1/2}(v=0)$ transition, although its low intensity and convolution with the depletions in the atom channel make its assignment less than

certain [183]. The loss of signal towards the high-energy end of the spectrum is not due to lack of transitions; the M $^2\Pi_i(\nu)\leftarrow$X $^2\Pi_{3/2}(\nu=0)$ transitions are expected around 24000 cm^{-1} and P$\leftarrow$X transitions lie further up still. Our visible OPO runs out of pulse energy at this point, preventing the scan from continuing further.

The mechanism creating enhancements in the atom channel from CuO resonances is explained in figure 2.9 (b). The visible photon excites one of many possible electronic transitions from the ground state of CuO, $X^2\Pi_i$. A non-resonant UV photon is then absorbed which causes dissociation of the CuO* into Cu*($^2D_{3/2}$) + O*(^{1}D). Cu* is subsequently ionised, non-resonantly, by further UV photons. This mechanism, however, cannot be inferred by looking at the spectrum in 2.8 alone - it has been deduced by imaging.

2.5 CuO Images

2.5.1 Determination of D_0(CuO)

Two-colour images were recorded in the Cu^+ channel. The species detected by the MCPs can be mass-selected by raising the MCPs from their resting potentials to their operating potentials at a specified time after the lasers fire. The atomic copper peaks are sufficiently well-resolved at the plates that we can distinguish between $^{63}Cu^+$ and $^{65}Cu^+$. By gating our detection window over the $^{63}Cu^+$ peak only, slightly sharper images are obtained. An example of a two-colour image is shown in figure 2.10. The visible and UV lasers fire within 30 ns of each other. The detector cannot discriminate between $^{63}Cu^+$ arising from one laser or both. The UV laser gives rise to a characteristic image, 2.10 (b), the origin of which is described fully in the next chapter. The two-colour image shown in 2.10 (a) is a sum of the UV-only image and an additional sharp ring. This ring disappears when the visible laser fires after the UV laser in time. The two-colour image and TKER spectrum, 2.10 (c), are obtained by subtracting the UV-only contribution (and the visible-only contribution where necessary). The result is a simple image containing a single ring.

An oxygen atom is assumed to be the Cu atom's cofragment, on the basis that the two-colour ring only appears when the visible laser is resonant with a transition in CuO. The total kinetic energy release can be calculated according to equation (2.9). TKER spectra at the F(ν)$\leftarrow$X(0) resonances are plotted in figure 2.11; ν=0 is shown fitted by a Gaussian function. Plotting the fitted TKER values against photon energy reveals a linear correlation with a slope of 1 (figure 2.12). This indicates that

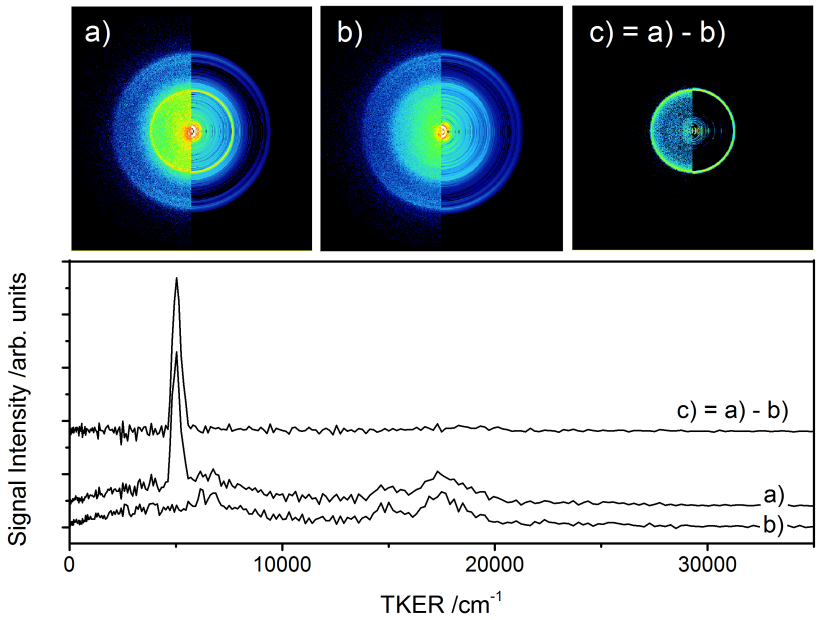

Figure 2.10: Two-colour images in the Cu^+ channel at the F(0)←X resonance. Images are shown with the raw data on the left and the reconstructed image on the right-hand side. (a) is recorded using both visible and UV lasers. (b) is recorded using only the UV laser. The UV-only contribution must be subtracted from (a). The result is an image containing a single ring, (c). The TKER spectra extracted from images (a)-(c) are shown below; spectrum (c) contains a single sharp peak.

a single visible photon photodissociates CuO into a single product channel, and confirms oxygen as the copper atom's cofragment.

All the points in figure 2.12 lie on a single line, leading to the somewhat surprising inference that all photodissociations across this large energy range occur into the same channel. Furthermore, extrapolating to zero TKER allows us to determine D_0(CuO) via equation (2.10). The number of visible photons involved has been shown to be 1, and, from figure 2.12 we see that when TKER=0, $h\nu_{vis}$=16194±242 cm^{-1}. The peak is two-colour, and therefore at least one UV photon must be used to dissociate CuO. Assuming the involvement of one UV photon, $nh\nu_{UV}$=37446.2 cm^{-1}. Finally, we assume Rodgers' D_0(CuO)=2.94±0.12 eV [201]. This leaves E_{int}=29928±1208 cm^{-1}. Fortunately, due to the relative sparsity of available electronic states of Cu* and O* at this energy, relatively few channels fall within this umbrella. All six Cu* ^2P_J + O* ^3P_J channels were ruled out on the grounds that we would expect to see a very broad peak resulting from the formation of 3 different O* ^3P_J states along with each Cu atom. This leaves only one product channel, Cu* $^2D_{3/2}$ + O* $^1D_2$. The internal energy of these states is extremely precisely known [211], allowing us to give a value of D_0 limited only by the uncertainty in our extrapolation to zero of the TKER (figure 2.12). Consequently,

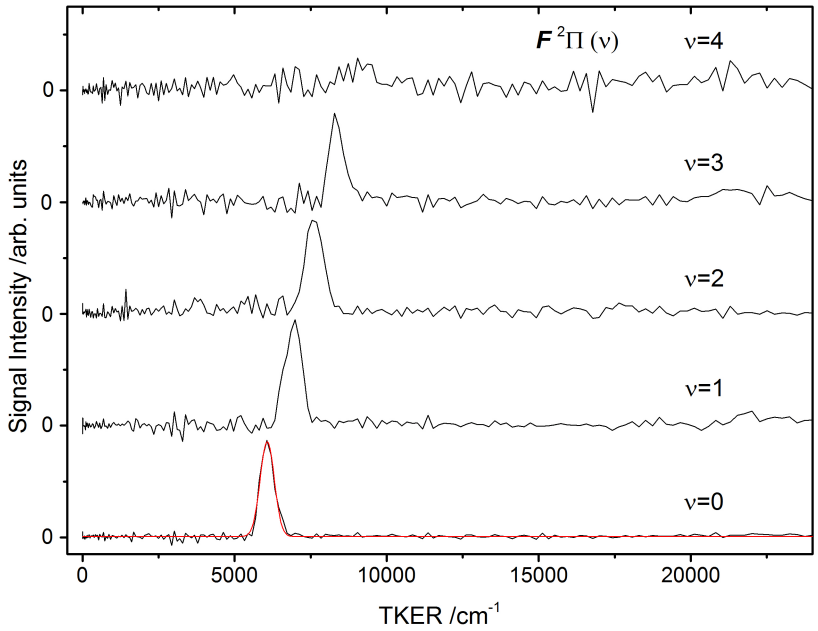

Figure 2.11: TKER spectra of the $^{63}Cu^+$ product produced by two-colour photodissociation of CuO via the F $^2\Pi(v$=0-4) states. A 1:1 correspondence between the increase in TKER and visible photon energy shows that only one visible photon is involved in the dissociation of CuO, and confirms the identity of the cofragment as oxygen.

D_0(CuO)=24527±242 cm^{-1}, or 3.041±0.030 eV.

Previous work has established a fairly wide range of experimental D_0(CuO) values. These values seem to increase with each experiment performed. For a long time, the standard value was taken to be Smoes' 1972 value: 2.76±0.22 eV [197]. However, this calculation relied on achieving an equilibrium in a hot oven between the gases emitted by a mixture of solid NiO and Cu. Watson later repeated many of Smoes' experiments and commented that D_0(CuO) varied depending on the method used to determine it, and that it was unlikely that equilibrium had been achieved by either party [198]. The preferred value therefore became Clemmer's preliminary value, included as an aside in a paper on ZnO, of 2.85±0.15 eV [199]. This was obtained by collision experiments on the Cu^+ + NO_2 system. A second paper from the Armentrout group studied the reactions of Cu^+ with a number of oxygen-containing neutral molecules and came up with a revised value of 2.94±0.12 eV in 1999 [201]. This remains the best D_0(CuO) determination to date, and our value lies just within the upper limit of its uncertainty. Finally, Vinckier *et al.* examined Cu atoms reacting with NO_2 in a fast-flow reactor and noted that the reaction remains thermoneutral from 303 to 762 K. From this they inferred that formation of Cu-O must almost exactly compensate for breaking the ON-O bond,

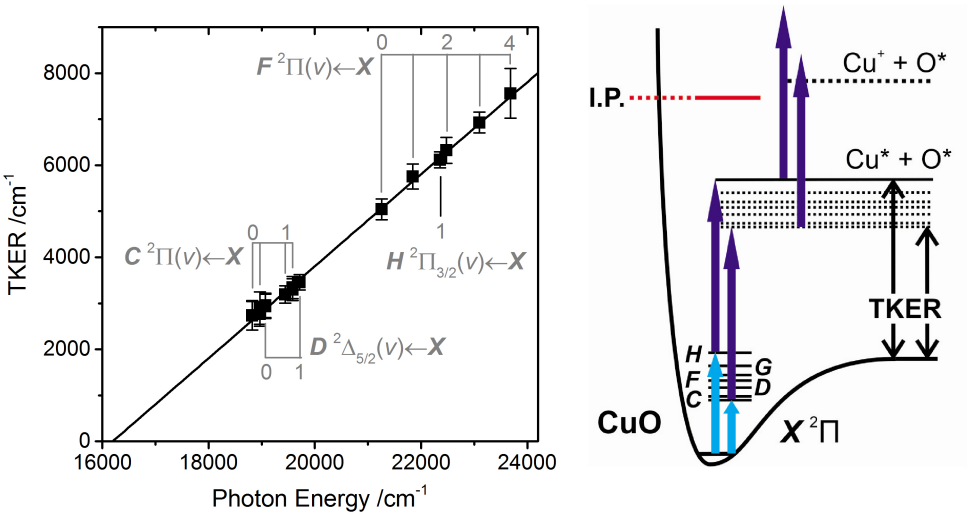

Figure 2.12: TKER plotted against photon energy. This plot's x-axis intercept is the visible photon energy at zero TKER. All the TKER points lie along a single line, despite the wide range of states they originate from (marked in grey). This implies that all CuO* observed dissociate into the same channel: Cu $^2D_{3/2}$ + O ^1D. The kinetic energy release is determined by the energy left over after absorption of one visible and one UV photon, D_0(CuO) and formation of Cu* + O*. Cu* is ionised in a non-resonant two-photon process by the UV laser.

which is known to have a dissociation energy D_0(ON-O)=3.116±0.008 eV [200], consistent with our determined value. Given well-known values for the ionisation energies of CuO (9.41±0.01 eV, determined from a photoionisation efficiency curve [212]) and Cu [213], a Hess cycle can be used to calculate $D_0(CuO^+)$=1.36±0.04 eV. This is very close to the determination by Rodgers of 1.35±0.12 eV [201], but below an older value obtained by Fisher of 1.62±0.15 eV [214].

2.5.2 Proof of the 1+1' mechanism

To confirm that the products formed really are Cu*($^2D_{3/2}$) + O*($^1D_2$), the laser was tuned to a resonant transition in the postulated metastable atomic copper product: $3d^{10}5p\ ^2P^0 \leftarrow 3d^9 4s^2\ ^2D_{3/2}$ [215]. This transition should be strongly forbidden, as it moves two electrons from the 4s orbital. However, it is seen to be strong, by us and previous workers [215], suggesting that it may be mis-assigned. In theory, *provided that changing the UV photon energy does not change the products which CuO forms by 1+1' photodissociation*, the Cu $^2D_{3/2}$ two-colour ring should 'light up' when the UV laser is tuned to the $^2P^0 \leftarrow {}^2D_{3/2}$ transition. In practice, this is not the case. Although the 1+1' products are found to be in the same product channel as before, the UV-only image in the background no longer looks like figure 2.10 (b). All the transitions in 2.10 (b) which relied on the J←X resonance to form Cu^+ are

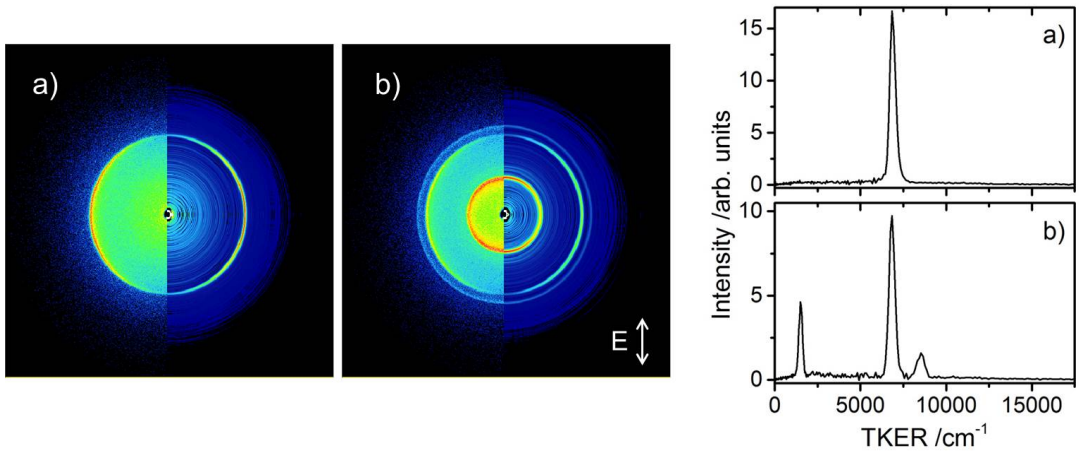

Figure 2.13: Two images taken with the UV laser tuned to a resonant transition out of the metastable Cu $^2D_{3/2}$ state, and their TKER spectra. a) is the UV-only image and shows a single intense ring (or peak) corresponding to 1-photon dissociation of Cu_2. In b) the visible laser (tuned to the CuO F(0)-X transition) fires 10 ns before the UV. Two additional rings (or peaks) corresponding to the photoproducts of CuO are visible.

suppressed when the laser is detuned from the J←X transition.

The one-colour image at 276.6 nm (the $3d^{10}5p\ ^2P^0 \leftarrow ^2D_{3/2}$ atomic resonance) is shown in 2.13 (a). It consists of a single sharp ring arising from one-photon dissociation of ground-state Cu_2 to form $Cu(^2S_{1/2})$ + $Cu^*(^2D_{3/2})$. The latter product is resonantly two-photon ionised via the $^2P^0$ state, creating an extremely bright ring. The two-colour image at the new UV energy is shown in figure 2.13 (b). In addition to the two-colour ring previously observed, a weak second channel appears at a large kinetic energy, just outside the one-colour ring of (a). An additional 1+1' dissociation product channel, $Cu^*(^2D_{5/2})$ + $O^*(^1D_2)$, is accessed by the new UV energy, and the $Cu^*(^2D_{5/2})$ product is non-resonantly ionised by the UV. The background for the two different UV energies is therefore not comparable, meaning that the brightness of the two-colour rings cannot be compared easily.

The wavelength-dependent Cu^+ signal can easily be compared when the apparatus is switched to time-of-flight mode. With the visible laser wavelength fixed at a CuO resonance, the UV laser is scanned across the $^2P^0 \leftarrow ^2D_{3/2}$ transition (figure 2.14). A significant enhancement is seen when the visible laser precedes the UV laser, *which disappears when the visible laser is switched off*. This proves that the visible laser creates $Cu^*(^2D_{3/2})$, and thus that our assignment is correct. The test is repeated by scanning the UV laser over the J-X transition in the dimer; no enhancement is seen, providing further proof that Cu_2 makes no contribution to the two-colour ring.

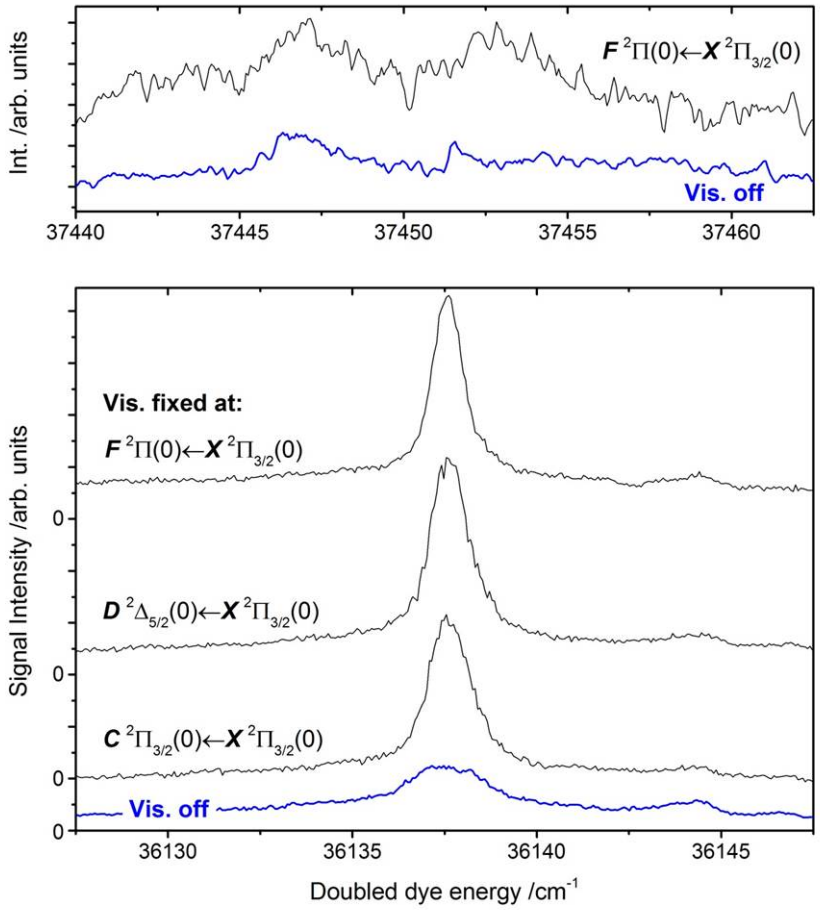

Figure 2.14: Resonantly enhanced product signals. Enhancements in the product signal are seen when the ionisation laser is tuned to a product resonance. The OPO, firing 10 ns before the UV laser, is fixed at an electronic transition in CuO and photodissociates it to form Cu $^2D_{3/2}$. In the top spectrum, the UV laser scans the J-X transition of Cu_2 and does not produce any enhancement in the Cu^+ signal. In the lower spectra, the UV laser scans the atomic resonance $^2P^0 \leftarrow ^2D_{3/2}$ and resonantly ionises the CuO dissociation product causing a large enhancement in the Cu^+ signal.

2.5.3 Anisotropies

Some anisotropy, *i.e.* a non-uniform angular distribution of product, is observable in many of the images recorded. The functional forms of angular distributions are known for a variety of dissociation conditions [216]. In the case of one-photon photodissociation of an unpolarised sample, using linearly-polarised light, this form is given by [217]:

$$I(\theta_\epsilon) = 1 + \beta P_2(cos\theta_\epsilon). \tag{2.11}$$

In equation (2.11), θ_ϵ is the angle between the polarisation direction of the linearly polarised light and the fragment's recoil direction, β is the spatial anisotropy parameter and P_2 is the second-order Legendre polynomial:

$$P_2(cos\theta_\epsilon) = \frac{1}{2}(3cos^2\theta_\epsilon - 1). \tag{2.12}$$

A parallel transition is one in which the transition dipole moment is parallel to the breaking bond. It corresponds to a β parameter of +2, which, when substituted into equation (2.11), shows that the photofragment angular distribution is maximal at θ_ϵ=0, 180^o and zero when θ_ϵ=90, 270^o. A perpendicular transition (in which the transition dipole moment is perpendicular to the breaking bond) has a spatial anisotropy parameter of -1 and maximal signal at θ_ϵ=90, 270^o.

A sample of our two-colour images, and their angular intensity distributions, is shown in figure 2.15. Although one visible and one UV photon are both required for photodissociation of CuO, the dissociation step itself is initiated by absorption of one photon by the excited state of CuO prepared by the visible laser. We might therefore expect to discern either parallel or perpendicular character in the anisotropy. The two transitions out of the C $^2\Pi$ state show some perpendicular character, while the transition out of the D $^2\Delta$ state is somewhat parallel in character. These observations are consistent with our assignment of these CuO* states as Π, Π and Δ. Assuming that Hund's case (a) applies to these states of CuO [175], parallel transitions are subject to the selection rule $\Delta(\Lambda)$=0, while perpendicular transitions obey $\Delta(\Lambda)$=$\pm$1. Given that all the CuO* studied dissociate to the same products, they all encounter the same dissociative state upon excitation. Dissociation from D $^2\Delta_{5/2}$ via this dissociative state is parallel (i.e. $\Delta(\Lambda)$=0 during excitation) and so we may conclude that the upper dissociative state is a Δ state also. Dissociations from the C $^2\Pi$ states therefore entail $\Delta(\Lambda)$=+1, and will be perpendicular transitions in this system.

However, the symmetry of the dissociative state cannot be firmly assigned. A number of studies have noted that Hund's case (a) may not be applicable to all states of CuO. The A state is believed to be better described by Hund's case (c), as an Ω=1/2 state rather than as $^2\Sigma^+$ [178]. In fact, it has been suggested that all electronic states in which Cu has a 3d^9 configuration may be better suited to a Hund's case (c) description [185]. Case (c) is distinguished from case (a) by very strong spin-orbit coupling, and results in a net angular momentum vector from both spin and orbital angular momenta, Ω, rather than these quantities being distinct from one another. In case (c), parallel transitions obey $\Delta(\Omega)$=0 rather than $\Delta(\Lambda)$=0. Accommodating re-assignment of these states in Hund's case (c) is not simple. All the symmetry assignments made so far have assumed Hund's case (a). As a result, they

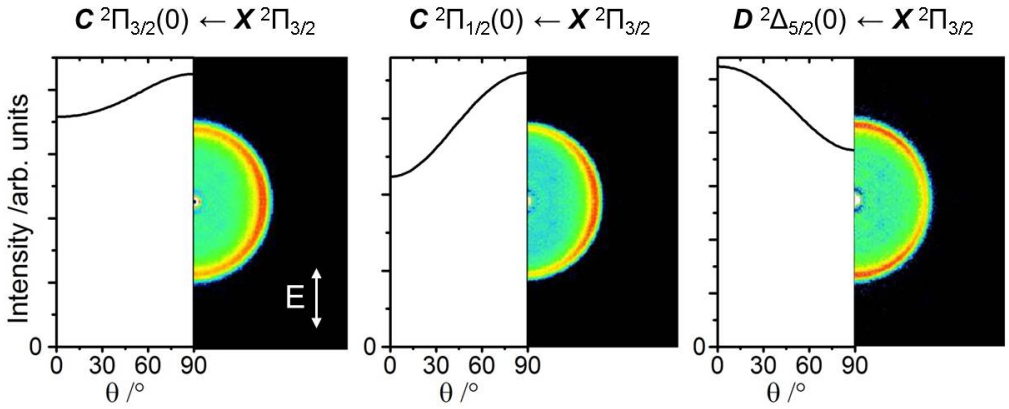

Figure 2.15: Anisotropy in the two-colour rings corresponding to dissociation of the ***C*** and ***D*** states of CuO. Both the rings, and their angular intensity distribution are shown. Dissociation of C-state CuO occurs with somewhat perpendicular character while dissociation of D-state CuO occurs with somewhat parallel character.

are not all necessarily correct; for instance, more $^2\Pi$ states have been assigned in the literature than is possible from the available electronic configurations [185]. The interlopers are believed, instead, to be contaminated quartet states which are calculated to be close by in energy. Calculation of $\Delta(\Omega)$ rather than $\Delta(\Lambda)$, therefore, will not be undertaken here. Further evidence for the applicability of Hund's case (c) is that, while only the anisotropies from the C and D state dissociations are shown in figure 2.15, anisotropy is also evident in our images of photodissociation from the F $^2\Pi$ state and is of slightly parallel character.

Finally, it must be noted that the angular intensity distributions in figure 2.15 do not drop to zero at any value of θ. As a result, the β parameters which can be fitted to these distributions fall a long way short of the extreme values +2 and -1. The most likely explanation is that given above; the participating states may well be inadequately defined by a single Russell-Saunders state. The true states are mixed in character and the transitions are therefore neither purely parallel nor purely perpendicular. Additionally, the timescale of the dissociation is unknown. If dissociation is not fast relative to the period of rotation, some smearing of the angular distribution will be observed. If the breaking bond has time to rotate away from the orientation in which it absorbed the photon before releasing the photofragments, those fragments will be spread over a broad angular range rather than being scattered parallel or perpendicular to the laser polarisation vector.

2.6 Concluding remarks

1+1' photodissociation of CuO has provided a neat demonstration of the ability of VMI to probe the photodissociation process from start to finish. The quantum states of the Cu and O products, $^2D_{3/2}$ and $^1D_2$ respectively, have been identified and their assignment confirmed by resonant ionisation of the copper product. The dissociation energy of the ground state, $X^2\Pi_{3/2}$, has been determined to be 3.041±0.030 eV. Additionally, knowledge of the symmetry of the initial state of CuO* (prepared by excitation with visible light) has led to some speculation about the symmetry of the dissociative state occupied by the dissociating species. The conclusion reached confirms that of previous authors: a Hund's case (c) assignment of the states of CuO is required to account for the anisotropies observed in our images.

Chapter 3

VMI of Copper Clusters

During the course of work on CuO, detailed in the previous chapter, it was observed that the visible laser produced a complex spectrum and rich images in the Cu^+ channel. Given that 3-4 visible photons are required to ionise Cu in this spectral region, such images were surprising. The numerous sharp rings observed mostly correspond to a non-resonant 3-photon dissociation of ground-state Cu_2 to form one ground-state copper atom and one highly excited one, Cu*. Cu* is ionisable with a single subsequent photon, which is why we are sensitive to such processes. Additional broad features in the Cu^+ images closely match the structure observed in images in the $Cu_2{}^+$ channel at the corresponding wavelengths. This provides evidence that the broad structures arise from fragmentation of Cu_n, n=3 being most probable. The TKER of peaks in the dimer images is calculated assuming that they arise from Cu_3 fragmentation. Reasonable fragmentation products and a $D_0(Cu_3)$ consistent with that found by previous workers are returned from a single-photon fit of the TKER data, along with evidence for a potential new state of Cu_3. Further evidence for trimer fragmentation comes from the ion yield spectra of Cu and Cu_2, which are identical in some regions, indicating a common origin. Finally, we observe a number of spectral peaks in both channels consistent with photodepletions observed by previous workers in the trimer channel. However, we do not observe Cu_3 directly.

3.1 Previous work on Copper Clusters

3.1.1 Copper Dimer

Morse's 1986 review gives a thorough description of much of what is known about Cu_2, and his labelling of its electronic states has been adopted universally [3]. Cu_2 has been the subject of special attention among transition metal clusters. It was first made in 1954 [218, 219]. All the early studies

formed Cu_2 in a King furnace and observed its emission spectrum, although not always with correct analyses [220]. The A and B states were identified in such studies, and the B state was conclusively assigned as $^1\Sigma_u^+$ [221, 222, 223]. According to a Hund's case (a) analysis, only one low-energy excited state with Σ symmetry was expected, and so the A state was designated as a Π state. The assignment was supported by Pesič and Weniger, who reported a Q-branch in the A-X transitions [224]. Lochet disagreed, however, [225] and was proved correct much later in 1989 by a detailed laser-induced fluorescence study on the A-X transition [226]. In their paper, McCaffrey *et al.* consider the known electronic states of Cu_2 to date and argue persuasively that a Hund's case (c) description of Cu_2 is appropriate.

In the meantime, gas-phase spectroscopists characterised the B state sufficiently precisely to find unexplained transitions within its spectral envelope. The C state was first observed in 1979 [43], but it was not confirmed as a dimer band until it was examined by LIF experiments in 1982 (these authors call it B') [227]. It was eventually fully characterised by laser photoionisation experiments in the Smalley group [79]. The number of known excited states of Cu_2 increased vastly in 1983 when Smalley's group published another paper featuring states F to J (which they label systems i-v; Morse's review suggests F to J) [80]. In fact, this paper placed upper and lower limits on the ionisation energies of Cu_2 to Cu_{29} using a number of fixed-frequency exciplex lasers. In 2000, a further seven bands were discovered, which extend into the ultraviolet and are in some cases acknowledged to be poorly characterised [228].

While the number of known states has greatly increased, the low-lying states have not been neglected. The first rotationally-resolved data were reported for the C-X band in 1991, and proved the Π symmetry of the C state [229]. The A-X and B-X systems followed in 1992 [209, 230]. These papers provide high-quality rotational constants and information about the Franck-Condon factors: only the first 3 vibrational levels of the C state are accessible from X(0), but a wide range of vibrational states of C are accessible from X(ν=2-4). A similarly short progression is observed from X(0) to the A state. The A, B and C states are particularly 'well-characterised' in that their rotational constants are accurately known, and their lifetimes have also been studied. The C state is particularly long-lived, having a lifetime of the order of a microsecond, while the B state appears to predissociate fairly rapidly, in around 40 ns [79, 231]. The B and C states may be interconverted by collision. The A state lifetime decreases as its vibrational state increases; A($\nu \geq 2$) may have similar lifetimes to the B state. These values are not well-known [231, 232].

Determination of $D_0(Cu_2)$ initially utilised mass spectrometric methods wherein the ratio Cu_2^+/Cu^+ was measured as a function of temperature. There was little variation in the values obtained: 2.1±0.3 eV [233], 2.0±0.1 eV [234], 2.21±0.11 eV [235], 1.97±0.09 eV [236], 1.98±0.04 eV, and 1.96±0.06 eV [237]. In a more recent spectroscopic attempt, Rohlfing and Valentini used a corrected Birge-Sponer plot and their LIF data on the G-X transition to calculate $D_e(Cu_2)$=16760±200 cm^{-1}, which yields $D_0(Cu_2)$=16627 cm^{-1}, or 2.061±0.025 eV [238]. More recently, collision-induced dissociation on cationic copper clusters has been used to determine $D_0(Cu_2^+)$=1.64±0.14 eV, and, using the ionisation energies of Cu and Cu_2 [80], a dissociation energy for the neutral species of 1.81±0.14 eV [114]. A subsequent CID study finds a slightly lower $D_0(Cu_2^+)$ of 1.57±0.08 eV [115]. Finally, collision-induced dissociation of Cu_2^- was combined with known electron affinities [30, 48, 87] to give $D_0(Cu_2)$=2.04±0.17 eV [112]. Hilpert's 1979 values, 1.98±0.04 eV and 1.96±0.06 eV by second and third law derivations respectively, remain the most commonly-cited values because of their internal consistency and small error bounds.

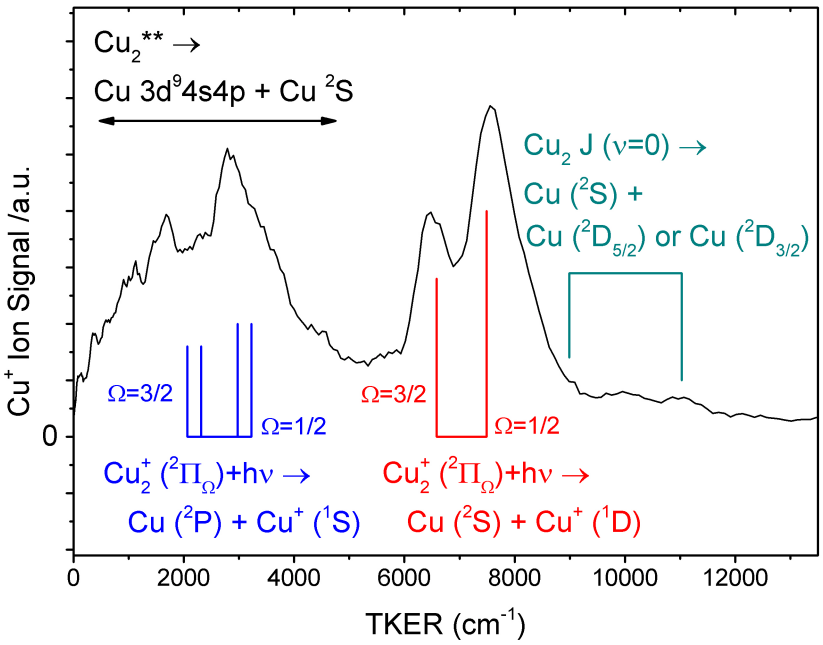

Figure 3.1: TKER spectrum in the Cu^+ channel after UV irradiation of Cu_2. The laser is resonant with the J(0)-X(0) transition of Cu_2, allowing resonant two-photon ionisation. A number of channels contribute to the image: one-photon dissociation of the $^2\Pi_{1/2,\,3/2}$ state of Cu_2^+ into Cu + Cu^+ creates the intense peaks. The broad low-energy envelope is believed to arise from dissociative autoionisation of Cu_2** and ionisation of the Cu* product.

Very recently, our group examined ultraviolet photodissociation of Cu_2 by VMI [142]. A typical TKER spectrum in the Cu^+ channel is shown in figure 3.1. The four distinguishable peaks arise from

photodissociation of Cu_2^+*. Cu_2 in the molecular beam is resonantly ionised in a two-photon process (R2PI) via the J state, to form the $X^2\Sigma_g^+$ ground state and both spin-orbit components of the excited $^2\Pi_\Omega$ state [239]. A subsequent UV photon dissociates Cu_2^+* into one of two possible channels: (i) Cu $^2P^0$ + Cu^+ $^1S_0$, or (ii) Cu $^2S_{1/2}$ + Cu^+ $^1D_2$, and the kinetic energy release varies accordingly. The breadth of the peaks in channel (ii) may be attributed to the existence of a number of vibrational states of the parent Cu_2^+*, but the same cannot be said for the peaks in channel (i). These peaks are overlaid with a third channel, believed to be the dissociative autoionisation of Cu_2**. If, upon absorbing two photons, Cu_2 is excited to a dissociative ionic state, bond-breaking and electron loss occur at a very ill-defined bond length. The energy carried away by the electron and the individual fragments is therefore broadly distributed, up to some maximum, and could explain the structure that we see in the image. Such behaviour has been observed previously during R2PI of Cu_2 via the J-state, but even so this feature cannot be assigned with great certainty [210]. A fourth channel, one-photon dissociation of the J state to form a resonant and a metastable Cu atom, is illustrated in figure 3.1, as there is some intensity in this region. Such varied dissociation dynamics illustrate the potential for complexity in copper cluster imaging, which will be a recurring theme of this chapter.

Cu_2 has been studied in matrices as well as in the gas phase. A disadvantage of studying neutral species deposited in a matrix is that mass selection is difficult; the first such work described a 'forest' of lines arising from Cu_n in methane, argon and dodecane matrices [240]. Some discrimination between species can be achieved by pumping known Cu_2 transitions and observing dissociation or fluorescence [241, 242]. Matrix spectroscopy cannot be directly compared to gas-phase spectroscopy as the matrix is not a totally inert carrier. Matrix trapping shifts the band positions of Cu_2 [242] and can even cause predissociation of trapped species. Multiple lifetimes may be observed if the trapped species sits in more than one kind of site [243]. For instance, the A and B states of Cu_2 are known to correlate to the Cu($^2S_{1/2}$) + Cu($^2D_{5/2}$) limit in the gas phase, but in a neon matrix they predissociate to form two Cu($^2S_{1/2}$) atoms. Being trapped adjacent to one another, the Cu($^2S_{1/2}$) products recombine and can form a triplet state, a $^3\Sigma_u^+$, which is identified by its red fluorescence [244]. Fluorescence observed in matrices uncovered a whole manifold of Cu_2 triplet states which gas-phase experiments were blind to due to the spin selection rules [227, 244, 245]. In 2011 Lecoultre *et al.* managed to simplify matrix studies by depositing mass-selected cationic clusters which are subsequently neutralised [139]. This allowed them to make some comparisons between matrix and gas-phase emission spectra for the smaller copper clusters. Lecoultre's paper is also useful as a summary of calculations performed on Cu_2 and Cu_3.

Small copper clusters have been subject to extensive theoretical study largely because of the quantity of experimental data available to corroborate theoretical findings [40, 246]. They are often used as a testing-ground for theoretical approaches [247, 248]. A common conclusion is that, despite the coinage metal clusters' many similarities to alkali metal clusters [29, 30, 53, 87] due to their nominal $3d^{10}4s^1$ atomic configuration, d-electron correlation effects are not negligible and the 3d electrons cannot be frozen into the core during calculations [249].

3.1.2 Copper Trimer

The extent of our knowledge of Cu_3 is limited when compared to the dimer, and relies much more heavily on calculation. The possibilities for the geometry of Cu_3 are fourfold: perfectly linear ($D_{\infty h}$, $^2\Sigma$); an equilateral triangle (D_{3h}, $^2E'$); a triangle with an acute apex angle (C_{2v}, $^2A_1$), and a triangle with an obtuse apex angle (C_{2v}, $^2B_2$). Early calculations, working from Moskovits' spectra [240], suggested the trimer to be linear in an argon matrix [250]. This assignment did not prove to be general. ESR data for Cu_3 trapped in an adamantane matrix suggested the obtuse-angled $^2B_2$ structure to be the ground state [251]. Raman spectroscopy of Cu_3 in an argon matrix suggested that Cu_3 has a triangular geometry removed from perfect D_{3h} symmetry by a Jahn-Teller distortion, but that the distorted forms are fluxional and alternate over a very small barrier between C_{2v} symmetries [252, 253]. ESR spectra in an N_2 matrix find the ground state to be $^2A_1$, a triangle with an acute apex angle [254].

Many studies in the gas phase make use of a known excitation of Cu_3 out of the ground state at around 540 nm, labelled the A←X transition. They collectively agree that the ground state is a Jahn-Teller distorted triangle. Evidence comes from resonant two-photon ionisation [81], laser-induced fluorescence [255, 256], and photodissociation spectroscopy [99, 257]. Differences in the spectra are accounted for by employing different barriers to pseudorotation between the Jahn-Teller distorted forms of the ground state in the accompanying theory. Many theoretical groups have attempted to describe this abundance of experimental data (particularly that taken by Rohlfing and Valentini) within the confines of a model, although none obtain a perfect fit [138, 247, 249, 258, 259]. The controversy surrounding the geometry of Cu_3 is dealt with extremely thoroughly by Morse's review [3]; it is interesting to note that, despite the remaining uncertainties surrounding it in 1986, Morse deems Cu_3 to be the best-understood of all the transition metal trimers.

High-level calculations generally do agree on a $^2B_2$ ground state, with the $^2A_1$ state as a saddle point or shallow minimum close by [136, 137, 138]. They also strongly suggest that the Cu_3 zero-point

energy exceeds the barrier to pseudorotation between the Jahn-Teller distorted components of the ground state and that is therefore best described as $^2E'$, on average [259, 258]. They cannot, however, settle the symmetry of the excited state in the progression starting at 540 nm. It was initially thought to be a $^2E''$ state [81, 256], but Morse showed in 1987 that the lines found at the time were consistent with a $^2A_1' \leftarrow ^2E'$ transition as well as a $^2E'' \leftarrow ^2E'$ transition [260]. The theoretical work performed on Cu_2 and Cu_3 to date has been summarised fairly thoroughly in 1997 [261], 2005 [140] and 2011 [139, 141].

The exact structure of the photodepletion spectrum of the trimer around 540 nm is particularly important in this chapter. Morse *et al.* studied Cu_3 in a resonant two-photon ionisation/ion-dip scheme in 1983 [81]. The data from reference [81] is reproduced in figure 3.2. In the resonant two-photon ionisation scheme (a), a tunable dye laser was scanned across the band and followed in time by an ionising photon from the fourth harmonic of a Nd:YAG laser. The Cu_3^+ signal was recorded. In the photodepletion scheme (b), the tunable dye laser was operated at very high power and followed, after a long time delay (to allow predissociation), by an ArF laser pulse to ionise any Cu_3 remaining in the beam. The use of these two schemes allows the differentiation of excitations leading to non-dissociative and dissociative states. As will be seen later in the chapter, we reproduce many of the lines in the Cu_3 photodepletion spectrum in the Cu^+ and Cu_2^+ channels of our own visible spectra.

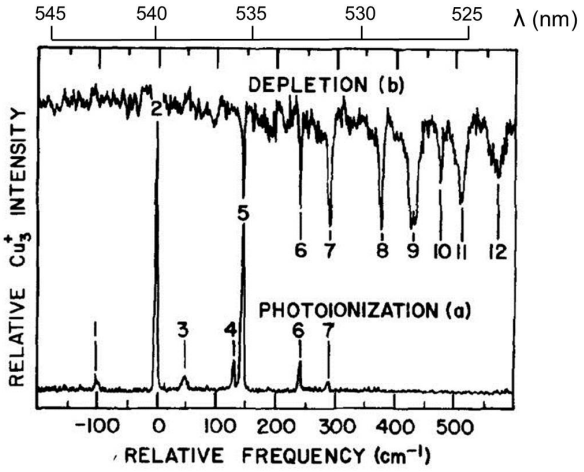

Figure 3.2: Resonant enhancements (series a) and depletions (series b) in the copper trimer signal, observed in photoionisation and ion-dip spectroscopy by Morse, Hopkins, Langridge-Smith and Smalley in 1983. The data is reprinted with permission from J. Chem. Phys. **79**, 5316 (1983). Copyright 1983, AIP Publishing LLC. The energy shown on the horizontal axis is relative to the band origin at 539.7 nm, or 18529 cm^{-1}.

Knickelbein also examined the Cu_3 A←X transition using 'ion-dip' spectroscopy, scanning a dye

laser across the transition followed 100 ns later by an ArF probe laser [257]. The resulting photodepletion spectrum of Cu_3 shows the same vibronic structure as was observed by Morse *et al.*; the peaks in figure 3.3 are therefore numbered for consistency with figure 3.2. As might be expected, only Morse's photodepletion bands (5-12) were observed by Knickelbein. The A(ν=0)←X(ν=0) transition is not among these, implying that A(ν=0) is stable to dissociation and decays radiatively instead. Additionally in Cu_3, a broad and structureless feature is observed to the blue of 500 nm. Knickelbein attributes this to a second excited state of the trimer, B, and suggests that its lack of structure may be explained by its strongly predissociative nature. The decorated trimers behave differently. Extremely strong depletions in the Cu_3Ar^+ and Cu_3Kr^+ signal are seen in a very broad feature centred around 516 nm, with a shoulder at 510 nm. Knickelbein notes the similarity in the shape of this feature to the vibronic envelope of the Cu_3 features and concludes that the presence of a rare gas atom shifts the A-X transition around 25 nm to the blue. He attributes the shoulder of the Cu_3-rare gas (Cu_3RG) band to shifted absorption by bands 7-12 and the sharper feature to absorption by bands 5-6. However, his assignment is necessarily cautious as the shift he invokes in the A-X band is unusually large, considering rare gas atoms are believed to interact weakly with neutral species.

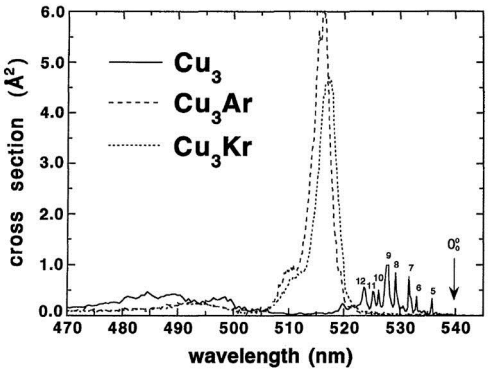

Figure 3.3: Photodepletion spectra of Cu_3, Cu_3Ar and Cu_3Kr. Reprinted with permission from J. Chem. Phys. **100**, 4729 (1994). Copyright 1984, AIP Publishing LLC. The bare cluster shows well-resolved peaks similar to those observed by Morse, and, centred at 485 nm, a broad band indicating predissociation of the state involved. The Cu_3-RG species, by comparison, show no fine structure but only a very broad, intense peak at 516 nm with a shoulder at 510 nm.

Of particular interest to us in VMI experiments is the dissociation energy, $D_0(Cu_3)$. This is not nearly as well-known as $D_0(Cu_2)$, partly due to a lack of a spectroscopic determination and partly due to a dearth of data. An attempt was made at a spectroscopic study by Jarrold and Creegan in 1990, studying the photodissociation of Cu_n^+ [100]. They performed laser fluence studies which suggested that dissociation of Cu_3^+ was a one-photon process at 440 nm and observed the onset of dissociation

around 410 nm (3.02 eV) but were unable to improve on $D_0(Cu_3^+)$=3.2±0.4 eV, calculable from a determination of $D_0(Cu_3)$ by Hilpert [3, 100, 262].

Non-spectroscopic methods have proved more successful in determining $D_0(Cu_3)$, although their results are not particularly consistent and have significant uncertainties. The atomisation energy was determined by Hilpert in 1980 (by measuring the ratio of Cu_2 to Cu_3 as a function of oven temperature) to be 3.05±0.14 eV [262]. Combining this with his second-law value for $D_0(Cu_2)$ [237] suggests that the process $Cu_3 \rightarrow Cu + Cu_2$ requires 1.07±0.18 eV. Using an average of Hilpert's Cu_2 data gives $D_0(Cu_3)$=1.08±0.19 eV [3]. Collision-induced dissociation (CID) studies on Cu_3^+ can access both product channels: (i) $Cu^+ + Cu_2$ or (ii) $Cu + Cu_2^+$. Channel (i) is thermodynamically favoured, as the ionisation energy of Cu_2 exceeds the ionisation energy of the atom. Ingólfsson *et al.* observed both channels and, using known ionisation energies, [29, 81] calculated $D_0(Cu_3)$=0.76±0.23 eV. Krückeberg *et al.* saw only channel (i) and determined $D_0(Cu_3^+)$=2.83±0.14 eV. Using known ionisation energies [29, 211] we may calculate the corresponding $D_0(Cu_3)$=0.90±0.18 eV. Spasov *et al.* performed CID experiments on the anions and, using known electron affinities [48], calculated $D_0(Cu_3)$=1.15±0.20 eV [112]. Our group has recently suggested a possible value of 0.605±0.030 eV; this value is treated with careful attention as it relies on an uncertain assignment [142]. A range of theoretical values have been presented. Those published up to 1986 are summarised by Langhoff *et al.* and range from 0.2 to 1.25 eV [138]. A more recent suggestion is 1.16 eV [140].

3.2 One Colour Spectroscopy

The Cu^+ ion yield spectrum was taken over the same region as the two-colour spectrum, 18000-24000 cm^{-1}, and is shown in figure 3.4. It contains a number of intense, sharp features, labelled (a) to (g), all arising from resonant ionisation via atomic transitions. These transitions have been assigned.

It is immediately evident from table 3.4 that all observed resonances originate in either the ground state of the copper atom, $^2S_{1/2}$, or the first metastable state, $^2D_{5/2}$. These are therefore the electronic states of Cu present in our beam. It is somewhat surprising that we see no transitions out of the upper spin-orbit component of the metastable state, $^2D_{3/2}$, which lies only 2000 cm^{-1} above $^2D_{5/2}$ and, like $^2D_{5/2}$, cannot decay to the ground state via a single-photon allowed transition in the Russell-Saunders coupling scheme (although $^2S_{1/2} \leftarrow {}^2D_{3/2}$ obeys the ΔJ=1 selection rule). However, scans such as those in figure 3.4 are not the only evidence that we do not have much $^2D_{3/2}$ in our molecular beam. The image shown in figure 2.13 (a) was taken with the UV laser resonant with the $3d^{10}5p\ ^2P^0 \leftarrow 3d^9 4s^2$

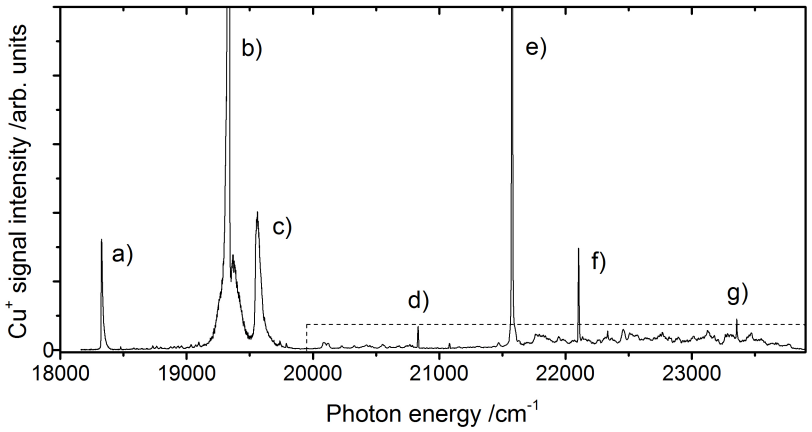

1 photon	2 photon	3 photon
b) $3d^{10}4p\ \mathbf{^2P^0_{1/2}} \leftarrow 3d^9 4s^2\ \mathbf{^2D_{5/2}}$	d) $3d^{10}6s\ \mathbf{^2S_{1/2}} \leftarrow 3d^9 4s^2\ \mathbf{^2D_{5/2}}$	a) $3d^{10}6p\ \mathbf{^2P^0_{1/2}} \leftarrow$
c) $3d^{10}4p\ \mathbf{^2P^0_{3/2}} \leftarrow 3d^9 4s^2\ \mathbf{^2D_{5/2}}$	e) $3d^{10}5s\ \mathbf{^2S_{1/2}} \leftarrow 3d^{10}4s\ \mathbf{^2S_{1/2}}$	$3d^{10}4s\ \mathbf{^2S_{1/2}}$
	f) $3d^{10}5d\ \mathbf{^2D^0_n} \leftarrow 3d^9 4s^2\ \mathbf{^2D_{5/2}}$	
	g) $3d^{10}6d\ \mathbf{^2D^0_n} \leftarrow 3d^9 4s^2\ \mathbf{^2D_{5/2}}$	

Figure 3.4: The photoion yield spectrum in the Cu^+ channel, using an OPO in the visible region. The sharp atomic transitions (a)-(g) are assigned and used to calibrate the spectrum. The atomic transitions leading to photoionisation all originate in either $^2S_{1/2}$ or $^2D_{5/2}$, suggesting that only the first excited state of copper, the lower spin-orbit component of the metastable D state, is significantly populated in our molecular beam. The boxed region is expanded in figure 3.5.

$^2D_{3/2}$ transition. If there was much $^2D_{3/2}$ in the beam, it would be resonantly ionised and produce a considerable central spot; when inspected, the image reveals a weak central spot. Similarly, when the UV laser is scanned over this resonant transition, only a modest enhancement is seen (figure 2.14). The enhancement is only 4-5 times as intense as the non-resonant background. For whatever reason, our ablation conditions do not appear to create much Cu $^2D_{3/2}$. UV studies of laser-ablated copper atoms have also noted numerous intense photoionising transitions from $^2D_{5/2}$ and none from $^2D_{3/2}$ [263]. Also of note in figure 3.4 is the presence of a fairly intense three-photon transition, (a), which serves as a reminder that the OPO is operated at a fairly high power; 8-12 mJ/pulse.

The $^{63}Cu^+$ signal is non-zero in between the labelled atomic transitions in figure 3.4. The $^{63}Cu^+$ spectrum is shown, magnified, in grey in figure 3.5. A hugely complex structure is revealed in both the $^{63}Cu^+$ and $^{63}Cu_2{}^+$ channels in the energy range 20000-24000 cm^{-1}. In order to assign such a

multitude of peaks, attempts must be made to extract simpler patterns from them. Experimentally, an obvious way to extract simpler series is to perform a power dependence study in order to determine the number of photons required to create each peak. The intensity of a peak resulting from an n-photon transition, $I_p(n)$, at a laser intensity I_l, is given by:

$$I_p(n) \propto I_l^n. \tag{3.1}$$

Unfortunately, reducing the laser power by 50% did not produce any observable change in the spectra, apart from greatly reducing their intensity. A significant change could, however, be effected by removing the focussing lens from our beam path. The resulting low-intensity spectra are shown in black in figure 3.5. In the low-intensity $^{63}Cu^+$ spectrum, the only intense peak remaining is the 2+1 photoionisation peak due to the atomic resonance labelled (e) in figure 3.4. As an aside, it is interesting to note that (e) is the only transition in this region originating in $^2S_{1/2}$; all transitions out of $^2D_{5/2}$ disappear in the low-intensity spectrum which may indicate that metastable states are not generated at all by ablation but rather by fragmentation of larger clusters.

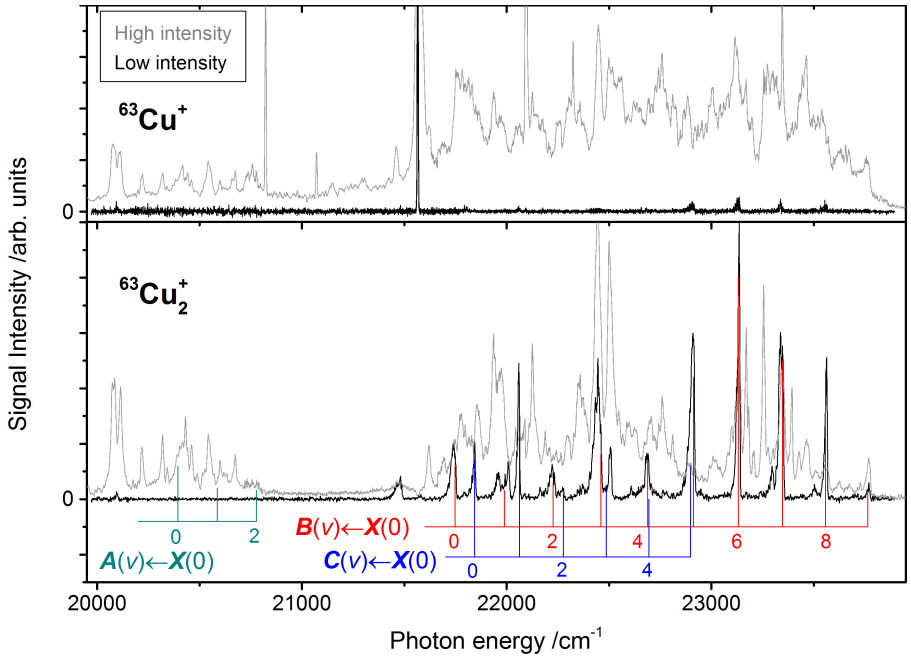

Figure 3.5: Ion yield spectra in the $^{63}Cu^+$ and $^{63}Cu_2{}^+$ channels. "High-intensity spectra", taken with a 25 cm focussing lens, are shown in black and low-intensity spectra, without a lens, in grey. The low-intensity $^{63}Cu_2{}^+$ spectrum consists of 1+2 photoionisation transitions from the Cu_2 ground state, X(v=0) to various vibrational levels of the Cu_2 B and C excited states. The low-power $^{63}Cu^+$ spectrum is the result of photodissociation of $Cu_2{}^{(+)}$. The high-power spectra have many more spectral features.

The dimer spectrum taken at low intensity is easily assigned by reference to known Cu_2 states [229]. Almost all peaks correspond to 1+2 resonant ionisation via the B and C states of Cu_2. The progression via the C state is fairly short, its only discernible members being C(ν=0-2)←X(ν=0), limited by unfavourable Franck-Condon factors [229]. The progression via the B-state is much longer, with ten transitions evident: B(ν=0-9)←X(ν=0). The most intense dimer peaks are reflected in the atom channel by a series of very small peaks between 22750 and 23700 cm^{-1}. These evidently also arise due to resonant absorption by Cu_2, either by photodissociation of Cu_2^+ or by photodissociation of Cu_2 and ionisation of the atomic cofragments.

3.2.1 The origin of features in the high-intensity photoion spectra

The low-intensity spectra in figure 3.5 are extremely helpful in establishing the origin of the complex structure of the high-intensity spectra. Firstly, the peaks in the low-intensity $^{63}Cu_2^+$ spectrum are also present in the high-intensity $^{63}Cu_2^+$ spectrum and are mirrored in the high-intensity $^{63}Cu^+$ spectrum. This shows that, even at high power, resonant 1+2 ionisation of Cu_2 X(ν=0) via its B and C states (and photofragmentation of Cu_2/Cu_2^+) creates many of the peaks in the 21500-23700 cm^{-1} region. Secondly, peaks appearing only at high intensity are likely to involve a total of four or more photons. The low-intensity spectrum does not show any peaks corresponding to A(ν)←X(ν=0) transitions because four photons are required to ionise Cu_2 at energies less than 21236 cm^{-1} [239]. Therefore, the transitions which appear at low intensity are likely to involve three photons or fewer, and transitions growing in at higher intensity should involve 4 or more photons. Thirdly, although not directly corresponding to simple A-X, B-X and C-X series, the high-intensity spectrum has features throughout the regions corresponding to those dimer bands. Since the individual peaks evidently do not correspond to transitions out of X(ν=0), they might be reasonably assumed to be derived from vibrationally excited Cu_2 X(ν). This is important, since the low-intensity spectrum suggests that our molecular beam is vibrationally cold, containing only X(ν=0).

Figure 3.6 illustrates an attempt to fit the congested region 21500-24000 cm^{-1} to transitions out of Cu_2 X(ν>0) levels. If the vibrational quantum numbers of the X, B and C states are all allowed to vary, approximately 130 lines sit in the region of figure 3.6, all with ν<20, and a transition may easily be found to fit every peak. Continuous vibrational progressions which fit the data are much more reliable than matches to individual peaks. The B-X and C-X series included in figure 3.6 were therefore required to fit at least three approximately adjacent peaks in both the $^{63}Cu^+$ and $^{63}Cu_2^+$ channels. However, interference from adjacent peaks means that this restriction is applied with some

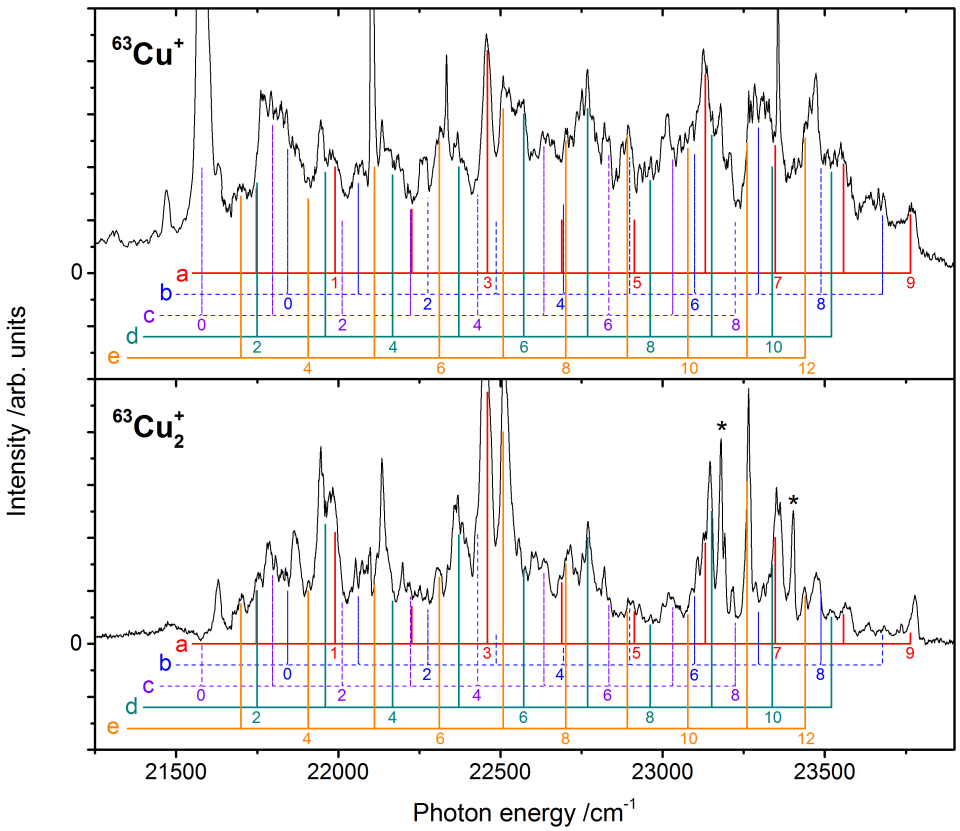

Figure 3.6: The vast majority of peaks in the high-power spectra between 21500 and 23750 cm^{-1} are fitted using transitions from a few vibrational levels of ground-state Cu_2 to a wide range of vibrational levels of the B and C states. Five series are shown: a is B(v)←X(0), b is C(v)←X(0) and c, d and e represent C(v)←X(1-3) respectively. b and c are much less important than a, d and e. The two starred peaks exactly match transitions out of X(4) to highly vibrationally excited C(v).

uncertainty. For instance, where two transitions are indistinguishably close under an intense peak, its intensity cannot be unambiguously assigned to either transition. Figure 3.6 should not be taken as an accurate fit, but rather as an illustration that the marked transitions are plausible. Nonetheless, the fit is of substantial value as it illustrates that remarkably few series are needed to fit most of the separate features in the spectrum. In addition to the transitions out of X(v=0) to B and C (marked as (a) and (b) respectively), three more series are used: C(v)←X(1, 2, 3) (labelled (c), (d), and (e) respectively). Unfavourable Franck-Condon factors restrict the C(v)←X(v=0) progression, series (b), and the C(v)← X(v=1) progression, series (c) [229]. Series (c) may also be restricted by a low intensity of X(v=1) in the beam, as will be discussed hereafter. Series (b) and (c) are consequently marked with dotted lines, as they account for very few peaks between them.

We are left with the interesting suggestion that *virtually all the additional peaks present in the high-*

intensity spectrum are accounted for by resonant ionisation and fragmentation out of the X(v=2) and X(v=3) states via the C state. The two intense peaks not matched by these series (starred in fig. 3.6) are perfectly coincident with transitions out of X(v=4) via the C state. Considering the simplicity of the fit, which uses only the positions of the vibronic band heads and makes no allowance for rotational structure, such correlation is remarkable, and suggests that the fit has some basis in truth.

A similar fit is possible in the A-state region, 20000-21000 cm^{-1}, but is not shown because it is much less secure. There are many fewer peaks in the A-state region, so long vibrational progressions are not observed. It is therefore more difficult to differentiate between true correlation and mere coincidence. Also, while it is known that Franck-Condon factors allow access to a wide range of vibrational levels of the C state from X(v>1), the same has not been shown for the A-state [229, 230]. Finally, the Cu^+ and $Cu_2{}^+$ high-intensity spectra are almost identical in this region, which suggests that both spectra reflect the Cu_3 photodissociation cross-section.

Having established that the peaks observed at high intensity may arise from Cu_2 X(v>0), a source of Cu_2 X(v>0) is sought. A reasonable suggestion is that hot Cu_2 forms by photodissociation of Cu_n, most probably Cu_3. A mechanism by which Cu_2 X(v>0) may be produced from nascent Cu_3 is illustrated in figure 3.7, along with pathways which subsequently produce Cu^+ and $Cu_2{}^+$. Pathways forming $Cu_3{}^+$ are excluded as $Cu_3{}^+$ is not observed. The figure is drawn to an energy scale, but the Morse parameters of the excited dimer states are unknown. Approximate dissociation energies of the excited states are given in references [226, 229] and values are chosen within their given limits to coincide with the order of published ω_e values.

On the left-hand side of figure 3.7, Cu_3 is dissociated with a single photon. This is feasible as $D_0(Cu_3)$ is approximately 8000 cm^{-1} [262]. The mechanism illustrated involves exciting Cu_3 to a dissociative state which correlates to the Cu $^2S_{1/2}$ + Cu_2 X(v) limit. The metastable ^2D_J states are also accessible atomic products in the one-photon scheme and cannot be ruled out. Regardless of which of these states is generated, the atomic products require three photons for ionisation and are likely to be detected weakly, except at the resonances identified in figure 3.4. The dimer product, however, can absorb a resonant photon and form Cu_2*. Cu_2* can decay in one of two ways. It may absorb a further two photons to exceed its ionisation limit and form $Cu_2{}^+$. Alternatively, on absorbing additional photons it may dissociate to neutral atomic products. Figure 3.7 shows an example wherein Cu_2* absorbs two photons before dissociating to one ground-state and one highly-excited atomic product; the latter may be ionised on absorption of a single subsequent photon. Lower photon order mechanisms are possible

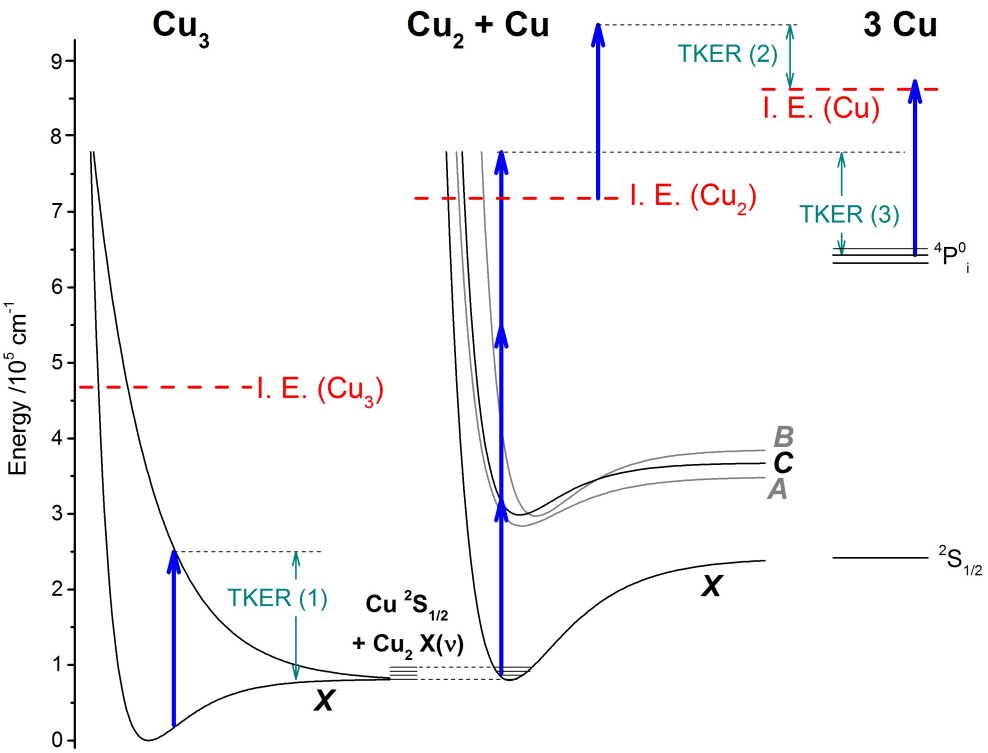

Figure 3.7: Possible methods of formation of Cu_2^+ and Cu^+ from Cu_3. Cu_3 is dissociated with one photon to Cu $^2S_{1/2}$+Cu_2 X(v>0). The vibrationally excited Cu_2 is resonantly 1+2-photon ionised via the C state. Cu_2^+ may absorb an additional photon to form Cu^+ + Cu. An alternative route to Cu^+ is illustrated on the right-hand side; Cu_2 X(v>0) is resonantly photodissociated in a 1+2 process to form Cu $^2S_{1/2}$ + Cu* and the Cu* product is ionised with one further photon. The figure is drawn to an energy scale, although the dissociation energies of the A, B and C states of Cu_2 are unknown.

(for instance, Cu_2* may dissociate after absorbing a single photon) but are not shown in fig. 3.7.

The Cu^+ signal is generated from Cu_2, sometimes resonantly, which creates the Cu^+ peak structure seen in figure 3.6 (although peak structure of both Cu^+ and Cu_2^+ channels is dependent on the photodissociation spectrum of Cu_3). At all wavelengths used, creation of Cu^+ from Cu_3 via one-photon dissociation of Cu_2^+ requires 5 photons. Formation of Cu^+ via three-photon dissociation of Cu_2 to form Cu + Cu* allows 1-photon ionisation of the excited atomic product, making this a 5-photon pathway at all wavelengths. However, two-photon dissociation of Cu_2 can only generate ground or metastable D-state atomic products which require three photons for ionisation. Generation of Cu^+ from Cu_3 by this latter route requires six photons and is less likely than the other two pathways. All the schemes suggested for the formation of Cu^+ and Cu_2^+ fulfil the requirement put forward in the discussion of figure 3.5: they involve more than three photons overall. Cu_2^+ is generated from Cu_3 with 4 photons, and Cu^+ with 5.

Before leaving the scheme of figure 3.7, it should be noted that X(v>0) does not appear to dissociate via the B state. The Franck-Condon factors may be prohibitive; the B $^1\Sigma_u$ state has an unusually long Cu-Cu distance and may be steep-sided enough that only B(v>>0) are accessible from X(v>0) [209]. Although the B state's lifetime is short at around 30 ns, it is long compared to a laser pulse length and sufficient to allow multiphoton absorption, should it be allowed [231].

3.2.2 Spectral evidence for the trimer

Having invoked the trimer in formation of our high-intensity spectra, the presence of Cu_3 in the molecular beam must be demonstrated. Discouragingly, there is no evidence of any signal in the Cu_3^+ channel at any wavelength from 410 to 550 nm (approximately 18000 to 24000 cm^{-1}), a span that encompasses all previously-observed transitions in Cu_3 [257]. Even more discouragingly, there is no evidence of Cu_3^+ in figure 3.8, a photoionisation spectrum taken with a 157 nm F_2 excimer. Cu_2 appears as a minor peak in figure 3.8 as its ionisation energy, 7.899 eV, slightly exceeds the excimer energy, 7.897 eV [210]. However, 7.897 eV far exceeds the ionisation energy of Cu_3, 5.80±0.04 eV [29], and excimers have often been used to ionise Cu_3 [81].

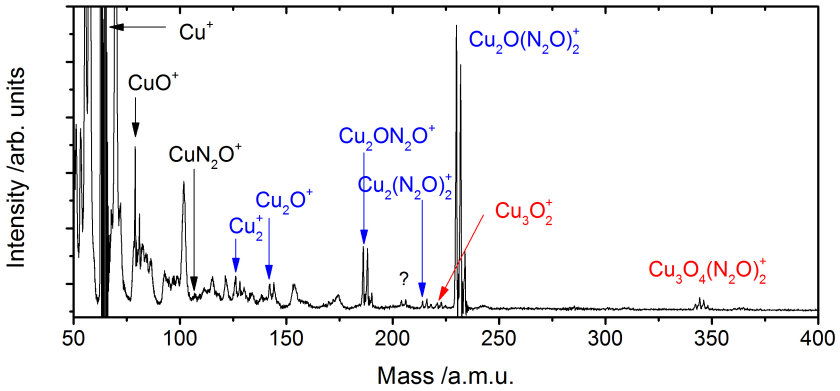

Figure 3.8: A variety of decorated copper clusters are visible in the TOF spectrum taken with the 157 nm F_2 excimer, but Cu_3^+ is conspicuous by its absence.

Nevertheless, the presence of Cu_3 must not immediately be discounted. Comparison of the low-energy region of our Cu^+ and Cu_2^+ with Morse's Cu_3 photodepletion spectra reveals some similarities. His original data was shown in figure 3.2, and his line positions are indicated in relation to the current spectra in figure 3.9. It appears that the current Cu^+ and Cu_2^+ spectra reproduce Morse's photodepletion lines 8-12 almost exactly. Lines 5 and 7 appear to be absent in the current spectra, and line 6 is only barely present. Morse's photoionisation lines 1-4 are marked in figure 3.9 as dotted lines, although we would not expect to observe them in Cu^+ and Cu_2^+ spectra. Reproducing Cu_3

photodepletion lines in the expected photofragment channels, Cu and Cu_2, is strong evidence for the existence of Cu_3 in our molecular beam.

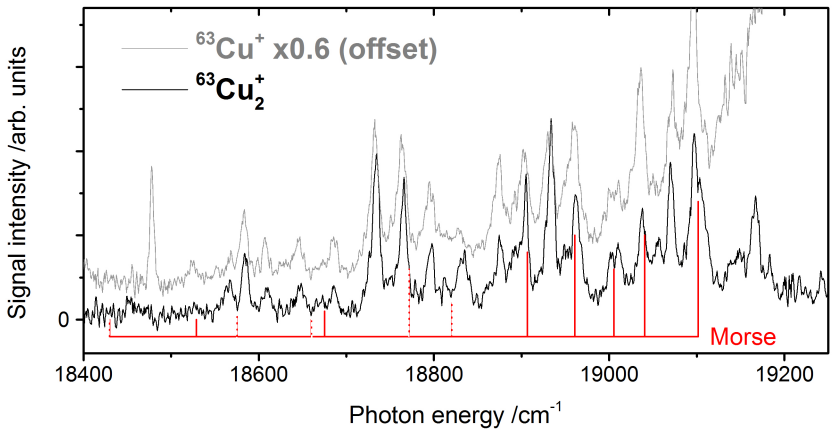

Figure 3.9: Cu_2^+ and Cu^+ spectra, overlaid to emphasise their almost identical structure which indicates a common origin. Cu_3 photodepletion lines observed by Morse are shown in red. Many of these appear to be reproduced in the present Cu_2^+ and Cu^+ spectra. Morse's Cu_3 photoionisation peaks are also marked in dotted lines but are not reproduced in the fragment channels.

Figure 3.9 illustrates the similarity of the spectra recorded in the Cu^+ and Cu_2^+ channels. The structure cannot be fitted by any known dimer transitions, and so must derive from a larger species which can dissociate to form Cu_2 and Cu. An argument for this larger species being Cu_3 in this region is that Cu_3 forms Cu and Cu_2 with *equal probability*; in forming one fragment, it must form the other. Spectra in the Cu_2^+ and Cu^+ channels therefore mirror one another.

Assuming Hilpert's $D_0(Cu_3)$ to be correct, only the ground electronic states of Cu and Cu_2 are energetically accessible by one-photon dissociation below 20000 cm^{-1}. The ground states require four photons for ionisation, and there are no dimer resonances in the 18400-19200 cm^{-1} region of figure 3.9. Therefore the signal in both Cu^+ and Cu_2^+ channels in figure 3.9 is likely to arise from non-resonant photoionisation of the ground-state Cu_3 dissociation products; *subsequent photodissociation of Cu_2 will be a minor contribution to the atom channel.* Non-resonant ionisation cross sections depend only on the electronic wavefunction of the parent state. As a result, identical intensity patterns would be expected in both Cu and Cu_2 product channels, with the existence of peaks reliant only on the dissociation cross section of Cu_3. This differs from the situation at higher energy in figures 3.5 and 3.6, where Cu_2 is photoionised, and photodissociated, via resonances with various vibrational levels of the Cu_2 B and C states. Here, the photodissociation and photoionisation cross sections of the intermediate states are overlaid on the intensity pattern arising from Cu_3 photodissociation. The

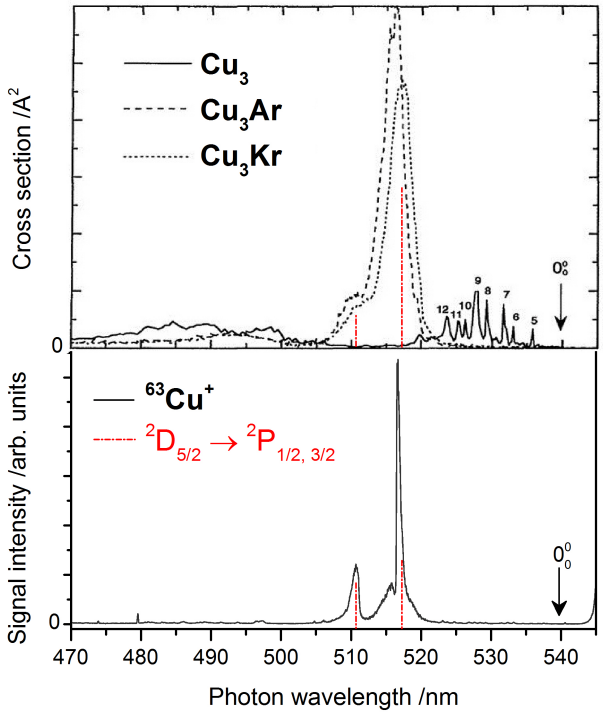

Figure 3.10: The current Cu^+ ion yield spectrum compared to Knickelbein's Cu_3 photodepletion cross sections (upper graph). The Cu_3RG spectra have significant features at 516nm with a shoulder at 510nm, whose shape is strongly reminiscent of an enhancement seen in the Cu^+ channel of our spectra. Knickelbein does not, however, see such a depletion in the case of the bare trimer. $^2P_{1/2,\,3/2} \leftarrow {}^2D_{5/2}$ transitions are marked in red.

structure in the Cu_2^+ and Cu^+ channels is therefore similar but not identical.

Knickelbein studied the trimer in its A←X region, and his photodepletion spectra are compared to the present data in figure 3.10 [257]. Knickelbein saw much the same structure as Morse in photodepletion of Cu_3, along with a broad photodissociation envelope which he ascribed to a predissociative trimer state, B. However, upon tagging Cu_3 with a rare gas atom (RG), the vibronic trimer structure disappeared and an extremely broad Cu_3RG depletion appeared instead. Comparison of the present Cu^+ enhancement and Knickelbein's Cu_3RG depletion reveals a striking similarity in shape. Knickelbein saw a single feature at 516 nm with a shoulder at 510 nm. The Cu^+ spectrum shows two separate features, peaking at 510 and 516 nm, whose intensity ratio and profile are strongly reminiscent of Knickelbein's depletion feature. Whilst it might be easy to conclude that our Cu^+ signal must therefore be the fragmentation product of decorated Cu_3, there are a number of flaws in this argument.

1. There is no argon or krypton present in the current experiment; the carrier gas used is helium containing 5-10% N_2O. While Cu_3N_2O may well form, it is highly unlikely to exhibit exactly

the same shift in the Cu_3 A←X transition as Cu_3Ar and Cu_3Kr.

2. The two features in the Cu^+ channel are centered on one-photon transitions out of the $^2D_{5/2}$ metastable state of the atom. This implies that their intensity is due to the presence of a Cu atom in the $^2D_{5/2}$ state which can resonantly absorb. Shifts in the frequency of the absorption would be expected if the Cu atom were tagged by a weakly-binding species, causing the broadening of the atomic transitions observed in figure 3.10.

The presence of this structure, and its similarity to Knickelbein's Cu_3RG depletions, remain no more than a curious observation. Another curiosity is that the structure of the peak centered at 516 nm is reminiscent of the classic winged profile arising from the P, Q and R branches of a rovibronic transition in a prolate top. If these large atomic enhancements do result from dissociation of decorated Cu_3, however, they provide further evidence for large quantities of Cu_3 in the beam which is not directly observed in figure 3.8 by photoionisation. It may be that 157 nm radiation tends to fragment Cu_3 produced by our source, rather than to ionise it.

3.3 Cu Images

As shown in the previous chapter, VMI is an extremely useful tool for determining the origin of spectral peaks. Given a fragment, VMI is potentially capable of identifying its cofragment and the exact quantum state of both fragmentation products, along with the 'photon order' of the fragmentation. To extract such firm conclusions requires a unique assignment of both fragments and their energy states. As will become apparent, this is not always possible.

Figure 3.11 shows a typical image in the Cu^+ channel, along with its kinetic energy release spectrum. In the previous chapter, CuO was observed to dissociate to a single limit, releasing products with a well-defined kinetic energy, forming a single sharp ring in the image and consequently a single sharp peak in the KER spectrum. The OPO, however, is operated at a much higher power and thus can access a range of multiple-photon dissociation channels. The images it produces are not easily fitted. An attempt is made using Gaussian functions, in order to identify peaks in the TKER spectrum; in reality, the peaks' shape need not conform to any such ideal function. The KER spectrum in figure 3.11 evidently contains several sharp peaks, some of which are easily identifiable in the accompanying image, and some of which are not. The fit additionally requires two very broad background peaks. 'Background' is perhaps an unsuitable term as they contain far more intensity than the sharp peaks

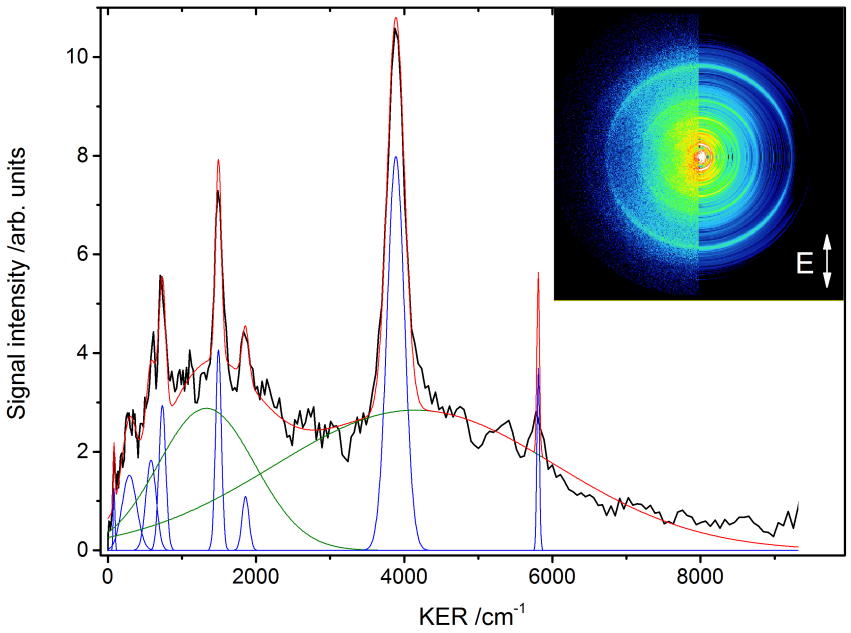

Figure 3.11: A typical Cu^+ image from the B and C state region, taken at 22895 cm^{-1}. The image is converted to a kinetic energy release spectrum, showing the intensity of the signal with the distance from the image's centre. It is fitted with Gaussian functions to aid assignment of the peaks; sharp peaks are visible, but two broad features are also needed to fit the spectrum adequately.

they sit underneath. The very different peak profiles suggest that the fragmentations occurring to create the Cu^+ image fall into two very different categories.

3.3.1 Three photon dimer dissociation

The sharp peaks such as those seen in figure 3.11 are considered separately to the broad background. Not all of the Gaussian functions used in the fit are distinguishable by eye as rings in the accompanying image. This is a particular problem at low energy. The only fitted peaks included in the following discussion are those that are sufficiently intense and sharp to be clearly visible by eye in the image. Three peaks meet these criteria in the KER spectrum of figure 3.11 at 733, 1494 and 3891 cm^{-1}. The location of the sharp peaks in the individual KER spectra is determined by the centre of the Gaussian function fitting the peak, and the uncertainty in that position is taken to be the full width at half maximum (FWHM) of the fitting function. KER values thus obtained are converted into TKER values by assuming a variety of reasonable cofragments. Figure 3.8 shows that there are many species in the beam that could release a copper atom: CuO, CuN_2O, Cu_2, Cu_2O, Cu_2N_2O, and so on are all possible candidates. The criterion for a suitable cofragment is that it must produce TKER points which lie on a straight line graph with an integer slope when plotted against photon energy, as all dissociation

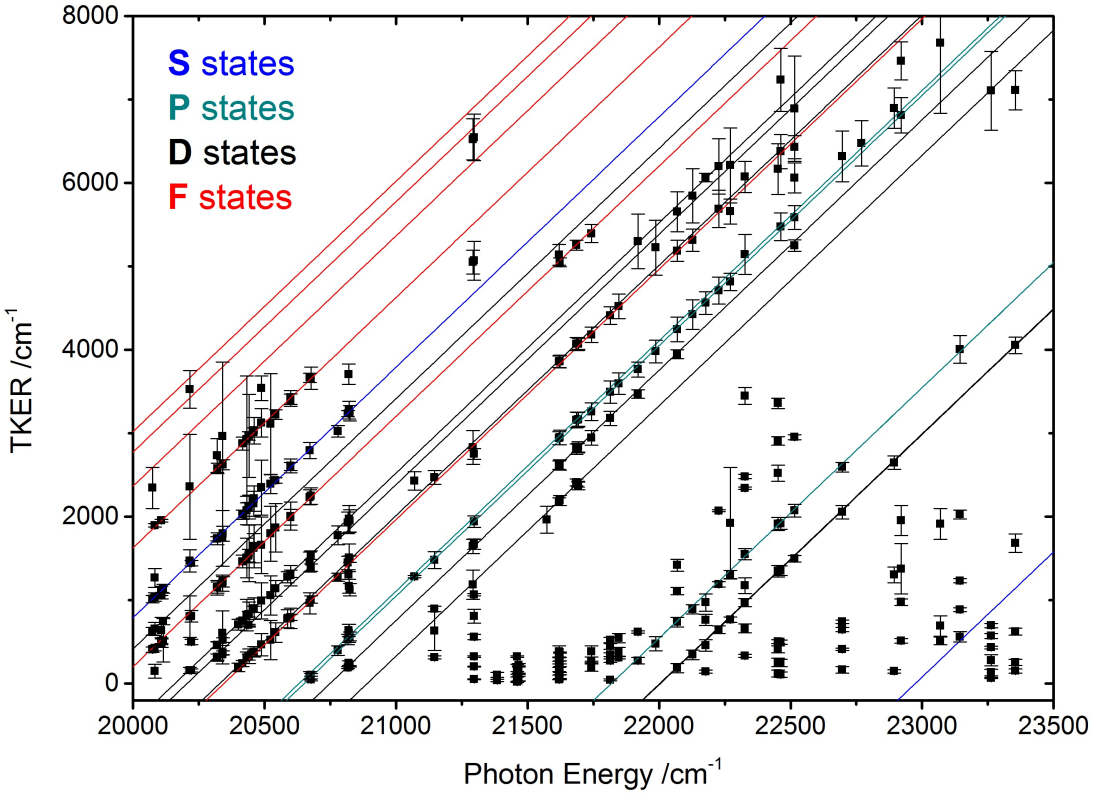

Figure 3.12: Peaks in the TKER spectra extracted from all images in the range 20000 to 23500 cm^{-1}, calculated assuming a Cu atom cofragment. Their uncertainties represent the FWHM of the TKER peak. *The lines are not fits*; they indicate the predicted positions of TKER peaks assuming a 3-photon dissociation of Cu_2 to form a ground-state and an excited copper atom, Cu*. Lines corresponding to an S-state Cu* are shown in blue, P-state in green, D-state in black and F-state in red. The majority of the TKER points lie on the lines.

processes must involve an integer number of photons.

The distribution of TKER peaks assuming an atomic copper cofragment is shown in figure 3.12. At first glance, it is apparent that a large majority of the points follow one of several linear trends. The slope of all these lines is exactly 3. No other cofragment can provide such a satisfactory fit to the data. This implies that almost *all* of the sharp peaks seen in the many images taken in the Cu^+ channel arise from three-photon dissociation of Cu_2 (or Cu_2^+, or even Cu_2^{2+}).

A linear TKER fit alone is insufficient to allow assignment of the dissociative process or processes occurring. The energy balance equation for three-photon dissociation of Cu_2, or Cu_2^+ is:

$$3h\nu = D_0(Cu_2) + E_{int}(Cu) + E_{int}(Cu^{(+)}) + \text{TKER} \tag{3.2}$$

Equation (3.2) assumes the dissociating species has zero internal energy; it is in its ground state. Spectroscopic evidence supports the assertion that nascent Cu_2 in the beam exists in its ground electronic and vibrational state (figure 3.5), although hot Cu_2 may be generated by dissociation of Cu_3. The point at which each of the linear series in figure 3.12 intercepts the horizontal axis is the photon energy at which TKER=0, *i.e.* the dissociation threshold. The intercepts in figure 3.12 are predictions. The experimental intercepts are found by fitting each series of points in the figure to a line with a gradient of 3. The intercepts are multiplied by 3 to account for the 3-photon nature of the dissociation, and Hilpert's $D_0(Cu_2)$ is subtracted [237]. The resulting energies are compared with the NIST database to see if they match any known internal energies for Cu + $Cu^{(+)}$ [211].

All intercepts obtained correspond closely to known energy levels of the neutral copper atom exceeding 42000 cm^{-1}. This number is significant as it is within one photon of the ionisation limit of Cu, 62317.46 cm^{-1} [211]. The mechanism for formation of almost all the sharp peaks in the Cu^+ images is therefore three-photon dissociation of neutral copper dimer to form one ground-state and one highly excited copper atom, Cu*. Cu* is ionised with a single subsequent photon.

$$Cu_2(X^1\Sigma_g^+) + 3h\nu \rightarrow Cu(^2S_{1/2}) + Cu^* + \text{TKER} \tag{3.3}$$

$$Cu^* + h\nu \rightarrow Cu^+ + e^-$$

All possible TKER peak positions, according to mechanism (3.3) and using Hilpert's $D_0(Cu_2)$ [237],

Configuration	State symbol	Energy /cm^{-1}
$3d^94s4p$	$^4F^0_{9/2}$	40909.16
	$^4F^0_{7/2}$	41153.47
	$^4F^0_{5/2}$	41562.93
	$^4F^0_{3/2}$	42302.58
$3d^{10}5s$	$^2S_{1/2}$	43137.23
$3d^94s4p$	$^4D^0_{7/2}$	43514.01
	$^4D^0_{5/2}$	44406.32
	$^4D^0_{3/2}$	44544.16
	$^4D^0_{1/2}$	44915.68
$3d^94s4p$	$^2F^0_{5/2}$	43726.24
	$^2F^0_{7/2}$	44963.26
$3d^94s4p$	$^2D^0_{3/2}$	46172.89
	$^2D^0_{5/2}$	46598.35
$3d^{10}5p$	$^2P^0_{3/2}$	49382.95
	$^2P^0_{1/2}$	49383.26
$3d^{10}4d$	$^2D_{3/2}$	49935.20
	$^2D_{5/2}$	49942.05
$3d^{10}6s$	$^2S_{1/2}$	52848.75

Table 3.1: Energy levels of Cu*, taken from [211]. When added to $D_0(Cu_2)$, they give the dissociation threshold for formation of Cu + Cu* from Cu_2.

are marked on figure 3.12. All accessible Cu* states are listed in table 3.1. They range from Cu $3d^9(^2D)4s4p(^3P^0)\ ^4F^0_{9/2}$ at 40909.16 cm^{-1}, whose corresponding predicted TKER is shown in red on the far left of figure 3.12, to $3d^{10}6s\ ^2S_{1/2}$ at 52848.751 cm^{-1} in blue on the far right of figure 3.12. Almost every possible fragmentation pathway appears to be manifest in the images, as peaks appear on almost all the lines.

To illustrate how these 3-photon dissociations appear in the Cu^+ images, the 22272 cm^{-1} image is depicted in figure 3.13. In this particular image, five dissociation channels result in five sharp rings. The channels are labelled on the image itself, while, on the right, all the Cu* energy levels from figure 3.12 are marked on a vertical energy scale. Those visible in the image are starred. The sharp peaks are evident, as is the broad background they sit upon; the image is very bright between the rings.

Three-photon dissociation may seem an unlikely process to observe. In the absence of an ionisation laser, however, the experiment becomes especially sensitive to processes which yield charged or easily ionisable products. In all probability, two-photon dissociation of Cu_2 occurs simultaneously, but throughout the energy range we have studied the only product states accessible to two-photon dissociation are ground state and the metastable $^2D_{5/2}$ and $^2D_{3/2}$. These require a further three photons for ionisation, and are therefore unlikely to be detected. Most Cu^+ images recorded lack an intense central spot, which proves that the ground and low-lying metastable states of Cu, which are abundant

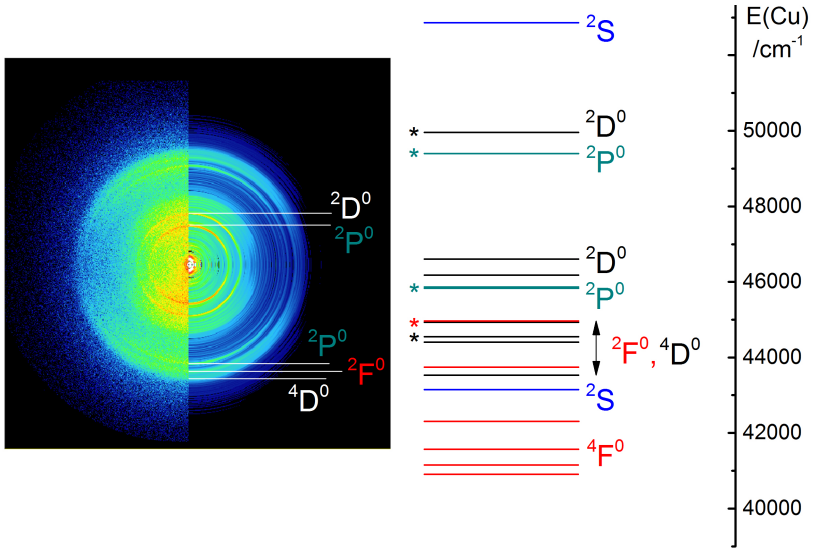

Figure 3.13: The image taken at 22272cm^{-1} in the Cu^+ channel, along with the energy levels creating its sharp rings. Sharp rings in the Cu^+ channel almost all arise from the 3-photon dissociation of Cu_2 to form one ground state and one highly excited Cu atom. The latter can be ionised with a single subsequent photon.

in the molecular beam, are not easily non-resonantly ionised with three or four photons and so do not appear strongly in the image.

3.3.2 Testing the three-photon assigment

In the previous chapter, once potential dissociation products had been identified, the assignment was tested. The ionisation laser was tuned to a resonant transition of the anticipated Cu $^2D_{3/2}$ product in order to observe an enhancement of the Cu^+ product signal. Such an approach is not possible following the three-photon Cu_2 dissociation described here. The ground state Cu product cannot be selectively tagged as it is implicated in all dissociative processes. The alternative, namely resonant tagging of the Cu* product, is unlikely to work either. It would be possible to excite an electron *via* a fully allowed, single-photon transition from many of the Cu* products to one of the vast number of known Rydberg states just below the ionisation level of the atom. However, resonant tagging relies on enhancing a single product's ionisation probability by providing a resonant ionisation pathway. In the case of highly excited Cu atoms, ionisation is already a facile, single-photon process. Adding in a laser subsequent to the visible pulse, resonant or not, will not affect the ionisation probability as ionisable species have already been ionised by the visible laser. The object of tagging is therefore defeated. However, the excellent accord between the predicted and observed locations of the TKER peaks in figure 3.12 provide sufficient proof of the three-photon mechanism in this case.

3.3.3 Low-TKER peaks in the 21000-24000 cm^{-1} region

A number of peaks in figure 3.12 do not lie on any of the predicted TKER lines, particularly at photon energies greater than 21000 cm^{-1} and low TKER. These were re-investigated using the fitting procedure described previously: a reasonable cofragment was assumed and a search performed for linear trends within the resulting TKER distribution. No product channels could be assigned with certainty. So many points are present within the small TKER range that no individual linear trend emerges with certainty. Figures 3.12 and 3.14 do not explicitly portray quite how congested this low-TKER region is, because TKER peaks which cannot be identified as rings in the image are not included. Although there is much intensity at small radii in the images, resolution is proportionally poorer at low KER where rings are distributed over a smaller number of pixels.

In addition to the absence of a linear trend, a unique assigment of these peaks is made challenging by the large number of energetically feasible processes which can produce these small kinetic energy releases. Even when the search is narrowed to processes producing Cu^+, or Cu atoms ionisable with a

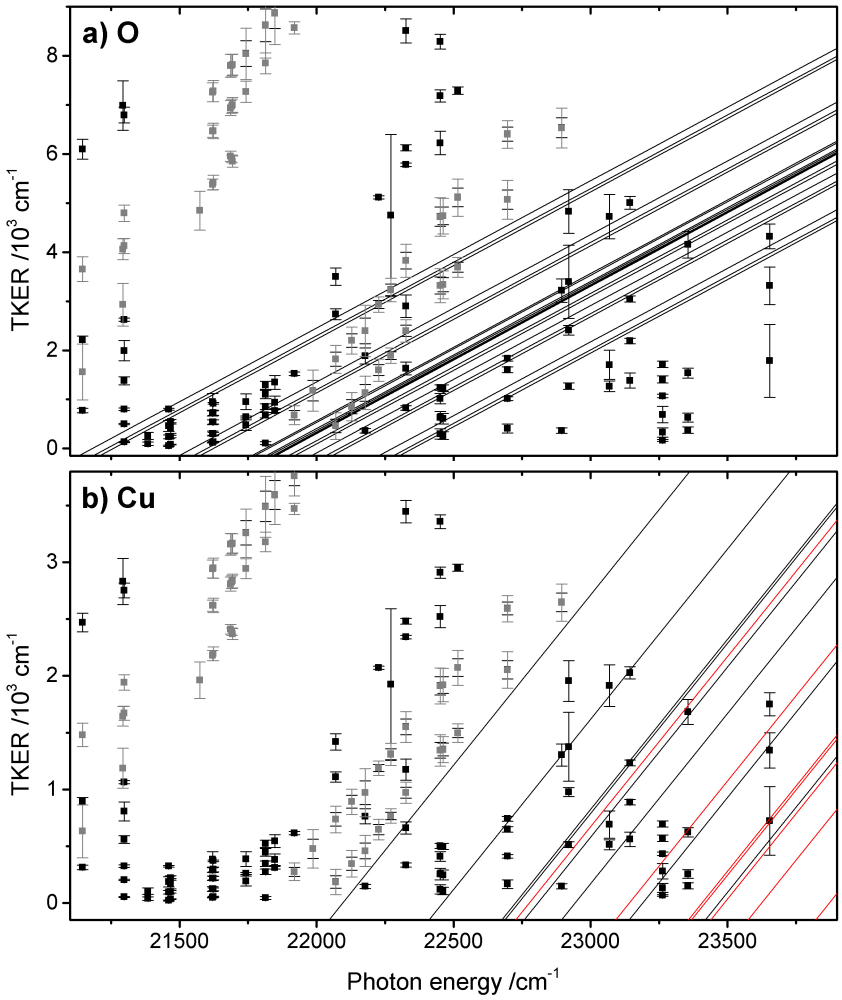

Figure 3.14: Low-TKER peaks from the Cu^+ images assuming (a) an O atom cofragment and (b) a Cu atom cofragment are shown. Peaks previously assigned to process (3.3) are greyed out. Lines indicate predicted positions of TKER peaks upon three-photon dissociation of CuO and Cu_2 which produce a Cu* atom ionisable with a single subsequent photon. In (a), the cofragment of Cu* is the O ^{3}P ground state. In (b), red and black lines show the expected TKER release accompanying a Cu $^2D_{5/2}$ and a Cu $^2D_{3/2}$ cofragment respectively.

single photon, the possibilities lying in this region are enormously numerous. By way of example, the predicted TKER lines arising from 3-photon dissociation of (a) CuO and (b) Cu_2 to produce highly excited Cu* products are shown in 3.14.

Figure 3.14 (b) includes the low-TKER data from figure 3.12. Any data points assigned to process (3.3) are 'greyed out'. The lines in this new figure show the predicted TKER after three-photon dissociation of Cu_2 to produce one highly-excited copper atom, Cu*, and one in a metastable D state. The black lines correspond to a Cu $^2D_{5/2}$ and the red lines to a $^2D_{3/2}$ cofragment. In both cases, the Cu* cofragment is ionisable with a single subsequent visible photon. A large number of previously-

unexplained points lie on these lines, but none have a sufficiently good match to allow a confident assignment. When considered in conjunction with figure 3.14 (a), a conclusive assignment on the basis of figure 3.14 (b) cannot be made with certainty.

Figure 3.14 (a) shows the TKER data from our images assuming an oxygen atom cofragment and our previously-determined D_0(CuO). [142] The black lines show the predicted TKER positions after 3-photon dissociation of CuO to produce Cu* and an oxygen atom in one of the three spin-orbit components of its triplet ground state, scheme (3.4):

$$\mathrm{CuO}(X^2\Pi_i) + 3h\nu \rightarrow \mathrm{O}(^3P_J) + \mathrm{Cu}^{(*)} + \mathrm{TKER} \tag{3.4}$$

$$\mathrm{Cu}^{(*)} + 1h\nu \rightarrow \mathrm{Cu}^+ + e^-$$

Only dissociations out of the lower spin-orbit component of the CuO ground state ($^2\Pi_{3/2}$) are shown in the figure. However, it is known from previous CuO spectroscopy that the X $^2\Pi_{1/2}$ state is present in small quantities in the molecular beam. This state gives rise to a second manifold of lines, identical to those already present but shifted 92 cm^{-1} downwards [194]. Again, all the Cu* states included are ionisable with a single subsequent visible photon. The region containing predicted TKER peaks in figure 3.14 is nearly a continuum, and imputing individual peaks to individual transitions becomes a hopeless exercise. Worse still, other very reasonable cofragments such as N_2O or Cu_2 have not yet been considered (although the sharpness of the peaks suggests atomic cofragments). The best that can be said here is that the low-TKER peaks may be fitted to a number of reasonable options, although no unique assigment has been made.

3.3.4 Calculation of $D_0(Cu_2)$

$D_0(Cu_2)$ is already fairly well-known [3], so a calculation of its value from our data will not add much of value to the body of experimental work on Cu_2. However, the enormous number of data points spread across the nine series visible in figure 3.12 should yield a value with very small uncertainty. Each series is fitted by a straight line with its slope fixed at 3. This yields a series of lines with some uncertainty in their x-intercept arising from the peak widths, which is the largest contribution to the uncertainty in our D_0 values as the atomic energy levels are very accurately known. However, in some cases, there are two possible candidates for the corresponding atomic state. For instance, the two components of $3d^{10}5p\ ^2P^0_{3/2,\,1/2}$ at 49382.95 and 49383.26 cm^{-1} both lie along one series of data points in figure 3.12. Similarly, $3d^{10}4d\ ^2D_{3/2,\,5/2}$ has components at 49935.20 and 49942.05

cm^{-1} which both correspond to a single data set. Either or both components may be contributing to the TKER peaks; they are indistinguishable. Since their separation is barely larger than the laser linewidth and comfortably within the inherent uncertainty of VMI, the inability to determine which series we have adds a very small contribution to the error in $D_0(Cu_2)$.

The other two series in figure 3.12 which lie close to multiple Cu* thresholds have larger potential errors. These two series are:

- either $3d^9(^2D)4s4p(^3P^0)\ ^4D^0_{1/2}$ at 44915.68 or $3d^9(^2D)4s4p(^3P^0)\ ^2F^0_{7/2}$ at 44963.26 cm^{-1}
- either $3d^9(^2D)4s4p(^3P^0)\ ^2P^0_{1/2}$ at 45820.94 or $^2P^0_{3/2}$ 45879.32 cm^{-1}

The first of these series is disregarded as its slope is found to be substantially different to 3, probably because both of the components mentioned are present, but cannot be easily disentangled. The second, when compared to all the other values, can be fairly confidently assigned to the Ω=3/2 component.

When the remaining series' intercepts are evaluated and averaged, $D_0(Cu_2)$ is found to be 16065±300 cm^{-1}, or 1.992±0.037 eV. This is strong confirmation of Hilpert's mass spectrometric determination [237]. Using the most recent values for the ionisation energy of Cu_2 [239], and Cu [213], this $D_0(Cu_2)$ value can be used to determine a value of $D_0(Cu_2^+)$=14673±340 cm^{-1}, or 1.819±0.042 eV. This is in excellent agreement with Sappey, Harrington and Weisshaar's $D_0(Cu_2^+)$=1.84±0.08 eV [210].

3.3.5 Low-energy Cu^+ images

Cu^+ images and TKER spectra shown thus far bear little relation to the spectral structure of figure 3.5. Thus far, the mechanism leading to off-axis intensity in the images does not rely on any resonant process; three-photon dissociation of Cu_2 and ionisation of the Cu* product occur non-resonantly. On the rare occasion that the photon energy is resonant with a B-X(v=0) or C-X(v=0) transition, the three-photon dissociation pathway may be enhanced but it competes with 1+2 ionisation. In theory, one can look for enhancements in the sharp peaks in images taken at B-X(v=0) and C-X(v=0) resonances compared to off-resonance images. However, direct comparison of the intensity of the sharp peaks is difficult as they are often small perturbations on the broad 'background structure' shown in figure 3.11. Besides, the origin of this background image intensity is as yet undetermined, and itself may be enhanced by B-X and C-X resonances, meaning that the sharp peaks in the image will not become any more distinct.

In fact, in the high intensity Cu^+ spectrum in figure 3.5, between 21400 and 23800 cm^{-1} the Cu^+

signal never drops to zero. Copper can be non-resonantly ionised with three photons at energies above 20772 cm^{-1}. However, the images throughout this region have little intensity at their centre, showing that a small fraction of the intensity in figure 3.5 is due to non-resonant ionisation of atomic copper in the beam, be it in its ground state or higher metastable states. Except at the atomic transitions labelled in figure 3.4, much of the Cu^+ signal in figure 3.5 is due to fragmentation of a larger species. Sharp features in the Cu^+ images have been explained in the previous sections but the broad features have not. Atomic cofragments typically have well-defined energies leading to very narrow TKER distributions and therefore cannot produce very wide features, except in the case of dissociative autoionisation. An alternative explanation for such broad structure is that the cofragment has a poorly-defined internal energy. This may result from an extremely long vibrational progression or an extensive range of closely-spaced internal energies, typical of a molecular cofragment.

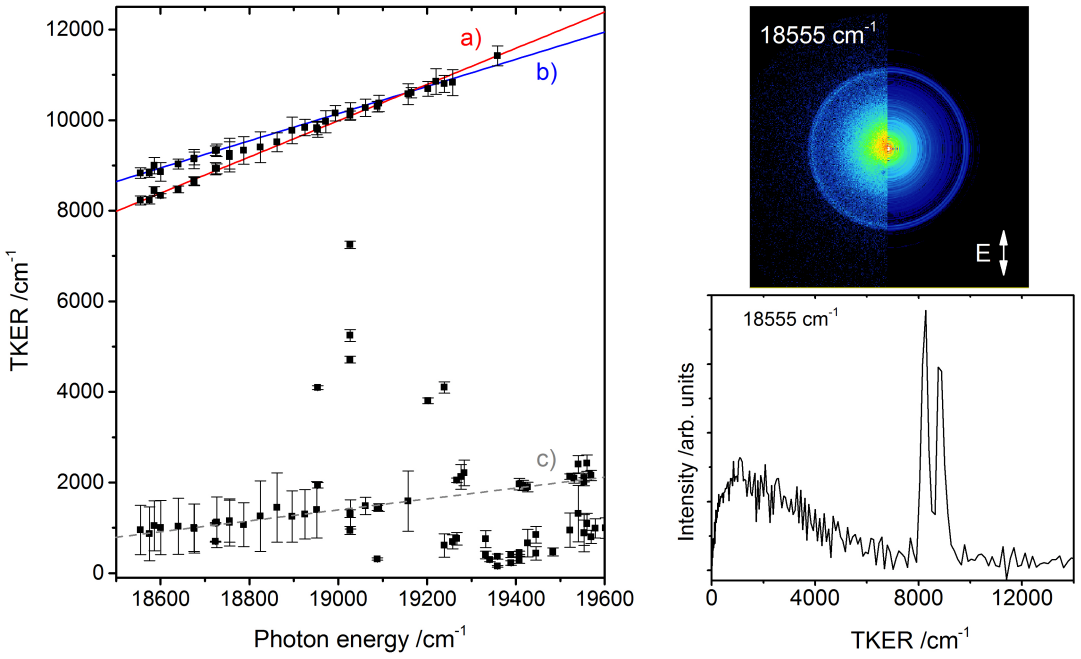

Figure 3.15: Cu^+ TKER peaks in the energy range 18400-19200 cm^{-1}, assuming an atomic copper cofragment. Series (a) is 4hν dissociation of Cu_2 to produce Cu + Cu* ($3d^{10}4d\ ^2D_n$). (b) is 3hν dissociation of Cu_2 to produce Cu + Cu* ($3d^{10}4p\ ^2P^0_{3/2}$). Series (c), even within its large uncertainties, cannot be matched to any known fragments and therefore cannot have a copper atom cofragment. An image and its TKER spectrum taken at 18555 cm^{-1} are shown, illustrating the sharp features at high TKER and broad peak at low TKER.

To obtain further information on the origin of this background structure, it is informative to study it in the 18400-19200 cm^{-1} region where the signal does drop away to almost nothing between peaks, as may be seen in figure 3.9. This region is also of interest as it contains the trimer A-X band. Figure

3.15 shows the TKER peaks in the Cu^+ channel in this energy range assuming an atomic copper cofragment. Also shown are the 18555 cm^{-1} image and its TKER spectrum. Once again, the image appears to consist of sharp peaks overlaid on a very intense, very broad structure. The image is much simpler at these low energies. The two series of sharp rings fit the same pattern as before: multiphoton dissociation of Cu_2 to form a highly excited, easily ionisable copper atom, Cu*. Series (a) corresponds to 4-photon dissociation of ground-state Cu_2, creating a ground state copper atom and Cu* $3d^{10}4d\ ^2D_{3/2}$ or $^2D_{5/2}$:

$$Cu_2(X^1\Sigma_g^+) + 4h\nu \rightarrow Cu(^2S_{1/2}) + Cu^*(^2D_n) + \text{TKER} \tag{3.5}$$

$$Cu^*(^2D_n) + h\nu \rightarrow Cu^+ + e^-$$

Series (b) corresponds to 3-photon dissociation of Cu_2, creating one ground state atom and Cu* $3d^{10}4p\ ^2P^0{}_{3/2}$ at 30783.7 cm^{-1}. This requires two subsequent photons for ionisation:

$$Cu_2(X^1\Sigma_g^+) + 3h\nu \rightarrow Cu(^2S_{1/2}) + Cu^*(^2P^0_{3/2}) + \text{TKER} \tag{3.6}$$

$$Cu^*(^2P^0_{3/2}) + 2h\nu \rightarrow Cu^+ + e^-$$

It seems that, at the 5-photon level, both 3+2 and 4+1 processes are observed with equal probability, as the intensities of the corresponding peaks in our TKER spectra appear similar.

The sharp rings in the image shown in figure 3.15 are well-separated from the broader feature. The broad features in the TKER spectra in this photon energy region are therefore sufficiently well-defined that they may be successfully fitted; single Lorentzian functions are required. As is evident from the TKER spectrum in figure 3.15, these functions are very wide and consequently the TKER peaks they represent have large uncertainties. They appear as series (c), which neither has an integer slope nor corresponds to any known atomic copper internal energies, but it shows a strong linear trend and is the first indication that the broad background in the images might be unravelled. It implies that the broad features do not arise from photodissociation of Cu_2.

The separation of broad and sharp features in the images taken between 18400 and 19200 cm^{-1} allows their intensities to be considered separately. In so doing, it becomes apparent that the sharp peaks do not cause the spectral structure in figure 3.9. The spectral peaks are expressed in the images by variations in the intensity of the broad, unresolved peak. This is illustrated in figure 3.16, which

shows the KER spectra obtained from images taken atop adjacent spectral peaks. Both images have approximately the same total intensity. In one, the sharp outer rings are bright, but in the other, they are not. Even where the sharp feature is intense, it contains less than half the intensity of the image. The total Cu^+ signal in this region is therefore not dependent on the photodissociation of Cu_2 X $^1\Sigma_g{}^+$ in the beam but rather on whatever process creates the broad feature.

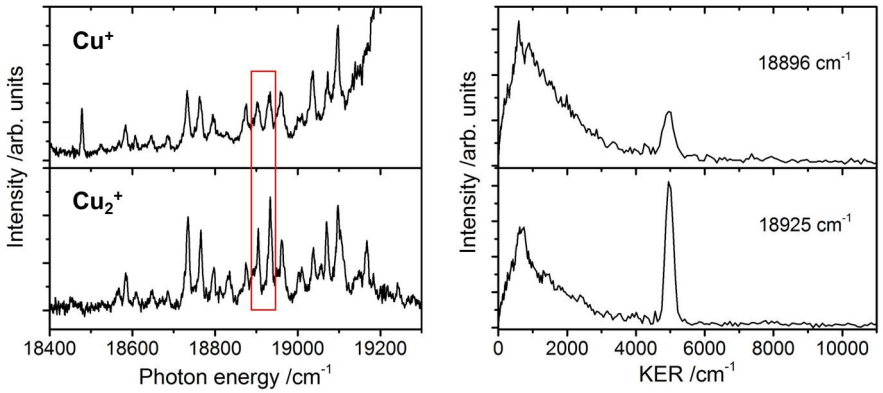

Figure 3.16: The KER spectra of images taken at adjacent spectral peaks, indicated by the red box on the $Cu^+/Cu_2{}^+$ visible spectrum on the left-hand side. In the Cu^+ image at 18896 cm^{-1}, the sharp rings corresponding to Cu_2 dissociation are bright; in the image at 18925 cm^{-1}, they are not, illustrating that spectral intensity does not correspond to the intensity of the sharp peaks in this region.

3.4 Cu_2 Images

3.4.1 Comparison with the atom channel

Fragmentation of Cu_3 was inferred at the start of this chapter as the origin of spectral structure in the Cu^+ and $Cu_2{}^+$ channels. If this is true, it must also be the origin of the broad features seen in the Cu^+ images. Features with a corresponding broad shape and kinetic energy release ought therefore to be visible in images of $Cu_2{}^+$. Images (a) and (b), taken in the atom and dimer channels at the same wavelength are shown in figure 3.17. The Cu^+ image (a) contains a sharp ring due to Cu_2 dissociation, with some less well-defined structure within it. The dimer image (b) has no well-defined features, but does contain an indistinct ring overlaid on a faint background. The structure of the ill-resolved features in (a) and (b) are similar, but the dimer ring is evidently smaller than that in the atom channel. The total kinetic energy release after dissociation is distributed between the two fragments according to equation (3.7):

$$KER(1) = TKER\left(\frac{m_2}{m_1 + m_2}\right). \tag{3.7}$$

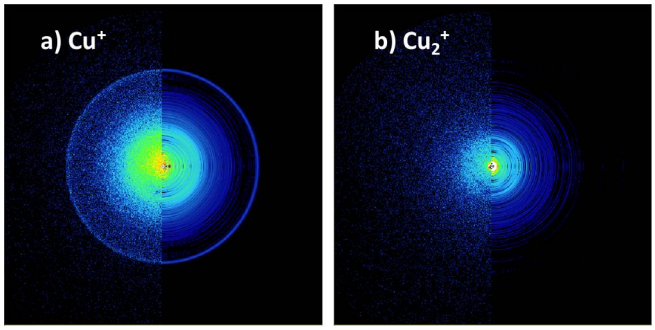

Figure 3.17: Images taken at 18925 cm^{-1}, (a) in the Cu^+ channel and (b) in the Cu_2^+ channel. The central, ill-resolved ring structure in both is somewhat similar. That in (b) is smaller, which is qualitatively consistent with a Cu_3 dissociation producing both Cu and Cu_2 fragments.

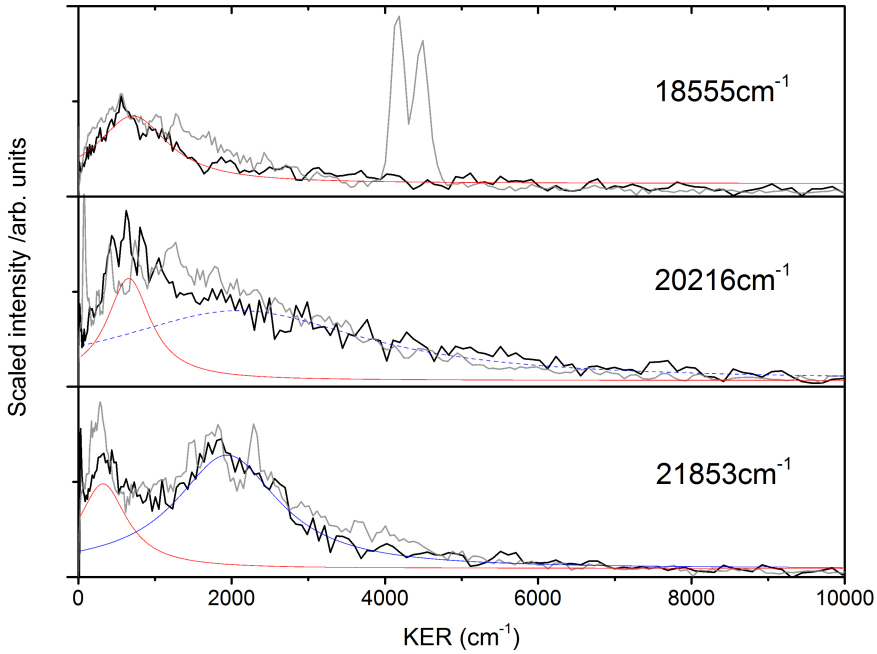

Figure 3.18: Cu_2^+ KER spectra (in black) scaled by a factor of 2 in the x-direction to match Cu^+ KER spectra (in grey) assuming a common Cu_3 parent. The dimer images' structure matches that of the atomic 'background'. Sharp atomic peaks complicate the picture and so the best coincidence is seen in their absence at low energy. Two Lorentzian functions are required to fit the dimer channel structure at high energy, but only one at low energy. Fitting functions are shown in red and blue, and do not correspond to any explicitly-predicted channel.

Therefore if Cu_3 is photodissociated to produce Cu_2 + Cu, the dimer will recoil with one third of the total kinetic energy release while the atomic product will carry off two thirds. By way of comparison, if Cu_2O were dissociating to produce either CuO + Cu or Cu_2 + O, a recoiling copper atom would take 56% of the available kinetic energy whereas Cu_2 would recoil with only 11%. The KER spectra in the Cu^+ and Cu_2^+ channels may be analysed to see if their features match up when a Cu cofragment

is assumed for Cu_2^+ and a Cu_2 cofragment for Cu^+.

Such a comparison is performed in figure 3.18. The atomic KER spectra (shown in grey) and the dimer KER spectra (shown in black) are illustrated at three energies. 18555 cm^{-1} lies in the lowest energy region studied, which contains the A←X band of the trimer. 20216 cm^{-1} lies in the region whose intensity may arise from Cu_2 A←X(v>0) transitions or Cu_3 resonances. 21853 cm^{-1} lies in the middle of the B-X and C-X transitions of Cu_2. This wide range of energies has been chosen to illustrate the evolution of the dimer images, and their atomic counterparts, over the full spectral range studied. At high energies, two distinct peaks are required to fit the dimer images. At low energies, only one fitting function is required. These fitting functions are shown in red and blue on the figure and are not intended to indicate correspondence with any predicted dissociation channel, but rather to emphasise the changing composition of the spectra. The particular wavelengths in figure 3.18 were selected for their minimal contribution, in the atom channel, from the sharp peaks arising from Cu_2 dissociation which obscure the broad structure. The atomic spectra appear without modification, directly extracted from the images. The dimer spectra have been scaled in two directions: vertically, so that their intensity matches that in the atom channel; and horizontally, by a factor of two. If the broad features in both Cu^+ and Cu_2^+ images do arise from dissociation of Cu_3, then the kinetic energy releases in both channels are related by:

$$KER(Cu) = KER(Cu_2)\left(\frac{m_{Cu_2}}{m_{Cu}}\right). \tag{3.8}$$

According to equation (3.8), scaling the KER in the dimer channel up by a factor of 2 should exactly match up any features arising from trimer dissociation with their counterparts in the atomic KER spectrum. Figure 3.18 shows that a good match between the entire broad structure is achieved across the two channels.

This is strong evidence for Cu_3 dissociation, but it does not rule out the possibility that a larger species, containing at least two copper atoms, is dissociating to produce Cu and Cu_2. However, in the event that a large species dissociates to produce Cu and Cu_2 in separate processes, Cu and Cu_2 are unlikely to be produced with a kinetic energy ratio of approximately 2:1. Additionally, the likelihood is small that both Cu and Cu_2 will be ejected from a larger species other than Cu_3 with equal probabilities at all wavelengths. Cu and Cu_2 must be formed (and ionised) with equal probability at all wavelengths to create a spectrum such as that in figure 3.9, where the Cu^+ intensity exactly mirrors the Cu_2^+ intensity. Consequently, it is likely (although not certain) that the broad features we observe arise

from Cu_3.

3.4.2 The mechanism of formation of Cu_2 images

Having established that both Cu^+ and Cu_2^+ images contain some signal likely to originate from Cu_3, a mechanism for producing this signal must be found. Such a mechanism has already been proposed in this chapter, in figure 3.7.

Step 1: Dissociation. Ground-state Cu_3 was assumed to be present in the beam, given that evidence suggests that the nascent Cu_2 distribution is electronically and vibrationally cold. Cu_3, in its X(0) state, is assumed to dissociate after absorption of a single visible photon [81, 257]. Dissociation is accompanied by a release of kinetic energy labelled TKER (1) in figure 3.7. The total kinetic energy release may not exceed the energy remaining after $D_0(Cu_3)$ is subtracted from the photon energy; a review of the Cu_2^+ images shows that this condition is met. By locating the approximate point at which the image signal drops to zero, the maximum total kinetic energy release may be evaluated and is always approximately 12000 cm^{-1} less than the photon energy, which is ample provision for $D_0(Cu_3)\approx$ 8000 cm^{-1} [262]. Upon dissociation, the products may be formed in excited states. Figure 3.7 shows the creation of a ground-state copper atom and a number of the vibrational levels of the X $^1\Sigma^+_g$ state of Cu_2. While no electronically excited states of Cu_2 are accessible, the first two metastable ^2D_J states of the Cu atom are accessible, although they are not shown in figure 3.7 for clarity.

Step 2: Ionisation of Cu_2. Once formed, Cu_2 requires three to four visible photons for ionisation. Figure 3.7 shows this occurring as a 1+2 resonant ionisation via the C state of Cu_2. The Cu_2^+ in our images therefore has its kinetic energy determined entirely by TKER (1). TKER (1) is not well-defined because it varies with the vibrational energy in the dimer fragment, and therefore the rings in the Cu_2^+ (and Cu^+) channels are fairly broad. Additionally, the initial Cu_3 species may have internal energy which broadens the energy release spectrum. The atomic product, which may be Cu $^2S_{1/2}$ or $^2D_{5/2,\,3/2}$, requires three or four visible photons for ionisation. Where Cu_2 resonances are available to assist photodissociation of Cu_2, no central spot is seen in the Cu^+ images. This suggests that non-resonant ionisation of low-energy states of copper does not make a large contribution to the Cu^+ channel above 21000 cm^{-1}. Consequently, Cu produced directly from Cu_3 dissociation is not seen in the Cu^+ images. However, in the 18400-19200 cm^{-1} region, the Cu^+ images have a central spot and the rings are generated by 3 or 4-photon ionisation of the Cu produced directly by dissociation of Cu_3. In the Cu_2 A-state region, Cu^+ may form by either route.

Step 3a: Dissociation of Cu_2^+. $D_0(Cu_2^+)$ has been determined to be around 14840 cm^{-1} [210]. Absorption of a single photon by Cu_2^+ throughout this wavelength range will therefore lead to dissociation to a ground-state copper atom and a ground-state copper ion, no electronically excited states being energetically accessible. The accompanying kinetic energy release is labelled TKER (2). Cu^+ arising from this mechanism will have an associated kinetic energy defined by the recoil of the dimer from Cu_3 dissociation, a third of TKER(1), which is subsequently broadened by the recoil energy the atom takes from dissociation of Cu_2^+, half of TKER(2).

Step 3b: Dissociation of Cu_2. Figure 3.7 shows, by way of example, the Cu_2 generated from Cu_3 undergoing three-photon dissociation to produce a highly electronically excited copper atom and a ground-state cofragment. Although three-photon dissociation is shown, a reasonable alternative would be two-photon dissociation of Cu_2. The photon order of the dissociation cannot be determined from the image because, as in step (3a), the kinetic energy release of the dimer species is not extricable from the Cu^+ image as it is overlaid on TKER(1). Instead, we must rely on conjecture. The three-photon mechanism would generate highly excited products which are ionisable with a single additional photon. Two-photon dissociation can only access states of Cu which require at least two subsequent photons for ionisation. In section 3.3, three-photon dissociation of Cu_2 (to form Cu* products ionisable with a single photon) was found to be the dominant mechanism. For reasons of internal consistency, therefore, three-photon dissociation of Cu_2 is invoked here in preference to two-photon dissociation of Cu_2 or one-photon dissociation of Cu_2^+, *i.e.* step **3a** is ignored in favour of step **3b**.

Step 4: Ionisation of Cu*. After either two- or three-photon dissociation of Cu_2, one of its atomic products must be ionised to generate the Cu^+ visible in the image.

3.4.3 Calculation of $D_0(Cu_3)$

The mechanism proposed above is plausible, compatible with spectroscopic data and consistent with the mechanism proposed for the origin of sharp peaks in the Cu^+ channel. It has not, however, been proven, and the troubling fact remains that Cu_3 has not been directly observed in our beam. In an attempt to strengthen the case made for dissociation of Cu_3 as the origin of structure in the spectra and images herein, quantitative examination of the dimer images is presented below. Whereas in the atom channel the difference between fitting with Lorentzian and Gaussian functions was found to be negligible, in the dimer channel Lorentzian functions provide a noticeably better fit. The data in figure 3.19 illustrates the TKER peak positions extracted from the dimer images assuming a Cu atom

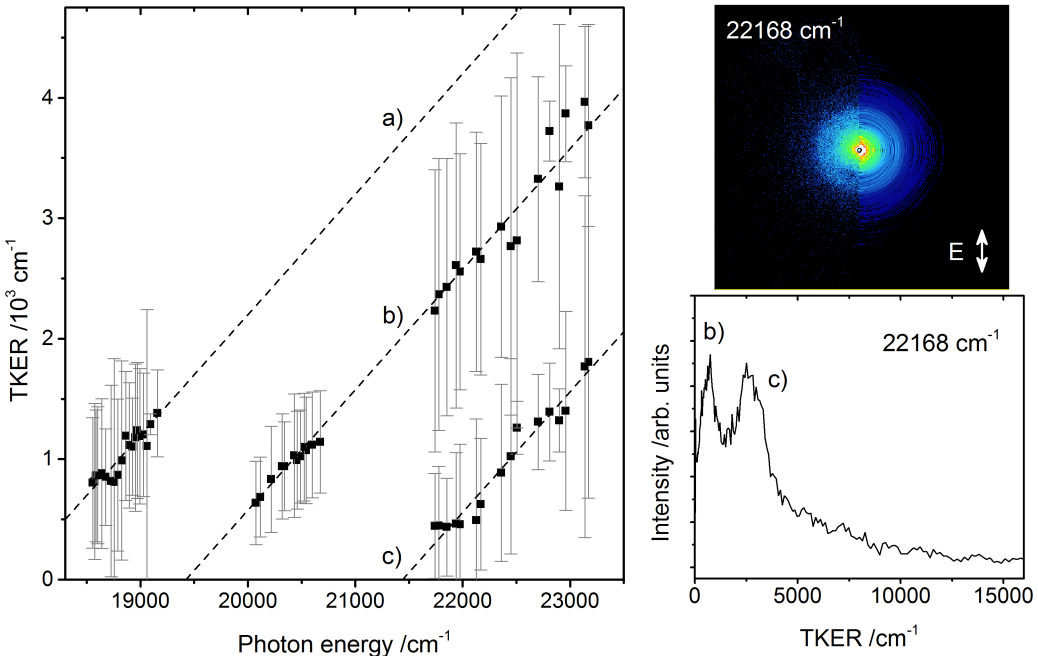

Figure 3.19: TKER peaks (assuming a Cu cofragment) extracted from the dimer images, an example of which is shown above. Large uncertainties arise because the rings are ill-defined and the TKER peaks broad. However, three distinct series are observable and they have 1-photon slopes. Series (a)-(c) are marked by dotted lines because $D_0(Cu_3)$ and $E_{int}(Cu_2)$ are not well known. The x-axis intercepts of these lines are consequently not indicative of thresholds, but simply of fits to the data.

cofragment. The TKER peaks shown here correspond only to TKER (1) in figure 3.7.

Somewhat surprisingly, in light of the sizeable uncertainties on the peak positions, the TKER peaks do appear to lie along approximately straight lines with an integer slope of 1. This supports the hypothesis that Cu_3 dissociates on absorption of a single photon, although the uncertainty in the slope is significant. More interesting is the fact that, upon fixing the slope to 1 and extrapolating to zero, series (b) and (c) have limits of 19423±700 and 21440±700 cm^{-1} respectively. Assuming $D_0(Cu_3)$=8200 cm^{-1} (Hilpert's data gives 8710±1530 cm^{-1}) [262] leaves product internal energies for series (b) and (c) of 11223 and 13240 cm^{-1} respectively. These values are close to the internal energies of the two metastable ^2D_J states in the copper atom, 11202.626 and 13245.443 cm^{-1} [211]. Series (b) and (c) may therefore be described by scheme (3.9)

$$Cu_3 + h\nu \rightarrow Cu_2(X(v)) + Cu(^2D_J). \tag{3.9}$$

Scheme (3.9) is exactly consistent with the mechanism proposed above: one-photon dissociation of Cu_3 to produce ground-state Cu_2 in a range of vibrational levels and a copper atom in a low-lying

electronic state.

The internal energy of the Cu product of Cu_3 dissociation in series (b) and (c) may be assigned with some certainty, but $E_{int}(Cu_2)$ may not, and this prevents precise determination of $D_0(Cu_3)$. If the product vibrational distribution were to peak at v=0, $E_{int}(Cu_2)$=0 and $D_0(Cu_3)$ could be approximately assigned as 8200 cm^{-1}. Spectroscopic evidence from figure 3.6 rather implies that much of the product distribution is in X(v=2, 3). An internal energy of 533-800 cm^{-1} must therefore be subtracted, leaving $D_0(Cu_3)\approx$7400-7700 cm^{-1}, which is within the uncertainty of Hilpert's determination. It does not therefore seem possible for us to improve on Hilpert's original determination; we rather confirm that $D_0(Cu_3)$ is approximately 1 eV.

While (b) and (c) provide confirmatory evidence for Cu_3 dissociation, series (a) in figure 3.19 is something of a puzzle. When extrapolated to zero TKER, and using our $D_0(Cu_3)$ of 8200 cm^{-1} for consistency, it suggests that the Cu + Cu_2 products must have an internal energy of 9600 cm^{-1}. This is not remotely close to any known states in Cu or Cu_2. Attempts to fit series (a) with a slope of 2 instead of 1 are far from satisfactory. The dimer is extensively studied and the existence of previously-unknown states in Cu_2 or Cu should probably be ruled out. Nonetheless, it is possible that the less well-understood triplet manifold of Cu_2 contains a previously-unobserved state at 9600 cm^{-1}.

Alternatively, we are dissociating an excited state of Cu_3 whose internal energy has not been accounted for. This is a particularly attractive option for series (a), as, unlike series (b) and (c), ground-state Cu_2 and Cu products would require four photons for ionisation in this low-energy regime. The images at these wavelengths do have central spots, suggesting that Cu and Cu_2 in the molecular beam are ionised from their ground states. If, however, an excited state of Cu or Cu_2 were to be produced by Cu_3 photodissociation, it may be ionisable in a three-photon process. The only experimentally-observed states of Cu_3 are the A and B states, and of these only the A state is characterised [257]. However, having attributed some of the spectral peaks in this region to A-X transitions in Cu_3, it is not possible to simultaneously attribute the image to existing A-state trimer in the beam. Nonetheless, it is interesting to note that if the A state were the origin of this structure, the products' internal energies (totalling approximately 28100 cm^{-1}) can only be matched by one combination: Cu_2 a $^3\Sigma^+_u$ at approximately 15420 cm^{-1} and Cu $^2D_{3/2}$ at 13245.443 cm^{-1} [211] which have a combined energy of 28665 cm^{-1} and are ionisable with three photons each. These values are compatible within the uncertainties of $D_0(Cu_3)$ and the origin of the a state, which is known only from matrix work [3].

Although difficult to assign, series (a) must not be ignored. Its counterpart in the atomic images,

labelled (c) in figure 3.15, indicates an internal energy of 9700 cm^{-1} when fitted assuming a Cu_2 cofragment, the same (within error) as the 9600 cm^{-1} value obtained from the dimer images. Although not apparently explicable with known states, this series is real.

3.5 Conclusions

In summary, this chapter has provided much indirect evidence that photodissociation of Cu_3 creates complex spectra and images in the Cu^+ and $Cu_2{}^+$ channels. Photodissociation of Cu_2 occurs throughout the energy range studied and allows us to extract an accurate value of $D_0(Cu_2)$. However, Cu^+ and $Cu_2{}^+$ created by photoionisation and dissociation of Cu_2 are not the only contribution to the images and spectra observed. Photodissociation of Cu_3 is suggested to cause the spectral structure in the Cu^+ and $Cu_2{}^+$ channels, along with a series of broad features in the images. Fitting these features suggests that Cu_3 is dissociated to Cu and Cu_2 in a single-photon process, but that the Cu_2 product is vibrationally excited and the kinetic energy release is consequently ill-defined. In two cases, the quantum states of the products may be determined but the images taken in the region of the Cu_3 A←X region have not yet been explained. The internal energy predicted by images in both the Cu^+ and $Cu_2{}^+$ channels does not correspond to any known states, suggesting that either a new triplet state of Cu_2 is formed, or that the dissociating Cu_3 is not in its ground state.

Other puzzles remain, and two of them will be emphasised here. Firstly, our inability to detect Cu_3, by single-photon 157 nm ionisation or in a multiphoton resonant process, remains troubling. It is probable, although not proven, that 157 nm photons efficiently fragment Cu_3. Two-colour experiments are desirable, to monitor the depletion of Cu_3 over the wavelength range of the OPO, although none of the ionising lasers tried thus far have proved useful. Secondly, the broad and highly intense features in the atom channel, centred on the atomic transitions at 510 and 516 nm, have not been explained. They present a knotty problem: their similarity to Knickelbein's data [257] and their inexplicable shape are most curious. The summary to this chapter therefore repeats Morse's 1986 conclusion: although Cu_3 is probably the best-studied of all homonuclear transition metal trimers, it is far from fully understood.

Chapter 4

Collisional activation of stored rhodium clusters

Fourier-transform ion cyclotron resonance (FT-ICR) allows long-term storage of charged clusters within stable cyclotron orbits in a magnetic field. The technique has been used to study collisions with argon of $Rh_nN_2O^+$ and $Rh_nON_2O^+$ (n=5, 6). The results are compared with previous infrared multiple photon dissociation (IR-MPD) experiments. Whereas $Rh_5N_2O^+$ mostly decays by desorption of N_2O, with only a small fraction of the parent ion undergoing surface reaction to make Rh_5O^+, $Rh_6N_2O^+$ mainly produces Rh_6O^+. Addition of an oxygen atom reduces the preference of $Rh_5N_2O^+$ to desorb N_2O and the surface reaction product of $Rh_5ON_2O^+$, $Rh_5O_2{}^+$, is favoured. However, the tendency of all species to desorb N_2O increases with collision energy due to the loose nature of the desorption transition state. Additional collision experiments with a reactive collision partner, ^{13}CO, were performed on the same rhodium clusters. Chemisorption of carbon monoxide deposits sufficient energy into the system to surmount both surface reaction and desorption barriers. However, unlike argon, ^{13}CO participates in subsequent reactions and can react with oxygen on the cluster surface, forming $^{13}CO_2$. ^{13}CO oxidation is rapid on the surface of the n=5 cluster but somewhat slower on the surface of the n=6 cluster, illustrating the importance of each individual atom to reaction in cluster chemistry. To assist with understanding the mechanism of the reaction, the structures of the reacting species are calculated at the density functional level of theory. Much of the work in this chapter has been published in J. Phys. Chem. A Vol. 117 (2013) p8855, "Collisional activation of N_2O decomposition and CO oxidation reactions on isolated rhodium clusters". I. Parry, A. Kartouzian, S. M. Hamilton, O. P. Balaj, M. K. Beyer and S. R. Mackenzie [264].

4.1 Experimental Technique

4.1.1 Development of FT-ICR

Fourier transform ion cyclotron resonance, FT-ICR, was developed in 1974 by Comisarow and Marshall [265]. It remains the highest-resolution technique available for mass spectrometry [266]. Its development combined a number of known techniques, the oldest of which was ion cyclotron resonance (ICR) [267]. Cyclotron motion arises because a moving ion trapped in a magnetic field, **B**, is accelerated into circular motion perpendicular to the direction of the field. Its period of orbit (cyclotron frequency) is determined by **B** and its mass-to-charge ratio. In 1932, Lawrence and Livingston suggested a method of increasing the speed of cyclotron motion. They trapped the charge between a pair of semi-circular electrodes, shown in figure 4.1 (a), and applied an oscillating voltage to the electrodes at the cyclotron frequency. Consequently, ions were accelerated at each pole of their circular path towards the opposing electrode [268].

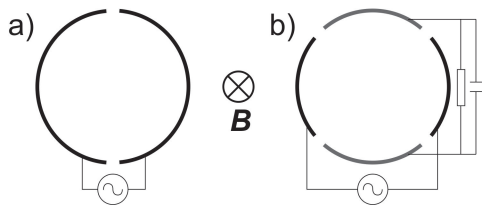

Figure 4.1: Electrodes used in ion cyclotron resonance. (a) allows a radio-frequency alternating voltage to be applied to two excitation electrodes and was first used by Lawrence and Livingston in 1932 [268]. (b) has two additional electrodes for detection of ions.

ICR was first used to detect ions, rather than simply accelerate them, by Hipple, Sommer and Thomas [269, 270]. Their arrangement was called an omegatron and more closely resembled figure 4.1 (a) than (b). Trapped H^+ ions were excited until they struck a detector, creating a measurable current.

The development to indirect ion detection was made in 1965 by Wobschall [271]. The electrode setup remained much the same as in figure 4.1 (a). Ions entered one end of the electrode pair, whose length was chosen to exceed the distance ions could diffuse through the gas in the cell before detection. The ions' presence was inferred from the detected voltage imbalance (or image current) across the electrodes as stored ions passed close by [271]. The magnetic field was scanned to find the ions' resonant frequency. The method was particularly advantageous as it allowed detection of ions as they underwent varying numbers of collisions and/or reactions. However, the magnetic field generated by a solenoid coil was too unstable to permit long-term storage [267, 272].

The final major precursor to FT-ICR was an ICR cell which could trap ions [273]. The trapping action was achieved by a pair of like-charged plates at each end of the cell, in conjunction with a pair of oppositely-charged side plates. A quadrupolar trapping field was created along the direction of the magnetic field. The cell increased the residence time of ions in the detection region from 1-2 microseconds to 100 microseconds. Unfortunately, ions had to be generated inside the cell and it was therefore modified for early FT-ICR experiments [265].

FT-ICR differed from these known techniques in three ways [267].

1. **B** was fixed and the frequency of the voltage applied to the electrodes was varied.

2. The single electrode pair used for both excitation and detection was replaced by two orthogonal electrode pairs, as in figure 4.1 (b).

3. One pair (the excitation plates) were subject to an oscillating applied voltage, while the other pair (the detection plates) were used to detect the image charge created by moving ion packets. For the first time, excitation and detection did not need to be simultaneous. The detected current was analysed by Fourier transform.

It is perhaps disingenuous to call these entirely new developments as, in 1971, Genequand reported a device called a resotron, which had all the attributes listed above except the analysis of the signal by Fourier transform [274]. The paper was almost entirely overlooked [267].

4.2 Principles of FT-ICR

4.2.1 Ions in magnetic fields

FT-ICR relies on a few simple physical principles, described in detail in Marshall and Hendrickson's 1998 primer [275]. They are outlined below.

Ions moving in a magnetic field experience a force which is given by:

$$\mathbf{F} = q\mathbf{v} \times \mathbf{B}, \tag{4.1}$$

where q is the ionic charge and **v** is the ion's velocity. The magnetic field generated for use in FT-ICR has some direction, **z**, and is therefore denoted as a vector in that direction, $\mathbf{B_z}$. Ions are often injected parallel to this field. However, $\mathbf{B_z}$ and **v** are rarely perfectly parallel and consequently their vector

product is non-zero and lies largely in the xy plane. Equation (4.1) therefore becomes:

$$\mathbf{F} = q\mathbf{v_{xy}} \times B_0, \tag{4.2}$$

where B_0 is the magnitude of $\mathbf{B_z}$, and $\mathbf{v_{xy}}$ is the ion's velocity in the plane perpendicular to $\mathbf{B_z}$.

Equations (4.1) and (4.2) are not the only way to describe the motion of the ion. As it accelerates in the xy plane, its velocity vector **v** rotates around the z axis, and the cross-product of equation (4.1) rotates with it: the particle thus describes a circle in the xy plane. It is therefore possible to employ the equations of circular motion. Centripetal acceleration obeys the relation:

$$a_{xy} = \frac{v_{xy}^2}{r}, \tag{4.3}$$

wherein r is the radius of the circle. Combining equation (4.3) with Newton's second law, $F = ma$, and substituting the result into equation (4.2) gives the relation:

$$\frac{mv_{xy}^2}{r} = qv_{xy}B_0, \tag{4.4}$$

which can be divided through by $2\pi m$ to get the *cyclotron equation*, an expression of the angular frequency of an ion:

$$\nu_c = \frac{qB_0}{2\pi m}. \tag{4.5}$$

ν_c is equal to $v_{xy}/2\pi r$. Equation (4.5) is significant as it shows that an ion's characteristic cyclotron frequency depends only on its mass m, charge q and the magnetic field strength B_0; ν_c is independent of the ion's velocity, and therefore of its kinetic energy and radius.

4.2.2 Resonant excitation

An ion's cyclotron frequency is determined by B_0 and m/q, but its velocity can be increased by resonant excitation. The ion sits within two pairs of electrodes of the general design shown in figure 4.1 (b). If a voltage is applied across the excitation plates, the ion will be accelerated away from one electrode and towards the other. In order to avoid deceleration of the ion when the xy-component of its velocity is reversed after half a rotation, the electric field must be switched off or its polarity reversed. For efficient resonant excitation, the electric field's polarity is reversed at double the ion's cyclotron frequency. The electric field in the cell is called a 'radio-frequency field' (RF field).

The energy transferred upon resonant excitation may be quantified. The power absorbed by a moving charge in the xy plane is given by:

$$P(t) = q\mathbf{E}(t) \cdot \mathbf{v_{xy}}, \tag{4.6}$$

where *P(t)* is the power absorbed and **E**(t) is the electric field strength in the cell at time *t*. At its maximum strength, the magnitude of **E**(t) is E_0:

$$E_0 = \frac{\beta V_{\text{p-p}}}{d}, \tag{4.7}$$

where β is a proportionality constant, $V_{p\text{-}p}$ is the peak-to-peak voltage difference over the voltage cycle and d is the distance between the electrode plates. The constant β arises as E_0 is not created by infinitely-extended electrodes but by finite plates. The true field is not spatially uniform, and its net effect is therefore reduced from its theoretical maximum. β is known for a number of common electrode geometries [275]. As $\mathbf{v_{xy}}$ varies with time, evaluation of equation (4.6) is not straightforward. It has been done, however, by resolving both the velocity and the electric field into their sinusoidally-varying time-dependent components in the x and y planes, and substituting the true **E**(t) for a time-averaged field [276]. The result obtained is that the final radius of the ion, after resonant excitation in an RF field, is:

$$r = \frac{\beta V_{\text{p-p}} t_{\text{exc}}}{2dB_0}, \tag{4.8}$$

where t_{exc} is the excitation time during which the RF field was switched on. Combining equations (4.8) and (4.4) gives the lab-frame kinetic energy of the ion, post-excitation:

$$E_{\text{kin}} = \frac{\left(q\beta V_{\text{p-p}} t_{\text{exc}}\right)^2}{8md^2{B_0}^2}. \tag{4.9}$$

Resonant excitation enables detection. Before excitation, the ions in the cell are not coherent. Any image current induced on one detection plate is therefore matched by an equal induced current on the opposing detection plate. Resonant excitation creates a coherent ion packet. Ions moving more slowly through the electric field experience greater acceleration until they 'catch up' with the other ions, creating an ion packet. Any image current induced on a detection plate by a coherent ion packet is not matched by an equal current on the opposite plate so a difference may be detected. Excitation further assists detection by bringing ions closer to the detection plates. Within the cell, the detected current is linearly proportional to the ions' cyclotron radius, and so the signal-to-noise ratio, S/N, is

greatly improved by resonant excitation [277]. As is evident from equation (4.8), this post-excitation radius is not dependent on the ions' mass and therefore, importantly, *all masses may be detected simultaneously with the same sensitivity.*

The optimal RF pulse shape required to excite ions in the cell to the same radius is not a simple sweep across all frequencies at constant amplitude [275]. The preferred method of generating the waveform describing the frequency and amplitude of the oscillating voltage which should be applied to the detection plates is called SWIFT: stored waveform inverse Fourier transform [278]. The desired final state of the system, including the phase and radius of each ion, is specified. The time-domain signal which would be detected from this ideal post-excitation system is generated. An inverse Fourier transform is performed upon it to extract the excitation waveform which should be applied to the excitation plates. The exact form of the SWIFT pulse has some flexibility. Reference [278] details some methods used to optimise the SWIFT waveform to minimise the peak-to-peak voltages and time length of the excitation pulse.

SWIFT excitation is not only useful for detection. SWIFT pulses are used to excite ions to specific velocities for collision-induced dissociation (CID) experiments, and to eject ions by exciting them to radii larger than the radius of the cell [278]. A particularly interesting use of tailored excitation is in 2D FT-ICR experiments, which are analogous to 2D NMR experiments. The similarity of FT-NMR to FT-ICR experiments has been pointed out: instead of nuclear spin precession, trapped ions undergo cyclotron motion after rf excitation [267]. It was established in 1987 that, by introducing a delay between excitation and detection pulses as an additional variable, it is possible to correlate detected products to their excited parent species [279]. Given that FT-ICR can isolate reactants, this is not a particularly important development for simple systems. The technique is useful when extended to very complex mixtures of reactants, which is possible when the excitation and detection pulses are carefully tailored using SWIFT [280].

4.2.3 Ion motion parallel to the field axis

Ions' motion in the z-direction is curtailed by end-plates, or trapping electrodes, held at a small positive (or negative) voltage to keep cations (or anions) in the cell [275]. The trapping voltage on the entrance plate must be reduced temporarily to allow ions into the cell through a hole in the entrance plate. The FT-ICR cell thus consists of a pair of opposing detection electrodes, a pair of opposing excitation electrodes and a pair of opposing trapping electrodes. The trapping electrodes create an

electric field which constrains the motion of the ion in the z-direction. The magnetic field itself acts as the constraint in the xy-plane. Different electrode shapes are used to variously optimise trapping, create more homogeneous electric fields in the cell and to improve transport in and out of the cell. The effect of trap shape on excitation, trapping and detection has been reviewed [65, 281, 282].

Imposing a trapping voltage in the z-direction has a complicating side effect: it introduces two additional modes of motion. One is a harmonic oscillation in the z-direction, caused by repulsion from the end-plates, often called 'trapping motion'. The other is magnetron motion, arising because the d.c. trapping potential has a radial component in the xy plane:

$$F = \frac{q\alpha V_{\text{trap}} r}{d'^2}, \tag{4.10}$$

where V_{trap} is the d.c. trapping voltage, α is (like β) a proportionality constant arising from the non-infinite plates [275], *d'* is the separation of the trapping plates and r is the radial extent of the field in the xy plane. This field pushes ions radially outwards from the cell's z-axis. The true force on the ion in the xy plane is obtained by adding equation (4.10) to equation (4.2). When xy-plane velocity $\mathbf{v_{xy}}$ is converted into angular velocity, $\omega_c = v_{\text{xy}}/r$:

$$F = m\omega_c^2 r = qB_0\omega_c r - \frac{q\alpha V_{trap} r}{d'^2}. \tag{4.11}$$

Equation (4.11) is independent of r and quadratic in ω_c, meaning that two angular velocities arise when it is solved. One of these corresponds to the cyclotron motion, and the other to magnetron motion. Magnetron motion causes ions to spiral (in the xy plane, about the magnetic field lines) around their already-spiral-shaped cyclotron path [275, 276].

Magnetron and trapping oscillations generally have much smaller magnitudes than the cyclotron frequency, and therefore do not greatly affect FT-ICR performance [275]. However, any motion along the z-axis increases the likelihood of ions escaping the cell, and if any magnetron frequencies happen to be excited by a SWIFT pulse then the magnetron motion becomes significant [276]. Trapping motion additionally affects the image charge that ions create, because the induced current depends on an ion's position in the cell [283]. Not only does the magnetron motion affect signal, but coupling between the different modes of motion in the cell introduces additional bands to the spectrum [284]. A more subtle effect of the trapping field is that, when ions are excited to larger radii, they partially escape from the radial field generated by the trapping plates (equation (4.10)). The potential energy

released is converted into kinetic energy, which must be accounted for in thresholds determined by CID [276].

4.2.4 Developments

Ion trap design is a fertile area of research, and has already been mentioned. Advances in trap design have been reviewed. [65, 266, 281] Incremental improvement in mass resolution is also achieved by increasing **B**. Magnetic field strength is key in determining the resolution of the FT-ICR technique [285]. The accuracy with which the cyclotron frequency, ν_c, can be measured increases with the number of cyclotron orbits completed during the detection time. The cyclotron frequency is linearly proportional to the magnetic field strength (equation (4.5)) and so the accuracy of measurement is directly proportional to B_0. Other detection limits such as the maximum trapping time and maximum detectable mass depend on B_0 [286]. Consequently, larger magnets are constantly being developed for use in FT-ICR [266].

A major advance in the processing of FT-ICR data has been made by phase-correcting the signal [287]. Some background is needed to explain the significance of phase in FT-ICR data. The processing of raw signal is shown schematically for $Rh_6N_2O^+$ stored in ^{13}CO in figure 4.2. The raw signal is Fourier-transformed in order to extract the constituent cyclotron frequencies ν_c:

$$F(\nu_c) = \int_{-\infty}^{\infty} F(t)e^{-i2\pi\nu_c t}dt = Re(\nu_c) + Im(\nu_c). \tag{4.12}$$

Fourier transformation of the time-domain signal, *F(t)*, to a frequency-domain signal $F(\nu_c)$, produces real and imaginary terms in ν_c. The solution to equation (4.12) is a sum of two spectra: the absorption spectrum, $A(\nu_c)$, which consists of sharp, positive peaks; and the dispersion spectrum, $D(\nu_c)$, consisting of broader peaks which have positive and negative intensity. Separation of $A(\nu_c)$ and $D(\nu_c)$ from $Re(\nu_c)$ and $Im(\nu_c)$ is non-trivial, especially in a complex spectrum where many peaks overlap. It is therefore usual to plot spectra in magnitude mode:

$$M(\nu_c) = \left[Re(\nu_c)^2 + Im(\nu_c)^2\right]^{1/2}. \tag{4.13}$$

However, if the relationship, $\phi(\nu_c)$, between $Re(\nu_c)$ and $Im(\nu_c)$ is known, the absorption mode spectrum may be extracted and plotted separately. This narrows peaks in the mass spectrum by up to a factor of 2, increasing precision and resolving power of the technique with no instrumental changes

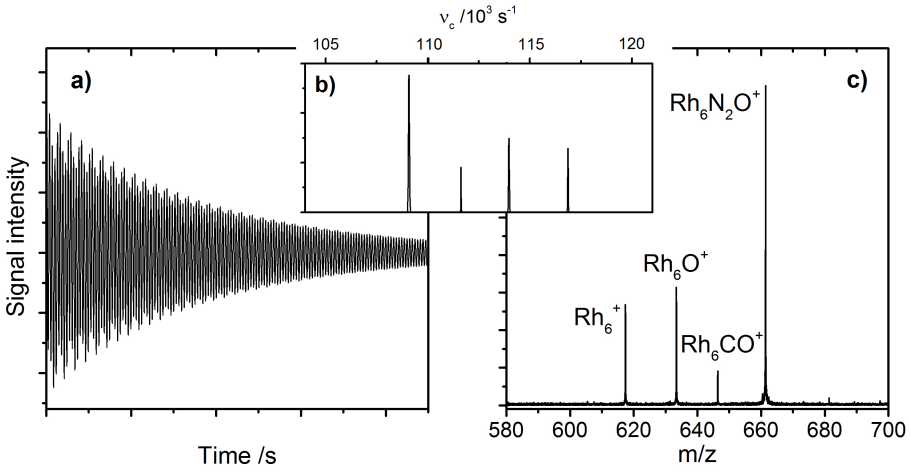

Figure 4.2: Schematic of extraction of a mass spectrum from a raw signal after 1 s storage of $Rh_6N_2O^+$ in ^{13}CO. (a) Schematic of a raw detected image current. (b) Cyclotron frequencies of the products. (c) Mass spectrum of $Rh_6N_2O^+$ stored in ^{13}CO for 1 s.

[266]. A practical method for obtaining $\phi(\nu_c)$ was proposed in 2010 [287, 288].

Advances in software and data processing have proceeded alongside the major developments mentioned above, and are discussed in detail in Marshall's numerous reviews. [266, 267, 277]

4.2.5 Sources of uncertainty

The peak-broadening effect of inhomogeneities in the electrostatic and magnetic fields has already been mentioned [281, 285, 286]. Cyclotron motion smooths out small deviations in the field in the xy plane, but not the z-direction [283, 284]. Mutual repulsion between ions situated in close proximity along the axis of the cell can cause the observed frequencies to shift, broaden and coalesce [277]. Of particular relevance in this chapter are uncertainties in the ions' frequencies caused by collisions with background gas molecules, which dampen ion cyclotron motion, transfer xy-plane velocity to z-axis velocity and broaden the mass peaks [276]. A Langevin model is suitable to describe low-energy ion-neutral collisions, but a hard sphere model is appropriate for high mass species at the higher energies accessed in FT-ICR [289]. High-resolution studies require low cell pressure to minimise collisional broadening effects.

4.3 Applications of FT-ICR

4.3.1 Uses of FT-ICR

FT-ICR is used wherever the need for very high mass resolution justifies its additional experimental complexity compared to simple time-of-flight (TOF) mass spectrometry. Each individual isotope of every element has a different mass defect, or small difference from an integer mass [290]. These defects can be used to uniquely determine the elemental (and even isotopic [287]) constitution; for instance, N_2 may be distinguished from CO. The capability to determine elemental composition, even in molecules of 10^2-10^3 Da, is useful in the examination of complex mixtures [291].

The suitability of FT-ICR for the study of biomolecules has led to its widespread use in structure determination. The peptide chain of a protein may be cleaved by any means: CID, IR-MPD, electron-capture dissociation and so on. Identification of the products allows protein sequencing. The technique has even been used on DNA [292]. Transfer of biomolecules into the gas phase and hence the ICR cell is frequently achieved by electrospray ionisation, ESI. Injection of ions into the cell may be used to add another dimension to the data. For instance, ESI into the ICR cell has been coupled to a liquid chromatography source. This separates solution-phase species chromatographically before online mass analysis and sequencing [293]. Matrix-assisted laser desorption ionisation (MALDI) has been used to desorb lipids from the ocular lens of a pig in a spatially-resolved manner, thus mapping the distribution of lipids on the lens surface by FT-ICR [294].

Accurate analysis of complex samples is also valued in petroleomics - the characterisation of crude oil and its products [266]. Elemental characterisation of a sample and its contaminants are of great interest. Unlike in the analysis of biomolecules, it is extremely undesirable to dissociate the molecules and thus distort the mass distribution; consequently a gentle two-colour ionisation process is preferred [295]. In a similar vein, mass spectrometric analyses of samples of synthetic polymers are of interest, to characterise the molecular weight distribution as well as elemental composition [296].

In addition to its high resolution, FT-ICR has the advantage of being able to store ions in the presence of a reaction gas and record mass spectra *in situ*. It can therefore be used to follow the progress of a reaction with time. This capability has been utilised most elegantly to perform a complete catalytic cycle on Pt_7^+ clusters [15]. Pt_7^+ clusters were stored in the ICR cell with a gas mixture of N_2O and CO, whereupon they were rapidly oxidised by N_2O to form Pt_7O^+ and $Pt_7O_2^+$. Subsequent reaction with CO reduced $Pt_7O_2^+$ and Pt_7O^+ clusters, forming CO_2. The power of FT-ICR in this

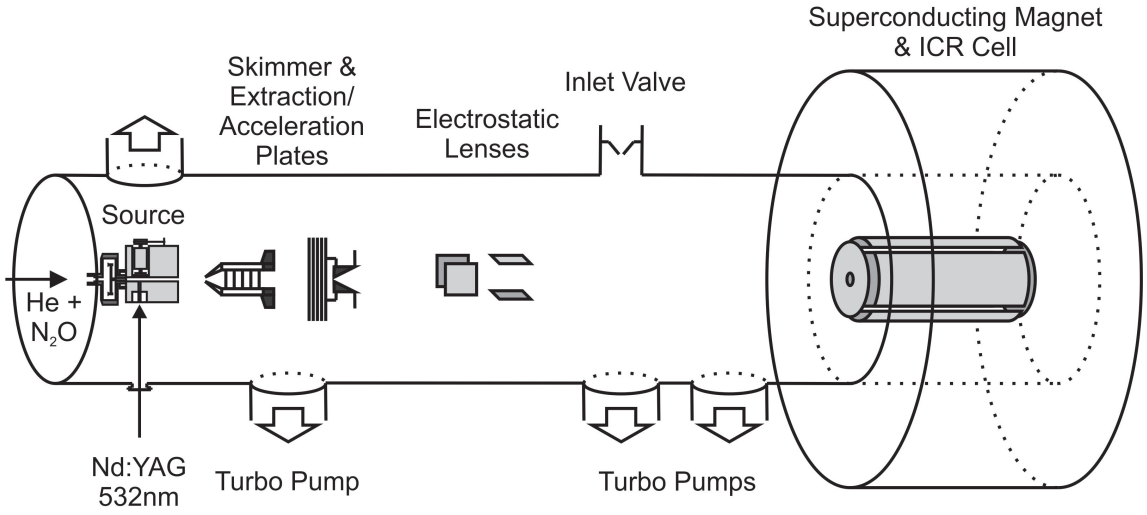

Figure 4.3: The FT-ICR instrument in Kiel. Not to scale. The cluster source is similar to the Oxford source. The whole apparatus is kept under vacuum by turbomolecular pumps. Ions produced by the cluster source are extracted by a series of ion optics and focussed into a cylindrical (infinity) cell at ultra-high vacuum sitting in a 4.7 T magnet, which may be filled with a target gas.

demonstration is that, after a number of catalytic cycles, all charged species except Pt_7O^+ may be ejected and the reaction allowed to continue. It is observed that the same steady state re-forms, proving the catalytic activity of the platinum cluster.

FT-ICR may be used to follow a reaction's progress in the absence of a neutral collision gas. If a reaction barrier is sufficiently low, and the reaction irreversible, it may be activated simply by the slow exchange of black-body radiation with the walls of the container [297]. This technique, known as black-body infrared radiative dissociation (BIRD), is discussed in the next chapter. Processes with higher reaction barriers may be activated by laser irradiation. IR-MPD of trapped ions in an FT-ICR was pioneered by Beauchamp and coworkers in 1978 [298]. Progress from these first studies, using a CO_2 laser, to present studies using FELIX and CLIO has been reviewed [68, 103].

4.3.2 The Kiel apparatus

The FT-ICR apparatus used in Kiel is shown schematically in figure 4.3. The Kiel laser ablation cluster source is very similar to that described in section 2.2. There are some differences, however. The gas pulse used to entrain the clusters is produced by a piezovalve backed with 20 bar of helium containing a trace (<0.1%) of N_2O. After leaving the cluster source, the molecular beam expands supersonically and is then skimmed. The apparatus is differentially pumped. Its lower-vacuum region houses the ion optics which extract, accelerate and focus ions into the ICR cell. Ion focussing is

necessary to overcome the 'magnetic mirror' effect whereby ions are repelled from the large magnetic field [290]. The ICR cell sits in the ultra-high vacuum region, at a base pressure of around $7x10^{-10}$ mbar. The inlet valve shown in figure 4.3 allows a collision gas to be admitted controllably into the ICR cell, and maintained at a fixed low pressure.

Together, the FT-ICR cell, magnet and electronics comprise a commercial Bruker Spectrospin CMS47X mass spectrometer, housing a 4.7 T superconducting magnet. The cell itself is a cylindrical infinity cell, 60 mm in diameter and length [299]. The cell is modified by the addition of a cooling jacket, which allows the flow of liquid nitrogen, cooled nitrogen gas or heated nitrogen gas around the cell. Temperatures between room temperature and 89 K are accessible [300].

4.4 Previous work on rhodium clusters

Rhodium is used as a heterogeneous catalyst in a number of processes. Key amongst these is its role in reducing nitrogen oxides in an automobile three-way catalytic converter [301]. Its ability to dehydrogenate alkanes and even crack C-C bonds [23], and its use in the Degussa process for activation of methane by forming HCN [302], are also important. Consequently, a very large number of extended surface studies have been performed on rhodium in the presence of nitrogen and carbon oxides [16, 303]. However, it is known that much heterogeneous catalysis does not occur on a perfectly-formed plane but at restructured or defect sites [11, 304]. Furthermore, it is believed that small gas-phase clusters are suitable models for such sites, and may be studied in isolation to reduce the complexity of the system [38, 305]. The ultimate aim of such cluster studies is to inform the development of real catalysts [19, 306]. Reactions of rhodium clusters with small molecules are therefore of great interest, and $Rh_n^{+/-}$ clusters have been much-studied by methods including FT-ICR. The reaction rates obtained generally fall into two categories: those which increase approximately monotonically with cluster size, and those which exhibit marked cluster size-effects [16, 264].

The small molecules whose adsorption and/or reaction rate with rhodium clusters varies smoothly with cluster size include CO [121], NO [26, 307], D_2 [25, 120], benzene [119, 124] and azidoacetonitrile [308]. There are exceptions to the trend among these molecules. While benzene physisorbs to large $Rh_n^{+/-}$ at a smoothly-varying rate, dehydrogenation reactions compete with physisorption on small clusters [119]. Another example is the adsorption of D_2 to neutral Rh_n. While the adsorption rate increases monotonically with n, the rate of increase slows significantly at n=9 [120].

The small molecules whose reaction rate with rhodium clusters varies significantly with cluster size include methane [302, 309], ethane [24] and other small alkanes [23, 123], and nitrous oxide [21, 310]. These molecules often show reaction rates very much slower than the collision rate. The rhodium cluster's charge may influence the rate; for example, small cationic rhodium clusters react with N_2O at rates which vary by more than an order of magnitude upon addition of a single Rh atom, but the anions' reaction rates appear almost independent of cluster size up to Rh_{17}^- [21]. The presence of co-adsorbates has also been found to be a complicating factor [302]. Rh_3Ar^+ and $Rh_3Ar_2^+$ can adsorb CH_4 and dehydrogenate it, forming $Rh_3CH_2^+$, while the bare parent cluster Rh_3^+ cannot adsorb methane at all [309]. This is put down to the evaporative cooling effect of argon loss upon CH_4 adsorption.

As was discussed in the Introduction, both geometric and electronic factors may affect the clusters' rates of reaction. Examples of both cases are seen in the chemistry of rhodium clusters. For instance, Rh_2^+, $RhPt^+$ and Pt_2^+ dehydrogenate CH_4 at approximately the same rate, suggesting that the geometry of M_2^+ determines the rate rather than its changing electronic structure [302]. No other Rh_n^+ clusters dehydrogenate CH_4. Similarly, the small $Rh_n^{+/-}$ clusters which *do* rapidly dehydrogenate benzene appear to do so irrespective of charge state, suggesting that the origin of their reactivity lies in their geometry [124]. By contrast, smooth variation of rate with cluster size is seen in the reaction rates of D_2 and N_2 with neutral rhodium clusters [120].

Metal cluster geometries are determined spectroscopically by 'action spectroscopy'. Their small dipole moments and low number density in the beam make conventional absorption and emission spectroscopy unsuitable. Instead, the cluster is tagged with a ligand, easily lost upon absorption, which is detectable with very high sensitivity by mass spectrometry. The infrared spectra thus obtained are compared with theoretical predictions from density functional theory (DFT) [91, 311]. Of relevance to the work in this chapter is the use of carbon monoxide to tag cationic, neutral and anionic rhodium clusters. [93, 95, 312] In almost all cases, CO prefers to sit on an 'atop' site, bound to a single rhodium atom, rather than a 'bridging' (μ^2) or 'hollow' (μ^3) site. Unusually, n=3, 4 prefer higher coordination sites. Cationic and neutral species have also been studied by vibrational spectroscopy at saturation coverage of CO [94]. The maximum number of CO molecules that can be arranged around a cluster gives some information about its structure, although that structure is heavily perturbed by the presence of so many strongly-bound ligands. The C-O vibrational frequency is affected by the rhodium cluster's charge [94], although collision experiments show that CO sticks to rhodium clusters

in all charge states approximately at the collision rate [121].

Also relevant here is previous work on the $Rh_nN_2O^+$ system by the Mackenzie group. Infrared multiple photon dissociation (IR-MPD) studies of argon-tagged $Rh_nN_2O^+$ (n=4-8) proved, in conjunction with DFT studies, that N_2O is molecularly adsorbed on an atop site via the nitrogen atom. The observed vibrational spectra of $Rh_nN_2O^+$ clusters have two bright modes, the asymmetric and symmetric N_2O stretch, which show slight blue shifts from their frequencies in free N_2O. The N_2O bends are of intermediate intensity, and the metal-metal modes have low intensities [310, 313].

Fragments other than the argon-loss product were observed, meaning that the N_2O molecule itself acts as a 'tag'. N_2O adsorbed on cationic rhodium clusters appears to be able to undergo either of two infrared-induced surface processes: decomposition, or N_2O reduction (4.14) and desorption (4.15).

$$Rh_nN_2O^+ + xh\nu \rightarrow Rh_nO^+ + N_2 \tag{4.14}$$

$$Rh_nN_2O^+ + xh\nu \rightarrow Rh_n{}^+ + N_2O. \tag{4.15}$$

As was expected from previous work on the $Rh_n{}^+ + N_2O$ system, the rates of these processes showed significant size dependence [21]. All clusters appear to be able to reduce N_2O except $Rh_5N_2O^+$, which decays only via N_2O desorption in high-power IR-MPD experiments.

In an attempt to understand the observed branching ratios between processes (4.14) and (4.15), the relevant reaction profiles were calculated at the DFT level of theory, using the TPSSh functional and the def2-TZVP basis set. The results for n=5, 6 are shown in figure 4.4. The situation is complicated by the existence of more than one low-lying spin state which may be occupied in the beam. However, the calculations clearly suggest a plausible explanation for the IR-MPD results: the energetic barrier to N_2O desorption is lower than the barrier to reduction on $Rh_5N_2O^+$, whereas the opposite is true for $Rh_6N_2O^+$. It is also interesting to note from figure 4.4 that the lowest-calculated N_2O reduction pathway requires a spare atop site on the rhodium cluster to allow direct oxygen adsorption onto the cluster surface.

Further experiments were performed on $Rh_nON_2O^+$. The same chemistry (reduction and/or desorption of N_2O) could be achieved by pumping the Rh-O stretch [310]. This suggests that the method by which energy is introduced to the cluster is not important as it can be internally redistributed into the appropriate vibrational modes to activate surface chemistry. One key difference was observed

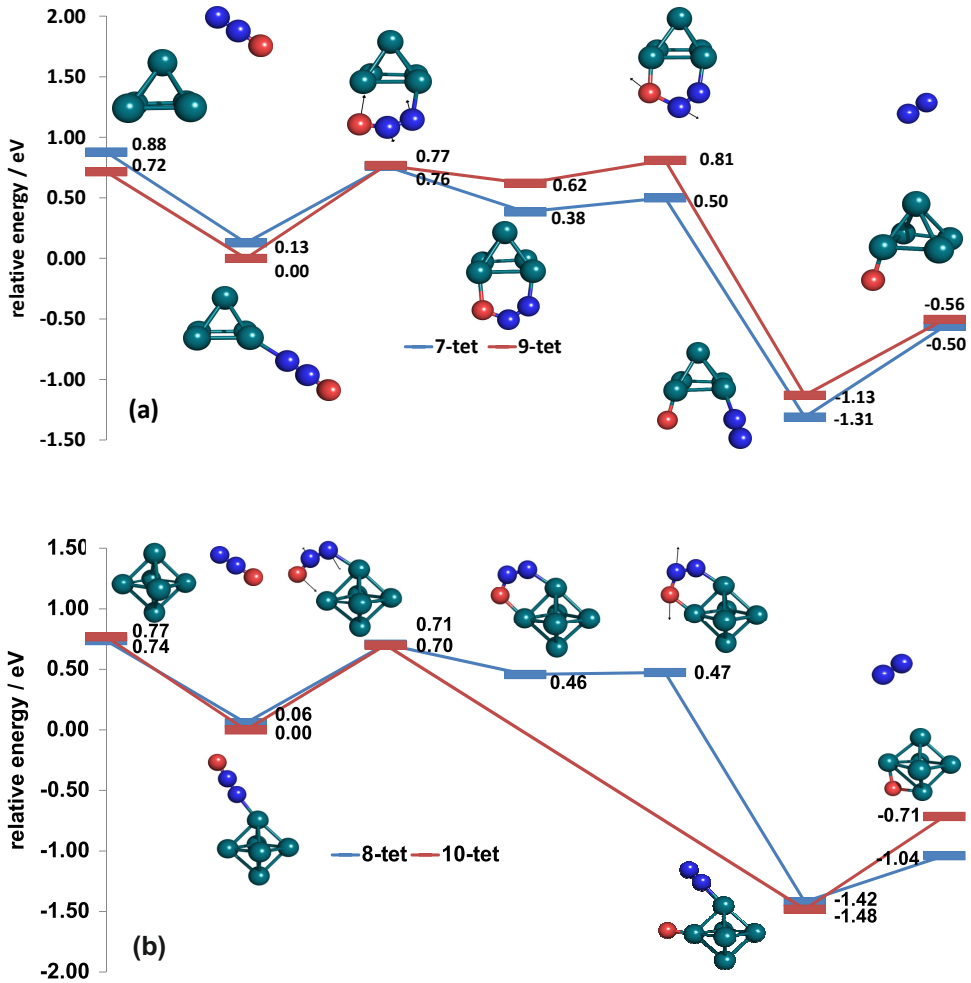

Figure 4.4: Calculated pathways for the decay of (a) $Rh_5N_2O^+$ and (b) $Rh_6N_2O^+$ in the two lowest-energy spin states, plotted in red and blue lines. Surface decomposition (N_2 loss) is the preferred decay route on $Rh_6N_2O^+$, while desorption (N_2O loss) has the lower barrier on $Rh_5N_2O^+$. All calculations for this figure were carried out by Suzy Hamilton using DFT, with the TPSSh functional and TZVP basis set.

on the $Rh_nON_2O^+$ clusters, however. $Rh_5ON_2O^+$ rapidly reduced N_2O to produce $Rh_5O_2^+$. DFT calculations suggested that the reason is a 'cooperative binding effect'. When oxygen and N_2O are coadsorbed on Rh_5^+, the oxygen's presence raises the N_2O desorption energy so much that it exceeds the reduction barrier, effectively closing the desorption channel [314].

Many of the features of rhodium cluster chemistry discussed previously are brought together in a 2012 paper by Yamada *et al.* [16]. The size-dependent catalytic activity of cationic rhodium oxide clusters was investigated in a CO/N_2O gas mixture for $Rh_nO_m^+$ (n=10-28, m ≥0). Starting from the

bare cluster, $Rh_nO_m^+$ products are observed on reaction with N_2O as the N_2 desorbs rapidly. There is evidence of a cooperative effect between surface-adsorbed O and N_2O species on clusters larger than Rh_{12}^+, such that Rh_nO^+ oxidises faster than Rh_n^+. The oxide clusters oxidise CO to CO_2 at a rate which increases with the cluster's oxygen coverage [16].

A number of recent theoretical papers concern rhodium clusters, and their mechanisms of interaction with small molecules [315]. Calculations of the CO+NO surface reaction on Rh_7^+ concur with the conclusions presented in this chapter about the energetic favourability of CO_2 formation from CO on the cluster surface [316]. Other reaction mechanisms considered include surface dissociation of NO on $Rh_n^{+/-}$ [317] and CO reactions with H_2 on Rh_6 [318].

Taken together, the previous work on rhodium clusters in the presence of N_2O and CO illustrates a highly complex system wherein any one of a number of factors may tip the balance in favour of or against reaction. Reaction barriers, desorption energies, cooperative effects, cluster surface area and geometry, cluster spin state and even an adsorbate's cluster surface position may all affect reactivity. It is consequently a system with much room for further work.

4.5 CID with argon

4.5.1 Experimental Results

The experimental procedure used for CID experiments with argon on $Rh_nO_mN_2O^+$ is illustrated in figure 4.5. To create the parent distribution shown in figure 4.5 (i), ions were accumulated in the cell over a series of 20 ablation cycles. Twenty cycles ensure that sufficient parent ion is collected in the cell. Various parameters may be tuned by trial and error to maximise the intensity of the desired species; most effective are the relative timings of ablation, extraction, cell opening (the time at which the trapping plates' voltage is dropped to allow ions into the cell) and so on.

Mass selection of the parent ion is achieved by using SWIFT to eject all other ions, creating spectrum 4.5 (ii) (a). Once isolated, the ion is excited using a resonant RF field pulse, according to equation (4.9). Excited ions are left in the cell for one second to allow collisions with argon, after which the remaining parent and the newly-created fragments are detected. Some fragmentation occurs even after a 1 μs excitation, which imparts barely any energy at all. Some ions in the cell must therefore have sufficient internal energy to react upon collision at thermal velocity. Although they have been cooled by supersonic expansion upon exiting the source, during the accumulation time (approximately 2 sec-

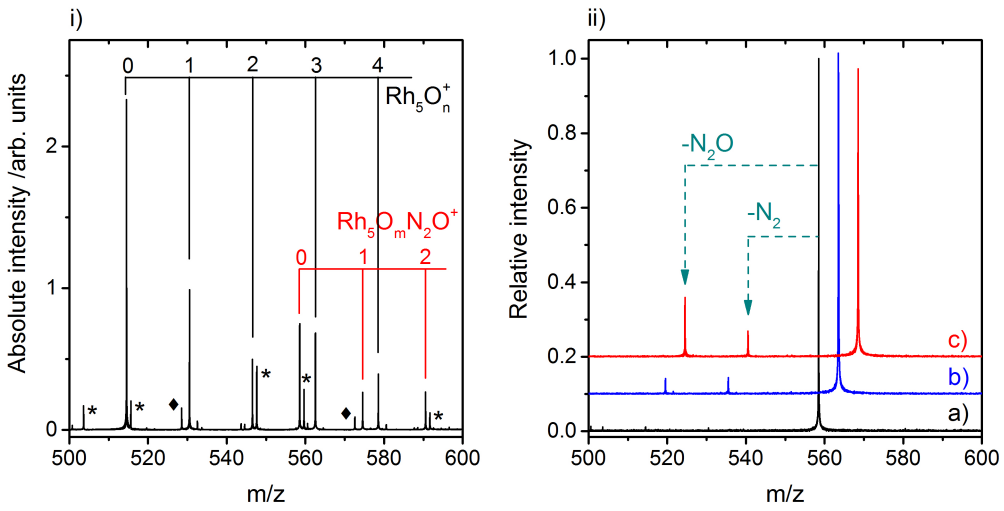

Figure 4.5: Production, isolation and excitation of $Rh_nO_mN_2O^+$ in $1.8x10^{-8}$ mbar argon. (i) Parent distribution containing $Rh_5O_n^+$, $Rh_5O_mN_2O^+$, Rh_5N^+-based peaks (diamonds) and Rh_4-based peaks (starred). (ii) (a) Mass spectrum after isolation of $Rh_5N_2O^+$. (b) and (c) are the results of exciting isolated $Rh_5N_2O^+$ for 1 and 500 μs respectively and storage in Ar for 1 s before detection.

onds) the clusters thermalise. They absorb energy via collision, black-body absorption from the cell wall and excitation by the trapping voltage. Highly axially-excited ions exit the cell when the trapping voltage is lowered to allow more ions in. The remaining distribution is therefore approximately at the temperature of the cell, 300 K. Consequently, the high-energy tail of the population distribution may undergo surface reaction upon thermal (non-excited) collision.

Mass spectrum 4.5 (c) illustrates the effect of increased resonant excitation on the stored cluster. Application of the resonant RF field for a longer time (t_{exc}) increases the lab-frame kinetic energy (E_{lab}), which increases the centre-of-mass energy for the colliding pair (E_{CoM}). A larger E_{CoM} results in a larger translation-to-vibration energy transfer on collision, which increases the extent of dissociation. E_{lab} and E_{CoM} may be interconverted by:

$$E_{CoM} = \frac{m_{gas}}{m_{ion} + m_{gas}} E_{lab}, \tag{4.16}$$

where m_{gas} is the mass of the background gas and m_{ion} is the mass of the ion [319].

The relative intensities of parent and products are therefore plotted as a function of E_{CoM} rather than t_{exc}, the excitation time, in figure 4.6. Adsorbed N_2O is seen to react in one of two ways: it may either desorb whole, or decompose on the surface to release N_2. Different parent ions show different branching ratios. $Rh_6N_2O^+$ mostly decays by surface decomposition to Rh_6O^+, although

some desorption product (Rh_6^+) is also visible. $Rh_5N_2O^+$, on the other hand, appears to favour simple desorption and Rh_5^+ is the major product channel. Addition of an oxygen atom to the cluster surface seems to reverse the relative barrier heights on the n=5 cluster. Surface decomposition and loss of N_2, forming $Rh_5O_2^+$, is the dominant decay pathway for $Rh_5ON_2O^+$. This supports the previous suggestion that the desorption energy of N_2O is larger on Rh_5O^+ than Rh_5^+ [314].

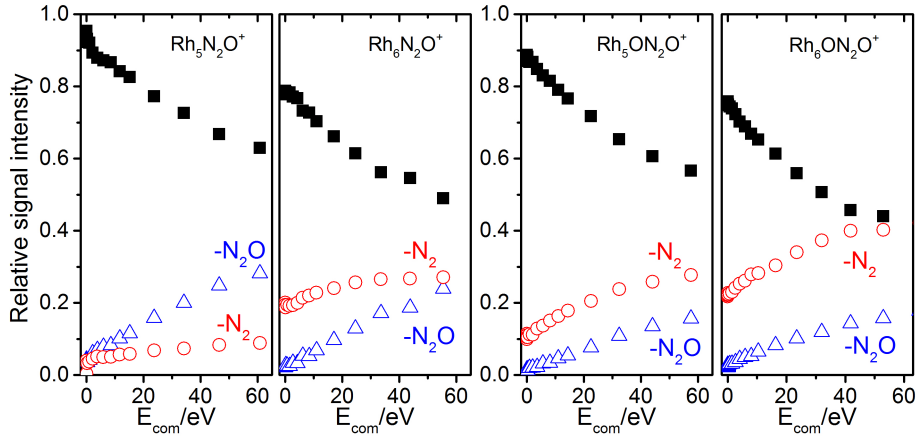

Figure 4.6: Collision-induced dissociation of $Rh_nO_mN_2O^+$ in $1.8x10^{-8}$ mbar argon as a function of centre-of-mass collision energy. In the case of $Rh_5N_2O^+$, N_2O loss occurs more rapidly than N_2 loss, suggesting that the reaction barrier is higher than the desorption barrier. The reverse is true for $Rh_6N_2O^+$. The addition of an O atom increases the preference for N_2 loss in both cases.

Close inspection of figure 4.6 shows that the branching ratio of the desorption and decomposition channels varies with E_{CoM}. In all cases, the desorption channel becomes more prevalent with increasing collision energy. The reasons for this originate in the differing Arrhenius prefactors for the two reaction channels, and require a somewhat subtle explanation. The amount of energy transferred into the clusters' modes increases with E_{CoM}. The clusters' average post-collision vibrational temperature therefore increases with E_{CoM}. According to the Arrhenius equation, the dependence of a reaction's rate constant k on temperature is given by:

$$k = Ae^{-E_a/RT}, \tag{4.17}$$

where A is the Arrhenius prefactor and E_a the activation energy. As T increases, the exponential term approaches 1 and k depends mostly on A, independent of E_a and T. The increased preference for N_2O desorption at higher E_{CoM} reflects the larger A-factor for desorption than for N_2O reduction. Transition-state theory shows that the A-factor is proportional to $e^{\Delta S^\ddagger/R}$, $\Delta S^\ddagger$ being the entropy of

formation of the transition state. The conclusion that the A-factor for desorption is larger than that for N_2O reduction is consistent with what is known about the mechanisms of these reactions. Desorption simply requires the elongation of a Rh-N bond which is not entropically demanding and therefore has a large $\Delta S^{\ddagger}$ (called a 'loose' transition state). Decomposition of N_2O requires significant rearrangement in order to deposit the oxygen atom onto the cluster surface, which is entropically unfavourable and causes a small $\Delta S^{\ddagger}$ and a 'tight' transition state. Although it would be interesting to investigate the continuation of the trend at larger E_{CoM}, the ion's maximum orbital radius (and hence velocity) are limited by the cell dimensions.

It is tempting to interpret the differing parent/product fractions at zero excitation as an indication of relative absolute barriers. However, other factors can affect the zero-excitation product intensities, such as imperfect ejection of these particular masses. Additionally, the parent ion distributions may consist of multiple isomers reacting at different rates. Evidence of this has been seen in the past for the Rh_n^+/N_2O system [21]. The discontinuity at 5 eV in the $Rh_5N_2O^+$ data in figure 4.6 certainly suggests that the parent distribution has a small, fast-reacting portion which decays very rapidly.

An attempt was made to analyse the data in figure 4.6 in a quantitative manner using a technique well-established in the literature on collision-induced dissociation [110, 320]. Relative intensities of parent and product ions are converted into reactive cross sections which are then fitted as a function of collision energy to extract a threshold. The initial non-zero product intensities in our case make numbers extracted from such fits meaningless. Additionally, simple fitting functions assume single collision conditions, and, as will be seen in section 4.7, this is only true where E_{CoM}<30-40 eV. The trends are reliable, however: the desorption cross section is smaller than the reaction cross-section for all clusters except $Rh_5N_2O^+$, and increases with E_{CoM}. The N_2O decomposition (or reduction) cross section slowly decreases as E_{CoM} increases.

4.5.2 Calculating the energy transferred on collision

The maximum E_{CoM} shown in figure 4.6 is around 60 eV. If all of this energy were to be deposited into vibration, the cluster would explode. Calculation of the fraction of E_{CoM} actually deposited into the cluster's vibrational modes by collision would be most useful. If taken in conjunction with the branching ratios, it could give some information about the relative barrier heights for surface decomposition and desorption of N_2O. However, calculation of the energy transfer upon collision requires knowledge of the potential energy surface upon which the collision occurs. A suitable empirical

model has been developed [321], but (i) it requires numerous fitting parameters and therefore considerably better data than is available here, and (ii) it fails in the face of our non-zero initial product intensities.

One simple, purely theoretical model for calculating translation to vibration energy transfer upon atom-polyatom collision models the polyatom as a diatomic [322]. It assumes:

1. a short lifetime of the collision complex;
2. interaction with a low-frequency vibrational mode (the metal-metal modes in a Rh_n^+ cluster are found to be low-frequency enough to satisfy this condition); and
3. low energy transfer to rotation.

The extent to which our system satisfies 1 and 3 is likely to vary with E_{CoM}.

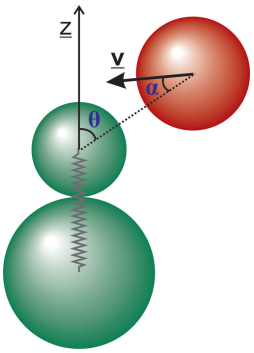

Figure 4.7: Collisional energy transfer between an atom and a cluster modelled as a diatomic. The energy transferred depends only on the angles θ and α, and the masses of the species involved.

The model is illustrated in figure 4.7. The 'diatom' is aligned along an axis z and collides with an incoming atom at velocity **v**. The angle that the line of centres of the two colliding atoms makes with z is called θ and with **v** is called α. The fraction of energy transferred to vibration upon collision under these conditions can be derived using conservation of energy and angular momentum (see reference [322]) and is given by:

$$\frac{E_{vib}}{E_{CoM}} = 4m\frac{cos^2\theta cos^2\alpha}{(1+m)^2} \tag{4.18}$$

where E_{vib} is the energy transfer to vibrational energy in the cluster modes. The quantity m depends on the mass of the collision gas atom m_{gas} (Ar in our case), the mass of the 'hit' atom, m_h (Rh in our case), and the mass of the rest of the cluster, $m_{tot\text{-}h}$ ($Rh_{n-1}N_2O$ in our case).

$$m = \frac{m_{gas}m_{tot-h}}{m_h(m_{gas}+m_h+m_{tot-h})}. \tag{4.19}$$

Dependence on the bond's force constant is not included, as the model expressly assumes a rapid collision with a weak bond. The hit atom is moved relative to the rest of the cluster, and does not feel much of the bond's spring effect during collision.

For a head-on collision (in which case both α and θ are zero), the transfer to rotation is zero. The transfer to vibration (assuming a rhodium atom is hit) is 70.5% of E_{CoM} for $Rh_5N_2O^+$ and 72.2% for $Rh_6N_2O^+$. The fraction of collisions which are head-on is, however, fairly small. Allowing α and θ to vary between $\pm\frac{\pi}{2}$ with uniform probability means that equation (4.18) becomes:

$$\left\langle \frac{E_{vib}}{E_{CoM}} \right\rangle = \int_{\frac{-\pi}{2}}^{\frac{\pi}{2}} \int_{\frac{-\pi}{2}}^{\frac{\pi}{2}} \frac{4m}{(1+m)^2} \frac{cos^2\theta}{\pi} \frac{sin^2\alpha}{\pi} d\theta d\alpha. \tag{4.20}$$

When solved, this equation finds an expected energy transfer of 6% for both $Rh_5N_2O^+$ and $Rh_6N_2O^+$. The diatom model is flawed and simply indicates that much less than 100% of E_{CoM} is transferred to vibration. However, it is consistent with a previous experimental estimate of 4±1.7% [323].

A preferable alternative would be to perform molecular dynamics simulations of Ar + $Rh_nN_2O^+$ collisions. Classical trajectory simulations have been performed on a similar system, namely collisions between an argon atom and Al_6 and Al_{13} clusters [324, 325]. The simulations show that translation to vibration transfer drops off rapidly as the point of collision moves from the centre to the edge of the cluster, but the percentage of the translational energy transferred also depends on relative velocity, mass and bond strength. Such simulations would be useful to compare to the experiments described here, but have not been undertaken in this project.

4.6 CID with carbon monoxide

Quantitative interpretation of the argon CID experiments proved difficult as there were too many unknowns. The number of collisions having occurred can be determined only probabilistically, and the efficiency with which they transfer energy to vibration is unknown. To overcome these problems, the colliding species is replaced by ^{13}CO. Carbon monoxide chemisorbs to the cluster approximately at the collision rate [121]. Upon chemisorption, a fixed (and, importantly, calculable) amount of energy is deposited into the cluster. The price paid for definite knowledge of E_{int}, however, is complication of the system. CO is not an inert adsorbate but rather reacts with other surface species.

4.6.1 Calculated binding energies

Minimum-energy structures of CO-decorated clusters were calculated using density functional theory (DFT). The TPSSh functional was used, having been found to perform well for decorated rhodium clusters in the past [310], and a suitably large basis set: def2-TZVP. The calculations were performed using the Turbomole package for electronic structure calculations [326]. The starting points for all calculations were the putative global minima obtained previously by the Mackenzie group for Rh_n^+ [91], Rh_nO^+ [314] and $Rh_nN_2O^+$ [310]. These structures were decorated with CO in various reasonable orientations and then optimised. Basis set superposition errors are neglected. The desorption energy of a monomer is calculated according to:

$$E_{desorp} = E_{cluster} + E_{monomer} - E_{decorated} \tag{4.21}$$

where E_{desorp} is the energy required to desorb a monomer from the cluster, $E_{cluster}$ is the cluster's energy, $E_{monomer}$ is the desorbing monomer's energy and $E_{decorated}$ is the decorated cluster's energy.

The desorption energies of CO from various clusters are shown in table 4.1. The calculations were performed in a number of spin states, as, in high-spin systems such as Rh_n^+, a number of spin states are accessible [327]. Global minima are shown in bold, and their structures are pictured. Minima calculated in different spin states do not necessarily have the same geometry. This is due to the large number of structures approximately at the same energy as the global minimum rather than any enormous effect of spin state on the structure. Not all spin states are low in energy, however, and $Rh_6N_2O^+$ has not been satisfactorily converged in the 2S+1=6 spin state.

All CO desorption energies appear to be approximately 2 eV, which greatly exceeds the calculated reaction barriers for both surface decomposition and desorption of N_2O, shown in the reaction profile of figure 4.4. Hence, upon CO chemisorption, both decay pathways for N_2O are energetically accessible. If N_2O desorption occurs, the remaining Rh_nCO^+ cluster will no longer have sufficient internal energy to desorb CO and so Rh_nCO^+ should be observed as a primary product. If, however, surface decomposition occurs, the reaction is sufficiently exothermic that even after N_2 desorption, CO can also desorb and Rh_nO^+ will be the observed product.

The Rh_nCO^+ structures in table 4.1 may be compared to the experimental results of Fielicke *et al.* [93, 95, 312]. The results are found to be at odds; experiments suggest that on Rh_5^+ and Rh_6^+, CO chemisorbs exclusively on atop sites. If calculated atop-bound structures of Rh_nCO^+ are used, the

Calculated desorption energy of CO /eV				
n	2S+1	Rh_nCO^+	$Rh_nO(CO)^+$	$Rh_n(N_2O)(CO)^+$
5	5	1.89	2.17	2.11[2]
	7	**2.22**	**2.29**	**2.27**
	9	1.67	2.06	1.75
		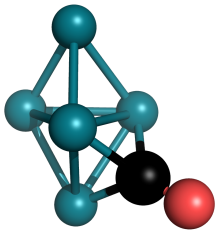	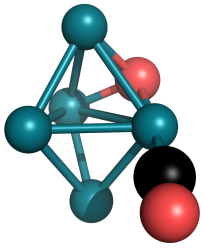	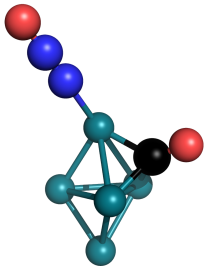
6	6	1.76[1]	1.71[2]	Not converged
	8	**1.78**	**2.32**	**1.89**
	10	1.78[1]	2.04	1.72[2]
	12	1.71	1.79	1.70[2]
		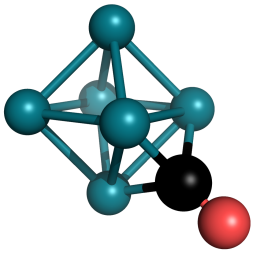	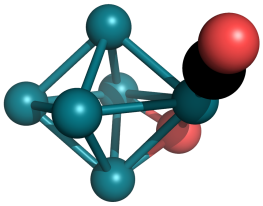	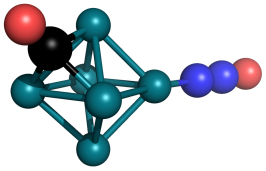

Table 4.1: Energy required to desorb CO from Rh_nCO^+, $Rh_nO(CO)^+$ and $Rh_n(N_2O)(CO)^+$ (n=5, 6). The minimum-energy structures are shown and their energies are given in bold. Not all the spin states have the same structures as the global minima; those marked [1] have CO in an atop site and those marked [2] have CO in a hollow site other than that shown.

binding energies of table 4.1 decrease slightly, but still exceed all previously-calculated barriers. This propensity of DFT to favour high-coordination sites of CO on transition metal surfaces is a known problem [135]. It has recently been shown that common DFT methods treat the lowest unoccupied molecular orbital of CO incorrectly, predicting too low an energy [328]. DFT therefore artificially favours sites which increase back-bonding (donation of electrons from the cluster to the pi-orbitals of the CO molecule).

Having calculated the energy deposited by CO chemisorption, its effect on the system is investigated. Calculation of new reaction profiles such as those in figure 4.4 would be extremely time-consuming

Calculated desorption energy of N_2O /eV				
n	2S+1	$Rh_nN_2O^+$	$Rh_nO(N_2O)^+$	$Rh_n(N_2O)(CO)^+$
5	5	0.73	1.11	0.95
	7	0.74	**1.10**	**0.78**
	9	**0.71**	Not available	0.80
		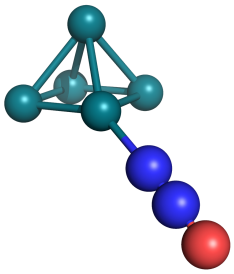	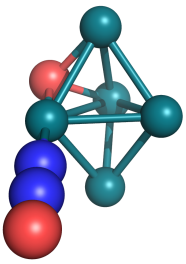	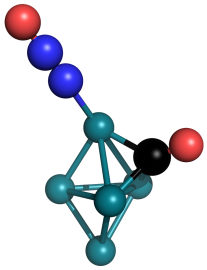
6	6	Not converged	0.59	0.80
	8	0.68	**0.99**	**0.76**
	10	**0.77**	Not available	0.71
	12	0.76	Not available	0.75
		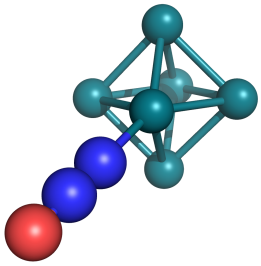	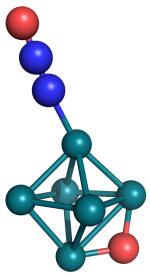	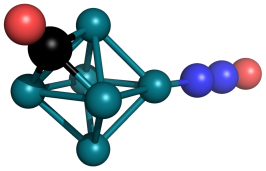

Table 4.2: Desorption energy of N_2O from $Rh_nN_2O^+$, $Rh_nO(N_2O)^+$ and $Rh_n(N_2O)(CO)^+$. The desorption energies of N_2O from $Rh_nN_2O^+$ and $Rh_nON_2O^+$ have been published elsewhere. [310, 314] The energies in bold are those of the global minima and their structures are shown.

and was not undertaken. However, the effect of coadsorbed CO on the desorption energy of N_2O was calculated. The result is shown in table 4.2, along with desorption energies of N_2O from Rh_n^+ and Rh_nO^+ taken from previous publications by the Mackenzie group [310, 314]. It is evident that the presence of CO does not change the N_2O desorption energy significantly from its value on the bare cluster. There is no sign of the cooperative effect seen in the presence of a coadsorbed oxygen atom.

Not only reactant molecules desorb from the cluster surface. Product molecules require energy to desorb, too. The products expected from the catalysed reaction of N_2O and CO are N_2 and CO_2. The desorption energies of the product species from the bare cluster are shown in table 4.3. The

Desorption energies of reaction products from Rh_n^+ /eV			
n	2S+1	N_2 from $Rh_nN_2^+$	CO_2 from $Rh_nCO_2^+$
5	7	0.79	0.40
	9	**0.68**	**0.39**
	11	0.76	0.46
		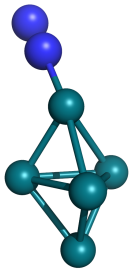	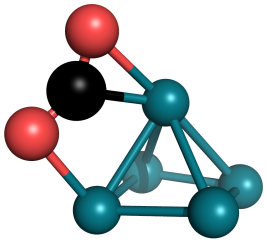
6	8	0.70	0.31
	10	**0.80**	**0.43**
	12	0.75	0.38
		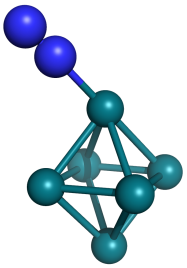	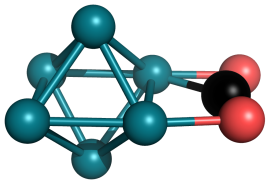

Table 4.3: Desorption energies of reaction products N_2 and CO_2 from Rh_n^+. Global minima are shown in bold and their structures are pictured. CO_2 is particularly weakly bound. N_2 is surprisingly strongly bound, but is produced in an exothermic reaction and is likely to be desorbed.

N_2 desorption energy is very similar to the N_2O desorption energy from Rh_n^+. N_2 is produced by the highly exothermic surface decomposition of N_2O, and even with a binding energy of 0.8 eV is likely to desorb immediately. The desorption energy of N_2 from $Rh_nO(N_2)^+$ is similar to that from $Rh_nN_2^+$ (see figure 4.4). The desorption energy of CO_2 is something of a surprise, being extremely low. Any CO_2 formed by surface reaction of O and CO, such as was observed by Yamada *et al.*, will be immediately lost from the cluster's surface [16].

4.6.2 ^{13}CO collisions with $Rh_nN_2O^+$

The collision experiments performed using ^{13}CO differ conceptually from the argon collision experiments. The stored cluster is not accelerated at all; length of storage time is the variable. Consulting

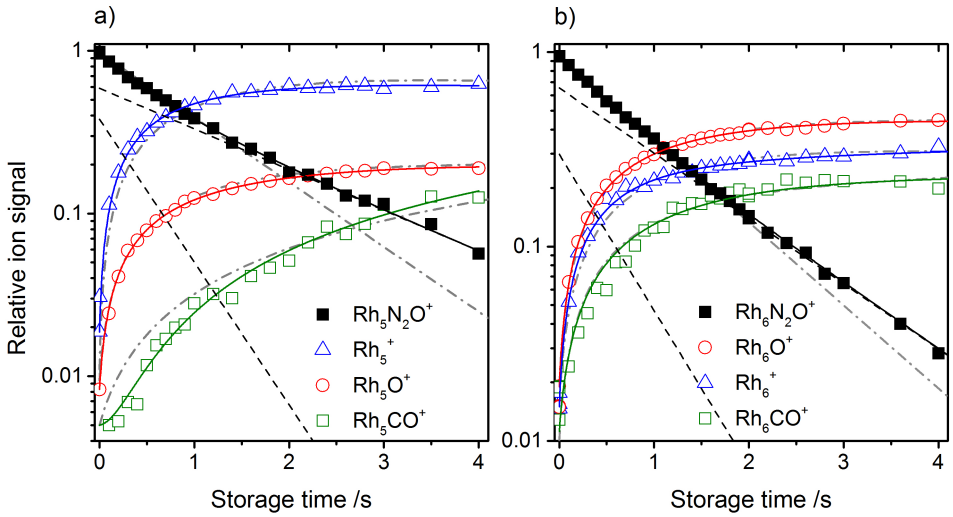

Figure 4.8: Reactions of $Rh_nN_2O^+$ stored in 2.6x10^{-8} mbar ^{13}CO. (a) shows $Rh_5N_2O^+$ and (b) $Rh_6N_2O^+$. Both undergo N_2O dissociation to release either N_2+CO or, in the case of further CO oxidation, N_2 + CO_2. CO oxidation is very fast on n=5. Substitution of N_2O for ^{13}CO on the surface of the cluster is not seen on n=5; Rh_5CO^+ is a secondary product formed by ^{13}CO addition to Rh_5^+. Solid lines show fits assuming two isomers of $Rh_nN_2O^+$; dotted lines are single isomer fits.

table 4.7 in section 4.7 shows that, for at least the first two seconds of storage time, the $Rh_nN_2O^+$ clusters probably experience one collision at most. Their internal energy is therefore determined by the chemisorption energy of CO (approximately 2 eV) and not altered by collisional heating or cooling effects. Furthermore, according to the findings of reference [121], the sticking probability of CO to $Rh_nN_2O^+$ is approximately 1. The effects of 'non-sticky' collisions of CO with the cluster are therefore not considered - all collisions are assumed to result in chemisorption.

The results for $Rh_nN_2O^+$ (n=5, 6) are shown in figure 4.8. The solid-line fits invoke two isomers of the $Rh_nON_2^+$ parent species, while the grey dot-dashed lines invoke only one. It is evident that $Rh_5N_2O^+$ requires at least two parent isomers for a suitable fit as the parent ion's decay is curved. The parent isomers decay with measurably different rates. The opportunities for isomerism in $Rh_5N_2O^+$ are plentiful: the nascent distribution may contain multiple spin states, multiple N_2O binding sites, multiple geometric structures of the Rh_5^+ skeleton or even a bimodal energy distribution. The presence of multiple isomers of parent transition metal clusters in a molecular beam has been suggested many times previously [26, 314, 327]. The differing decays of the two parent isomers are shown in figure 4.8 by dotted lines. The rate of decay of the faster-reacting isomer is uncomfortably large compared to the collision rate, suggesting either that the fit is imperfect or that one parent isomer is internally hot and capable of desorbing N_2O before collision with CO.

The simplest mechanism to describe all the products observed in figure 4.8 is:

Primary reactions

k_0 $Rh_nN_2O^+ + CO \rightarrow Rh_n^+ + N_2 + CO_2$ "reduction-oxidation"

k_1 $Rh_nN_2O^+ + CO \rightarrow Rh_nCO^+ + N_2O$ "displacement"

k_2 $Rh_nN_2O^+ + CO \rightarrow Rh_nO^+ + N_2 + CO$ "N_2O decomposition"

Secondary reactions

k_3 $Rh_nO^+ + CO \rightarrow Rh_n^+ + CO_2$ "CO oxidation"

k_4 $Rh_n^+ + CO \rightarrow Rh_nCO^+$ "addition"

The fitted rate constants according to this mechanism, k_i, are shown in table 4.4. CO is in large excess so k_i are pseudo-first order rate constants. One important additional detail should be noted here. Due to the mass coincidence between a likely product, Rh_nOCO^+, and the parent $Rh_nN_2O^+$, labelled ^{13}CO was used in order to distinguish these species and to allow selective ejection of $Rh_nO^{13}CO^+$ during the isolation process.

Reactions of $Rh_5N_2O^+$ with ^{13}CO are shown in figure 4.8 (a). The prevalent reaction pathway upon

Pseudo first order reaction rate constants k_i (s^{-1})					
	$Rh_5N_2O^+$		$Rh_6N_2O^+$		
	Two isomers		Two isomers		One isomer
	A	B	A	B	A
%	61	39	69	31	100
k_0	0.40	1.80	0.11	1.13	0.33
k_1	0.00	0.00	0.26	0.00	0.19
k_2	0.17	0.23	0.41	0.72	0.46
k_3	0.03		0.02		0.01
k_4	0.06		0.00		0.03

Table 4.4: Pseudo first order rate constants for the surface reactions occuring when $Rh_nN_2O^+$ collides with ^{13}CO according to the reaction scheme above. The relative values of these rate constants are more reliable than the absolute values, the latter having an uncertainty of at least 30%, largely due to uncertainty in the cell pressure.

^{13}CO chemisorption is the "reduction-oxidation" reaction. The chemisorption energy of ^{13}CO drives N_2O reduction, forming an oxide. The intermediate species $[Rh_5O(^{13}CO)(N_2)^+]$ desorbs N_2 and $^{13}CO_2$ extremely rapidly, leaving Rh_5^+. The speed of ^{13}CO oxidation on the cluster surface is something of a surprise; it forms so quickly that the intermediate $Rh_5O^{13}CO^+$ is not seen. The rapid loss of CO_2, after formation, is predictable from the very low binding energy of $^{13}CO_2$ (table 4.3).

The other surprise in the $Rh_5N_2O^+$ + ^{13}CO data is that ^{13}CO does not displace N_2O to any great extent. Rh_5CO^+ cannot be fitted as a primary product and shows a clear induction period at short storage times. Instead it arises exclusively from ^{13}CO sticking to Rh_5^+. It is not clear why this should be so. Calculations in table 4.2 do not indicate that the presence of CO greatly increases the desorption energy of N_2O. N_2O decomposition (and subsequent CO desorption) is observed, and that process has previously been suggested to have a higher barrier than desorption [310, 314]. The results in figure 4.8 (a) rather suggest that, in the presence of surface CO, N_2O displacement is not seen because N_2O is oxidised on the cluster surface extremely rapidly. In turn this suggests that, in the presence of surface CO, N_2O desorption is less energetically favourable than surface decomposition.

$Rh_6N_2O^+$ (figure 4.8 (b)) behaves differently to $Rh_5N_2O^+$. All three primary processes suggested in the reaction scheme occur: reduction-oxidation, displacement and N_2O decomposition. As might have been predicted from previous data, the oxidative reactions occur faster than the displacement reaction. [310, 314] Reduction-oxidation to produce bare Rh_6^+ is seen, but Rh_6O^+ is the major product. This shows that the preferred decay pathway after surface decomposition of N_2O is CO desorption. CO oxidation also occurs, forming CO_2 and Rh_6^+, but at a slower rate than CO desorption. We may speculate as to the reasons for the differences between the cluster sizes. CO oxidation is probably slower on n=6 than n=5 as n=6 has more internal degrees of freedom in which to dissipate the heat of N_2O reduction. This makes all reactions proportionally slower and disfavours CO oxidation. Additionally, Rh_6^+ has a larger surface area than Rh_5^+ and so the probability of O and CO meeting on the surface in order to react is lower too.

Kinetic fits such as are shown in table 4.4 provide interdependent rate constants which cannot be relied upon with great certainty. In an attempt to fix some of the pseudo-first order rate constants in table 4.4, individual components of the reaction scheme were stored in the ICR cell under the same conditions as the parent. The results of storing isolated Rh_6O^+ in 2.6×10^{-8} mbar ^{13}CO are shown in figure 4.9. The problem is immediately apparent: Rh_6O^+ produced in the source is internally cold, whereas Rh_6O^+ produced by reaction is internally excited. Rh_6O^+ from the cluster source reacts

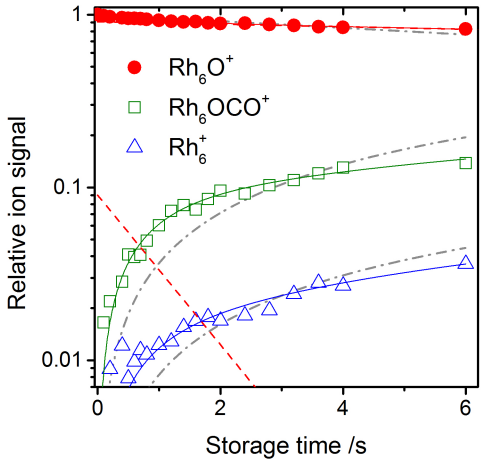

Figure 4.9: Reactions of Rh_6O^+ in 2.6x10^{-8} mbar ^{13}CO. Upon addition of ^{13}CO, the Rh_6OCO^+ complex is either cooled (radiatively or collisionally), or loses CO_2. The single isomer fits, shown in grey dot-dash lines, are highly unsatisfactory. The two-isomer fits, shown in solid colour lines, are good.

very slowly, forming Rh_6^+ at a rate of 0.002 s^{-1}. It is cold enough to add ^{13}CO to form Rh_6OCO^+ at a rate of 0.132 s^{-1}. The parent distribution contains at least two isomers; rate constants are given for the isomer with a relative abundance of 90%. Rate constants extracted from figure 4.9 cannot therefore be substituted into the kinetic fit of $Rh_6N_2O^+$ to reduce the number of parameters needed. The experiment on isolated Rh_6O^+ is nonetheless of value as further evidence of surface oxidation of CO by an oxygen atom on Rh_n^+.

4.6.3 ^{13}CO collisions with $Rh_nON_2O^+$

In IR-MPD experiments, and the argon collision experiments described in this chapter, addition of an oxygen atom to Rh_5^+ was found to significantly affect the reactivity of adsorbed N_2O [264, 310]. ^{13}CO collision experiments were therefore performed on $Rh_nON_2O^+$ (figure 4.10) for comparison.

The data in figure 4.10 is not quite as high-quality as that in figures 4.8 and 4.9 due to the lower abundance of $Rh_nON_2O^+$ in the beam and the larger number of reaction channels available reducing the signal-to-noise ratio. The following reaction scheme is the simplest way of describing potential reactions in the $Rh_nON_2O^+$ system.

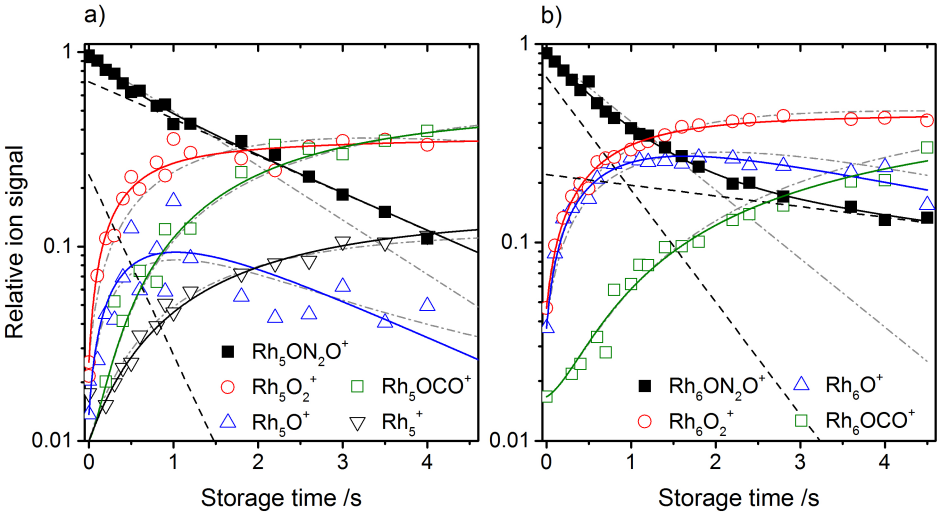

Figure 4.10: Reactions of (a) $Rh_5ON_2O^+$ and (b) $Rh_6ON_2O^+$ in 2.6x10^{-8} mbar ^{13}CO. Fits assuming two isomers of parent are shown in solid colour, while fits assuming a single isomer are shown in grey dot-dash lines. N_2O decomposition accompanied by ^{13}CO desorption to form $Rh_nO_2^+$ is the dominant channel in both (a) and (b). N_2O decomposition accompanied by oxidation of ^{13}CO to produce Rh_nO^+ is observed in both cases. Rh_5O^+ reacts further to $Rh_5^+ + CO_2$ but Rh_6O^+ does not.

Primary Reactions

k_0' $Rh_nON_2O^+ + CO \rightarrow Rh_nO^+ + N_2 + CO_2$ "reduction-oxidation"

k_1' $Rh_nON_2O^+ + CO \rightarrow Rh_nOCO^+ + N_2O$ "displacement"

k_2' $Rh_nON_2O^+ + CO \rightarrow Rh_nO_2^+ + N_2 + CO$ "N_2O decomposition"

k_5' $Rh_nON_2O^+ + CO \rightarrow Rh_n^+ + N_2O + CO_2$ "displacement-oxidation"

Secondary Reactions

k_3 $Rh_nO^+ + CO \rightarrow Rh_n^+ + CO_2$ "CO oxidation"

k_3' $Rh_nO_2^+ + CO \rightarrow Rh_nO^+ + CO_2$ "CO oxidation"

k_4' $Rh_nO^+ + CO \rightarrow Rh_nOCO^+$ "CO addition"

In this reaction scheme, the rate constant k_n' is analogous to the rate constant k_n in the previous scheme, but in the presence of an additional oxygen atom. The best fits found using two isomers are shown in figure 4.10 as solid colour lines, while single-isomer fits are shown by dot-dash grey lines. The corresponding rate constants are shown in table 4.5.

At first glance, the additional oxygen atom on Rh_5^+ seems to slow reduction-oxidation. $Rh_5O_2^+$ is the major product of $Rh_5ON_2O^+ + {}^{13}CO$, by N_2O reduction. By comparison, the major product

Pseudo first order reaction rate constants k_n' (s^{-1})						
	$Rh_5ON_2O^+$			$Rh_6ON_2O^+$		
	Two isomers		One isomer	Two isomers		One isomer
	A	B	A	A	B	A
%	75	25	100	76	24	100
k_0'	0.34	0.00	0.23	0.64	0.07	0.38
k_1'	0.00	0.00	0.00	0.00	0.00	0.00
k_2'	0.06	2.14	0.33	0.67	0.05	0.41
k_3	0.23		0.11	0.00		
k_3'	0.00		0.10	0.00		0.02
k_4'	1.44		1.48	0.24		0.26
k_5'	0.03	0.00	0.08			
k_6'	0.00		0.00			

Table 4.5: Pseudo first order rate constants for the reactions of $Rh_nON_2O^+$ (n=5, 6) in $2.6x10^{-8}$ mbar ^{13}CO. The results of fits using one and two isomers are shown; curvature in the parent ion decay suggests two are necessary. The absolute values of the rate constants have uncertainties of at least 30%.

upon $Rh_5N_2O^+$ collision with ^{13}CO was Rh_5^+, the result of reduction-oxidation. Examination of the rate constants in table 4.5 shows that both N_2O reduction and reduction-oxidation are rapid on the cluster surface, although N_2O reduction is somewhat faster. The reason that Rh_5O^+ is not a particularly abundant product is that it can react further with CO to produce Rh_5^+. It is somewhat surprising that CO desorption is more likely than CO oxidation on $Rh_5O_2CO^+$ while the opposite is true on the cluster less abundant in oxygen, Rh_5OCO^+. This rather suggests a cooperative effect of the second surface oxygen atom, either raising the barrier to CO oxidation or lowering the barrier to CO desorption.

N_2O decomposition was the dominant process upon $Rh_6N_2O^+$ collision with ^{13}CO, and this remains the case on $Rh_6ON_2O^+$. The effect of an additional oxygen atom on the Rh_6^+ cluster therefore differs from that on the Rh_5^+ cluster; the relative preference for N_2O decomposition versus reduction-oxidation does not change. The oxygen does have an effect, however: it suppresses the displacement reaction. The rate constants in table 4.5 suggest that this is not because oxidative processes have speeded up, rather the rate of displacement is relatively slowed. This suggests a cooperative effect whereby the surface oxygen atom increases the binding energy of N_2O. In fact, no displacement

reactions are seen at all on the surface of $Rh_nON_2O^+$. All fits suggest that Rh_nOCO^+ is a secondary product resulting from CO addition to Rh_nO^+.

While the rates of reduction-oxidation, N_2O decomposition and displacement are in the same order for $Rh_5ON_2O^+$ and $Rh_6ON_2O^+$, figures 4.10 (a) and (b) are not identical. This is because Rh_5O^+ reacts with CO to produce $Rh_5^+ + CO_2$, while Rh_6O^+ only adds CO. To test whether this result is an inherent function of these cluster sizes or simply an effect of the internal energies of Rh_nO^+ produced by $Rh_nON_2O^+$, isolated Rh_nO^+ were stored in ^{13}CO in the cell. The results for n=6 appear in figure 4.9. Storage of Rh_5^+ under the same conditions shows that surface oxidation of CO by O does occur more rapidly on n=5 than n=6 by a factor of 8. However, complications arising due to parent cluster isomerism and the uncertainty of the parent ion's temperature mean that this result must be treated qualitatively rather than quantitatively.

4.7 Calculation of collision rates

Although the ICR cell is kept under ultra-high vacuum conditions, it inevitably contains some gas. In the experiments described in this chapter, it is deliberately filled with a low pressure of either Ar or ^{13}CO. In the next chapter, the cell gas is whatever residual species cannot be evacuated from the cell by the turbopumps, probably mostly N_2. Calculation of the collision rate of the stored rhodium clusters with these gases will allow determination of the expected number of collisions in a given storage time.

Methods for calculation of the collision rate between ions and polar molecules are known. The oldest is Langevin's 1905 equation for the collision cross section of a point charge with a polarisable molecule:

$$\sigma_{Langevin} = \frac{q}{2v\epsilon_0}\sqrt{\frac{\alpha}{\mu}} \tag{4.22}$$

where v is the relative velocity of the ion, α is the polarisability of the neutral molecule in C m^2 V^{-1} and μ is the reduced mass of the collision complex [329]. Langevin's theory does not take account of any permanent dipole in the neutral molecule. In 1973, Su and Bowers modified Langevin's equations to account for the preference of a neutral molecule to orient its permanent dipole in a favourable electrostatic configuration with respect to the ion [330]. For this reason, their theory is called average

dipole orientation (ADO) theory. The ADO collision cross-section is given by:

$$\sigma_{ADO} = \frac{q}{2v\epsilon_0}\frac{1}{\sqrt{\mu}}\left(\sqrt{\alpha} + \frac{c\mu_D}{\sqrt{\mu}v}\right) \tag{4.23}$$

where all symbols have the same meaning as in equation (4.22). μ_D is the permanent dipole of the neutral molecule in C m and c is the 'dipole locking constant', specific to each molecule, representing the tendency of the molecule to adopt a favourable alignment with the ion during collision. In the absence of a permanent dipole, equation (4.23) reduces to equation (4.22).

Both of these theories treat the ion as a point charge. In the case of large transition metal clusters, such an assumption is unsuitable, as the geometric cross section of the cluster is comparable to σ_{ADO}. Kummerlöwe and Beyer developed the surface charge capture (SCC) model, wherein metal clusters are treated as perfectly-conducting spheres in which the charge can migrate to any point on the cluster surface [121]. The hard-sphere portion of the cross section is consequently stretched from a single point to a circle with the same radius as the cluster. The cluster radius is added to the ADO radius to give the SCC radius. The SCC cross-section, σ_{SCC}, can therefore be much larger than σ_{ADO}. The bare Rh_n^+ cluster radius may be approximated from bulk metal parameters according to:

$$r_{cluster} = \left(\frac{3nm_x}{4\pi\rho}\right)^{1/3} \tag{4.24}$$

where n is the number of cluster atoms, m_x is the atomic mass and ρ is the density of the bulk metal.

Collision cross-sections of Rh_n^+ / Å^2					
n	Collision Partner	σ_{HSD}	$\sigma_{Langevin}$	σ_{ADO}	σ_{SCC}
5	CO	59	131	138	378
	Ar		120	120	348
	N_2		121	121	350
6	CO	76	131	138	417
	Ar		120	120	386
	N_2		121	121	388

Table 4.6: Collision cross-sections of Rh_n^+ with neutral gas molecules. The hard-sphere collision cross sections, σ_{HSD}, are small as they do not account for electrostatic interactions. The point-charge models, $\sigma_{Langevin}$ and σ_{ADO} vary only minimally with n. Data used for these calculations was taken directly from reference [121] and NIST.

Table 4.6 lists the collision cross-sections calculated for Rh_n^+ using the methods described above. The velocity is taken to be the mean relative velocity of the ion-neutral pair at 300 K. The Langevin and ADO models treat the cluster as a point charge, so the cross-sections they find for the n=5, 6 clusters are almost identical. Also included is the hard-sphere cross section σ_{HSD}, calculated from the radius of equation (4.24). σ_{HSD} neglects electrostatic interactions with the neutral molecule and is much smaller than the other values. This suggests that the majority of cluster-neutral collisions are due to the electrostatic interaction between the ion and the polarisable neutral molecule. Consequently the presence of N_2O on the cluster surface will have little effect on the collision rate.

Table 4.6 illustrates the enormous variation in σ with model. Fortunately, Rh_n^+ + CO collision experiments have previously been performed and calibrated to extract an exact collision rate [121]. These experiments show that, although large $Rh_n^{+/-}$ clusters are well-modelled by the SCC theory, classical ADO theory performs better for n≤6. ADO theory is therefore preferred for $Rh_n^{+/-}$ (n≤6) with the caveat that at high relative collision velocities, such as may be obtained by resonant excitation in FT-ICR, the hard-sphere model may be most appropriate [289]. σ_{ADO} thus represents a high-collision-energy minimum to the reaction cross section. The bulk of the experiments described here have been performed at low velocities, where electrostatic models remain valuable.

Collision cross sections may be converted to collision frequencies using the simple relation:

$$\nu_{coll} = N\sigma v, \tag{4.25}$$

where ν_{coll} is the collision frequency and N is the number density of the collision gas. In table 4.6 the velocity was calculated using the mean relative speed of ion and cluster at 300 K:

$$< v_{rel} >= \sqrt{\frac{8k_BT}{\pi\mu}}. \tag{4.26}$$

A more accurate method of calculating v_{rel} is to integrate over the true distribution of velocities in the experiment. A programme is available to perform this integral [121]. Uncertainties remain despite this improvement, due to the unknown axial velocity acquired from the trapping voltage and uncertainties in the calculation of N. The true pressure in the ICR cell must be obtained from the measured pressure using a unitless empirical correction factor:

$$p_{cell} = p_{meas} \times \frac{G}{0.36\alpha + 0.3}. \tag{4.27}$$

Pressure-dependent Rh_n^+ collision frequencies using ADO theory				
n	Collision Partner	p_{cell} /mbar	Collision frequency /s^{-1}	Time between collisions /s
5	CO	2.6±0.7x10^{-8}	0.429±0.116	2.333±0.630
	Ar	1.8±0.5x10^{-8}	0.219±0.059	4.576±1.236
	N_2	7.4±2.0x10^{-10}	0.011±0.003	95.171±25.696
6	CO	2.6±0.7x10^{-8}	0.427±0.115	2.343±0.633
	Ar	1.8±0.5x10^{-8}	0.217±0.059	4.603±1.243
	N_2	7.4±2.0x10^{-10}	0.010±0.003	95.583±25.807

Table 4.7: Collision frequencies at cell operating pressures, calculated using ADO theory integrated over the Maxwell distribution of relative velocities. The CO and Ar pressures were chosen to allow reactions to occur on a suitable timescale for FT-ICR. At the cell's base pressure, collisions are unlikely on the timescale of the experiment. Uncertainty in the true cell pressure leads to an error of 27% in the collision frequencies.

G, a geometry factor accounting for the fact that the pressure is measured outside the cell, is specific to the instrument (3.6±1.0). α is the polarisability of the gas being measured, in 10^{-40} C m^2 V^{-1}.

The resulting collision frequencies are shown in table 4.7. ADO theory is used, which reduces to Langevin's theory in the absence of a permanent dipole. The pressures shown are the cell's operating pressures for each experiment, and their calculation (equation (4.27)) carries an uncertainty of approximately 30%. The CO and Ar pressures were chosen to allow collision-induced reaction to occur on the FT-ICR timescale of a few seconds. The base pressure of the cell (≈7x10^{-10} mbar) is determined by limitations of the vacuum system, and is sufficiently low to make collisions unlikely on the timescale of the experiment.

4.7.1 Concluding remarks

Argon collisions with $Rh_nN_2O^+$ and $Rh_nON_2O^+$ induce either N_2O reduction, accompanied by loss of N_2, or N_2O desorption. This same reactivity has been seen previously following IR excitation of these clusters [310]. N_2O reduction and desorption appear to occur regardless of the method by which activation energy is introduced to the cluster. Not only are the same reactions observed, but collisional activation and high-intensity IR-MPD experiments also seem to result in the same branching ratios. $Rh_5N_2O^+$ is the only cluster studied which desorbs N_2O more rapidly than reducing it. The rate of reduction is increased relative to the desorption rate in the oxide clusters. Argon collision experiments do not merely repeat the conclusions of IR-MPD experiments; they provide additional information.

Argon collision experiments in an FT-ICR have allowed us to observe the branching ratio between desorption and reduction as a function of collision energy. An increasing preference for desorption is seen as the collision energy imparted to the clusters increases. This is consistent with what little is known of the transition states for the two processes. Desorption is an entropically undemanding process and so has a large Arrhenius pre-factor. When a cluster's internal energy is sufficient surmount both desorption and reaction barriers, their relative rate is influenced by the Arrhenius factors. Hence desorption is increasingly favoured as internal energy increases.

Collision experiments with ^{13}CO deposit a fixed, calculable chemisorption energy into the cluster's vibrational modes. This drives rapid reduction of N_2O with loss of N_2 on all $Rh_nO_mN_2O^+$ clusters studied. However the presence of ^{13}CO on the cluster's surface significantly perturbs the system, meaning that N_2O desorption is no longer the fastest process occurring on $Rh_5N_2O^+$. In fact, desorption occurs only on the $Rh_6N_2O^+$ cluster after ^{13}CO collision. Calculations indicate that the desorption energy of N_2O is not greatly affected by the presence of co-adsorbed ^{13}CO; the changes must therefore be induced in the reaction barrier. A second 'perturbing' effect of ^{13}CO on the $Rh_nO_mN_2O^+$ on the cluster system is its interaction with surface oxygen atoms. Rhodium clusters catalyse the gas-phase conversion of N_2O + CO to N_2 + CO_2. Rh_5O^+ oxidises CO particularly efficiently. Whilst this has previously been observed for clusters larger than Rh_{10}^+, our experiments show the same is true of smaller rhodium clusters.

Chapter 5

Black Body Infrared Radiative Dissociation of $Rh_n(N_2O)_m^+$

Unimolecular dissociation of stored $Rh_n(N_2O)_m^+$ has been observed in the absence of collision gas. The low pressure and long storage time of FT-ICR allow the observation of black body infrared induced radiative dissociation (BIRD). The reactions of $Rh_nN_2O^+$ observed are the same as those seen previously by IR-MPD and CID experiments, namely N_2O reduction and desorption. However, different branching ratios are observed by BIRD. The BIRD results imply that reduction has the lower barrier on all clusters, with desorption of N_2O promoted at higher energies by its favourable entropy. The assumption that the reactions observed in the absence of a collision gas are black-body radiation induced was tested in two ways. Firstly, the cell was cooled to 100 K, at which temperature absorption of black-body radiation effectively ceases. The clusters' lifetime in the cell was seen to increase tenfold. A second test of the BIRD mechanism involves increasing the number of adsorbed N_2O molecules. The NO stretch of N_2O is the only major absorbing mode in $Rh_n(N_2O)_m^+$, and so the rate of black body absorption increases linearly with m. The rate of decay of $Rh_n(N_2O)_m^+$ also increases approximately linearly with m, further proving that BIRD is occurring in this system. Deviations from linearity are shown to mirror the desorption rate of N_2O from $Rh_n(N_2O)_m^+$. In the case of n=5, the variation in desorption rate is consistent with desorption energies calculated by DFT. Master equation modelling of the $Rh_5(N_2O)^+$ system finds reasonable reaction barriers, comparable to those found by DFT, confirming that BIRD is the operative mechanism. Part of this data has been accepted for publication as "Chemical reactivity on gas-phase metal clusters driven by blackbody infrared radiation", Angew. Chem. Int. Ed., DOI 10.1002/anie.201409483.

5.1 Development of BIRD

5.1.1 History and development

Black body radiation was first proposed as a means of activating unimolecular decay by Perrin in 1919 [331]. At the time, the hypothesis was rejected on the grounds that ultraviolet absorption would be required to overcome reaction barriers, which was impossible due to the low UV radiation density. In 1922, the Lindemann mechanism was proposed, accounting for unimolecular dissociation by non-reactive collisional excitation [332]. Measured pressure dependences of unimolecular dissociation were found to be consistent with Lindemann's predictions: pressure-independent at high pressure, and first-order dependence at low pressures [331]. Consequently, Perrin's 'radiation theory of chemical action' was abandoned.

The conditions for observation of unimolecular dissociation in the absence of collision were realised with the development of FT-ICR [297]. Ultra-high vacuum conditions minimise collision-induced dissociation, and the long storage period permits slow black body absorption. These conditions were extensively utilised for IR-MPD studies of small molecules using CO_2 lasers at low power [298, 333, 334]. In 1991, Dunbar noticed that if a molecule only absorbs at a single wavelength, then excitation by a CW laser at that wavelength is equivalent to irradiation by a black body source [335]. Increasing laser fluence is equivalent to increasing the black body field's temperature, so E_a may be extracted by varying laser fluence. Dunbar's experiments used a low-power CO_2 laser, which restricted him to systems absorbing around 9.4 to 10.6 μm [336].

Results from 'true' BIRD, using a black body field as the radiation source, were first published in 1994 by McMahon's group [337, 338]. They observed the unimolecular decay rate of clusters such as $Cl^-(H_2O)_n$ at various pressures of buffer gas. Extrapolation of these rates predicted the same non-zero rate at zero pressure, regardless of buffer gas used. Furthermore, the decay rate became totally independent of pressure below 10^{-7} mbar. They concluded that the unimolecular decay observed below 10^{-7} mbar was due to absorption of black body radiation. Metastable ions were ruled out due to the perfect first-order kinetics, prior thermalisation of the distribution with a pulse of buffer gas, and the slow timescale of the decay. McMahon's group performed further tests of the BIRD mechanism for small ligated clusters using deuteration [339]. Deuteration of species such as $[(CH_3)_2CO]Cl^-$ does not materially affect the Cl-O bond strength, or the collision cross-section. However, it lowers the vibrational frequency of the C-H bonds towards the maximum of the black body distribution. The

observed BIRD rate increases as expected.

BIRD is usually a slow method of thermal decomposition. It should therefore be possible to extract Arrhenius parameters from the unimolecular decay rate constant by varying the temperature of the black body field. However, there are complicating factors governing the decay rate. The first of these is kinetic shift, wherein the observed threshold energy (E_0) exceeds the true activation energy (E_a) [340]. Large molecules distribute their internal energy (E_{int}) over many modes, and the probability of sufficient energy collecting in the dissociating mode may be low until E_{int} far exceeds E_a. Secondly, dissociation must compete with emission. Molecules which can decay radiatively at internal energies around E_a are less likely to dissociate, which raises E_0 above E_a [336]. By the same token, inefficient absorbers react slowly [341]. Thirdly, the parent population is not constant over time. There may be an induction period during which a cold parent distribution thermalises with its surroundings, or during which a hot parent distribution loses its metastable species [342, 343]. Small molecules whose E_{int} exceeds E_a rapidly dissociate, leaving a 'truncated' rather than a thermal distribution [335]. Significant modelling is therefore needed to relate the threshold energy obtained to E_a. This is discussed in the next section.

BIRD was used to examine large biomolecules in 1996 by Evan Williams at Berkeley [343]. Such large species dissociate slowly but exchange energy with their surroundings extremely rapidly. The reacting population maintains a true Boltzmann distribution, as rapid absorption repopulates internal energy levels above E_0 when they are depleted by reaction. Williams termed this the 'rapid exchange limit', or REX limit [344, 345, 346]. Proof that the dissociation rate in the REX limit is not determined by the black-body absorption rate was obtained from dissociation of singly- and doubly-protonated bradykinin. These necessarily have almost identical absorption rates, but dissociate at very different rates. Fitting the rate constants according to

$$k = Ae^{-E_0/k_BT} \tag{5.1}$$

shows that the difference in dissociation rate arises from a difference in the Arrhenius pre-factor, A, rather than a large difference in E_a [343].

Arrhenius factors found by BIRD for unimolecular dissociation of molecules in the REX limit are equal to the Arrhenius factors for molecules in the high-pressure limit [345]. In both cases, rate is independent of pressure. The size of the A factor can be used to give information about the transition

state for unimolecular dissociation [347]. According to transition state theory,

$$A = \frac{k_B T}{h} e^{\Delta S^{\ddagger}/R} \tag{5.2}$$

so the larger A is, the 'looser' or more entropically favourable the transition state is deemed to be. For instance, in studying dissociation of protonated ubiquitin (U^{n+}), Williams noted that dissociation of U^{11+} forms two ions by simple cleavage of the peptide chain and has an A factor of 10^{17} s^{-1}. U^{5+} decays by loss of H_2O via a 6-member ring transition state, and has a much lower A factor of around 10^{12} s^{-1}. Interpretation of experimental A factor in terms of $\Delta S^{\ddagger}$ is impossible for small molecules as their rate of dissociation is determined by the 'up-pumping rate'; the rate at which the population is excited above E_0 by the black body field [344]. A factors obtained from equation (5.1) are much smaller than their high-pressure limiting values for small molecules [348].

Large or small, for a molecule to be studied by black body experiments it must satisfy certain criteria. It must dissociate at temperatures accessible to the heated or cooled FT-ICR cell, approximately 100 to 500 K. It must be sufficiently stable to survive injection into the cell and isolation. Its dissociation energy must therefore be of the order of 50-200 kJ mol^{-1} (roughly 0.5 to 2.0 eV) [297]. In an attempt to use BIRD to dissociate more stable species, and reduce the time taken to perform an experiment, sources of radiation equivalent to a hot black body have been sought [349]. 'Grey bodies' such as a tungsten filament positioned in the cell can generate very high temperatures and even visible photons, but the radiation is distributed unevenly throughout the cell, unlike a true black body field [350, 351, 352]. High temperature sources have often been used to study dissociation of short-lived species such as radicals, generated by electron impact. The electron-producing filament must be rapidly pulsed to avoid producing additional radiation in the cell [353, 354].

The use of a CO_2 laser as a black body source was re-examined in 1999, and the approach was found to be able to yield E_a, although not the Arrhenius prefactor [355]. The technique was named 'FRAGMENT'. CW IR-MPD, or FRAGMENT, replicates true BIRD results when a linear relationship is observed between the dissociation rate constant and the laser intensity. Even under these conditions, true BIRD results are reproduced only qualitatively by FRAGMENT [356, 357]. Nonetheless, the technique was used to sequence large DNA molecules by observing their fragmentation [358]. The theoretical model for FRAGMENT may be improved for species in the REX limit by including the Boltzmann distribution and a non-zero emission rate [359].

5.1.2 Master equation modelling

As has been mentioned, the rate of dissociation under BIRD conditions depends on molecular size [297]. Small molecules dissociate immediately above E_0. The rate of dissociation far exceeds the rate of absorption to energies above E_0, and the rate of emission from energy levels above E_0. Small molecules therefore have zero population in all energy levels above E_0. This has a knock-on effect on the energy levels which can absorb a single photon to exceed E_0. These levels are depleted by absorption, but not repopulated by emission from higher energy levels. Their population is consequently decreased [340]. Large molecules, by contrast, dissociate very slowly compared to their rates of absorption and emission. So although energy levels exceeding E_0 lose population due to dissociation, they are rapidly repopulated by absorption. The population retains a Boltzmann-like distribution which is shifted to slightly lower energy [346]. The populations are illustrated in figure 5.1.

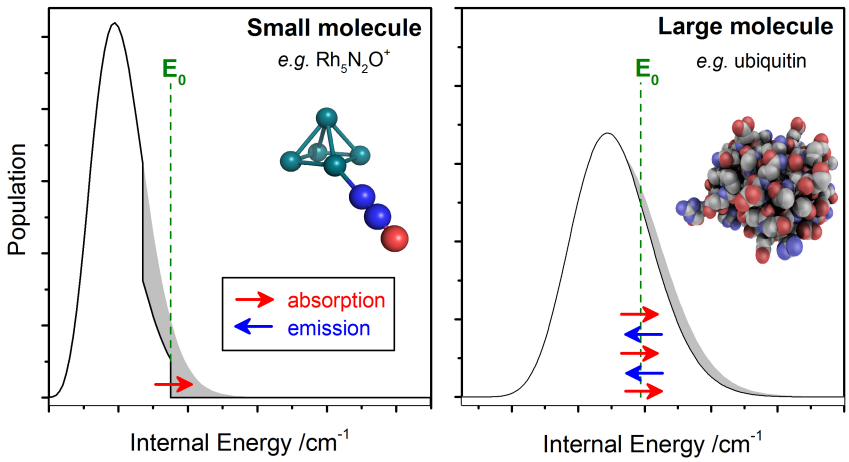

Figure 5.1: Size-dependent population distributions under BIRD conditions. The Boltzmann distributions for the same species in the absence of reaction are shown in grey. The small molecule's energy levels above the threshold (E_0) are depleted by reaction, but the large molecule has significant population above E_0 as these levels are rapidly repopulated by absorption. The image of ubiquitin, a common test molecule for BIRD, is reproduced from [360].

The rate of dissociation is determined in small molecules by the rate at which the population is pumped over the barrier by absorption [361]. E_0 and A values obtained from the dissociation rates of small molecules are therefore unrepresentative of the transition state. Large molecules' dissociation rates are independent of pumping rate and are determined solely by the ease with which molecules whose energy exceeds E_0 can form the transition state [297].

Hydrocarbons of less than 100 degrees of freedom are typically classified as 'small', while those with

more than 200 degrees of freedom are typically 'large' [297, 340]. However, $Rh_n(N_2O)_m^+$, being heavily decorated with chromophores, is unlikely to conform to this standard model. In fact, most species studied by BIRD do not necessarily fall into either extreme size limit. Some modelling of the kinetics under BIRD conditions is therefore desirable. The initial modelling method used by Dunbar was a random walk simulation. Absorption, emission and reaction are assigned an energy-dependent probability and an ensemble of particles sample the energy surface, each energy step being determined probabilistically until dissociation occurs [335]. Similar random walk simulations have been used in the interpretation of data from grey body experiments using a tungsten filament heat source [350].

The rigorous alternative to such Monte-Carlo simulations is master equation modelling [336, 338, 345, 350]. The master equation accounts for energy changes in the molecule using exact rates rather than probabilities [362]. To track the instantaneous changes in population, the energy of the system must be grained. An energy grain of 100 cm^{-1} is typical [97], but the systems studied here are small enough to allow a grain of 10 cm^{-1}. Energy graining discretizes the system into a number of energy levels, i. The aim of master equation modelling is to construct a transport matrix, **J**, whose off-diagonal elements J_{ij} describe the rate of population transfer from level j to level i [345]. In the absence of collision, these elements are dictated solely by absorption and emission of radiation. J_{ij} will be non-zero only if the molecule has a vibrational transition at the corresponding energy. Diagonal elements J_{ii} describe a population change in level i which does not create population in any other level: the rate constant for loss of population from level i by dissociation.

$$\mathbf{J} = \begin{pmatrix} k_{diss}(E_0) & k_{0\leftarrow 1} & \cdots & k_{0\leftarrow i} \\ k_{1\leftarrow 0} & k_{diss}(E_1) & \cdots & k_{1\leftarrow i} \\ \vdots & \vdots & \ddots & \vdots \\ k_{i\leftarrow 0} & k_{i\leftarrow 1} & \cdots & k_{diss}(E_i) \end{pmatrix} \tag{5.3}$$

Absorption and emission rates are dictated by the vibrational modes of the molecule. Absorption at energy $hc\tilde{\nu}$ (in wavenumber) is governed by the Einstein B coefficient:

$$B(\tilde{\nu}) = \frac{I(\tilde{\nu})}{N_A h\tilde{\nu}} \tag{5.4}$$

where $I(\tilde{\nu})$ is the integrated absorption coefficient for the transition, in m mol^{-1} [363]. $B(\tilde{\nu})$ also controls the rate of stimulated emission of $\tilde{\nu}$ photons, but stimulated emission is extremely slow at

normal black body energy densities and may be neglected [346]. Equation (5.4) does not directly give the elements of the transport matrix J_{ij}. The stimulated absorption coefficient must be multiplied by the energy density, $\rho(\tilde{\nu})$, of the black body field at energy $hc\tilde{\nu}$ [363]:

$$\rho(\tilde{\nu}) = \frac{8\pi hc\tilde{\nu}^3}{e^{hc\tilde{\nu}/k_BT} - 1}. \tag{5.5}$$

Finally, the variation in $I(\tilde{\nu})$ with vibrational quantum number in an anharmonic oscillator must be accounted for. The usual approximation is $I_n = I_0(n + 1)$ [338]. The $n + 1$ factor in the absorption rate constant must be weighted by the probability that vibrational mode $\tilde{\nu}$ contains n quanta in the absorbing molecule. The molecule's internal energy E_i is distributed over all vibrational modes. A large number of ways of creating E_i are possible, and mode $\tilde{\nu}$ will contain n quanta only in a small fraction of these distributions. The fraction of the distributions where mode $\tilde{\nu}$ is occupied n times, p_n, can be calculated using the Beyer-Swinehart algorithm [364]. The final expression for the absorption rate constant (and thus **J** elements J_{ij}) is therefore:

$$k_{abs}(\tilde{\nu}) = \frac{8\pi c\tilde{\nu}^2 I(\tilde{\nu})}{N_A(e^{hc\tilde{\nu}/k_BT} - 1)} \times p_n \times (n + 1). \tag{5.6}$$

Equation (5.6) must be summed over all possible n for each $i \leftarrow j$ transition.

While stimulated emission is neglected, spontaneous absorption is not. The Einstein coefficient for spontaneous emission is [363]:

$$A(\tilde{\nu}) = \frac{8\pi c\tilde{\nu}^2 I(\tilde{\nu})}{N_A} \tag{5.7}$$

which has no dependence on the surrounding black body field and so is not multiplied by $\rho(\tilde{\nu})$. However, the occupancy of level $\tilde{\nu}$ does affect the emission rate, and so must be included:

$$k_{emm}(\tilde{\nu}) = \frac{8\pi c\tilde{\nu}^2 I(\tilde{\nu})}{N_A} \times p_n \times n. \tag{5.8}$$

Spontaneous emission rates $k_{emm}(\tilde{\nu})$ are the non-zero off-diagonal elements J_{ji} of matrix **J**.

The dissociation rate constants are calculated using Rice-Ramsperger-Kassel-Marcus theory.

$$k_{diss}(E) = \frac{\sigma N^{\ddagger}(E - E_0)}{h\rho(E)}. \tag{5.9}$$

Equation (5.9) gives the energy-dependent RRKM dissociation rate constant, $k_{diss}(E)$. $N^{\ddagger}(E\text{-}E_0)$ is the

number of ways of distributing energies up to E-E_0 among the modes of the transition state. $\rho(E)$ is the density of states in the parent molecule at energy E. σ is the degeneracy of the path. Equation (5.9) calculates the purely statistical probability that a molecule with sufficient internal energy to surmount the barrier E_0 will distribute that energy among its vibrational modes such that the transition state is formed. $k_{diss}(E)$ are the elements J_{ii} of matrix **J**.

Once constructed from rate constants $k_{abs}(E)$, $k_{emm}(E)$ and $k_{diss}(E)$, a special property of **J** is exploited. *The least negative eigenvalue of* ***J*** *is the steady-state unimolecular decay rate constant for the system, and its corresponding eigenvector is the steady-state population*. This has been proven in reference [362], and the proof is given in Appendix A.

The problem therefore reduces to one of finding **J**'s eigenvalues and eigenvectors. In our case, **J** is constructed from equations (5.4) to (5.9) in a programme written in C. Transition energies and intensities are taken from the DFT calculations detailed later in this chapter. The eigenvalues of **J** are found using the standard Matlab routine. The least negative of these (λ_0) is entered back into the C programme, which calculates **J**-λ_0**I**, because

$$(\mathbf{J} - \lambda_0\mathbf{I})\mathbf{e_0} = 0, \tag{5.10}$$

I being the identity matrix. Equation (5.10) can be solved to find eigenvector $\mathbf{e_0}$. The method used involves interchanging rows and subtracting multiples of one row of the matrix from another until it is in 'upper diagonal form'. Starting at the bottom of the matrix, each row can then be substituted into the one above to find successive elements of eigenvector $\mathbf{e_0}$. Apart from the Matlab routine, all code used has been appended.

Finding the eigenvalues of **J** may be computationally costly and, in the small molecule limit, a different modelling approach is preferred [297, 340]. Dunbar described the truncated Boltzmann model for a small molecule with one active vibrational mode, $\tilde{\nu}$, [335] making use of Tolman's theorem:

$$E_a = \langle\text{energy of reacting molecules}\rangle - \langle\text{energy of all molecules}\rangle \tag{5.11}$$

which allows calculation of the activation energy without using any calculated transition intensities, which are often not well known [340]. Evaluation of equation (5.11) requires knowledge of the reactive population distribution, which Dunbar calculated used the following assumptions about $P_R(E)$, the probability that a molecule in the reactive distribution has energy E. The non-reactive (Boltzmann)

distribution is defined as $P_{NR}(E)$.

1. All molecules whose internal energy exceeds E_0 dissociate instantly, so $P_R(E>E_0) = 0$.

2. The energy region E_0-$hc\tilde{\nu} \rightarrow E_0$ is depleted as molecules in this region absorb one photon and dissociate. Loss via absorption is not counteracted by emission from higher levels. Therefore $P_R(E_0\text{-}hc\tilde{\nu} < E < E_0)$ is less than $P_{NR}(E_0\text{-}hc\tilde{\nu} < E < E_0)$.

3. At all energies below E_0-$hc\tilde{\nu}$, the reactive population distribution equals the non-reactive population distribution: $P_R(E < E_0\text{-}hc\tilde{\nu}) = P_{NR}(E < E_0\text{-}hc\tilde{\nu})$.

Reactive depletion in the region E_0-$hc\tilde{\nu} < E < E_0$ arises from the reduced rate of formation of these energy levels. An expression may be inferred for the population at E in this region:

$$\frac{P_R(E)}{P_{NR}(E)} = \frac{k_{abs}P_{NR}(E - hc\tilde{\nu})}{k_{abs}P_{NR}(E - hc\tilde{\nu}) + k_{emm}P_{NR}(E + hc\tilde{\nu})}, \tag{5.12}$$

wherein the reactive population distribution in the region E_0-$hc\tilde{\nu} \rightarrow E_0$ is formed only by absorption from lower levels (whose population is equal to their non-reactive population). The non-reacting population in this region is created by absorption from lower levels and emission from upper levels. The distribution is illustrated in figure 5.1 (a). Absorption and emission rate constants are fairly safely assumed to be independent of E. Using the fact that in the non-reacting Boltzmann distribution $k_{abs}P_{NR}(E - hc\tilde{\nu}) = k_{emm}P_{NR}(E)$, the right-hand side of equation (5.12) reduces to a calculable constant factor; the quantities in equation (5.11) may therefore be easily computed [335].

The model of equation (5.12) required modification for use in this thesis, as preliminary work showed reactive depletion in the region E_0-$2hc\tilde{\nu} \rightarrow E_0$-$hc\tilde{\nu}$ to be non-negligible. Additionally, $Rh_n(N_2O)_m^+$ have multiple modes $\tilde{\nu}_m$ absorbing and emitting radiation, which equation (5.12) cannot account for. Finally, transition intensities calculated by DFT (once their intensities are scaled) are deemed to be sufficiently close to their true values that the energy dependence of the absorption and emission rate constants was worth including [365]. Equation (5.12) therefore becomes:

$$\frac{P_R(E)}{P_{NR}(E)} = \frac{\sum_m k_{abs}(E - hc\tilde{\nu}_m)P_R(E - hc\tilde{\nu}_m) + \sum_m k_{emm}(E + hc\tilde{\nu}_m)P_R(E + hc\tilde{\nu}_m)}{\sum_m k_{abs}(E - hc\tilde{\nu}_m)P_{NR}(E - hc\tilde{\nu}_m) + \sum_m k_{emm}(E + hc\tilde{\nu}_m)P_{NR}(E + hc\tilde{\nu}_m)}, \tag{5.13}$$

from which $P_R(E)$, which is not known, cannot be easily removed. A simplifying assumption is made: *in each energy region, the reactive population distribution $P_R(E)$ is related to the non-reactive population distribution $P_{NR}(E)$ by a scalar constant c.* In assigning these energy regions, two more

simplifying assumptions are made. Firstly, only the NO stretches are included, as all other modes are essentially IR-inactive at 300 K (this will be discussed later; see figure 5.3). Secondly, where multiple N_2O molecules are adsorbed, the NO stretches are of similar energy so are defined by a single energy region, whose lower boundaries are determined by the largest mode, $\tilde{\nu}_l$. The following substitutions are made:

$E < (E_0\text{-}2hc\tilde{\nu}_l)$	$P_R(E) = P_{NR}(E)$	$c_0 = 1$
$(E_0\text{-}2hc\tilde{\nu}_l) < E < (E_0\text{-}hc\tilde{\nu}_l)$	$P_R(E) = c_1 P_{NR}(E)$	c_1 unknown
$(E_0\text{-}hc\tilde{\nu}_l) < E < E_0$	$P_R(E) = c_2 P_{NR}(E)$	c_2 unknown
$E > E_0$	$P_R(E) = 0$	$c_3 = 0$

All the populations in equation (5.13) are thereby expressed in terms of the non-reacting population. $P_{NR}(E)$ is simply a Boltzmann distribution, calculable using the Beyer-Swinehart algorithm [364]. The energy-dependent absorption and emission rates are obtained from equations (5.6) and (5.8). The only unknowns in equation (5.13) are the constants c_1 and c_2. A programme has been written, in C, to substitute numerical values into equation (5.13) at each energy and to solve the resulting simultaneous equations for c_1 and c_2. This programme is appended for the use of future researchers. The programme then applies the coefficients to the non-reacting Boltzmann distribution, creating a steady-state truncated Boltzmann distribution. The steady state unimolecular dissociation rate constant, k_{diss}, is obtained from this reactive distribution by calculating the rate of absorption across the barrier, E_0:

$$k_{diss} = \int_{E_0 - hc\tilde{\nu}_l}^{\infty} k_{abs}(E) P_R(E). \tag{5.14}$$

5.1.3 Applications

Use of BIRD to determine the Arrhenius prefactor and hence to deduce the transition state of a large molecule's unimolecular dissociation has been mentioned [343, 347]. BIRD has also been used to deduce the structure of biomolecules before dissociation. For example, the large A factor (indicating minimal rearrangement) observed upon elimination of NH_3 from bradykinin was used to infer a pre-existing salt-bridge structure between the -COOH and -NH_2 groups at either end of the peptide [344]. Determination of E_0 for dimers of amino acids shows that the arginine dimer's E_0 is unusually large. This is evidence of its zwitterionic structure in the gas phase [366]. A very different approach to obtaining structural information from BIRD has been reported for the dissociation of a protein-oligosaccharide complex. Successive functional groups are replaced to prevent their participation in H-bonding, and the effect on the black body dissociation energy is noted. The sensitivity of BIRD

to small differences in E_0 makes it preferable to CID for this purpose [367]. Significant reductions in E_0 identify groups which are cross-linked in the structure. [368] Similarly, E_0 and A values for loss of successive solvent molecules from a gas-phase protein can be used to map the protein's unfolding and hence its gas-phase solvated structure [369]. This identifies differences between gas- and solution-phase structures of proteins [370].

Fragmentation of peptides by BIRD can be used to obtain sequence information. This has proved useful in analysis of DNA because the gentle approach 'boils off' adducts such as H_2O without entirely destroying the parent molecule [292]. Other large proteins have been sequenced using BIRD, the technique being advantageous as it allows fine control of energy deposition and therefore 'tunability' of the extent of backbone cleavage [371]. Black body induced fragmentation of biomolecules has yielded some particularly interesting results. The first BIRD study of a multi-protein complex yielded a record-breaking Arrhenius prefactor: 10^{39} s^{-1} [372]. Such large A factors allow observation of processes with very high thresholds. The origin of these enormous A factors is disputed. They may result from the release of restricted internal rotations [368], or the softening of numerous vibrational modes once the rigid complex is broken up [370]. There is no conclusive evidence either way.

BIRD can be used to determine bond strengths in a wide variety of systems. The strength of the non-covalent interactions maintained during the electrospray process [373], and relative bond strengths of the neurotransmitter protein leucine encephalin to M^+ (H <Li <Na <K <Rb), have been found by BIRD [374]. In turn, bond strengths have been used to determine gas-phase basicity [365, 375, 376], and the extraordinarily large dissociation energies of paired nucleobases suggest that Watson-Crick base pairing is retained in the gas phase [365, 377]. Trends in the binding energies of successive water molecules to divalent metal ions are indicative of their coordination shell size [96, 97, 98]. The bonds in partially-solvated Ru(II) complex ions, which are of great interest in catalysis, have also been investigated by BIRD [378, 379].

The use of BIRD to examine ion-doped water clusters, $M^{+/-}(H_2O)_n$, is somewhat different to the unimolecular fragmentation of biomolecules [297, 380]. $M^{+/-}(H_2O)_n$ can cool evaporatively as they absorb radiation, leading to a steady decrease in the cluster size during storage time [380]. The end-points of these decays have been used to infer the size of coordination shells about Al^{n+} [381]. Certain sizes of water cluster undergo black body induced dissociation particularly slowly. These are so-called 'magic number' clusters, and their stability is attributed to formation of strongly-bound clathrate structures [382, 383].

Depending on the nature of $M^{+/-}$, the water clusters may also exhibit reactivity, which has been used to examine solution-phase chemistry on a very small scale [384]. The preference for $H^+(HCl)(H_2O)_n$ to evaporate HCl rather than H_2O at certain values of n allows determination of the number of water molecules needed to solvate H^+ and Cl^-, and hence the structure of the solvated species [385]. The behaviour of Mg^+ in these 'nanosolutions' is even more complex. $Mg^+(H_2O)_{n>20}$ evaporates H_2O upon black body irradiation until n=20, at which point hydrogen atoms are also eliminated. This shows that at least 20 H_2O are needed to solvate Mg^{2+} and an electron. When n <20, insufficient solvation energy is released to compensate for the ionisation of Mg^+ and so the ion reacts with a water molecule instead, producing $MgOH(H_2O)_{n'}{}^+$ [386]. Vanadium reacts similarly [387]. Another interesting example of chemistry in these nanosolutions is the determination of solubility. Under BIRD conditions, $Na^+(HCl)(H_2O)_n$ retains 12 water molecules but $Ag^+(HCl)(H_2O)_n$ retains only 4. AgCl precipitates out of 'solution' and so only sufficient H_2O to solvate H^+ are required in the Ag^+ case [388, 389].

An unusual application of BIRD has been the attempt to determine the efficiency of collisional energy transfer. Using E_0 from BIRD experiments, the additional energy transferred to an ion distribution by collision at varying kinetic energies was calculated. The uncertainty in the calculated energy transfer is large as multiple collisions occur and low-energy collisions are not detected. An initial figure of 9.6% E_{CoM} transfer between 4 and 6 eV collision energy was obtained [390]. A later attempt, which sought to rectify some of the previous uncertainties, settled on an efficiency factor of 4±1.7% [323].

5.1.4 Errors

The major source of error is uncertainty in the temperature of the black body field [347]. This is not only due to small temperature fluctuations during the experiment. During cooled-cell experiments, room-temperature radiation may leak into the cell through its orifices and alter the black body field created by the cell's cooling mechanism [361]. Temperature uncertainty also arises because the thermocouples used to measure temperature are placed around the cell, but its internal temperature may differ. Thermocouples inside the cell must be removed during an experiment to avoid disrupting ion orbits [391]. Calibration of the measured temperature to the true cell temperature must be performed, which itself carries some uncertainty [372, 391]. Typical uncertainties are therefore up to ±10 K [392]. In addition to uncertainty in the cell temperature, the ions' initial internal energy distribution is unknown. An induction period is often used in fitting BIRD data to account for any initial thermalisation required [356]. The effect of these errors on k_{diss} is very difficult to quantify.

Other sources of error include loss of ions from the cell at long storage times [346, 347], residual collisional energy transfer [338] and variation in detection efficiency [343]. Detection efficiency is dependent on the ions' charge, which does not affect the experiments described herein but is a concern for BIRD studies of biomolecules, which dissociate to give products carrying different charges.

Fitting A and E_0 parameters to BIRD data can involve significant uncertainty because A and E_0 are not independent [347]. However, such errors may be reduced by comparison with other experiments and computational modelling of the system. Extraction of the A parameter from BIRD data has some inherent error as it is assumed to be temperature-independent. In fact, $\Delta S^{\ddagger}$, the determining factor in A, does depend on temperature, and neglecting this dependence introduces uncertainty [393]. Computational models introduce their own uncertainty into calculated parameters; transition intensities are particularly poorly addressed by calculation [356, 378]. The size of the fitting error varies greatly between data sets.

5.2 Relevant Previous Work

The $Rh_n^+ + N_2O$ system has been the subject of numerous studies to date [16, 21, 310, 313, 314]. However, re-considering $Rh_nN_2O^+$ under BIRD conditions is worthwhile, for reasons illustrated in figure 5.2. Previous excitation methods used include collision, CO chemisorption and multiple IR photon absorption. These methods are likely to raise the cluster's internal energy far above both calculated reaction barriers. The relative activation entropy of each process becomes important in determining their branching ratio at such high internal energies. Excitation under BIRD conditions is very much slower. If absorption does not result in rapid dissociation, spontaneous emission is likely to occur before a second absorption. Only the NO stretch absorbs (see figure 5.3), so BIRD very specifically probes the region within 1300 cm^{-1} of the lowest barrier of $Rh_nN_2O^+$. As is shown in figure 5.2, this energy region is the high-energy tail of the $Rh_6N_2O^+$ population distribution. Figure 5.2 emphasises that, for small molecules, BIRD dissociation is limited by the rate of absorption across the barrier; entropy plays no part. The BIRD rate is therefore extremely sensitive to barrier height.

Prior determination of the vibrational spectra of $Rh_nN_2O^+$, both theoretically and experimentally, has been extremely useful to this work [310]. The calculated vibrational spectrum of $Rh_5N_2O^+$ is shown in figure 5.3, along with the experimentally-observed positions of the NO and NN stretches. Also marked is the black body field at 300 K. These spectra confirm that $Rh_nN_2O^+$ is a suitable candidate for BIRD: the NO stretch is intense and lies in a spectral region of significant black body energy

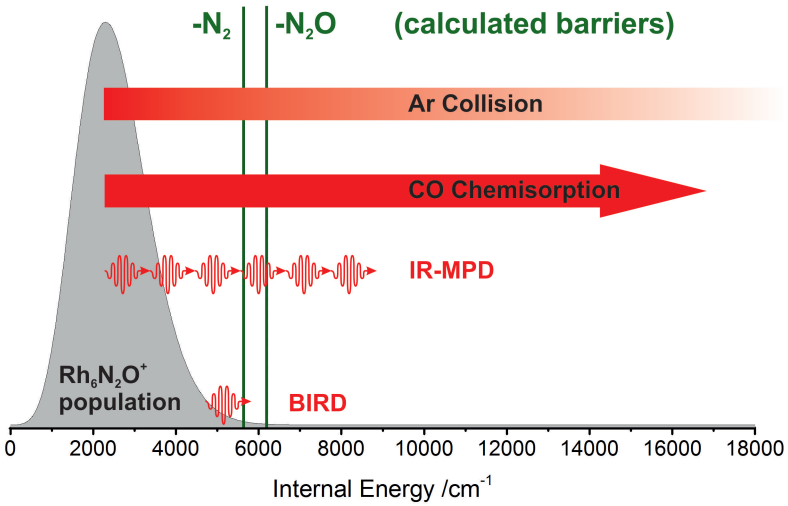

Figure 5.2: Comparison of excitation methods. All features are to scale: the internal energy distribution of $Rh_6N_2O^+$ at 300 K, calculated reaction barriers, photon energy, and energy change upon excitation. Most methods excite the cluster far above both barriers. BIRD probes only the high-energy tail of the distribution and is exceedingly sensitive to barrier height.

density. The 300 K black body field will therefore be able to excite the cluster at an appreciable rate. This is important as extremely long storage times lead to errors due to ion loss [347, 346]. Additionally, figure 5.3 shows that the Rh-Rh modes and N_2O bends of $Rh_nN_2O^+$ have minimal intensity, while the NN stretch lies in a region of low black body intensity at 300 K. Their absorption may therefore be neglected when modelling the data, which considerably simplifies our analysis.

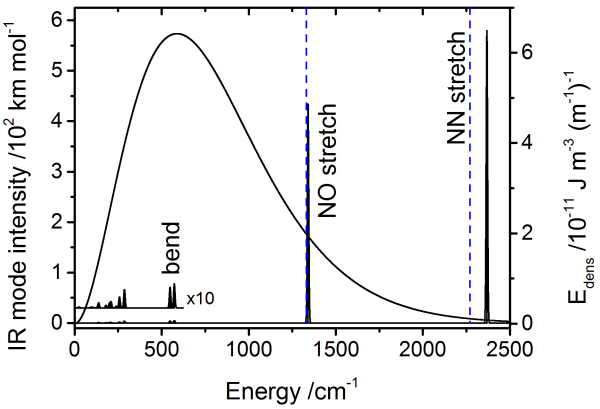

Figure 5.3: Overlap of the vibrational spectrum of $Rh_5N_2O^+$ with the black body field at 300 K. The calculated vibrational spectrum is plotted, and the position of bands identified by IR-MPD is shown by dotted lines. Only the NO stretch overlaps with an intense region of the black body field.

5.3 $Rh_nN_2O^+$ BIRD

5.3.1 Experiments at 300 K

The results of storing $Rh_nN_2O^+$ (n=4-6) in a 300 K black body field for a few seconds are shown on the left-hand side of figure 5.4. The decay pathways observed are the same as those seen previously: N_2O reduction (5.15) and desorption (5.16).

$$Rh_nN_2O^+ \rightarrow Rh_nO^+ + N_2 \tag{5.15}$$

$$Rh_nN_2O^+ \rightarrow Rh_n^+ + N_2O \tag{5.16}$$

The decay of the parent cluster to Rh_nO^+/Rh_n^+ are fitted using both one isomer (dot-dashed lines) and two isomers (solid lines) of parent ion. Although the latter gives a slightly better fit, the improvement is minimal and one isomer is deemed to be sufficient. The single isomer fits account for all data from 0 to 8-10 s without the need to include an induction period. This indicates that the parent cluster distributions are thermalised to 300 K (with the parent distribution truncated at E_0) at t=0, consistent with previous studies on mass-selected ions using this instrument [394].

The rates from these fits are shown in table 5.1. The collision frequency for Rh_n^+ at the cell's base pressure (around $7x10^{-10}$ mbar) is 0.01 s^{-1}. This translates to one collision approximately every 95 s, compared to the clusters' storage time of 8-10 s. The rates in table 5.1 far exceed collision rate and the method of activation is safely attributable to infrared absorption rather than collision [381].

$Rh_nN_2O^+$ decay rates at 300 K (s^{-1})			
	$Rh_4N_2O^+$	$Rh_5N_2O^+$	$Rh_6N_2O^+$
Reduction (N_2 loss)	0.041	0.040	0.149
Desorption (N_2O loss)	0.024	0.027	0.00

Table 5.1: BIRD rates at 300 K for $Rh_nN_2O^+$, n=4-6. Reduction of N_2O is the fastest process in all cases, releasing N_2. Collisions are unlikely to occur on the timescale of the experiment.

The data in table 5.1 and figure 5.4 are surprising when considered in the light of previous results. According to previous studies of $Rh_nN_2O^+$, n=5 is the 'odd one out' of the series, having an unusually low rate of N_2O reduction [21, 310]. In previous studies, the major product of $Rh_5N_2O^+$ after excitation has been the desorption product, Rh_5^+ [264, 310]. The present BIRD data shows N_2O

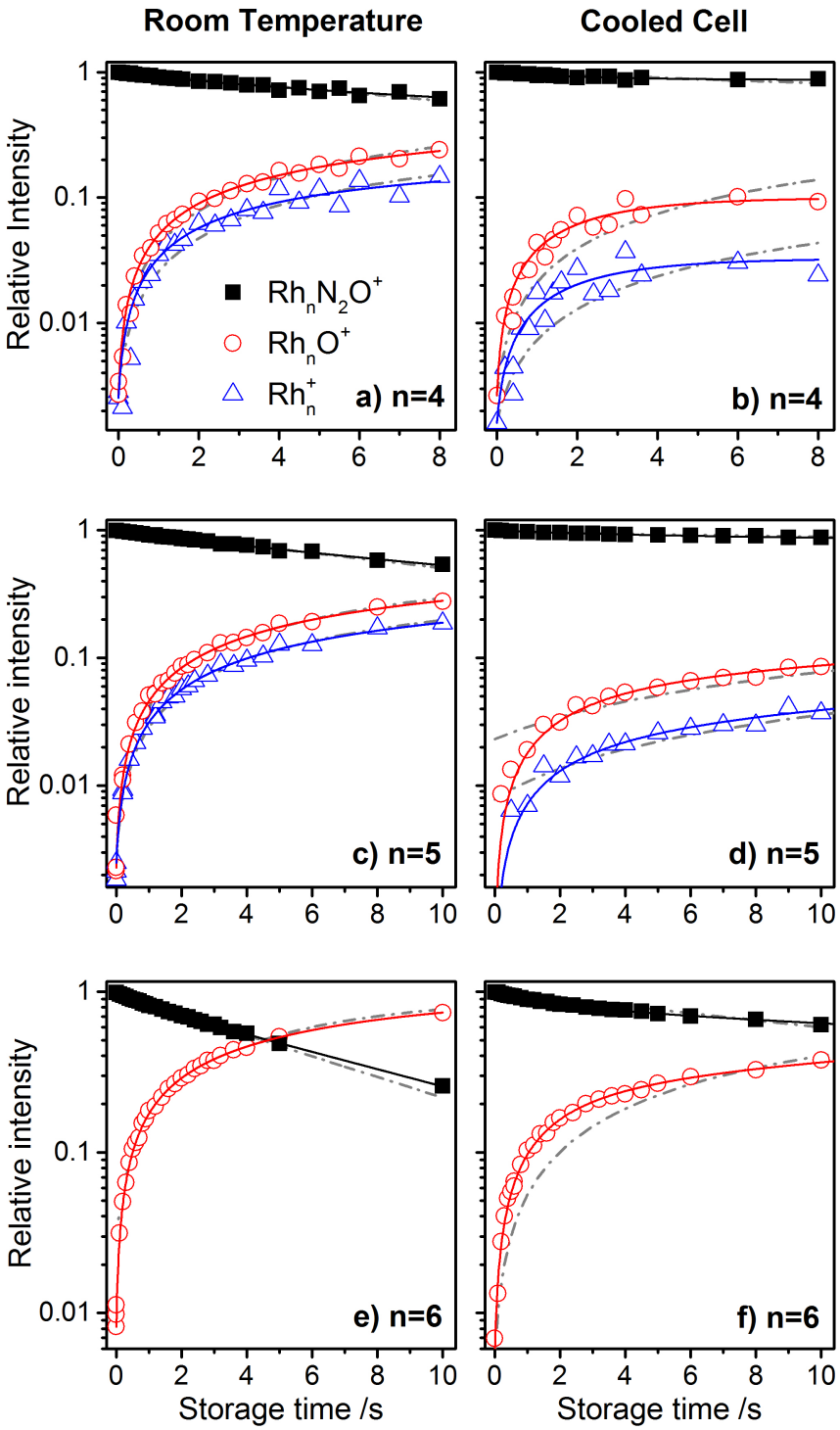

Figure 5.4: Black body infrared radiative dissociation of $Rh_nN_2O^+$ at two temperatures. (a), (c) and (e) were recorded at room temperature which varied from 295 to 298 K, and (b), (d) and (f) were recorded in a cooled cell at approximately 100 K. N_2O decomposition is the fastest decay route in all cases. Two isomer fits in solid lines, one isomer fits in dot-dashed lines. Two isomers are necessary for the low-temperature data, indicating an induction period during which hot ions dissociate rapidly.

reduction to be the dominant channel *for all values of n*. The 'odd one out' is rather the n=6 cluster, which shows an unusually large rate of N_2O reduction and no evidence of N_2O desorption.

The present data is not incompatible with previous results, but does necessitate some re-interpretation. It suggests that the N_2O reduction barrier is lower than the desorption barrier for all $Rh_nN_2O^+$ studied. The over-representation of desorption in previous experiments is an entropic effect. The desorption transition state is extremely easy to form, so corresponds to a very large Arrhenius prefactor. As a cluster's internal energy increases, the exponential term in equation (5.1) approaches 1 and so the rate constant is increasingly determined by the *A* factor alone. Previous excitation methods were capable of raising the clusters' internal energy far above both barriers, tipping the branching ratio towards desorption (which has the large A factor) in all cases. $Rh_5N_2O^+$, BIRD results show, has an N_2O reduction barrier only slightly lower than that for desorption. The bare Rh_5^+ cluster became the dominant product upon sufficient excitation. $Rh_6N_2O^+$ has a reaction barrier which is significantly lower than the desorption barrier, and the vibrational excitation achieved by previous experiments was not sufficient to make Rh_6^+ the dominant decay product.

5.3.2 Experiments at 100 K

Also shown in figure 5.4 are the results of storing $Rh_nN_2O^+$ in the cooled ICR cell at approximately 100 K. The cell's measured base pressure remained the same. It is immediately evident that the rate of decay decreases with the drop in temperature. It is possible to find the parent ion's dissociation rate, k_{diss}, at a number of temperatures and thus to extract the ion's Arrhenius parameters *A* and E_0. Unfortunately, with the limited time available to us in Kiel, the experiment could be performed at only two temperatures. The low-temperature experiments do provide useful qualitative information: they prove that the activating mechanism is infrared absorption as the rate decreases with temperature.

In fact, it is something of a surprise to see any decay at all at 100 K. Figure 5.5 shows that the maximum of the black body field at 100 K is shifted so far away from the bright modes of $Rh_nN_2O^+$ that they barely absorb at all. Black body activation is effectively 'switched off'. Another excitation mechanism must occur at 100 K; the literature suggests a number of possibilities. At low temperature, radiation leakage into the cell from the room-temperature field surrounding it may induce dissociation [361]. Alternatively, the ions' trapping motion can cause collisions with the residual gas in the ICR cell which have non-negligible energies. Collisional excitation will become noticeable in the absence of a faster black body activation mechanism.

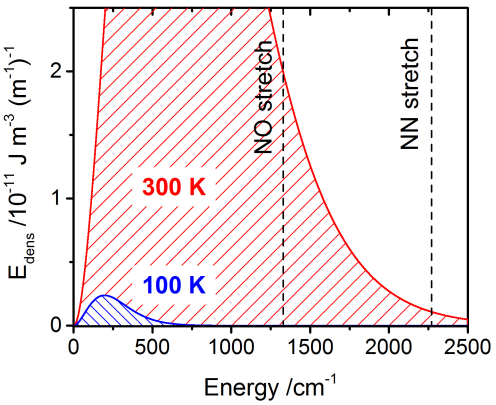

Figure 5.5: Overlap of the black body field with the experimentally-observed vibrational modes of $Rh_5N_2O^+$ at 300 K and 100 K. At 100 K, the black-body field does not overlap with either bright mode and black body activation is effectively switched off.

The activation mechanism at 100 K may, in part, be explained by considering the fitted rate constants. They are shown in table 5.2. A single parent isomer provides a very unsatisfactory fit in these cases. The characteristics of the two isomers for all $Rh_nN_2O^+$ are remarkably similar: roughly 10% of the parent ion reacts extremely quickly, while the remaining 90% of the parent ion distribution reacts extremely slowly. Isomer A decays more rapidly than the rate of black body decay at 300 K (table 5.1). This pattern of behaviour being common to all $Rh_nN_2O^+$ implies that it does not arise from geometric or electronic isomerism. Instead, the fitting of two isomers is a way of accounting for an induction period during which a metastable fraction of the parent isomer decays rapidly, leaving the thermalised majority to decay much more slowly. The small metastable fraction is masked by the more rapid decay of the majority at 300 K. The effect of lowering the temperature of the black body field is therefore to increase the lifetime of $Rh_nN_2O^+$ in the cell from 15.5, 14.8 and 6.7 s to >200,

$Rh_nN_2O^+$ decay rates at 100 K (s^{-1})						
	$Rh_4N_2O^+$		$Rh_5N_2O^+$		$Rh_6N_2O^+$	
	A	B	A	B	A	B
%	13	87	7	93	19	81
Reduction (N_2 loss)	0.348	0.000	0.232	0.004	0.480	0.023
Desorption (N_2O loss)	0.111	0.000	0.082	0.002	0.000	0.000

Table 5.2: BIRD rates at 100 K for $Rh_nN_2O^+$, n=4-6. Two isomers are needed to fit the data satisfactorily. In all cases, the minor isomer is a small fraction of the parent and reacts much faster than BIRD permits, and is probably internally excited. Collisions are likely on the timescale of the experiment.

154 and 43 s respectively for n=4-6. The 100 K lifetimes are limited by collision and absorption of leaked-in 300 K radiation.

5.3.3 Barriers to reaction

While no quantitative value may be set on E_0 with data available at two temperatures, some limits on the relative energy thresholds may be established. In a small molecule, the population is depleted immediately above the lowest energy barrier, $E_0{}^1$. Where there are two or more available product channels, the process or processes with higher barriers will only be observed if they are surmountable by one-photon absorption from the population remaining below $E_0{}^1$. When the molecule absorbs at only one wavelength, as in $Rh_nN_2O^+$, only processes with barriers exceeding $E_0{}^1$ by less than that photon energy will be observed. This principle is illustrated in figure 5.6.

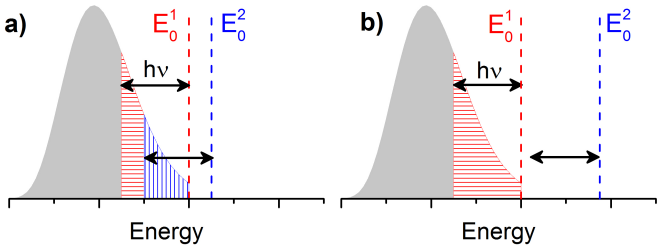

Figure 5.6: The effect of relative barrier heights on BIRD rates in small molecules. Case (a), where the two barriers are separated by less than one absorbed photon's energy ($hc\tilde{\nu}$), allows both products to be observed. In case (b), one barrier exceeds the other by more than 1 $hc\tilde{\nu}$ and no population is available to be excited into the upper reaction channel.

Figure 5.6 illustrates that the branching ratio observed depends strongly on the population which can attain each barrier upon absorption of a photon. Barriers to N_2O reduction and desorption in $Rh_4N_2O^+$ and $Rh_5N_2O^+$ must therefore be almost identical. Both processes are observed at very similar rates in these clusters, so they must have similar populations available to them. Given that the population falls away rapidly at the high-energy tail of the $Rh_nN_2O^+$ distribution, the difference between $E_0{}^1$ and $E_0{}^2$ can be no more than a hundred wavenumbers or so. This is consistent with calculations performed on the $Rh_5N_2O^+$ system, which suggested $E_0{}^1$ and $E_0{}^2$ to be very similar. [314] However, calculations on $Rh_6N_2O^+$ also predicted a fairly small energetic preference for N_2O reduction. [310] The fact that BIRD experiments show no desorption at all indicates that the difference in barriers must be rather more marked than this; modelling suggests closer to 1000 cm^{-1} than 100 cm^{-1}.

5.3.4 Effect of additional O atoms

Previously, addition of an oxygen atom to the $Rh_5N_2O^+$ cluster has inverted the N_2O reduction and desorption rates, making desorption the slower process [264, 310]. No such reversal will be seen in BIRD as reduction is already preferred on $Rh_5N_2O^+$. However, the branching ratio of $Rh_5ON_2O^+$ might be expected to tip further in favour of reduction. This is indeed the case; the reduction product $Rh_5O_2^+$ is observed, but the desorption product Rh_5O^+ is not seen even after 40 seconds.

5.4 $Rh_n(N_2O)_m^+$ BIRD

In a further test of the black body mechanism, the number of absorbing species on $Rh_nN_2O^+$ was varied. Increasing the number of absorbing molecules in a cluster increases the rate of absorption and hence of black body induced dissociation. This has been observed for water clusters, ammonia clusters and even $SF_5^+(SF_6)_n$ clusters [394, 395, 396]. An approximately linear relationship is observed between the number of absorbers and the rate of dissociation. Observation of a similar relationship in the case of $Rh_n(N_2O)_m^+$ would provide confirmatory evidence that black body absorption causes dissociation of these clusters, rather than collision or the decay of metastable species.

5.4.1 Calculation of structures and spectra

The variation in absorption rate with the number of adsorbed N_2O on $Rh_n(N_2O)_m^+$ may be predicted from their calculated structures. Infrared spectra are extracted from the global minima. All calculations were performed at the DFT level of theory with the TPSSh functional and the def2-TZVP basis set. These conditions have previously been found to perform well for rhodium clusters [264, 310].

The starting points for all of these calculations were the $Rh_nN_2O^+$ structures found previously by the Mackenzie group [310]. In extending these calculations to $Rh_n(N_2O)_m^+$, both electronic and geometric variables were taken into account. A wide range of spin states was considered for each cluster [6, 35]. Additionally, although $Rh_nN_2O^+$ binds N_2O via its terminal N atom to a single rhodium atom, other binding modes were considered. $Rh_5(N_2O)_2^+$ was used as a test molecule to examine the possibility that multiple N_2O species on the cluster surface stabilise other binding modes. All combinations of N-bound, O-bound, NN-bound, NO-bound and terminal-NO bound structures in atop (μ^1), bridging (μ^2) and hollow (μ^3) sites were tested. Without exception, the terminal N atom bound to an atop site was found to be the lowest-energy structure. For all other $Rh_n(N_2O)_m^+$, therefore, only N-atop structures were considered. The results are shown in table 5.3.

Calculated global minimum structures of $Rh_n(N_2O)_m^+$				
m	n=4	n=5	2S+1	
			(n=4)	(n=5)
1	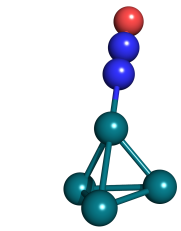	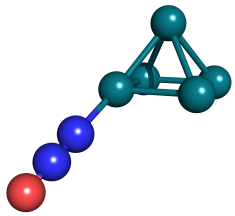	8	9
2	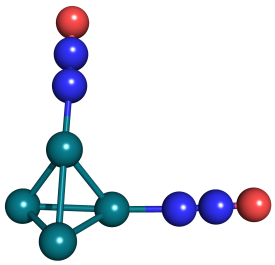	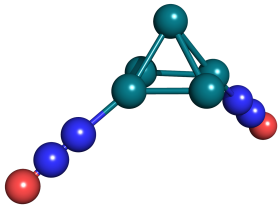	8	9
3	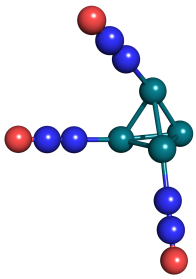	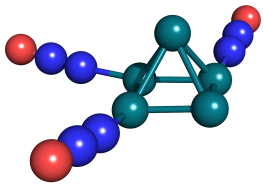	2	5
4	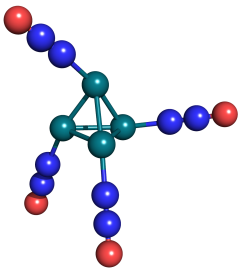	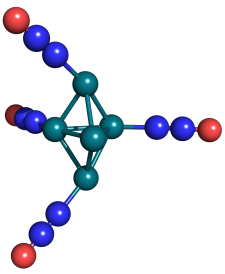	2	3
5	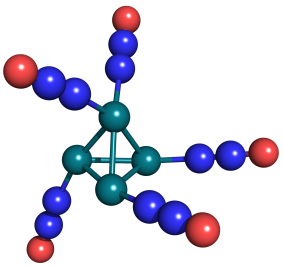	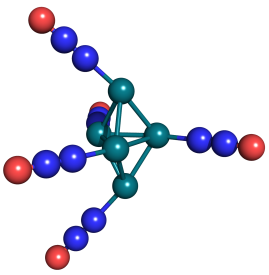	2	3

Table 5.3: Calculated structures of $Rh_n(N_2O)_m^+$, and their spin states. Only the global minima are shown. All N_2O are atop-bound.

It may be seen from table 5.3 that multiple adsorbed N_2O do affect the cluster's geometry and spin state. Electron pairing increases greatly with the number of attached N_2O. $Rh_5N_2O^+$ has 8 unpaired electrons, while $Rh_5(N_2O)_5^+$ has only 2. The same is true of the n=4 cluster: $Rh_4N_2O^+$ has 7 unpaired electrons while $Rh_4(N_2O)_5^+$ has only 1. The same effect has been observed with oxygen atoms adsorbed on rhodium clusters, and perhaps indicates that unpaired electrons become involved in bonding [397]. Geometric effects are limited to the n=5 cluster. $Rh_5(N_2O)_m^+$ has two low-lying geometric isomers of the metal skeleton: a square-based pyramid and a trigonal bipyramid. While m≤3, the former is preferred, but at m=4/5 the balance appears to be slightly tipped in favour of the latter structure. $Rh_4(N_2O)_m^+$ has only one low-lying isomer of the metal skeleton: the tetrahedron. Its shape is affected very little by the adsorbed species. Similarly, although the number of N_2O ligands affects the preference of Rh_5^+ to form a trigonal bipyramid, the metal skeletons themselves are affected very little.

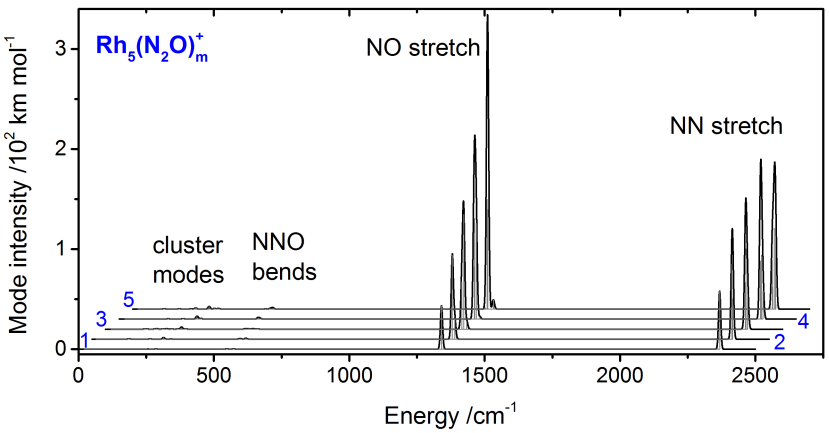

Figure 5.7: Calculated vibrational spectra of the global minima of $Rh_5(N_2O)_m^+$, m=1-5. Each successive spectrum is offset by 50 cm^{-1}. The stick spectrum is shown in grey and its convolution with Gaussian functions is shown in black. The spectra all look remarkably alike; there is no significant shift in their frequencies and no cooperative modes appear. The NO and NN stretches are shown in more detail in figure 5.8.

The minimal effect of adsorbed N_2O on the Rh_n^+ skeleton, and vice versa, is visible in the calculated vibrational spectra. The calculated stick spectra, and their convolution with Gaussian broadening functions, are shown for $Rh_5(N_2O)_m^+$ in figure 5.7. Each spectrum is offset for clarity, but the energies of the NO and NN stretches barely change at all, and remain quite similar to their energies in free N_2O. Each adsorbed N_2O does not appear to interfere with the others, as there are no low-frequency cooperative vibrational modes. The metal-metal modes are the only ones to be affected by varying

the number of N_2O ligands, but they are so weakly-absorbing that their differences have a negligible effect on the rate of IR absorption. The $Rh_4(N_2O)_m^+$ spectra are not shown as they look virtually identical to those of $Rh_5(N_2O)_m^+$.

It may appear at first glance that figure 5.7 shows some intensity-stealing from the NN stretch by the NO stretch in $Rh_5(N_2O)_m^+$. Closer inspection of these modes shows that this is not the case. When viewed on a larger scale (shown in figure 5.8), it appears that the contributing stick spectra are simply closer together in the NO stretching region. They therefore create a narrow, tall peak while the NN stretch is broad and low. Their integrated intensity follows the pattern seen in the m=1-4 spectra.

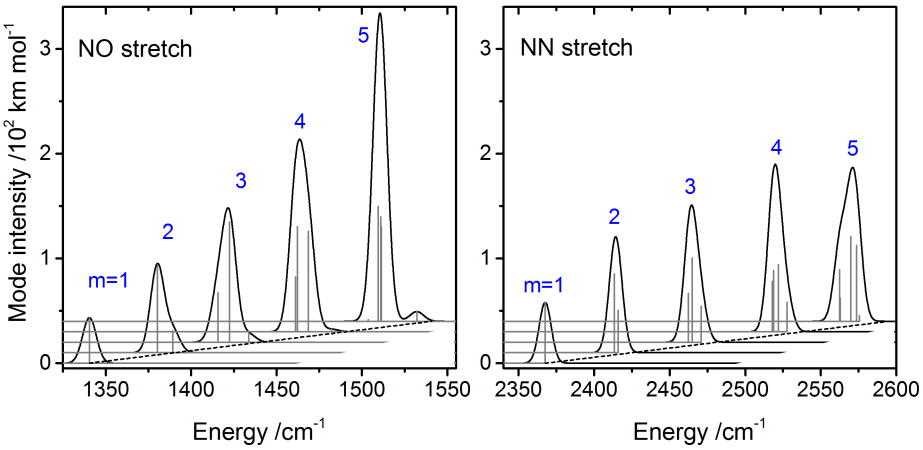

Figure 5.8: Detail of figure 5.7 showing the NO and NN stretches. The modes of each N_2O are not linearly added but lend intensity to one another. The peaks' total intensities vary approximately linearly with m. The dotted lines indicate the positions of the $Rh_5N_2O^+$ NN and NO stretches; at larger m, a very slight red shift from these values is observed.

The variation in intensity of the NO and NN stretches in $Rh_n(N_2O)_m^+$ is not perfectly linear. Figures 5.7 and 5.8 show that the NO and NN stretches of each individual adsorbate are very slightly affected by the presence of other N_2O. While the energy of each NN and NO stretch in $Rh_n(N_2O)_m^+$ cluster is virtually unaffected by m, the intensity of these modes is. Figure 5.8 in particular emphasises that many of these transitions borrow intensity from their neighbours, so that although m individual transitions are present in each band, not all of them are intense. For instance, the NO stretch of $Rh_5(N_2O)_5^+$ has a faint shoulder at high energy.

Black body absorption rates are found by convoluting each vibrational spectrum with the black body field at 300 K. The absorption rates of $Rh_n(N_2O)_m^+$ are shown in figure 5.9. Despite variation in the intensity of individual modes, *the rate of absorption varies almost linearly with m*. Figure 5.9

separates out the rate of absorption via the NO stretches alone, and shows that it accounts for nearly all of the total. The dominance of absorption via the NO stretch has been mentioned previously in this chapter, but is quantified here for the first time. Also shown in figure 5.9 are the absorption rates of other low-lying isomers of $Rh_5(N_2O)_m^+$. In many cases, the global minimum lies only slightly below other geometric isomers in energy, and the global isomer cannot therefore be identified with certainty within the accuracy of DFT calculations. The isomers marked in figure 5.9 are those lying less than 1500 cm^{-1} above the global minimum. No such low-lying structures are identified for $Rh_4(N_2O)_5^+$. It is interesting to note that, although the trend is approximately linear, the trend in the rate of absorption may be presented as somewhat non-linear by choosing appropriate isomers from figure 5.9.

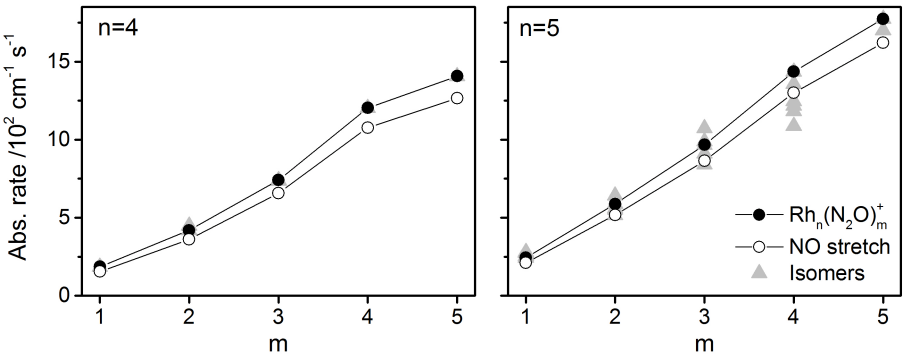

Figure 5.9: Rate of absorption of energy (in cm^{-1} s^{-1}) of $Rh_n(N_2O)_m^+$. Filled circles show the absorption rate of the global minimum structure, and empty circles show the energy absorbed by its NO stretch alone. Grey triangles show the absorption rate of other low-lying isomers. All rates are calculated at 300 K.

Calculated desorption energy of N_2O from $Rh_n(N_2O)_m^+$ /eV		
m	$Rh_4(N_2O)_m^+$	$Rh_5(N_2O)_m^+$
1	0.76	0.71
2	0.69	0.69
3	0.69	0.65
4	0.74	0.82
5	0.68	0.80

Table 5.4: tab: Calculated desorption energy of N_2O from $Rh_n(N_2O)_m^+$. All DFT calculations use the TPSSh functional and def2-TZVP basis set.

Successive desorption energies, E_{des} of N_2O from $Rh_n(N_2O)_m^+$ may be calculated using:

$$E_{des}(Rh_n(N_2O)_m)^+) = E(Rh_n(N_2O)_{m-1}^+) + E(N_2O) - (Rh_n(N_2O)_m^+). \quad (5.17)$$

This calculation does not allow for relaxation of the $Rh_n(N_2O)_{m-1}^+$ product as desorption is facile and expected to be rapid. E_{des} energies are shown in table 5.4; they do not vary significantly with m. This is consistent with the fact that adsorbed N_2O do not appear to affect each other's electronic structure. Nonetheless, there is some variation in the desorption energy E_{des} with m, and the same pattern is observed on both n=4 and n=5. E_{des} decreases from m=1 to m=3, the latter being a minimum, before rising to a maximum at m=4. Both absorption rate and reaction barrier height affect BIRD rate. Calculations indicate that absorption rate increases linearly with m, and therefore that variations in rate will reflect barrier height. It would be interesting to undertake calculations to find the N_2O reduction barriers for $Rh_n(N_2O)_m^+$, although there has been insufficient time to do so here.

5.4.2 Dissociation rates of the parent ion

The prediction made for a black-body-induced decay mechanism was that the dissociation rate would vary approximately linearly with the number of absorbing species. An increase is indeed seen in the decay rates k_{obs} of $Rh_n(N_2O)_m^+$ with m. The data is shown in figures 5.10 and 5.11. However, these figures both show small deviations from linearity in k_{obs}. While figure 5.9 showed that low-lying isomers with a range of absorption rates have been found for $Rh_5(N_2O)_m^+$, no such isomers have been found for $Rh_4(N_2O)_m^+$. A non-linear absorption rate is therefore a possible cause for deviations from linearity in n=5 but not n=4. Other explanations are sought which are suitable in both cases.

Figure 5.10 compares the changes in k_{obs} with m to the N_2O desorption rate (k_{des}) and the size of the desorption energy (E_{des}). At first glance, it is evident that the total decay rate k_{obs} mirrors the desorption rate, k_{des}:

$$Rh_n(N_2O)_m^+ \rightarrow Rh_n(N_2O)_{m-1}^+ + N_2O. \quad (5.18)$$

Comparison of graphs (b) and (c) in figure 5.10 shows that k_{des} is consistent with the calculated N_2O desorption energies. The desorption energy has a local minimum at m=3 and a maximum at m=4; consequently the desorption rate is significant at m=3 but the desorption channel is closed at m=4. $Rh_5(N_2O)_5^+$ is the only cluster which does not fit the pattern. Its calculated E_{des} is only slightly smaller than that for $Rh_5(N_2O)_4^+$, but its k_{des} is ten times larger. This is consistent with the proposed mechanism for N_2O reduction on the cluster surface, which requires a vacant atop site to bind oxygen.

When m=n, there are no vacant atop sites so the lowest-energy N_2O reduction pathway is closed off; only higher-energy reduction pathways are available. Inspection of the products of $Rh_5(N_2O)_5^+$ shows that, although large, E_{des} is the lowest barrier and therefore desorption is the fastest process to occur on this cluster. Desorption from m=5 is therefore accelerated by a means other than low E_{des}, namely, a lack of competing lower-barrier processes.

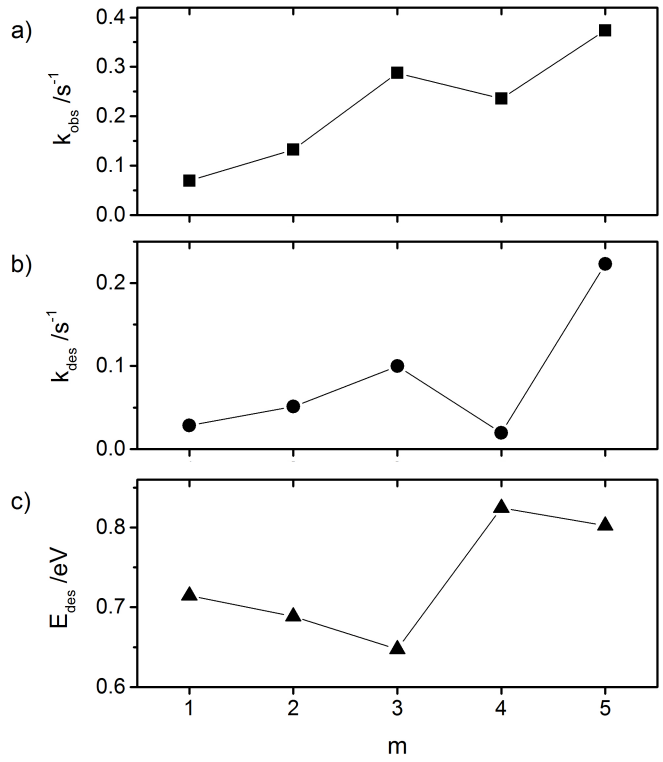

Figure 5.10: (a) the observed decay rate of the parent ion, k_{obs}. (b) the N_2O desorption rate, k_{des}. The patterns of these two rates resemble one another. Comparison with the calculated desorption energy (E_{des}) in (c) suggests that desorption rates are determined by E_{des}.

It has been established that the m-dependence of E_{des} dictates k_{des}. The effect of k_{des} on k_{obs} (k_{des} appears to cause the deviations from linearity of the trend in k_{obs}) has not yet been discussed. In all $Rh_5(N_2O)_m^+$ where m<5, N_2O reduction is faster than desorption, so E_{des} must exceed the reduction barrier. In a small molecule, the total rate of reaction is determined by the lowest energy barrier, $E_0{}^1$. Referring back to figure 5.6 shows that the position of upper barriers relative to $E_0{}^1$ will affect the branching ratio of products, but not the total population available for reaction, which is determined solely by $E_0{}^1$. In small molecules the rate of reaction is the rate of absorption of this population. The fact that E_{des} causes the non-linearity in k_{obs} of $Rh_5(N_2O)_{m<5}^+$, despite its not being the lowest energy barrier, suggests that these clusters are *not* in the small molecule limit.

The N_2O reduction barrier has not been calculated for all $Rh_5(N_2O)_m^+$. However, if all non-linearity in k_{obs} is due to variations in the desorption rate, this suggests that the reaction barrier is either constant or increases linearly with m. As has been noted previously, multiple reaction barriers are present. Although the reduction pathway which places an oxygen atom on a vacant atop site is probably the lowest-energy pathway, others are possible. This is shown by the formation of primary reduction products by $Rh_5(N_2O)_5^+$ and $Rh_4(N_2O)_{4,5}^+$ which do not have vacant atop sites. Other possibilities include placing the O atom on a bridging site or the same site as the binding N atom.

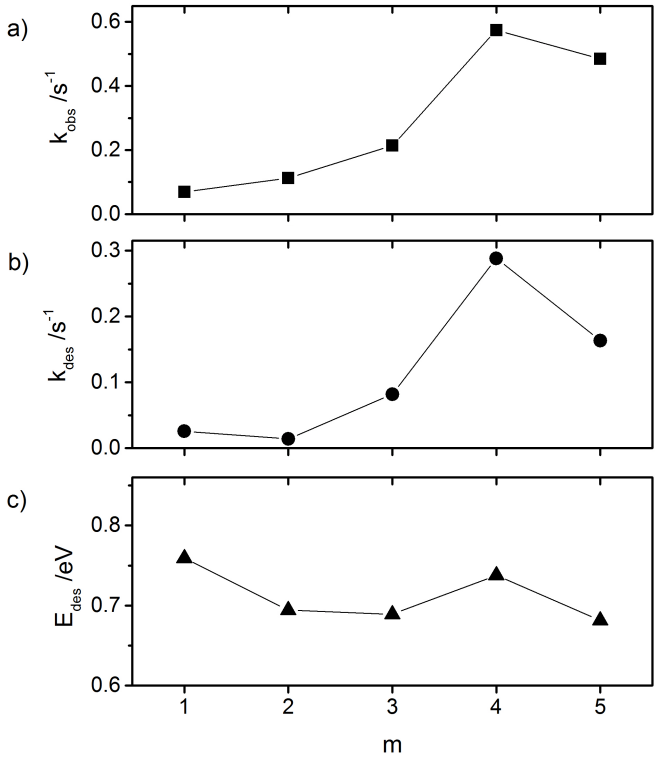

Figure 5.11: (a) Variation in the dissociation rate of $Rh_4(N_2O)_m^+$, k_{obs}, with m. (b) N_2O desorption rate, k_{des}. (a) and (b) resemble one another. Comparison with the calculated desorption energy (E_{des}) in (c) suggests that desorption rates and energies do not correlate with one another. However, variation in E_{des} is small, suggesting they may not be the reason for variation in k_{des}.

Just as in the case of n=5, the trend the total decay rate, k_{obs} of $Rh_4(N_2O)_m^+$ is mirrored by the desorption rate k_{des}. However, the similarity ends there: k_{des} in no way correlates with the calculated desorption energy E_{des}. The comparison is seen in figure 5.11.

In part, this is explained by the 'vacant site' argument. The m=n cluster, $Rh_4(N_2O)_4^+$, has no vacant sites to allow the low-energy reduction pathway to occur. The desorption barrier becomes the lowest on the molecule and desorption is accelerated relative to other processes. $Rh_4(N_2O)_3^+$ is seen to be

the dominant product from black body decay of $Rh_4(N_2O)_4^+$. However, using this argument one would expect desorption from $Rh_4(N_2O)_5^+$ to be the fastest process. It is not; reduction is faster than desorption. This implies that a reduction channel which does not require a vacant atop site is lowered below the desorption barrier in $Rh_4(N_2O)_5^+$. However, a fast reduction rate cannot explain the drop in k_{obs} between m=4 and m=5.

We are left with two possibilities. Firstly, the calculated desorption energies of $Rh_4(N_2O)_m^+$ may be wrong, due to a failure to find true global minima. A larger E_{des} for m=5 would account for the slow desorption of N_2O and the drop in k_{obs} between m=4 and m=5. Alternatively, both k_{des} and k_{obs} may be dictated by variations in the barrier to N_2O reduction with m. This is supported by the small variation in calculated E_{des} on the n=4 cluster; the range is only 0.078 eV (630 cm^{-1}). By contrast, the range of E_{des} on $Rh_5(N_2O)_m^+$ is 0.177 eV (1430 cm^{-1}). Both of these alternatives may be true and cannot be distinguished without extensive further calculation.

5.4.3 $Rh_5(N_2O)_m^+$ products

Thus far, the total decay rate of the parent ion has been considered, along with the dominant product channel. However, the more N_2O molecules are adsorbed on the cluster surface, the more complex reactions can occur. The experimental data for all $Rh_5(N_2O)_m^+$, along with kinetic fits, is shown in figure 5.12. The parent ion is shown as a solid square, primary products as hollow shapes and secondary products with a cross. Low-intensity products have a significant spread about their fit lines, which are consequently more uncertain. Similarly, lower parent peak intensity reduces the signal-to-noise ratio of the data for larger m.

It has been mentioned previously that kinetic fits are not proof of mechanism, but rather identify the simplest mechanism that accounts for the time-dependent intensities of the products using fewest parameters. The same is true here. One parent isomer is found to be sufficient in all cases. Where possible, all products have been fitted as primary products formed directly from the parent, but some secondary processes are evident and are considered in turn.

Figure 5.12 (a) shows the black body decay of $Rh_5N_2O^+$, and has been discussed previously. 5.12 (b) looks very similar to (a): N_2O reduction is the faster decay process, with desorption only slightly slower. The energy released by the reduction process is sufficient to boil off the remaining N_2O, so the hot $Rh_5ON_2O^+$ product produced directly after reduction is not seen. The reduction product is Rh_5O^+. The desorption product, $Rh_5N_2O^+$ can decay as in (a). However, unlike the approximately

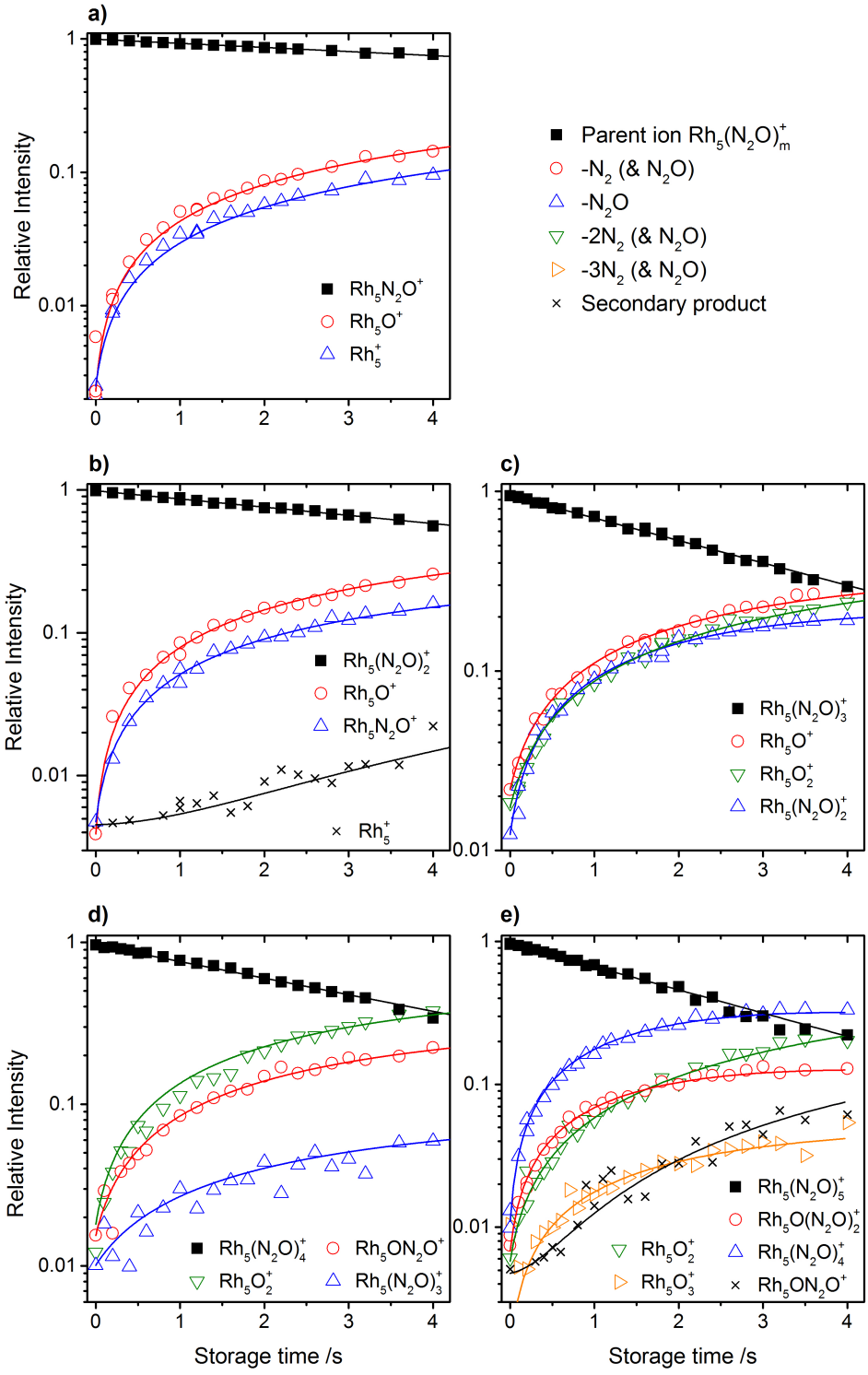

Figure 5.12: BIRD decay of $Rh_5(N_2O)_m^+$. (a) to (e) show m=1-5 respectively. The trend in the desorption rate traces the calculated desorption energy for m=1-4, but is artificially accelerated on m=5 as it does not compete with the facile reaction pathway which requires an empty atop site. N_2O decomposition occurs on all cluster sizes. The energy released by N_2O reduction can trigger further reduction reactions, and/or desorb additional N_2O molecules.

thermal distribution of $Rh_5N_2O^+$ present in (a), the $Rh_5N_2O^+$ desorption product in (b) is produced cold. It therefore decays very slowly to form Rh_5O^+ and Rh_5^+. The former product is a minor perturbation to the large amount of Rh_5O^+ produced directly from $Rh_5(N_2O)_2^+$.

5.12 (c) shows the black body decay of $Rh_5(N_2O)_3^+$. Reduction of a single N_2O molecule remains the dominant pathway. Enough energy is released to boil off both additional adsorbed N_2O, producing Rh_5O^+. However, the hot $Rh_5O(N_2O)_2^+$ can also undergo a rapid subsequent reduction and desorption producing $Rh_5O_2^+$. The low E_{des} of N_2O from $Rh_5(N_2O)_3^+$ allows rapid formation of the desorption product $Rh_5(N_2O)_2^+$. This appears to undergo slow reaction to form $Rh_5O_2^+$, but this secondary rate constant is extremely small.

5.12 (d) shows the black body decay of $Rh_5(N_2O)_4^+$. A large E_{des} means that the desorption product, $Rh_5(N_2O)_3^+$, forms slowly. Its intensity is sufficiently low, and its broad spread of values is such that any secondary losses occurring from $Rh_5(N_2O)_3^+$ are not discerned. The dominant product is instead $Rh_5O_2^+$, showing that two reductions provide sufficient energy to desorb all remaining adsorbed N_2O. The other primary product is $Rh_5ON_2O^+$, showing that, in the n=4 case, a single N_2O reduction produces enough energy to desorb only two further N_2O molecules. $Rh_5ON_2O^+$ does not undergo further desorption to Rh_5O^+, reflecting the large desorption barrier on the oxidised cluster [314]. If it does undergo reduction to $Rh_5O_2^+$, the effect on the $Rh_5O_2^+$ product intensity is small.

5.12 (e) shows the black body decay of $Rh_5(N_2O)_5^+$. As was discussed previously, there are no vacant atop sites on the cluster, which inhibits the low-energy N_2O reduction pathway. Desorption becomes the lowest-energy pathway, and $Rh_5(N_2O)_4^+$ the dominant product. This is not to say that there are no reduction pathways possible in the absence of vacant sites. A number of primary reduction products are visible: $Rh_5O(N_2O)_2^+$, $Rh_5O_2^+$ and $Rh_5O_3^+$. The first of these shows that if the reduction barrier on $Rh_5(N_2O)_5^+$ can be surmounted, enough energy is released to desorb two adsorbed N_2O molecules. The number of products present here means that any number of combinations of secondary (and tertiary) reactions may be fitted. By comparison to 5.12 (d), the major product $Rh_5(N_2O)_4^+$ is fitted as decaying to $Rh_5ON_2O^+$ and $Rh_5O_2^+$. $Rh_5O(N_2O)_2^+$ also appears to decay to the secondary product $Rh_5ON_2O^+$.

$Rh_4(N_2O)_m^+$ behaves much like $Rh_5(N_2O)_m^+$ under black body conditions. $Rh_4(N_2O)_{1\text{-}3}^+$ undergo N_2O reduction (accompanied by loss of all remaining N_2O) a little faster than desorption. Unlike $Rh_5(N_2O)_3^+$, $Rh_4(N_2O)_3^+$ does not form a dioxide. $Rh_4(N_2O)_4^+$ behaves much like $Rh_5(N_2O)_5^+$: with no vacant sites available, desorption is the fastest process although higher-energy paths produc-

ing oxides are observed forming $Rh_4ON_2O^+$, $Rh_4O_2^+$ and $Rh_4O_3^+$. $Rh_4(N_2O)_5^+$ decays somewhat anomalously. Instead of losing its weakly adsorbed N_2O, it rapidly forms $Rh_4ON_2O^+$. This indicates that the presence of 5 N_2O on Rh_4^+ either raises the desorption barrier or lowers the reaction barrier significantly compared to other $Rh_m(N_2O)_m^+$. Such a departure from the trends in barriers on other $Rh_n(N_2O)_m^+$ implies that the true structure of $Rh_4(N_2O)_5^+$ may differ from that proposed in table 5.3.

5.4.4 Master equation modelling of $Rh_5(N_2O)_m^+$

Thus far, the small molecule limit has been assumed, to the extent that the most abundant product is deemed to be produced by the process with the lowest reaction barrier. However, the evident influence of the desorption rate, k_{des}, on the total decay rate, k_{obs}, despite desorption appearing to have the higher barrier, contradicts this assumption. The population distribution and threshold energy may be obtained from master equation modelling. Both the full transport matrix and the truncated Boltzmann approaches will be used. Master equation modelling is particularly convenient for the $Rh_n(N_2O)_m^+$ systems studied because the vibrational spectra of these species have been calculated. The m=1 spectra have also been experimentally measured [310]. Often, the exact vibrational modes and their intensities are unknown [340, 342, 374]. However, even with our better-than-average knowledge of the vibrations of the system, two unknowns remain.

The first of these is the structure of the transition state, whose vibrational modes are needed to calculate the RRKM dissociation rate constant from equation (5.9). Instead, the modes of the parent ion are inspected and one of the bends which moves an oxygen atom towards a rhodium atom is removed. This creates an approximation to the vibrational spectrum of the transition state. This method of creating a transition state spectrum has been tested on $Rh_5N_2O^+$ for which the transition state has been calculated. The 'true' and 'approximate' transition state spectra find exactly the same barrier. This is because the RRKM rate depends on the number of ways the transition state can be created. The bulk of these rely on filling different permutations of the large number of low-frequency modes. The N_2O-based modes are much larger and contribute to a small fraction of the number of energy permutations at the transition state. Changes in these modes consequently have little effect on k_{diss}.

The other unknown arises in the transition intensities of the calculated spectra. DFT calculations are known to poorly determine accurate transition intensities and it is common to scale them by a factor between 1 and 5 [342, 346, 365, 375]. Higher-level calculations require a smaller scaling factor [378]. The effect of a range of scaling factors on calculated threshold energy is illustrated in figure

5.13. The truncated Boltzmann modelling method is used. The scaling factor does have an effect, but the uncertainty introduced (a few hundred wavenumbers) is small compared to the size of the barriers invoked (a few thousand wavenumbers). The barriers are found by trial and error, and are the thresholds that reproduce the experimentally-observed dissociation rate constant for the ion.

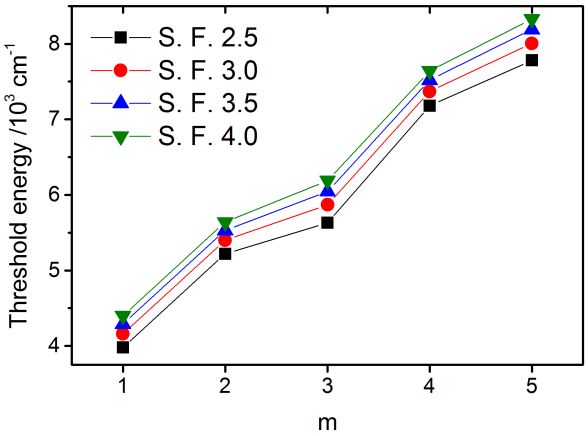

Figure 5.13: Influence of scaling factor on the calculated threshold energy (E_0) for BIRD decay of $Rh_5(N_2O)_m^+$. Large percentage changes in the scaling factor lead to a difference of only a few hundred wavenumbers in the calculated E_0. This error is not large compared to the calculated thresholds of several thousand wavenumbers.

Having established that the unknown factors in our model do not compromise the validity of the master equation model, the two approaches are compared. The final populations for each $Rh_5(N_2O)_m^+$ cluster are shown in figure 5.14. These populations are calculated using appropriate barriers at two scaling factors: 2.5 and 4.0.

Sharp thresholds at E_0, E_0-$hc\tilde{\nu}$ and E_0-$2hc\tilde{\nu}$ are visible in both truncated Boltzmann and transport matrix methods. This confirms that $Rh_5N_2O^+$ is indeed a small molecule; above the threshold, dissociation occurs rather than emission. A number of 'waves' appear in the population of $Rh_5N_2O^+$ using the transport matrix model. These are localised energies which are depleted by absorption and subsequent reaction via bending modes. At the larger scaling factor, the increased rates of radiative processes smooth out these waves.

For all $Rh_5(N_2O)_{m>1}^+$, there are no sharp cutoffs in the population calculated with the transport matrix method. This reflects a transition out of the small molecule regime, as the additional chromophores make spontaneous emission fast enough to compete with dissociation when $E>E_0$. At m≥4, the steady state population obtained by the transport matrix strongly resembles the parent ion's Boltzmann dis-

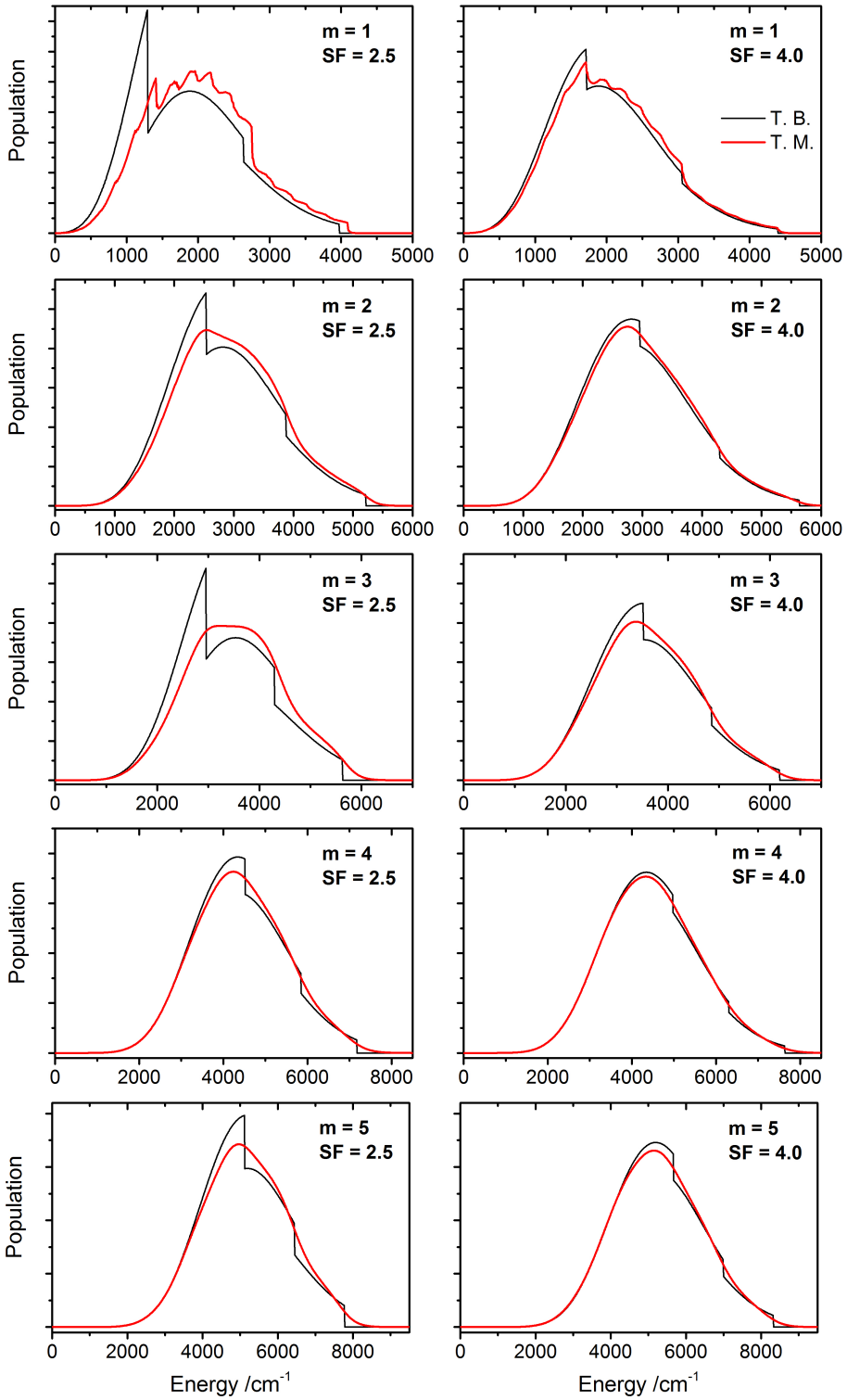

Figure 5.14: Steady-state populations of $Rh_5(N_2O)_m^+$ decaying in a black-body field at 300 K, calculated using a truncated Boltzmann (T. B.) distribution (thin black line) and the transport matrix (T. M.) method (thick red line). Sharp thresholds at E_0, E_0-$\tilde{\nu}$ and E_0-$2\tilde{\nu}$ are visible in the m=1 cluster but no others, suggesting that m=1 is the only true 'small molecule' present. The truncated Boltzmann distribution is a better approximation to the full master equation model at larger scaling factors.

tribution. This is not to say that $Rh_5(N_2O)_{4,5}^+$ lie in the large molecule limit, but that they certainly do not lie in the small molecule limit. Considerable population density lies above the threshold calculated by the transport matrix. BIRD rates observed for larger-m clusters will therefore have some dependence on the corresponding Arrhenius prefactor. The lack of desorption from $Rh_5(N_2O)_4^+$ is therefore very strong evidence for a large E_{des} in this case, as the desorption process is accompanied by a much larger A factor than any rearrangement resulting in N_2O reduction.

It is notable in figure 5.14 is that the truncated Boltzmann model mirrors the more accurate steady-state distribution from the transport matrix model quite closely at a scaling factor of 4. This is not unexpected, as rapid emission and absorption between the two energy regions below E_0 smooths out their population differences. However, the truncated Boltzmann approximation is specifically designed for the small molecule limit, so its reproducing both the k_{diss} and (almost) the steady state population distribution obtained by the more general method is surprising. The truncated Boltzmann distribution manages to achieve an approximation to the true distribution and rate by employing an artificially large energy barrier. The fitted barriers found by the two modelling methods to achieve this final distribution are compared in figure 5.15.

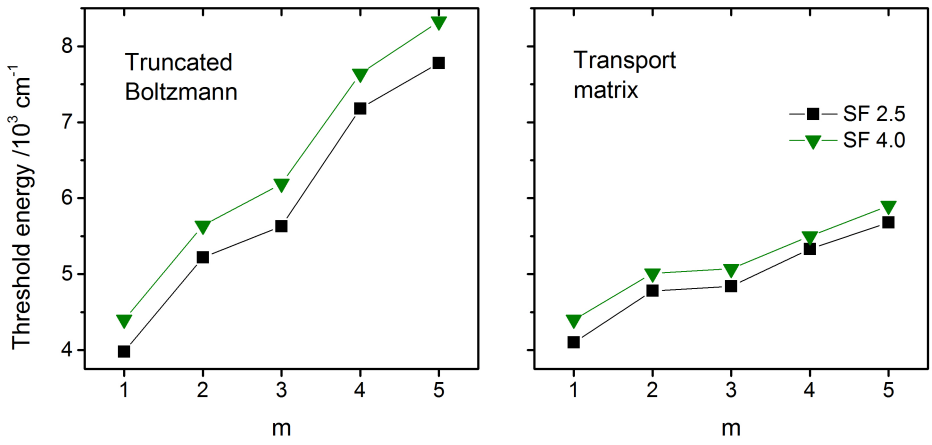

Figure 5.15: Difference in calculated thresholds, E_0, using a transport matrix as opposed to a truncated Boltzmann distribution. The truncated Boltzmann model requires artificially large threshold energies to replicate the experimental dissociation rate.

At m=1, the truncated Boltzmann and transport matrix models predict energy thresholds within 20 cm^{-1} of one another, as can be seen in Figure 5.15. This figure also illustrates the failure of the truncated Boltzmann model at larger m quite effectively. By not accounting for the ability of the larger clusters to decay radiatively as well as dissociatively, it pushes up the fitted E_0 to unrealistically

large values. The more accurate modelling technique predicts an approximately linear increase in the threshold, which, experiment suggests, corresponds to the reaction barrier for N_2O reduction in the m=1-4 case. It is interesting that the variation in threshold fitted by the master equation does not correspond to the variation in k_{obs} found experimentally, as in figure 5.10. The master equation used here does not calculate the branching ratio of products above the threshold, it is simply concerned with the decay of the parent ion.

The most important feature of figure 5.15 is not its demonstration of large molecule behaviour in $Rh_5(N_2O)_m^+$ but the fact that the threshold energies calculated by the master equation are so close to the barriers predicted by DFT calculations. Calculations published in reference [314] suggest reaction barriers around 0.7 eV for $Rh_5N_2O^+$. Barriers obtained for the same species by master equation modelling are around 0.53 eV. Given the known inaccuracies of DFT, and the limitations on the accuracy of the BIRD rates, such agreement is excellent and provides further proof of the BIRD mechanism in this case. Similar conclusions are expected for master equation modelling of $Rh_4(N_2O)_m^+$, although there has not yet been time to perform these calculations.

5.5 Concluding remarks

The ability of black body radiation to activate the decay of $Rh_n(N_2O)_m^+$ species has been proven via the reaction's dependence on temperature and the number of absorbing species present. Furthermore, master equation modelling of the decay has calculated barriers consistent with those from density functional theory calculations on $Rh_5N_2O^+$. The surprising result is that only $Rh_5N_2O^+$ shows true small molecule behaviour. All larger species' decay rates are affected by reaction pathways other than that with the lowest barrier. The decay rate of $Rh_5(N_2O)_m^+$ therefore does not increase perfectly linearly with m. Variations in the desorption rate cause deviations from linearity in the trend. The dissociation rate of $Rh_4(N_2O)_m^+$ also increases with m, with its deviations from linearity reflecting k_{des}. However, the k_{des} values are not consistent with calculated desorption energies of N_2O from $Rh_4(N_2O)_m^+$, suggesting that either the desorption energies are incorrect or that both k_{des} and k_{obs} are dictated by the unknown N_2O reduction barrier. Further calculations are needed on $Rh_4(N_2O)_m^+$.

Chapter 6

Conclusions and outlook

The clusters studied in this thesis range in size from two atoms (CuO and Cu_2) to twenty atoms ($Rh_5(N_2O)_5^+$). Even within this small range, the increasing complexity of the systems necessitates a change in approach. The photodissociation of CuO and Cu_2 may be studied by VMI. The technique yields the quantum states of the parent and fragment species, the photon order of the dissociation and the accompanying kinetic energy release. Photodissociation of Cu_3 may be observed with VMI, but the conclusions that may be drawn are not clear-cut. The molecular cofragment, Cu_2, is produced in a range of quantum states which all contribute to the images. The kinetic energy release of the fragments becomes poorly-defined, even in a system as simple as Cu_3, and a unique assignment of the products' quantum states is difficult. For the study of even larger systems, reactant mass-selection is required, and so $Rh_n(O)N_2O^+$ and $Rh_n(N_2O)_m^+$ clusters were studied using FT-ICR. Even in the small size range $Rh_5(N_2O)_m^+$ where m=1-5, a transition out of the small size regime is observed during BIRD studies.

In chapter 2, the visible spectrum of copper oxide (CuO) was recorded in the Cu^+ channel. A visible OPO was used to excite electronic transitions in CuO, and a UV laser to dissociate the excited CuO* and to ionise the atomic copper product. Between 18000 and 24400 cm^{-1}, transitions are observed from the lower spin-orbit component of the CuO ground state, X $^2\Pi_{3/2}$, to almost all available excited states (namely C, D, E, F, G and H). G $^2\Sigma^+$, however, sits underneath the 2-photon 4s-5s transition in the copper atom and so is swamped in the Cu^+ images. Additionally, very weak transitions are seen from the upper spin-orbit component of the ground state, X $^2\Pi_{1/2}$, to the C state, but X $^2\Pi_{1/2}$ is much less abundant than X $^2\Pi_{3/2}$ in the molecular beam.

Images taken in the Cu^+ channel at the CuO resonances show that CuO dissociates via a single

pathway over the whole energy range. A single visible photon excites CuO to CuO*, and CuO* is dissociated by a single UV photon to Cu* $^2D_{3/2}$ + O* $^1D_2$ in a 1+1' process. Cu* is photoionised upon absorbing two non-resonant UV photons. The mechanism was tested by tuning the UV laser to a resonance of the Cu* product, $3d^{10}5p\ ^2P^0 \leftarrow 3d^9 4s^2\ ^2D_{3/2}$ at 36138 cm^{-1} (the spin-orbit components of $^2P^0$ are separated by 0.32 cm^{-1}). A significant enhancement was observed in the Cu^+ signal at the Cu $^2D_{3/2}$ resonance, despite the fact that this transition is expected to be very weak, implying that it may be incorrectly assigned. A very minor enhancement was seen in the absence of the OPO, as there is little Cu $^2D_{3/2}$ in the molecular beam. The large energy range over which the CuO dissociation occurs into this channel allows a very accurate determination of D_0(CuO), and, using known ionisation energies, $D_0(CuO^+)$. These findings are given in table 6.1. The results of our experiments on CuO have been published in reference [142].

The anisotropies of the Cu^+ rings arising from CuO* dissociation are not consistent with with the symmetries attributed to the CuO* electronic states. Both Π and Δ states appear to undergo parallel transitions to the same dissociative state, which is impossible. However, the state symmetries used are assigned using a Hund's case (a) description, which is known to be an unsuitable model for the spin-orbit coupling in CuO. For instance, more $^2\Pi$ states have been assigned on the basis of LIF experiments than are possible from the available electronic configurations. The work in chapter 2 therefore confirms the need for re-assignment of the symmetries of the electronic states of CuO using a Hund's case (c) description.

Chapter 3 repeats the spectroscopy of chapter 2 using only the OPO. Both Cu^+ and $Cu_2{}^+$ are observed, despite their high ionisation potentials. At low laser intensity, only resonant ionisation processes are observed: 1+2 photoionisation of Cu_2 X $^1\Sigma_g{}^+(0)$ via B(ν) and C(ν), and various atomic resonances. These experiments prove that the Cu_2 present in the beam is electronically and vibrationally cold. When the laser intensity is increased, the ion yield spectra in the Cu^+ and $Cu_2{}^+$ channels become highly complex. In the region of the Cu_2 B and C electronic states, many of the additional peaks may be fitted by resonant transitions out of the vibrationally excited Cu_2 ground state. In the 21500-24000 cm^{-1} region, much of the new structure corresponds to peaks in the two series C(ν)←X(2, 3). The origin of hot Cu_2 in the beam is suggested to be photodissociation of larger Cu_n, most likely Cu_3. Further evidence of photodissociation of Cu_3 is found in the ion yield spectrum. Between 18400 and 19200 cm^{-1}, the Cu^+ and $Cu_2{}^+$ channels appear identical. The only parent Cu_n expected to produce Cu and Cu_2 with identical yields is Cu_3. Furthermore, a number of peaks are in the same position as

peaks previously observed in photodepletion spectroscopy of Cu_3. Cu_3 is known to have an excited state in this region; the Cu_3 A←X band head is at 18529 cm^{-1}.

Images in the Cu^+ channel have two 'types' of feature: sharp peaks, and very broad structures. At many photon energies, the sharp peaks comprise a fairly small fraction of the total signal in the image. The sharp peaks are independent of spectral structure; although hard to quantify, the intensity in the Cu^+ and Cu_2^+ spectra arises mainly from the broad features in the images. The origin of the sharp features is identified as non-resonant three-photon dissociation of Cu_2 to produce one ground-state and one highly excited copper atom, Cu*. Cu* is ionised by absorption of a single subsequent photon; almost all Cu* between $^4F^0_{3/2}$ at 42302.58 cm^{-1} and $^2D_{5/2}$ at 49942.051 cm^{-1} are observed as cofragments. This gives us a very large number of TKER points from which $D_0(Cu_2)$ may be determined with a very small uncertainty; see table 6.1. At photon energies less than 19596 cm^{-1}, Cu* produced by three-photon dissociation requires 2 photons for ionisation. One such 3+2 process is observed, as is a 4-photon dissociation producing Cu* ionisable with one photon.

Images taken in the Cu_2^+ channel do not show any sharp peaks, but their broad structures bear a striking resemblance to the broad features observed underneath the sharp peaks of the Cu^+ images. In fact, when the KER spectra are scaled, Cu^+ assuming a Cu_2 cofragment and Cu_2^+ assuming a Cu cofragment, they match one another extremely closely. This is good evidence that the Cu_2^+ off-axis intensity in the images arises from photodissociation of Cu_3. Although the features in the Cu_2^+ TKER spectra are broad, an attempt was made to extract the peaks' centres using Lorentzian functions. The results yield three series, all corresponding to one-photon dissociation of Cu_3. The uncertainties are such that previous determinations of $D_0(Cu_3)$ cannot be improved (see table 6.1). Two of the series can be clearly identified as producing various vibrational levels of X $^1\Sigma_g^+(v)$ and a metastable copper atom, Cu $^2D_{5/2}$ or $^2D_{3/2}$. The third series, however, corresponds to an internal energy of around 9600 cm^{-1}, which is less than the lowest known internal energies of both Cu and Cu_2. It is possible that the state is a previously-unobserved member of the Cu_2 triplet manifold. Alternatively, the parent Cu_3 may be excited and its internal energy has not been accounted for (although the observation of Cu_3 A←X photodepletion lines implies not).

A number of further experiments are suggested by this chapter. Most pressing is the question of whether the enhancements seen in the Cu^+ and Cu_2^+ channels may be correlated with depletions in Cu_3. The 157 nm excimer used herein contains ample energy to ionise Cu_3 but appears not to do so, and probably dissociates it instead. It might be informative, therefore, to attempt a two-colour ex-

periment using a lower-energy excimer, or a doubled dye output near the 5.8 eV ionisation threshold, to monitor the abundance of Cu_3. Previous workers have enhanced their yield of Cu_3 by cooling the cluster channel using liquid nitrogen. This would be a useful addition to our experiment. To understand the 9600 cm^{-1} internal energy predicted by the Cu_2^+ images, high-level calculations examining the triplet manifold of Cu_2 to look for further states would be useful. Additionally, laser fluence studies to confirm that photodissociation of Cu_3 is a one-photon process would make the assignments given in chapter 3 more secure.

Chapter 4 considered much larger clusters, $Rh_nN_2O^+$ and $Rh_nON_2O^+$ (n=5, 6). These clusters were studied in an FT-ICR mass spectrometer, which allows the parent ion to be isolated. Collision experiments were performed using both Ar and ^{13}CO as collision partners. At the energies used, Ar does not stick to $Rh_n(O)N_2O^+$ but transfers translational energy into the cluster's vibrational modes upon collision. The exact amount of energy transferred is unknown, but is evidently sufficient to activate one of two processes on the cluster surface: N_2O desorption, or N_2O reduction resulting in loss of N_2 and oxide formation. These same reactions have been seen previously in IR-MPD experiments on the $Rh_n(O)N_2O^+$ system. Collision experiments replicate not only the reaction channels of the IR-MPD experiments, but also their branching ratios. All species studied favour N_2O reduction, except $Rh_5N_2O^+$, whose dominant decay channel is N_2O desorption. The branching ratios are believed to reflect the relative barriers to desorption and reduction, and illustrate the effect of a single adsorbed oxygen atom on the barriers to surface processes. It is noticed that desorption is increasingly favoured as collision energy increases. This is suggested to be an entropic effect: the extremely loose transition state for desorption leads to a very large Arrhenius prefactor. High collision energies lead to high effective vibrational temperatures, whereupon the favourable *A*-factor for desorption compared to reduction influences their relative rates.

^{13}CO is not an inert collision partner, but rather chemisorbs on the cluster, releasing a fixed amount of energy (calculated to be ≈2 eV). This is sufficient to overcome all calculated reaction barriers, and $Rh_6N_2O^+$ exhibits both N_2O reduction and desorption upon the chemisorption of ^{13}CO. However, adsorbed ^{13}CO also reacts with adsorbed oxygen atoms, releasing $^{13}CO_2$ to form bare Rh_6^+. ^{13}CO does not appear to perturb the $Rh_6N_2O^+$ system enormously, as CO oxidation is a minor channel. On $Rh_5N_2O^+$, however, the barrier to N_2O reduction and subsequent CO oxidation is so low on the intermediate $Rh_5(N_2O)(^{13}CO)^+$ species that Rh_5^+ is the dominant product. No desorption is seen at all. On the oxide clusters, $Rh_nON_2O^+$, the N_2O reduction barrier is sufficiently lowered that (i) it

is the fastest process on both n=5 and n=6, meaning that $Rh_nO_2^+$ is the dominant product in both cases, and (ii) no N_2O desorption is seen; it is too slow to compete. Calculations suggest that the N_2O desorption barrier is not greatly affected by the presence of CO. Once again, the n=5 cluster appears to be able to oxidise ^{13}CO on its surface extremely rapidly. However, the product of N_2O reduction and CO oxidation, Rh_5O^+, can oxidise another ^{13}CO, leading to a Rh_5^+ product. Rh_6^+ is not seen. The ability of Rh_nO^+ to oxidise ^{13}CO was tested by storing these clusters in a ^{13}CO atmosphere, and the Rh_5^+ cluster was found to be more efficient. The experiments described in chapter 4 have been published in reference [264].

Further calculations would improve our understanding of the results in chapter 4. Molecular dynamics simulations of the energy transfer upon the clusters' collisions with Ar would give us a quantitative understanding of these experiments. Our interpretation is currently only qualitative. Calculated reaction pathways for the ^{13}CO-decorated clusters would also be useful in establishing whether the origin of the rapid CO oxidation on the n=5 cluster is a result of cluster geometry, or an electronic effect.

Chapter 5 makes use of the ultra-high vacuum and long-term storage conditions of the FT-ICR to study the decay of $Rh_nN_2O^+$ (n=4-6) activated by black body radiation. BIRD experiments are an extremely gentle method of heating the cluster, whereas the activation methods described previously (IR-MPD and collision) are capable of rapidly depositing enough energy into the cluster to surmount both desorption and reduction barriers. In the case of small molecules, BIRD rates are determined solely by the rate at which molecules can absorb enough energy to cross the reaction barrier. BIRD experiments on $Rh_nN_2O^+$ consequently show surprising product branching ratios. N_2O decomposition is the dominant process on all cluster sizes, even n=5. No desorption at all is observed from $Rh_6N_2O^+$. These results necessitate a re-interpretation of the data in the previous chapter. BIRD results prove that the desorption barrier is higher than the reduction barrier on both $Rh_5N_2O^+$ *and* $Rh_6N_2O^+$. However, the loose transition state for desorption favours this process, particularly at higher internal cluster energies. The reduction barrier is sufficiently low on $Rh_6N_2O^+$ that reduction is the dominant process in IR-MPD and CID experiments, but not on $Rh_5N_2O^+$.

In order to prove that black body radiation is indeed activating the chemistry seen in chapter 5, the BIRD experiments on $Rh_nN_2O^+$ were repeated in a black body field at 100 K. A tenfold increase was seen in the lifetimes of the stored clusters. As a further test of the BIRD mechanism, the number of adsorbed N_2O was increased. In the absence of many body effects, the BIRD rate is expected to vary with absorption rate, and consequently to increase linearly with the number of N_2O chro-

mophores. Such an increase in rate is indeed observed for $Rh_n(N_2O)_m^+$ (n=4, 5; m=1-5), although it is not perfectly linear. DFT calculations imply that this cannot be attributed to non-linear variation in absorption rate. Extracting the rates of the individual processes occurring on each cluster shows that non-linearity in the BIRD dissociation rate with m is due to non-linear variations in the desorption rate with m. In the case of $Rh_5(N_2O)_m^+$, the N_2O binding energies calculated by DFT predict the exact trend in N_2O desorption rate which is observed. Calculations on $Rh_4N_2O^+$ predict very little variation in N_2O binding energy with m, suggesting that the true minima have perhaps not been found in this case. Master equation modelling was performed on the $Rh_5(N_2O)_m^+$ clusters using their calculated vibrational spectra. The reaction barrier obtained from the master equation is extremely close to the reaction barriers calculated by DFT for the $Rh_5N_2O^+$ cluster. Reasonable barriers are obtained for all other cluster sizes. The modelling process yields a surprising result: only the m=1 cluster conforms to an ideal 'small molecule' description. Larger clusters exchange black body radiation surprisingly rapidly with their environment, given their small size, and are slow to dissociate at energies significantly above their reaction barriers. A paper describing the BIRD experiments has been accepted by Angew. Chem. Int. Ed., DOI: 10.1002/anie.201409483.

There is clearly further calculation to be done in the case of $Rh_4(N_2O)_m^+$. Master equation modelling of the $Rh_4(N_2O)_m^+$ system will be carried out in the near future. The accuracy of master equation modelling is dependent on the accuracy of the IR spectrum. A more thorough search for the global minima of each cluster, perhaps using a basin-hopping algorithm to find a wider range of starting points, would give us more certainty in the calculated N_2O binding energies and $Rh_4(N_2O)_m^+$ structures. However, it may be the case that the desorption rate is not determined by the desorption energy alone but is also affected by an N_2O reduction rate which varies non-linearly with m. Calculation of possible N_2O reduction transition states, and hence reaction barriers, on these structures would therefore be useful.

Species	Dissociation Energy /eV This work	Dissociation Energy Previous (year)
CuO	3.041±0.030	2.76±0.22 (1972) [197] 2.48 (1974) [176] 2.85±0.15 (1991) [199] 3.116±0.008 (1994) [200] 2.94±0.12 (1999) [201]
CuO^+	1.36±0.04	1.62±0.15 (1990) [214] 1.35±0.12 (1999) [201]
Cu_2	1.992±0.037	2.0±0.1 (1957) [234] 2.21±0.11 (1957) [235] 1.97±0.09 (1960) [236] 1.98±0.04, 1.96±0.06 (1979) [237]
Cu_2^+	1.819±0.042	1.84±0.08 (1989) [210]
Cu_3	1.02±0.19	1.07±0.18 (1980) [262]

Table 6.1: Dissociation energies obtained by VMI, compared with previous values.

Appendix A

Eigenvalues of the transport matrix

J acts upon a column vector, **x**(t), which has i elements describing the population at each energy level E_i in the system at time t. The action of **J** upon a population **x**(t) for a time δt produces a new population **x**(t+δt):

$$\mathbf{J}\mathbf{x}(t)\delta t = \mathbf{x}(t + \delta t). \tag{A.1}$$

However, the population changes while absorption, emission and reaction occur, so equation (A.1) only holds for extremely short δt. The exact formulation of equation (A.1) is therefore:

$$\mathbf{J}\mathbf{x}(t) = \frac{d\mathbf{x}(t)}{dt} \tag{A.2}$$

which shows that **J**x(t) gives the instantaneous rate at time t. A solution to equation (A.2) is found:

$$\mathbf{x}(t) = \mathbf{x}(0)e^{\mathbf{J}t}. \tag{A.3}$$

This can be shown to be true by differentiating $\mathbf{x}(0)e^{\mathbf{J}t}$, substituting $e^{\mathbf{J}t}$ for its power series:

$$e^{\mathbf{J}t} = \mathbf{I} + \mathbf{J}t + \frac{1}{2!}\mathbf{J}^2t^2 + \cdots . \tag{A.4}$$

The relationship in equation (A.2) is thus shown to be true; the differential of $\mathbf{x}(0)e^{\mathbf{J}t}$ is $\mathbf{J}\mathbf{x}(0)e^{\mathbf{J}t}$.

The problem remains that the initial population **x**(0) is not exactly known; it may be slightly warmer or cooler than the cell temperature. [342, 336, 343, 344, 356] Additionally, $e^{\mathbf{J}t}$ is not easy to compute. Both problems are surmountable using the eigenvectors, $\mathbf{e_k}$, of **J**. The transport matrix's eigenvectors $\mathbf{e_k}$ form a complete set; this means that any vector may be expressed as a sum of eigenvectors $\mathbf{e_k}$

weighted by coefficients, a_i. The initial population may therefore be expressed as:

$$\mathbf{x}(0) = \sum_{k=0}^{k=i} a_k \mathbf{e_k}. \tag{A.5}$$

The problematic $e^{\mathbf{J}t}$ term now acts on eigenvectors. Action of a matrix on an eigenvector returns the eigenvector multiplied by an eigenvalue, λ_k. Action of a function of a matrix on its eigenvector returns the eigenvector and the appropriate function of the eigenvector. In this case:

$$e^{\mathbf{J}t}\mathbf{e_k} = e^{\lambda_k t}\mathbf{e_k} \tag{A.6}$$

which can be substituted into equation (A.3), along with equation (A.5), to give:

$$\mathbf{x}(t) = \sum_{k=0}^{k=i} e^{\lambda_k t} a_k \mathbf{e_k}. \tag{A.7}$$

All the eigenvalues λ_k of $\mathbf{J}$ are negative. [362] It is evident from equation (A.7) that, after some induction period, only the term with least negative eigenvalue (λ_0) will significantly contribute to $\mathbf{x}$(t). All others drop away to zero. This gives rise to the statement above: the least negative eigenvalue of $\mathbf{J}$ is its steady state unimolecular rate constant, and its corresponding eigenvalue is the steady state population.

Appendix B

Code used in thesis

All examples given below utilise the calculated vibrational spectrum of $Rh_5N_2O^+$.

B.1 Full transport matrix

This C programme calculates the transport matrix, **J**, and, if given the eigenvalue λ_0, calculates the eigenvector of **J** corresponding to λ_0.

```
#include <stdio.h>
#include <math.h>
#include <stdlib.h>
#include <string.h>
int bs_count(int * bs_frequency, double * p_bs, int n_bs, int k_bs); /*Function*/
int main()
{
/*Physical constants, values taken from NIST*/
double h_planckSI=6.62606957*pow(10,-34); /*Planck's Constant in J s*/
double conversion_cm_J=1.9864457*pow(10,-23); /*Conversion cm-1 to J*/
double h_planck=h_planckSI/conversion_cm_J; /*Planck's constant in cm-1 s*/
double pi=3.14159265; /*Pi*/
double c_light=299792458; /*Speed of light in a vacuum in m s-1*/
double k_boltz=1.3806488*pow(10,-23); /*Boltzmann constant in J K-1*/
double n_avo=602214129*pow(10,15); /*Avogadro's constant*/
double euler=2.71828183; /*Euler's number, basis of the natural logarithm*/
/*Parameters which must be changed for each Rhn(N2O)m complex studied*/
int n_modes=18; /*Number of vibrational modes in parent species*/
int n_N2O=1; /*Number of N2O species in the parent species*/
/*Parameters describing the transition state*/
```

```
int n_tsl=1; /*This is the number of transition states leading to products*/
double* tsp_energy;
tsp_energy=(double*)malloc(n_tsl*sizeof(double));
tsp_energy[0]=4400; /*These are the barrier heights of each TS above the G.S.*/
/*input required for Beyer-Swinehart algorithm*/
double bs_quantum=10; /*Energy grain size*/
double maximum_energy=7000; /*MKB: "Energy range covered", units cm-1."*/
int n_levels=(int)(maximum_energy/bs_quantum); /*Number of discrete energy levels
    in simulation*/
int n_temp=1; /*no. of temperatures*/
double scale_factor=4.0; /*Factor for scaling of IR intensities*/
int i, j, k, m, n, k0; /*Dummy variables*/
double q;
/*Array initialisation; must be done dynamically*/
double* well; /*Initial population, well[n_levels]*/
well=(double*)malloc(n_levels*sizeof(double));
double* eigenvector_B; /*Final population*/
eigenvector_B=(double*)malloc(n_levels*sizeof(double));
int well_energy; /*Zero-point energy*/
int* well_frequency; /*Vibrational frequencies in units of bs_quantum*/
well_frequency=(int*)malloc(n_modes*sizeof(int));
double* exact_frequency; /*Exact vibrational frequencies in cm-1*/
exact_frequency=(double*)malloc(n_modes*sizeof(double));
double* well_intensity; /*Intensity of vibrational modes in km mol-1*/
well_intensity=(double*)malloc(n_modes*sizeof(double));
double* einstein_a; /*Einstein A coefficients for spontaneous emission*/
einstein_a=(double*)malloc(n_modes*sizeof(double));
double* einstein_rb; /*Einstein B coeffs convoluted with black body field*/
einstein_rb=(double*)malloc(n_modes*sizeof(double));
double** tsp_exact_frequency; /*Exact vibrational modes of each TS in cm-1*/
tsp_exact_frequency=(double**)malloc(n_tsl*sizeof(double));
for (i=0;i<n_tsl;i=i+1){
    tsp_exact_frequency[i]=(double*)malloc((n_modes-1)*sizeof(double));
}
int** tsp_frequency; /*Vibrational modes of each TS in units of bs_quantum*/
tsp_frequency=(int**)malloc(n_tsl*sizeof(int));
for (i=0;i<n_tsl;i=i+1){
    tsp_frequency[i]=(int*)malloc((n_modes-1)*sizeof(int));
}
double**k_rad_abs; /*Absorption rate constants*/
```

```
k_rad_abs=(double**)malloc(n_levels*sizeof(double));
for (i=0;i<n_levels;i=i+1){
    k_rad_abs[i]=(double*)malloc(n_levels*sizeof(double));
}
double**k_rad_emm; /*Emission rate constants*/
k_rad_emm=(double**)malloc(n_levels*sizeof(double));
for (i=0;i<n_levels;i=i+1){
    k_rad_emm[i]=(double*)malloc(n_levels*sizeof(double));
}
double** k_wp; /*RRKM rate constants*/
k_wp=(double**)malloc(n_tsl*sizeof(double));
for (i=0;i<n_tsl;i=i+1){
    k_wp[i]=(double*)malloc(n_levels*sizeof(double));
}
double** matrix_J; /*J matrix to hold all rate constants*/
matrix_J=(double**)malloc(n_levels*sizeof(double));
for (i=0;i<n_levels;i=i+1){
    matrix_J[i]=(double*)malloc(n_levels*sizeof(double));
}
double* t_amb; /*Temperatures at which the iteration will be performed*/
t_amb=(double*)malloc(n_temp*sizeof(double));

/*The user must now enter the data*/
t_amb[0]=300; /*Reading in temperature(s)*/
double ZPE_well_0=0;  /*The zero point energy of the reactant in wavenumber*/
well_energy=(int)(ZPE_well_0/bs_quantum+0.5); /*Convert ZPE to bs_quantum*/
exact_frequency[0]=20.93; /*Exact vibrational frequencies of the ground state*/
exact_frequency[1]=26.47;
exact_frequency[2]=67.66;
exact_frequency[3]=91.25;
exact_frequency[4]=101.15;
exact_frequency[5]=119.92;
exact_frequency[6]=135.50;
exact_frequency[7]=138.03;
exact_frequency[8]=179.83;
exact_frequency[9]=199.58;
exact_frequency[10]=208.78;
exact_frequency[11]=238.41;
exact_frequency[12]=257.43;
exact_frequency[13]=285.93;
```

```
exact_frequency[14]=547.98;
exact_frequency[15]=572.41;
exact_frequency[16]=1340.50;
exact_frequency[17]=2367.66;
well_intensity[0]=0.08724; /*Exact vibrational frequencies of the TS*/
well_intensity[1]=0.11802;
well_intensity[2]=0.03156;
well_intensity[3]=0.12253;
well_intensity[4]=0.15686;
well_intensity[5]=0.03103;
well_intensity[6]=0.25295;
well_intensity[7]=0.80333;
well_intensity[8]=0.51258;
well_intensity[9]=0.87430;
well_intensity[10]=1.20425;
well_intensity[11]=0.31441;
well_intensity[12]=2.12925;
well_intensity[13]=3.62576;
well_intensity[14]=4.08428;
well_intensity[15]=4.74573;
well_intensity[16]=434.27717;
well_intensity[17]=579.57248;
    for (j=0; j<n_modes; j=j+1) /*Modes converted to units of bsq*/
        {
        well_frequency[j]=(int)(exact_frequency[j]/bs_quantum+0.5);
        well_intensity[j]=scale_factor*well_intensity[j];
        if (well_frequency[j]==0)
            {
            well_frequency[j]=1;
            }
        }
tsp_exact_frequency[0][0]=20.93; /*Exact transition state frequencies*/
tsp_exact_frequency[0][1]=26.47;
tsp_exact_frequency[0][2]=67.66;
tsp_exact_frequency[0][3]=91.25;
tsp_exact_frequency[0][4]=101.15;
tsp_exact_frequency[0][5]=119.92;
tsp_exact_frequency[0][6]=135.50;
tsp_exact_frequency[0][7]=138.03;
tsp_exact_frequency[0][8]=179.83;
```

```
tsp_exact_frequency[0][9]=199.58;
tsp_exact_frequency[0][10]=208.78;
tsp_exact_frequency[0][11]=238.41;
tsp_exact_frequency[0][12]=257.43;
tsp_exact_frequency[0][13]=285.93;
tsp_exact_frequency[0][14]=547.98;
tsp_exact_frequency[0][15]=1340.50;
tsp_exact_frequency[0][16]=2367.66;
for (i=0; i<n_tsl; i=i+1) /*Convert TS modes to units of bsq*/
    {
    for (j=0; j<(n_modes-1); j=j+1)
        {
        tsp_frequency[i][j]=(int)(tsp_exact_frequency[i][j]/bs_quantum+0.5);
        if (tsp_frequency[i][j]==0)
            {
            tsp_frequency[i][j]=1;
            }
        }
    }
/*Write input to a file so that it can be checked if need be.*/
FILE *input_pointer;
input_pointer=fopen("input.txt", "w");
fprintf(input_pointer, "n_modes = %d\nn_N2O = %d\n\n", n_modes, n_N2O);
fprintf(input_pointer, "n_tsl=%d\n", n_tsl);
for (i=0;i<n_tsl;i=i+1){
    fprintf(input_pointer, "tsp_energy[%d] = %lf\n", i, tsp_energy[i]);
}
fprintf(input_pointer, "\nbs_quantum = %lf\nmaximum_energy = %lf\nn_levels = %d\
    nn_temp = %d\nscale_factor = %lf\n\n", bs_quantum, maximum_energy, n_levels,
    n_temp, scale_factor);
for (i=0;i<n_temp;i=i+1){
    fprintf(input_pointer, "t_amb[%d]=%lf\n", i, t_amb[i]);
}
fprintf(input_pointer, "\nZPE_energy_0 = %lf\n\n", ZPE_well_0);
    for (j=0;j<n_modes;j=j+1){
        fprintf(input_pointer, "exact_frequency[%d]=%lf well_frequency[%d]=%d
            well_intensity[%d]=%lf\n", j, exact_frequency[j], j, well_frequency[j
            ], j, well_intensity[j]);
    }
    fprintf(input_pointer, "\n");
```

```
for (i=0;i<n_tsl;i=i+1){
    for(j=0;j<(n_modes-1);j=j+1){
        fprintf(input_pointer, "tsp_exact_frequency[%d][%d]=%lf tsp_frequency[%d
            ][%d]=%d\n", i, j, tsp_exact_frequency[i][j], i, j, tsp_frequency[i][
            j]);
    }
    fprintf(input_pointer, "\n");
}
fclose(input_pointer);
printf("The input has been written to file\n");

int i_temp; /*An index allowing us to loop over temperature*/
FILE *Einstein_coeff_pointer;
int n_bs;
int k_bs;
double sum_of_states;
double pkm;
double k_abs;
double k_emm;
int j_new;
double * p_bs;        /*Pointer to p_bs array to be declared dynamically*/
int * bs_frequency;    /*bs_frequency array pntr to be declared dynamically*/
int i_tsl; /*An index allowing us to loop over transition states*/
int tsl_start; /*Variable to allow conversion of energy barriers to bs_quantum*/
double density_of_states;
double population;
double divisor;
double temp; /*Temporary variable allowing us swap rows of matrix_J*/
FILE * k_wp_pointer;
FILE * population_pointer;
FILE * matrix_J_pointer;
FILE * eigenvector_B_pointer;
double lambda_0;

/*Open a very large loop over temperatures*/
for (i_temp=0;i_temp<n_temp;i_temp=i_temp+1){
    for (j=0;j<n_levels;j=j+1){ /*First zero the arrays of radiative rates*/
        for (k=0;k<n_levels;k=k+1){
            k_rad_abs[j][k]=0;
            k_rad_emm[j][k]=0;
```

```
            matrix_J[j][k]=0;
        }
    }
/*Calculate the Einstein coefficients and write them to file*/
Einstein_coeff_pointer=fopen("einstein_coefficients.txt", "a+");
fprintf(Einstein_coeff_pointer, "Temperature: %.3f K\n", t_amb[i_temp]);
    for (j=0; j<n_modes; j=j+1){
        einstein_rb[j]=8*pi*c_light*exact_frequency[j]*exact_frequency[j]*10000*
            well_intensity[j]*1000/(n_avo*(pow(euler, (h_planckSI*c_light*
            exact_frequency[j]*100/(k_boltz*t_amb[i_temp])))-1));
        einstein_a[j]=8*pi*c_light*exact_frequency[j]*exact_frequency[j]*10000*
            well_intensity[j]*1000/n_avo;
        fprintf(Einstein_coeff_pointer, "[%d] absorp. coeff.: %.12lf  emiss.
            coeff.: %.12lf\n", j, einstein_rb[j], einstein_a[j]);
        }
fclose(Einstein_coeff_pointer);
/*Now calculate radiative transition rates between levels of same well*/
printf("Calculating radiative rates at t_amb[%d]\n", i_temp);
    for (j=well_energy; j<n_levels; j=j+1)
        {
        n_bs=j-well_energy;
        k_bs=n_modes-1;
        bs_frequency=(int*)calloc(k_bs+1, sizeof(int));
        for (k=0; k<=k_bs; k=k+1)
            {
            bs_frequency[k]=well_frequency[k];
            }
            p_bs=(double*)calloc(n_bs+1, sizeof(double));
        bs_count(bs_frequency, p_bs, n_bs, k_bs);
        sum_of_states=p_bs[n_bs];  /*No. of ways of arranging energy n_bs*/
        free(p_bs);
        free(bs_frequency);
        for (k=0; k<n_modes; k=k+1) /*pkm, probability mode k is populated m
            times*/
            {
                for (m=0; m<=((j-well_energy)/well_frequency[k]); m=m+1)
                    {
                    n_bs=j-well_energy-m*well_frequency[k];
                    k_bs=n_modes-2;
                    bs_frequency=(int*)calloc(k_bs+1, sizeof(int));
```

```
for (k0=0; k0<=k_bs; k0=k0+1)
    { /*Removes k from the set of populable modes*/
        if (k0<k)
            {
            bs_frequency[k0]=well_frequency[k0];
            }
        else {
            bs_frequency[k0]=well_frequency[k0+1];
        }
    }
    p_bs=(double*)calloc(n_bs+1, sizeof(double));
    bs_count(bs_frequency, p_bs, n_bs, k_bs);
    if (sum_of_states==0) /*if E. level j can't be made*/
        {
        if (m==0)
            {
            pkm=1;
            }
        else {
            pkm=0;
        }
        }
    else {
            pkm=(p_bs[n_bs])/sum_of_states;
    }
    free(p_bs);
    free(bs_frequency);
    k_abs=pkm*(m+1)*einstein_rb[k]; /*absorp. rate.*/
    j_new=j+well_frequency[k];
    if (j_new>=n_levels)
        {
        j_new=n_levels-1;
        }
    k_rad_abs[j_new][j]=k_abs+k_rad_abs[j_new][j];
    k_rad_abs[j][j]=k_rad_abs[j][j]-k_abs;
    matrix_J[j_new][j]=k_abs+matrix_J[j_new][j];
    matrix_J[j][j]=matrix_J[j][j]-k_abs;
    if (m>0) /*emission rate*/
    {
        k_emm=pkm*m*einstein_a[k];
```

```
                                j_new=j-well_frequency[k];
                                if (j_new<well_energy){
                                    k_emm=0;
                                }
                                else {
                                k_rad_emm[j_new][j]=k_rad_emm[j_new][j]+k_emm;
                                k_rad_emm[j][j]=k_rad_emm[j][j]-k_emm;
                                matrix_J[j_new][j]=matrix_J[j_new][j]+k_emm;
                                matrix_J[j][j]=matrix_J[j][j]-k_emm;
                                }
                            }
                        } /*end of loop over mode occupancy (index m)*/
                } /*end of loop over n_modes (index k)*/
            } /*End of loop over n_levels, (index j)*/
printf("Calculating elements of k_wp\n"); /*Now calculate the RRKM rates.*/
for (i_tsl=0;i_tsl<n_tsl;i_tsl=i_tsl+1){
    tsl_start=(int)((tsp_energy[i_tsl])/bs_quantum+0.5);
        for (j=tsl_start;j<n_levels;j=j+1){
            n_bs=j-tsl_start; /*Excess E. above barrier in bs_quantum*/
            k_bs=n_modes-2;
            bs_frequency=(int*)calloc(k_bs+1, sizeof(int));
            for (k=0;k<=k_bs;k=k+1){
                bs_frequency[k]=tsp_frequency[i_tsl][k];
            }
            p_bs=(double*)calloc(n_bs+1, sizeof(double));
            bs_count(bs_frequency, p_bs, n_bs, k_bs);
            sum_of_states=0;
            for (k=0;k<=n_bs;k=k+1){
                sum_of_states=sum_of_states+p_bs[k];
            }
            free(bs_frequency);
            free(p_bs);
            /*Calculate density of states in reactant well*/
            n_bs=j-well_energy;
            k_bs=n_modes-1;
            bs_frequency=(int*)calloc(k_bs+1, sizeof(int));
            for (k=0;k<=k_bs;k=k+1){
                bs_frequency[k]=well_frequency[k];
            }
            p_bs=(double*)calloc(n_bs+1, sizeof(double));
```

```
            bs_count(bs_frequency, p_bs, n_bs, k_bs);
            density_of_states=p_bs[n_bs]/bs_quantum;
            free(p_bs);
            free(bs_frequency);
            k_wp[i_tsl][j]=sum_of_states/(h_planck*density_of_states);
            matrix_J[j][j]=matrix_J[j][j]-k_wp[i_tsl][j];
        }
} /*Is the new end of the loop over i_tsl.*/
/*Now initialise the population at t_amb[i_temp]*/
printf("Calculating initial population at %.2lf K\n", t_amb[i_temp]);
    n_bs=n_levels-well_energy;
    k_bs=n_modes-1;
    bs_frequency=(int*)calloc(k_bs+1, sizeof(int));
    for (j=0;j<=k_bs;j=j+1){
        bs_frequency[j]=well_frequency[j];
    }
    p_bs=(double*)calloc(n_bs+1, sizeof(double));
    bs_count(bs_frequency, p_bs, n_bs, k_bs);
    for (j=0; j<n_levels;j=j+1){
        if (j<well_energy){
            well[j]=0;
        }
        else {
        well[j]=(p_bs[j-well_energy]*pow(euler, (-(j-well_energy)*bs_quantum*
            h_planckSI*c_light*100)/(k_boltz*t_amb[i_temp])));
        }
    }
    free(p_bs);
    free(bs_frequency);
/*Now normalise the initial population:*/
    population=0;
    for (j=0;j<n_levels;j=j+1){
        population=population+well[j];
    }
    for (j=0;j<n_levels;j=j+1){
        well[j]=well[j]/population;
    }
printf("Writing matrix_J to file\n");
matrix_J_pointer=fopen("matrix_J.txt", "w");
for (i=0;i<n_levels;i=i+1){
```

```
    for (j=0;j<n_levels;j=j+1){
     fprintf(matrix_J_pointer, "%.12lf\n", matrix_J[i][j]);
    }
}
fclose(matrix_J_pointer);
/*Using eigenvalue calculated in matlab to obtain steady-state population*/
printf("Enter lambda_0 as calculated in matlab:\n");
printf("(Enter 0 if eigenvalue is not yet calculated)\n");
scanf("%lf", &lambda_0);
printf("You entered lambda_0=%lf\n", lambda_0);
if (lambda_0==0){
    printf("You entered an eigenvalue of zero; programme will be terminated.");
    break;
}
for (i=0;i<n_levels;i=i+1){ /*Find (A-lambdaI)x=0*/
    matrix_J[i][i]=matrix_J[i][i]-lambda_0;
}
/*Use Gaussian elimination to solve; after Sureshkumar and McRae, MIT, 1997.*/
for (i=0;i<n_levels;i=i+1){ /*Loop over each column in turn*/
    q=fabs(matrix_J[i][i]); /*Initial guess at 'largest pivot'*/
    m=i; /*Dummy variable stores row with largest pivot in column i*/
    for (j=(i+1);j<n_levels;j=j+1){
        if (fabs(matrix_J[j][i])>q){
            q=fabs(matrix_J[j][i]);
            m=j;
        }
    }
    if (m !=i){ /*If there's a larger pivot in column i below row i, swap rows*/
        printf("swap rows %d and %d:\n", i, m);
        for (j=0;j<n_levels;j=j+1){
            temp=matrix_J[i][j];
            matrix_J[i][j]=matrix_J[m][j];
            matrix_J[m][j]=temp;
        }
    }
    /*Now element i,i is larger than all elements j>=i,i make all j>i,i 0*/
    for (j=(i+1);j<n_levels;j=j+1){ /*j is now an index over all rows below i*/
        if (matrix_J[j][i] !=0){
            q=matrix_J[j][i]/matrix_J[i][i];
            for (k=0;k<n_levels;k=k+1){ /*k is an index over columns here*/
```

```
                matrix_J[j][k]=matrix_J[j][k]-q*matrix_J[i][k];
            }
        }
    }
} /*Close loop over the number of columns*/
/*Calculate the eigenvector B, the steady-state population*/
for (i=0;i<(n_levels-1);i=i+1){
    j=n_levels-i-1;
    eigenvector_B[j]=matrix_J[j][n_levels-1];
    for (k=j+1;k<(n_levels-1);k=k+1){
        eigenvector_B[j]=eigenvector_B[j]+matrix_J[j][k]*eigenvector_B[k];
    }
    eigenvector_B[j]=-eigenvector_B[j]/matrix_J[j][j];
}
eigenvector_B[n_levels-1]=eigenvector_B[n_levels-2]; /*J is overdetermined so the
     largest number cannot be found*/
/*Finally, normalise:*/
population=0;
for (i=0;i<n_levels;i=i+1){
    population=population+eigenvector_B[i];
}
for (i=0;i<n_levels;i=i+1){
    eigenvector_B[i]=eigenvector_B[i]/population;
}
/*Print out the population(s) calculated*/
population_pointer=fopen("population.txt", "a+");
fprintf(population_pointer, "temperature = %.2lf\n\n", t_amb[i_temp]);
fprintf(population_pointer, "Initial population:\n\n");
    for (j=0;j<n_levels;j=j+1){
        fprintf(population_pointer, "well[%d]=%lf\n", j, well[j]);
    }
fprintf(population_pointer, "\nFinal population:\n\n");
    for (j=0;j<n_levels;j=j+1){
        fprintf(population_pointer, "eigenvector_B[%d]=%lf\n", j, eigenvector_B[j
            ]);
    }
fprintf(population_pointer, "\n\n");
fclose(population_pointer);
} /*end of loop over n_temp (index i_temp*/
getchar();
```

```
return 0;
}

int bs_count(int * bs_frequency, double * p_bs, int n_bs, int k_bs)
{
int flag_bs, i_bs, j_bs, jp1_bs, m_bs, mmj_bs; /*Define the variables needed:*/
flag_bs=0;
for (i_bs=0; i_bs<=k_bs; i_bs=i_bs+1)
    {
    if ((bs_frequency[i_bs]>n_bs)&&(flag_bs==0))
        { /*vib. frequencies exceeding n_bs are excluded. */
        k_bs=i_bs-1;
        flag_bs=1;
        }
    }
for (i_bs=0; i_bs<=k_bs; i_bs=i_bs+1) /*Now for the bs algorithm itself.*/
    {
    j_bs=bs_frequency[i_bs];
    jp1_bs=j_bs+1;
    if (j_bs<=n_bs)
        {
            p_bs[j_bs]=p_bs[j_bs]+1;
        }
    for (m_bs=jp1_bs; m_bs<=n_bs; m_bs=m_bs+1)
        {
        mmj_bs=m_bs-j_bs;
        if ((m_bs<=n_bs)&&(mmj_bs<=n_bs))
            {
                p_bs[m_bs]=p_bs[m_bs]+p_bs[mmj_bs];
            }
        }
    }
p_bs[0]=1;
return 0;
}
```

B.2 Truncated Boltzmann method

This C programme calculates the steady-state population obtained after truncating the non-reacting Boltzmann population at a given threshold. The rate of reaction is calculated from this population. The code is identical to that given above up to line 158, and this section will not be reproduced. The new parameters are defined using the following code.

```
double* exact_cutoffs; /*Boundaries between regions of parameterised distribution */
exact_cutoffs=(double*)malloc((2*n_N2O+3)*sizeof(double));
    exact_cutoffs[0]=ZPE_well_0; /*Fill the array exact_cutoffs*/
    exact_cutoffs[2*n_N2O+1]=tsp_energy[0];
    exact_cutoffs[2*n_N2O+2]=maximum_energy;
    for (j=1;j<=n_N2O;j=j+1){
        exact_cutoffs[j]=tsp_energy[0]-2*exact_frequency[n_modes-n_N2O-j];
        exact_cutoffs[j+n_N2O]=tsp_energy[0]-exact_frequency[n_modes-n_N2O-j];
    }
/*Remove parameter boundaries which are extremely close together*/
int n_parameters;
n_parameters=2*n_N2O+2;
    for (j=0;j<(2*n_N2O+1);j=j+1){
        if ((exact_cutoffs[j+1]-exact_cutoffs[j])<2*bs_quantum){
            n_parameters=n_parameters-1;
            printf("exact_cutoffs[%d]=%lf is within 2bsq of exact_cutoffs[%d]=%lf
                 hence n_parameters=%d\n", j+1, exact_cutoffs[j+1], j,
                exact_cutoffs[j], n_parameters);
        }
    }
/*Allocate the arrays which have n_parameters as a dimension*/
int* cutoffs;
cutoffs=(int*)malloc(n_parameters*sizeof(int));
double** matrix_A; /*Matrix of popln coefficients from P(E)r/P(E)nr ratio*/
matrix_A=(double**)malloc(n_parameters*sizeof(double));
for (i=0;i<n_parameters;i=i+1){
    matrix_A[i]=(double*)malloc(n_parameters*sizeof(double));
}
double** matrix_a2; /*Unknown coefficients of our population*/
matrix_a2=(double**)malloc((n_parameters-2)*sizeof(double));
for (i=0;i<(n_parameters-2);i=i+1){
    matrix_a2[i]=(double*)malloc((n_parameters-2)*sizeof(double));
```

```
}
double* vector_b; /*Vector; the RHS of the matrix equation*/
vector_b=(double*)malloc((n_parameters-2)*sizeof(double));
double* well_coefficients; /*Vector of population parameters*/
well_coefficients=(double*)malloc(n_parameters*sizeof(double));
/*Fill array cutoffs[n_wells][n_parameters]*/
k=0;
    cutoffs[0]=(int)(exact_cutoffs[0]/bs_quantum+0.5);
    for (j=1; j<(2*n_N2O+3);j=j+1){
        if ((exact_cutoffs[j]-exact_cutoffs[j-1])>=2*bs_quantum){
            cutoffs[j-k]=(int)(exact_cutoffs[j]/bs_quantum+0.5);
        }
        else {
            k=k+1;
        }
    }
/*Write input to a file.*/
FILE *input_pointer;
input_pointer=fopen("input.txt", "w");
fprintf(input_pointer, "n_modes = %d\nn_N2O = %d\n\n", n_modes, n_N2O); /*
    Reactant parameters*/
fprintf(input_pointer, "n_tsl=%d\n", n_tsl); /*Transition state parameters*/
for (i=0;i<n_tsl;i=i+1){
    fprintf(input_pointer, "tsp_energy[%d] = %lf\n", i, tsp_energy[i]);
}
fprintf(input_pointer, "\nbs_quantum = %lf\nmaximum_energy = %lf\nn_levels = %d\
    nn_temp = %d\nscale_factor = %lf\n\n", bs_quantum, maximum_energy, n_levels,
    n_temp, scale_factor);
for (i=0;i<n_temp;i=i+1){
    fprintf(input_pointer, "t_amb[%d]=%lf\n", i, t_amb[i]);
}
fprintf(input_pointer, "\nZPE_energy_0 = %lf\n\n", ZPE_well_0);
    for (j=0;j<n_modes;j=j+1){
        fprintf(input_pointer, "exact_frequency[%d]=%lf well_frequency[%d]=%d
            well_intensity[%d]=%lf\n", j, exact_frequency[j], j, well_frequency[j
            ], j, well_intensity[j]);
    }
    fprintf(input_pointer, "\n");
for (i=0;i<n_tsl;i=i+1){
    for(j=0;j<(n_modes-1);j=j+1){
```

```
        fprintf(input_pointer, "tsp_exact_frequency[%d][%d]=%lf tsp_frequency[%d
            ][%d]=%d\n", i, j, tsp_exact_frequency[i][j], i, j, tsp_frequency[i][
            j]);
    }
    fprintf(input_pointer, "\n");
}
    for (j=0;j<(2*n_N2O+3);j=j+1){
        fprintf(input_pointer, "exact_cutoffs[%d]=%lf\n", j, exact_cutoffs[j]);
    }
    fprintf(input_pointer, "\n");
    for (j=0;j<n_parameters;j=j+1){
        fprintf(input_pointer, "cutoffs[%d]=%d\n", j, cutoffs[j]);
    }
    fprintf(input_pointer, "\n");
fclose(input_pointer);
printf("The input has been written to file\n");
/*Open the loop over temperature*/
int i_temp; /*Index allowing loop over temperature*/
FILE *Einstein_coeff_pointer;
int n_bs;
int k_bs;
double sum_of_states;
double pkm;
double k_abs;
double k_emm;
int j_new;
double * p_bs;        /*p_bs array pointer*/
int * bs_frequency;    /*bs_frequency array pointer*/
int i_tsl; /*Index allowing loop over transition states*/
int tsl_start; /*Variable to convert E barriers to bs_quantum*/
double density_of_states;
double population;
double divisor;
double temp;
FILE * k_wp_pointer;
FILE * population_pointer;
FILE * matrix_A_pointer;
FILE * population_parameters;
FILE * rate_printout;
```

Having generated the new matrices required, the code becomes the same as that in the previous section, lines 210-364, wherein the radiative and reactive rates are calculated, along with the initial population. Rates are not copied to a matrix **J**, however, so lines 284, 285, 296, 297, and 334 are excluded. The subsequent calculation of the coefficients relating the truncated to the non-reactive distribution is described in the following code.

```
for (j=0;j<n_parameters;j=j+1){ /*Set elements of matrix_A to zero*/
        for (k=0;k<n_parameters;k=k+1){
            matrix_A[j][k]=0;
        }
    }
/*Fill matrix_A with the coefficients of our population parameters*/
    matrix_A[0][0]=cutoffs[1]-cutoffs[0];
    printf("matrix_A[0][0]=%d-%d=%lf\n", cutoffs[1], cutoffs[0], matrix_A[0][0]);
    for (j=1;j<(n_parameters-1);j=j+1){
        for (k=cutoffs[j];k<cutoffs[j+1];k=k+1){ /*Calculate P(E=k) in the
            absence of reaction and assign it to temporary variable 'divisor'*/
            divisor=0;
            for (m=1;m<=n_N2O;m=m+1){
                k0=n_modes-n_N2O-m;
                divisor=divisor+k_rad_abs[k][k-well_frequency[k0]]*well[k-
                    well_frequency[k0]]+k_rad_emm[k][k+well_frequency[k0]]*well[k
                    +well_frequency[k0]];
            }
            for (m=1;m<=n_N2O;m=m+1){ /*Calculate the contribution to P(E=k), in
                the presence of reaction, due to absorption*/
                n=0;
                k0=n_modes-n_N2O-m;
                if ((k-well_frequency[k0])>=cutoffs[n+1]){
                    n=n+1;
                }
                matrix_A[j][n]=matrix_A[j][n]+k_rad_abs[k][k-well_frequency[k0]]*
                    well[k-well_frequency[k0]]/divisor;
            }
            for (m=1;m<=n_N2O;m=m+1){ /*Calculate the contribution to P(E=k), in
                the presence of reaction, due to emission*/
                n=n_parameters-1;
                k0=n_modes-n_N2O-m;
                if ((k+well_frequency[k0])<cutoffs[n]){
                    n=n-1;
```

```
                }
                matrix_A[j][n]=matrix_A[j][n]+k_rad_emm[k][k+well_frequency[k0]]*
                    well[k+well_frequency[k0]]/divisor;
            }
        }
    }
    /*Convert matrix to the form Ax=0 by taking away diagonal matrix of coeffs*/
    for (j=0;j<n_parameters;j=j+1){
        matrix_A[j][j]=matrix_A[j][j]-(cutoffs[j+1]-cutoffs[j]);
    }
matrix_A_pointer=fopen("matrix_A.txt", "a+"); /*Print matrix A*/
fprintf(matrix_A_pointer, "t_amb[%d]=%.2lf\n n_parameters=%d\n\n", i_temp, t_amb[
    i_temp], n_parameters);
fprintf(matrix_A_pointer, "Before manipulation, matrix_A[%d][%d] is:\n\n",
    n_parameters, n_parameters);
    for (j=0;j<n_parameters;j=j+1){
            for (k=0;k<n_parameters;k=k+1){
        fprintf(matrix_A_pointer, "%lf     ", matrix_A[j][k]);
    }
    fprintf(matrix_A_pointer, "\n");
}
fclose(matrix_A_pointer);

/*Now extract matrix_a2 and vector_b out of matrix_A; removes the 0 and 1
    coefficients which would otherwise make it impossible to find a solution*/
    for (j=1;j<(n_parameters-1);j=j+1){
        vector_b[j-1]=-matrix_A[j][0];
        for (k=1;k<(n_parameters-1);k=k+1){
            matrix_a2[j-1][k-1]=matrix_A[j][k];
        }
    }
matrix_A_pointer=fopen("matrix_A.txt", "a+"); /*Print matrix_a2*/
fprintf(matrix_A_pointer, "\n\n Reduced matrix_a2 and vector b are:\n");
    for (j=0;j<(n_parameters-2);j=j+1){
            fprintf(matrix_A_pointer, "b[%d]=%.3lf", j, vector_b[j]);
            fprintf(matrix_A_pointer, "      matrix_a2 row %d:  ", j);
            for (k=0;k<(n_parameters-2);k=k+1){
        fprintf(matrix_A_pointer, "%3.3lf     ", matrix_a2[j][k]);
    }
    fprintf(matrix_A_pointer, "\n");
```

```
}
fclose(matrix_A_pointer);
/*Pivot and solve matrix_a2.  After program 'Gauss', R. Sureshkumar (MIT) 10th
    January 1997,   Modified by J. McRae (MIT) 22nd October 1997*/
    for (j=0;j<(n_parameters-2);j=j+1){ /*Loop over each column in turn*/
        q=fabs(matrix_a2[j][j]); /*Initial 'largest pivot' is variable q*/
        printf("The initial guess at largest pivot is: fabs(matrix_a2[%d][%d])=%
            lf\n", j, j, q);
        m=j; /*stores the row which contains the largest pivot*/
        for (k=(j+1);k<(n_parameters-2);k=k+1){
            if (fabs(matrix_a2[k][j])>q){
                q=fabs(matrix_a2[k][j]);
                printf("Row change: q=%lf in column %d\n", q, j);
                m=k;
            }
        }
        if (m !=j){ /*If larger pivot in col. j below row j, swap rows*/
            printf("Swap rows %d and %d\n", m, j);
            temp=vector_b[j];
            vector_b[j]=vector_b[m];
            vector_b[m]=temp;
            for (k=0;k<(n_parameters-2);k=k+1){
                temp=matrix_a2[j][k];
                matrix_a2[j][k]=matrix_a2[m][k];
                matrix_a2[m][k]=temp;
            }
            printf("new row j=%d is:\n", j);
            printf("(vector_b[%d]=%lf)\n", j, vector_b[j]);
            for (k=0;k<(n_parameters-2);k=k+1){
                printf("%lf   ", matrix_a2[j][k]);
            }
            printf("\nnew row m=%d\n", m);
            printf("(vector_b[%d]=%lf)\n", m, vector_b[m]);
            for (k=0;k<(n_parameters-2);k=k+1){
                printf("%lf   ", matrix_a2[m][k]);
            }
        }
        /*Now jj is larger than all j>i,j make all j>i,j zero*/
        for (k=(j+1);k<(n_parameters-2);k=k+1){ /*k is index over rows below j*/
            if (matrix_a2[k][j] !=0){
```

```
            q=matrix_a2[k][j]/matrix_a2[j][j];
            printf("matrix_a2[%d][%d]=%lf, matrix_a2[%d][%d], q=%lf\n", k, j,
                matrix_a2[k][j], j, j, matrix_a2[j][j], q);
            vector_b[k]=vector_b[k]-q*vector_b[j];
            for (m=0;m<(n_parameters-2);m=m+1){ /*m is now a column index*/
                matrix_a2[k][m]=matrix_a2[k][m]-q*matrix_a2[j][m];
            }
            }
        }
    } /*Close loop over number of columns*/
/*Print out matrix after Gaussian elimination*/
matrix_A_pointer=fopen("matrix_A.txt", "a+");
fprintf(matrix_A_pointer, "\n After Gaussian elimination, vector_b and matrix_a2
    are:\n\n");
    for (j=0;j<(n_parameters-2);j=j+1){
            fprintf(matrix_A_pointer, "vector_b[%d]=%lf       matrix_a2 row %d:
                  ", j, vector_b[j], j);
            for (k=0;k<(n_parameters-2);k=k+1){
                fprintf(matrix_A_pointer, "%lf     ", matrix_a2[j][k]);
            }
        fprintf(matrix_A_pointer, "\n");
    }
fclose(matrix_A_pointer);
/*Now solve the simultaneous equations*/
    well_coefficients[0]=1;
    well_coefficients[n_parameters-1]=0;
    for (j=1;j<(n_parameters-1);j=j+1){
        k=n_parameters-j-1;
        well_coefficients[k]=vector_b[k-1];
        for (n=k+1;n<(n_parameters-1);n=n+1){
            well_coefficients[k]=well_coefficients[k]-matrix_a2[k-1][n-1]*
                well_coefficients[n];
        }
        well_coefficients[k]=well_coefficients[k]/matrix_a2[k-1][k-1];
    }
    for (j=0;j<n_parameters;j=j+1){
        printf("well_coefficient[%d]=%lf\n", j, well_coefficients[j]);
    }
/*Now print the well coefficients to file*/
population_parameters=fopen("population_parameters.txt", "a+");
```

```
fprintf(population_parameters, "at t_amb[%d]=%.2lf, the population parameters
    calculated are:\n", i_temp, t_amb[i_temp]);
    for (j=0;j<(n_parameters-1);j=j+1){
        fprintf(population_parameters, "For E<%d, well_coefficients[%d]=%lf\n",
            cutoffs[j+1], j, well_coefficients[j]);
    }
    fprintf(population_parameters, "For E>=%d, well_coefficients[%d]=%lf\n\n",
        cutoffs[n_parameters-1], n_parameters-1, well_coefficients[n_parameters
        -1]);
fclose(population_parameters);
/*Calculate population in presence of reaction, and write to file*/
    population=0;
    for (j=0;j<(n_parameters-1);j=j+1){
        for (k=cutoffs[j];k<cutoffs[j+1];k=k+1){
            final_well[k]=well[k]*well_coefficients[j];
            population=population+final_well[k];
        }
    }
    for (k=cutoffs[n_parameters-1];k<n_levels;k=k+1){
        final_well[k]=well[k]*well_coefficients[n_parameters-1];
    }
    for (j=0;j<n_levels;j=j+1){ /*Normalise population*/
        final_well[j]=final_well[j]/population;
    }
population_pointer=fopen("population.txt", "a+");
fprintf(population_pointer, "temperature = %.2lf\n\n", t_amb[i_temp]);
fprintf(population_pointer, "Initial population:\n\n");
    for (j=0;j<n_levels;j=j+1){
        fprintf(population_pointer, "well[%d]=%lf\n", j, well[j]);
    }
fprintf(population_pointer, "\nFinal population:\n\n");
    for (j=0;j<n_levels;j=j+1){
        fprintf(population_pointer, "final_well[%d]=%lf\n", j, final_well[j]);
    }
fprintf(population_pointer, "\n\n");
fclose(population_pointer);
/*Calculate the rate of product formation & distribution*/
for (i=0;i<n_tsl;i=i+1){ /*Set amount of product formed to zero*/
    dprod[i]=0;
}
```

```
k0=(int)(tsp_energy[0]/bs_quantum+0.5); /*This is the effective barrier*/
    for (j=k0;j<n_levels;j=j+1){
        for (k=0;k<k0;k=k+1){
            divisor=0;
            for (i_tsl=0;i_tsl<n_tsl;i_tsl=i_tsl+1){
                divisor=divisor+k_wp[i_tsl][j];
            }
            for (i_tsl=0;i_tsl<n_tsl;i_tsl=i_tsl+1){
                dprod[i_tsl]=dprod[i_tsl]+k_rad_abs[j][k]*final_well[k]*k_wp[
                    i_tsl][j]/divisor;
            }
        }
    }
    printf("dprod[0]=%lf, dprod[1]=%lf\n", dprod[0], dprod[1]);
/*Check total rate equals rate of absorption across the barrier*/
q=0;
k0=(int)(tsp_energy[0]/bs_quantum+0.5);
    for (j=k0;j<n_levels;j=j+1){
        for (k=0;k<k0;k=k+1){
            q=q+k_rad_abs[j][k]*final_well[k];
        }
    }
printf("total amount of product = %lf\n", q);
/*Now write all of these to file.*/
rate_printout=fopen("Calculated_rate.txt", "a+");
fprintf(rate_printout, "Temperature = %.2lf K\n", t_amb[i_temp]);
fprintf(rate_printout, "total rate = %lf\n", q);
fprintf(rate_printout, "Rates by channel:\n");
for (i_tsl=0;i_tsl<n_tsl;i_tsl=i_tsl+1){
        printf("dprod[%d]=%lf\n", i_tsl, dprod[i_tsl]);
    fprintf(rate_printout, "channel %d: %lf\n", i_tsl, dprod[i_tsl]);
}
fprintf(rate_printout, "\n");
fclose(rate_printout);
```

Finally, the closure of the loops over temperature and the main programme, and the sub-routine containing the Beyer-Swinehart algorithm, are the same as in the code above, lines 444-480, and will not be repeated here.

Bibliography

[1] W. A. de Heer. The physics of simple metal clusters: experimental aspects and simple models. *Reviews of Modern Physics*, 65(3):611, 1993.

[2] P. Jena and A. W. Castleman. Clusters: A bridge across the disciplines of physics and chemistry. *Proceedings of the National Academy of Sciences*, 103(28):10560–10569, 2006.

[3] M. D. Morse. Clusters of transition-metal atoms. *Chemical Reviews*, 86(6):1049–1109, 1986.

[4] H. Hahn and R. S. Averback. The production of nanocrystalline powders by magnetron sputtering. *Journal of Applied Physics*, 67(2):1113–1115, 1990.

[5] H. Takagi, H. Ogawa, Y. Yamazaki, A. Ishizaki, and T. Nakagiri. Quantum size effects on photoluminescence in ultrafine Si particles. *Applied Physics Letters*, 56(24):2379–2380, 1990.

[6] A. J. Cox, J. G. Louderback, and L. A. Bloomfield. Experimental observation of magnetism in rhodium clusters. *Physical review letters*, 71(6):923, 1993.

[7] P. Schnabel, M. Irion, and K. G. Weil. Evidence for low-pressure catalysis in the gas phase by a naked metal cluster: the growth of benzene precursors on iron (Fe_4^+). *The Journal of Physical Chemistry*, 95(24):9688–9694, 1991.

[8] H. Häkkinen, S. Abbet, A. Sanchez, U. Heiz, and U. Landman. Structural, electronic, and impurity-doping effects in nanoscale chemistry: supported gold nanoclusters. *Angewandte Chemie International Edition*, 42(11):1297–1300, 2003.

[9] A. Perez, P. Melinon, V. Dupuis, P. Jensen, B. Prevel, J. Tuaillon, L. Bardotti, C. Martet, M. Treilleux, and M. Broyer. Cluster assembled materials: a novel class of nanostructured solids with original structures and properties. *Journal of Physics D: Applied Physics*, 30(5):709, 1997.

[10] S. H. Baker, S. C. Thornton, K. W. Edmonds, M. J. Maher, C. Norris, and C. Binns. The construction of a gas aggregation source for the preparation of size-selected nanoscale transition metal clusters. *Review of Scientific Instruments*, 71(8):3178–3183, 2000.

[11] A. Cho. Connecting the dots to custom catalysts. *Science*, 299(5613):1684–1685, 2003.

[12] A. T. Bell. The impact of nanoscience on heterogeneous catalysis. *Science*, 299(5613):1688–1691, 2003.

[13] L. A. DeLouise and N. Winograd. Adsorption and desorption of NO from Rh(111) and Rh(331) surfaces. *Surface Science*, 159(1):199–213, 1985.

[14] A. W. Castleman Jr. Cluster structure and reactions: gaining insights into catalytic processes. *Catalysis letters*, 141(9):1243–1253, 2011.

[15] O. P. Balaj, I. Balteanu, T. J. Roßteuscher, M. K. Beyer, and V. E. Bondybey. Catalytic oxidation of CO with N_2O on gas-phase platinum clusters. *Angewandte Chemie International Edition*, 43(47):6519–6522, 2004.

[16] A. Yamada, K. Miyajima, and F. Mafuné. Catalytic reactions on neutral Rh oxide clusters more efficient than on neutral Rh clusters. *Physical Chemistry Chemical Physics*, 14(12):4188–4195, 2012.

[17] M. Haruta. Size-and support-dependency in the catalysis of gold. *Catalysis Today*, 36(1):153–166, 1997.

[18] M. Valden, X. Lai, and D. W. Goodman. Onset of catalytic activity of gold clusters on titania with the appearance of nonmetallic properties. *Science*, 281(5383):1647–1650, 1998.

[19] D. J. Harding and A. Fielicke. Platinum group metal clusters: From gas-phase structures and reactivities towards model catalysts. *Chemistry-A European Journal*, 20(12):3258–3267, 2014.

[20] S. M. Lang, T. M. Bernhardt, M. Krstić, and V. Bonačić-Koutecký. The origin of the selectivity and activity of ruthenium-cluster catalysts for fuel-cell feed-gas purification: A gas-phase approach. *Angewandte Chemie International Edition*, 53(21):5467–5471, 2014.

[21] D. Harding, M. S. Ford, T. R. Walsh, and S. R. Mackenzie. Dramatic size effects and evidence of structural isomers in the reactions of rhodium clusters, $Rh_n^{\pm}$, with nitrous oxide. *Physical Chemistry Chemical Physics*, 9(17):2130–2136, 2007.

[22] J. L. Elkind, F. D. Weiss, J. M. Alford, R. T. Laaksonen, and R. E. Smalley. Fourier transform ion cyclotron resonance studies of H_2 chemisorption on niobium cluster cations. *The Journal of chemical physics*, 88(8):5215–5224, 1988.

[23] C. Adlhart and E. Uggerud. C-H activation of alkanes on Rh_n^+ (n=1-30) clusters: size effects on dehydrogenation. *The Journal of chemical physics*, 123(21):214709–214709, 2005.

[24] I. Balteanu, O. P. Balaj, M. K. Beyer, and V. E. Bondybey. Size-dependent dehydrogenation of ethane by cationic rhodium clusters in the gas phase. *International Journal of Mass Spectrometry*, 255:71–75, 2006.

[25] D. M. Cox, P. Fayet, R. Brickman, M. Y. Hahn, and A. Kaldor. Abnormally large deuterium uptake on small transition metal clusters. *Catalysis letters*, 4(4-6):271–278, 1990.

[26] M. S. Ford, M. L. Anderson, M. P. Barrow, D. P. Woodruff, T. Drewello, P. J. Derrick, and S. R. Mackenzie. Reactions of nitric oxide on Rh_6^+ clusters: abundant chemistry and evidence of structural isomers. *Physical Chemistry Chemical Physics*, 7(5):975–980, 2005.

[27] A. Bérces, P. A. Hackett, L. Lian, S. A. Mitchell, and D. M. Rayner. Reactivity of niobium clusters with nitrogen and deuterium. *Journal of Chemical Physics*, 108:5476–5490, 1998.

[28] L. Lian, C. Su, and P. B. Armentrout. Collision-induced dissociation of Fe_n^+ (n= 2–19) with Xe: Bond energies, geometric structures, and dissociation pathways. *The Journal of chemical physics*, 97(6):4072–4083, 1992.

[29] M. B. Knickelbein. Electronic shell structure in the ionization potentials of copper clusters. *Chemical physics letters*, 192(1):129–134, 1992.

[30] K. J. Taylor, C. L. Pettiette-Hall, O. Cheshnovsky, and R. E. Smalley. Ultraviolet photoelectron spectra of coinage metal clusters. *The Journal of chemical physics*, 96(4):3319–3329, 1992.

[31] E. A. Rohlfing, D. M. Cox, and A. Kaldor. Photoionization measurements on isolated iron-atom clusters. *Chemical Physics Letters*, 99(2):161–166, 1983.

[32] S. Yang and M. B. Knickelbein. Photoionization studies of transition metal clusters: Ionization potentials for Fe_n and Co_n. *The Journal of Chemical Physics*, 93(3):1533–1539, 1990.

[33] I. M. Billas, A. Chatelain, and W. A. De Heer. Magnetism from the atom to the bulk in iron, cobalt, and nickel clusters. *Science*, 265(5179):1682–1684, 1994.

[34] D. C. Douglass, A. J. Cox, J. P. Bucher, and L. A. Bloomfield. Magnetic properties of free cobalt and gadolinium clusters. *Physical Review B*, 47(19):12874, 1993.

[35] B. V. Reddy, S. N. Khanna, and B. I. Dunlap. Giant magnetic moments in 4d clusters. *Physical review letters*, 70(21):3323, 1993.

[36] H. Zhai and L.-S. Wang. Probing the electronic structure of early transition metal oxide clusters: Molecular models towards mechanistic insights into oxide surfaces and catalysis. *Chemical Physics Letters*, 500(4):185–195, 2010.

[37] L.-S. Wang, H. Wu, S. R. Desai, and L. Lou. Electronic structure of small copper oxide clusters: From Cu_2O to Cu_2O_4. *Physical Review B*, 53(12):8028, 1996.

[38] P. B. Armentrout. Reactions and thermochemistry of small transition metal cluster ions. *Annual review of physical chemistry*, 52(1):423–461, 2001.

[39] C. J. Cramer and D. G. Truhlar. Density functional theory for transition metals and transition metal chemistry. *Physical Chemistry Chemical Physics*, 11(46):10757–10816, 2009.

[40] M. Witko and H. Beckmann. Ab initio MRD CI calculations for ground and excited states of Cu_2 molecule. *Molecular Physics*, 47(4):945–957, 1982.

[41] E. J. Robbins, R. E. Leckenby, and P. Willis. The ionization potentials of clustered sodium atoms. *Advances in Physics*, 16(64):739–744, 1967.

[42] S. Van De Meerakker, H. L. Bethlem, and G. Meijer. Taming molecular beams. *Nature Physics*, 4(8):595–602, 2008.

[43] D. R. Preuss, S. A. Pace, and J. L. Gole. The supersonic expansion of pure copper vapor. *The Journal of Chemical Physics*, 71(9):3553–3560, 1979.

[44] R. A. Larsen, S. K. Neoh, and D. R. Herschbach. Seeded supersonic alkali atom beams. *Review of Scientific Instruments*, 45(12):1511–1516, 1974.

[45] J. B. Anderson and J. B. Fenn. Velocity distributions in molecular beams from nozzle sources. *Physics of Fluids (1958-1988)*, 8(5):780–787, 1965.

[46] K. Sattler, J. Mühlbach, and E. Recknagel. Generation of metal clusters containing from 2 to 500 atoms. *Physical Review Letters*, 45(10):821, 1980.

[47] A. Wagner and T. M. Hall. Liquid gold ion source. *Journal of Vacuum Science & Technology*, 16(6):1871–1874, 1979.

[48] J. Ho, K. M. Ervin, and W. C. Lineberger. Photoelectron spectroscopy of metal cluster anions: Cu_n^-, Ag_n^-, and Au_n^-. *The Journal of chemical physics*, 93(10):6987–7002, 1990.

[49] I. Katakuse, T. Ichihara, Y. Fujita, T. Matsuo, T. Sakurai, and H. Matsuda. Mass distributions of copper, silver and gold clusters and electronic shell structure. *International journal of mass spectrometry and ion processes*, 67(2):229–236, 1985.

[50] S. Pratontep, S. J. Carroll, C. Xirouchaki, M. Streun, and R. E. Palmer. Size-selected cluster beam source based on radio frequency magnetron plasma sputtering and gas condensation. *Review of scientific instruments*, 76(4):045103, 2005.

[51] G. Ganteför C. Cha and W. Eberhardt. New experimental setup for photoelectron spectroscopy on cluster anions. *Review of scientific instruments*, 63(12):5661–5666, 1992.

[52] G. Ganteför, H. R. Siekmann, H. O. Lutz, and K. Meiwes-Broer. Pure metal and metal-doped rare-gas clusters grown in a pulsed arc cluster ion source. *Chemical Physics Letters*, 165(4):293–296, 1990.

[53] C-Y. Cha, G. Ganteför, and W. Eberhardt. Photoelectron spectroscopy of Cu_n^- clusters: Comparison with jellium model predictions. *The Journal of chemical physics*, 99(9):6308–6312, 1993.

[54] T. G. Dietz, M. A. Duncan, D. E. Powers, and R. E. Smalley. Laser production of supersonic metal cluster beams. *The Journal of Chemical Physics*, 74(11):6511–6512, 1981.

[55] V. E. Bondybey and J. H. English. Laser induced fluorescence of metal clusters produced by laser vaporization: Gas phase spectrum of Pb_2. *The Journal of Chemical Physics*, 74(12):6978–6979, 1981.

[56] M. A. Duncan. Invited review article: Laser vaporization cluster sources. *Review of Scientific Instruments*, 83(4):041101, 2012.

[57] S. Nonose, Y. Sone, K. Onodera, S. Sudo, and K. Kaya. Structure and reactivity of bimetallic cobalt-vanadium (Co_nV_m) clusters. *Journal of Physical Chemistry*, 94(7):2744–2746, 1990.

[58] S. C. O'Brien, Y. Liu, Q. Zhang, J. R. Heath, F. K. Tittel, R. F. Curl, and R. E. Smalley. Supersonic cluster beams of III–V semiconductors: Ga_xAs_y. *The Journal of chemical physics*, 84(7):4074–4079, 1986.

[59] A. Fielicke, A. Kirilyuk, C. Ratsch, J. Behler, M. Scheffler, G. von Helden, and G. Meijer. Structure determination of isolated metal clusters via far-infrared spectroscopy. *Physical review letters*, 93(2):023401, 2004.

[60] E. C. Honea, M. L. Homer, J. L. Persson, and R. L. Whetten. Generation and photoionization of cold Na_n clusters; n to 200. *Chemical Physics Letters*, 171(3):147–154, 1990.

[61] N. R. Walker, G. A. Grieves, J. B. Jaeger, R. S. Walters, and M. A. Duncan. Generation of "unstable" doubly charged metal ion complexes in a laser vaporization cluster source. *International Journal of Mass Spectrometry*, 228(2):285–295, 2003.

[62] P. Brucat, L.-S. Zheng, C. Pettiette, S. Yang, and R. E. Smalley. Metal cluster ion photofragmentation. *The Journal of chemical physics*, 84(6):3078–3088, 1986.

[63] A. O'Keefe, J. J. Scherer, A. L. Cooksy, R. Sheeks, J. Heath, and R. J. Saykally. Cavity ring down dye laser spectroscopy of jet-cooled metal clusters: Cu_2 and Cu_3. *Chemical Physics Letters*, 172(3):214–218, 1990.

[64] St. Becker, K. Dasgupta, G. Dietrich, H. Kluge, S. Kuznetsov, M. Lindinger, K. Lützenkirchen, L. Schweikhard, and J. Ziegler. A Penning trap mass spectrometer for the study of cluster ions. *Review of scientific instruments*, 66(10):4902–4910, 1995.

[65] S. Guan and A. G. Marshall. Ion traps for Fourier transform ion cyclotron resonance mass spectrometry: principles and design of geometric and electric configurations. *International journal of mass spectrometry and ion processes*, 146:261–296, 1995.

[66] M. Maier-Borst, D. B. Cameron, M. Rokni, and J. H. Parks. Electron diffraction of trapped cluster ions. *Physical Review A*, 59(5):R3162, 1999.

[67] C. Walther, St. Becker, C. Dietrich, H.-J. Kluge, M. Lindinger, K. Lützenkirchen, L. Schweikhard, and J. Ziegler. Photo fragmentation of metal clusters stored in a Penning trap. *Zeitschrift für Physik D Atoms, Molecules and Clusters*, 38(1):51–58, 1996.

[68] N. C. Polfer. Infrared multiple photon dissociation spectroscopy of trapped ions. *Chemical Society Reviews*, 40(5):2211–2221, 2011.

[69] I. S. Gilmore and M. P. Seah. Ion detection efficiency in SIMS: Dependencies on energy, mass and composition for microchannel plates used in mass spectrometry. *International Journal of Mass Spectrometry*, 202(1):217–229, 2000.

[70] W. D. Knight, K. Clemenger, W. A. de Heer, and W. A. Saunders. Polarizability of alkali clusters. *Physical Review B*, 31(4):2539, 1985.

[71] P. Weis. Structure determination of gaseous metal and semi-metal cluster ions by ion mobility spectrometry. *International Journal of Mass Spectrometry*, 245(1):1–13, 2005.

[72] M. F. Jarrold and J. E. Bower. Mobilities of metal cluster ions: Aluminum and the electronic shell model. *The Journal of chemical physics*, 98(3):2399–2407, 1993.

[73] P. Weis, T. Bierweiler, E. Vollmer, and M. M. Kappes. $Au_9^{(+)}$: Rapid isomerization reactions at 140 K. *Journal of Chemical Physics*, 117(20):9293–9297, 2002.

[74] D. Schooss, M. N. Blom, J. H. Parks, B. v Issendorff, H. Haberland, and M. M. Kappes. The structures of Ag_{55}^+ and Ag_{55}^-: Trapped ion electron diffraction and density functional theory. *Nano letters*, 5(10):1972–1977, 2005.

[75] A. Lechtken, C. Neiss, M. M. Kappes, and D. Schooss. Structure determination of gold clusters by trapped ion electron diffraction: Au_{14}^-–Au_{19}^-. *Physical Chemistry Chemical Physics*, 11(21):4344–4350, 2009.

[76] A. Lechtken, D. Schooss, J. R. Stairs, M. N. Blom, F. Furche, N. Morgner, O. Kostko, B. von Issendorff, and M. M. Kappes. Au_{34}^-: a chiral gold cluster? *Angewandte Chemie International Edition*, 46(16):2944–2948, 2007.

[77] W. D. Knight, K. Clemenger, W. A. de Heer, W. A. Saunders, M. Y. Chou, and M. L. Cohen. Electronic shell structure and abundances of sodium clusters. *Physical review letters*, 52(24):2141, 1984.

[78] W. Ekardt. Work function of small metal particles: Self-consistent spherical jellium-background model. *Physical Review B*, 29(4):1558, 1984.

[79] D. E. Powers, S. G. Hansen, M. E. Geusic, A. C. Puiu, J. B. Hopkins, T. G. Dietz, M. A. Duncan, P. R. R. Langridge-Smith, and R. E. Smalley. Supersonic metal cluster beams: laser photoionization studies of Cu_2. *The Journal of Physical Chemistry*, 86(14):2556–2560, 1982.

[80] D. E. Powers, S. G. Hansen, M. E. Geusic, D. L. Michalopoulos, and R. E. Smalley. Supersonic copper clusters. *The Journal of Chemical Physics*, 78(6):2866–2881, 1983.

[81] M. D. Morse, J. B. Hopkins, P. R. R. Langridge-Smith, and R. E. Smalley. Spectroscopic studies of the jet-cooled copper trimer. *The Journal of chemical physics*, 79(11):5316–5328, 1983.

[82] M. D. Morse, G. P. Hansen, P. R. R. Langridge-Smith, L. Zheng, M. E. Geusic, D. L. Michalopoulos, and R. E. Smalley. Spectroscopic studies of the jet-cooled nickel dimer. *The Journal of chemical physics*, 80(11):5400–5405, 1984.

[83] D. Yang and P. A. Hackett. ZEKE spectroscopy of free transition metal clusters. *Journal of Electron Spectroscopy and Related Phenomena*, 106(2):153–169, 2000.

[84] D. Yang, A. M. James, D. M. Rayner, and P. A. Hackett. Pulsed field ionization zero kinetic energy photoelectron spectroscopy of small vanadium clusters. Using velocity slip as a mass selector. *Chemical physics letters*, 231(2):177–182, 1994.

[85] K. F. Willey, C. S. Yeh, and M. A. Duncan. Mass-analyzed threshold ionization spectroscopy of Al-Ar. *Chemical physics letters*, 211(1):156–160, 1993.

[86] M. S. Ford and S. R. Mackenzie. Preparing transition-metal clusters in known structural forms: The mass-analyzed threshold ionization spectrum of V_3. *The Journal of chemical physics*, 123(8):084308, 2005.

[87] D. G. Leopold, J. Ho, and W. C. Lineberger. Photoelectron spectroscopy of mass-selected metal cluster anions. I. Cu_n^-, n= 1–10. *The Journal of chemical physics*, 86(4):1715–1726, 1987.

[88] C. L. Pettiette, S. H. Yang, M. J. Craycraft, J. Conceicao, R. T. Laaksonen, O. Cheshnovsky, and R. E. Smalley. Ultraviolet photoelectron spectroscopy of copper clusters. *The Journal of chemical physics*, 88(9):5377–5382, 1988.

[89] A. Schweizer, J. M. Weber, S. Gilb, H. Schneider, D. Schooss, and M. M. Kappes. Electronic photodissociation spectroscopy of $Au_4^+.Ar_n$, n= 0–4: Experiment and theory. *The Journal of chemical physics*, 119(7):3699–3710, 2003.

[90] G. Gregoire and M. A. Duncan. Infrared spectroscopy to probe structure and growth dynamics in Fe^+-$(CO_2)_n$ clusters. *The Journal of chemical physics*, 117(5):2120–2130, 2002.

[91] D. J. Harding, P. Gruene, M. Haertelt, G. Meijer, A. Fielicke, S. M. Hamilton, W. S. Hopkins, S. R. Mackenzie, S. P. Neville, and T. R. Walsh. Probing the structures of gas-phase rhodium cluster cations by far-infrared spectroscopy. *The Journal of chemical physics*, 133(21):214304, 2010.

[92] P. Gruene, D. M. Rayner, B. Redlich, A. van der Meer, J. T. Lyon, G. Meijer, and A. Fielicke. Structures of neutral Au_7, Au_{19}, and Au_{20} clusters in the gas phase. *Science*, 321(5889):674–676, 2008.

[93] A. Fielicke, G. von Helden, G. Meijer, D. P. Pedersen, B. Simard, and D. M. Rayner. Size and charge effects on the binding of CO to small isolated rhodium clusters. *The Journal of Physical Chemistry B*, 108(38):14591–14598, 2004.

[94] I. Swart, F. de Groot, B. M. Weckhuysen, D. M. Rayner, G. Meijer, and A. Fielicke. The effect of charge on CO binding in rhodium carbonyls: From bridging to terminal CO. *Journal of the American Chemical Society*, 130(7):2126–2127, 2008.

[95] A. Fielicke, G. von Helden, G. Meijer, D. B. Pedersen, B. Simard, and D. M. Rayner. Size and charge effects on the binding of CO to late transition metal clusters. *The Journal of chemical physics*, 124(19):194305, 2006.

[96] S. E. Rodriguez-Cruz, R. A. Jockusch, and E. R. Williams. Hydration energies of divalent metal ions, $Ca^{2+}(H_2O)_n$ (n= 5-7) and $Ni^{2+}(H_2O)_n$ (n= 6-8), obtained by blackbody infrared radiative dissociation. *Journal of the American Chemical Society*, 120(23):5842–5843, 1998.

[97] S. E. Rodriguez-Cruz, R. A. Jockusch, and E. R. Williams. Hydration energies and structures of alkaline earth metal ions, $M^{2+}(H_2O)_n$, n= 5-7, M= Mg, Ca, Sr, and Ba. *Journal of the American Chemical Society*, 121(38):8898–8906, 1999.

[98] S. Rodriguez-Cruz, R. A. Jockusch, and E. R. Williams. Binding energies of hexahydrated alkaline earth metal ions, $M^{2+}(H_2O)_6$, M= Mg, Ca, Sr, Ba: Evidence of isomeric structures for magnesium. *Journal of the American Chemical Society*, 121(9):1986–1987, 1999.

[99] M. B. Knickelbein. The copper trimer and its argon van der Waals complex: An anomalous shift in the $\tilde{A} \leftarrow \tilde{X}$ photodissociation spectrum. *The Journal of chemical physics*, 100(3):2388–2390, 1994.

[100] M. F. Jarrold and K. M. Creegan. Photodissociation of copper clusters, Cu_n^+(n= 3-8), in the 370-710 nm wavelength region. *International Journal of Mass Spectrometry and Ion Processes*, 102:161–181, 1990.

[101] K. F. Willey, D. L. Robbins, C. Yeh, and M. A. Duncan. Laser photodissociation spectroscopy of mass-selected metal clusters. *Faraday Discussions*, 92:269–277, 1991.

[102] K. LaiHing, P. Y. Cheng, T. G. Taylor, K. F. Willey, M. Peschke, and M. A. Duncan. Photodissociation in a reflectron time-of-flight mass spectrometer: a novel mass spectrometry/mass spectrometry configuration for high-mass systems. *Analytical Chemistry*, 61(13):1458–1460, 1989.

[103] J. R. Eyler. Infrared multiple photon dissociation spectroscopy of ions in Penning traps. *Mass spectrometry reviews*, 28(3):448–467, 2009.

[104] M. N. R. Ashfold, H. N. Nahler, A. J. Orr-Ewing, O. P. J. Vieuxmaire, R. L. Toomes, T. N. Kitsopoulos, I. A. Garcia, D. A. Chestakov, S.-M. Wu, and D. H. Parker. Imaging the dynamics of gas phase reactions. *Physical Chemistry Chemical Physics*, 8(1):26–53, 2006.

[105] W. S. Hopkins, S. M. Hamilton, P. D. McNaughter, and S. R. Mackenzie. VUV photodissociation dynamics of diatomic gold, Au_2: A velocity map imaging study at 157 nm. *Chemical Physics Letters*, 483(1):10–15, 2009.

[106] B. Baguenard, J. C. Pinaré, C. Bordas, and M. Broyer. Photoelectron imaging spectroscopy of small tungsten clusters: Direct observation of thermionic emission. *Physical Review A*, 63(2):023204, 2001.

[107] R. B. Cody and B. S. Freiser. Collision-induced dissociation in a Fourier-transform mass spectrometer. *International Journal of Mass Spectrometry and Ion Physics*, 41(3):199–204, 1982.

[108] St. Becker, G. Dietrich, H.-U. Hasse, N. Klisch, H.-J. Kluge, D. Kreisle, St. Krückeberg, M. Lindinger, K. Lützenkirchen, L. Schweikhard, H. Weidele, and J. Ziegler. Collision induced dissociation of stored gold cluster ions. *Zeitschrift für Physik D Atoms, Molecules and Clusters*, 30(4):341–348, 1994.

[109] S. C. Richtsmeier, E. K. Parks, K. Liu, L. G. Pobo, and S. J. Riley. Gas phase reactions of iron clusters with hydrogen. I. Kinetics. *The Journal of chemical physics*, 82(8):3659–3665, 1985.

[110] M. T. Rodgers, K. M. Ervin, and P. B. Armentrout. Statistical modeling of collision-induced dissociation thresholds. *The Journal of chemical physics*, 106(11):4499–4508, 1997.

[111] S. K. Loh, D. A. Hales, L. Lian, and P. B. Armentrout. Collision-induced dissociation of Fe_n^+ (n= 2–10) with Xe: Ionic and neutral iron binding energies. *The Journal of Chemical Physics*, 90(10):5466–5485, 1989.

[112] V. A. Spasov, T.-H. Lee, and K. M. Ervin. Threshold collision-induced dissociation of anionic copper clusters and copper cluster monocarbonyls. *Journal of Chemical Physics*, 112(4):1713–1720, 2000.

[113] L. Lian, C. Su, and P. B. Armentrout. Collision-induced dissociation of Ni_n^+ (n= 2–18) with Xe: Bond energies, geometrical structures, and dissociation pathways. *The Journal of chemical physics*, 96(10):7542–7554, 1992.

[114] O. Ingólfsson, U. Busolt, and K. Sugawara. Energy-resolved collision-induced dissociation of Cu_n^+ (n=2-9): Stability and fragmentation pathways. *Journal of Chemical Physics*, 112:4613–4620, 2000.

[115] S. Krückeberg, L. Schweikhard, J. Ziegler, G. Dietrich, K. Lützenkirchen, and C. Walther. Decay pathways and dissociation energies of copper clusters, Cu_n^+ ($2 \leq n \leq 25$), Cu_n^{2+} ($15 \leq n \leq 25$). *Journal of Chemical Physics*, 114:2955–2962, 2001.

[116] E. K. Parks, B. J. Winter, T. D. Klots, and S. J. Riley. The structure of nickel clusters. *The Journal of chemical physics*, 94(3):1882–1902, 1991.

[117] M. Beyer, C. Berg, G. Albert, U. Achatz, and V. E. Bondybey. Coordinative saturation of cationic niobium- and rhodium-argon complexes. *Chemical physics letters*, 280(5-6):459–463, 1997.

[118] E. K. Parks, B. H. Weiller, P. S. Bechthold, W. F. Hoffman, G. C. Nieman, L. G. Pobo, and S. J. Riley. Chemical probes of metal cluster structure: reactions of iron clusters with hydrogen, ammonia, and water. *The Journal of Chemical Physics*, 88(3):1622–1632, 1988.

[119] C. Berg, M. Beyer, T. Schindler, G. Niedner-Schatteburg, and V. E. Bondybey. Reactions of benzene with rhodium cluster cations: Competition between chemisorption and physisorption. *The Journal of chemical physics*, 104(20):7940–7946, 1996.

[120] M. R. Zakin, D. M. Cox, and A. Kaldor. Gas-phase rhodium cluster chemistry: Influence of adsorbate electronic structure on reaction rate. *The Journal of chemical physics*, 89(2):1201–1202, 1988.

[121] G. Kummerlöwe and M. K. Beyer. Rate estimates for collisions of ionic clusters with neutral reactant molecules. *International Journal of Mass Spectrometry*, 244(1):84–90, 2005.

[122] T. H. Lee and K. M. Ervin. Reactions of copper group cluster anions with oxygen and carbon monoxide. *The Journal of Physical Chemistry*, 98(40):10023–10031, 1994.

[123] C. Adlhart and E. Uggerud. Mechanisms of catalytic dehydrogenation of alkanes by rhodium clusters Rh_n^+ probed by isotope labelling. *International Journal of Mass Spectrometry*, 249:191–198, 2006.

[124] C. Berg, M. Beyer, U. Achatz, S. Joos, G. Niedner-Schatteburg, and V. E. Bondybey. Effect of charge upon metal cluster chemistry: Reactions of Nb_n and Rh_n anions and cations with benzene. *The Journal of chemical physics*, 108(13):5398–5403, 1998.

[125] M. Brack. The physics of simple metal clusters: self-consistent jellium model and semiclassical approaches. *Reviews of Modern Physics*, 65(3):677, 1993.

[126] K. Clemenger. Ellipsoidal shell structure in free-electron metal clusters. *Physical Review B*, 32(2):1359, 1985.

[127] P. Hohenberg and W. Kohn. Inhomogeneous electron gas. *Physical review*, 136(3B):B864, 1964.

[128] W. Kohn and L. J. Sham. Self-consistent equations including exchange and correlation effects. *Physical Review*, 140(4A):A1133, 1965.

[129] J. P. Perdew, A. Ruzsinszky, L. A. Constantin, J. Sun, and G. Csonka. Some fundamental issues in ground-state density functional theory: A guide for the perplexed. *Journal of Chemical Theory and Computation*, 5(4):902–908, 2009.

[130] S. Kurth and J. P. Perdew. Role of the exchange-correlation energy: Nature's glue. *International Journal of Quantum Chemistry*, 77(5):814–818, 2000.

[131] U. von Barth and L. Hedin. A local exchange-correlation potential for the spin polarized case. i. *Journal of Physics C: Solid State Physics*, 5(13):1629, 1972.

[132] J. P. Perdew, K. Burke, and M. Ernzerhof. Generalized gradient approximation made simple. *Physical review letters*, 77(18):3865, 1996.

[133] J. Tao, J. P. Perdew, V. N. Staroverov, and G. E. Scuseria. Climbing the density functional ladder: Nonempirical meta-generalized gradient approximation designed for molecules and solids. *Physical Review Letters*, 91(14):146401, 2003.

[134] V. N. Staroverov, G. E. Scuseria, J. Tao, and J. P. Perdew. Comparative assessment of a new nonempirical density functional: Molecules and hydrogen-bonded complexes. *The Journal of chemical physics*, 119(23):12129–12137, 2003.

[135] P. J. Feibelman, B. Hammer, J. K. Nørskov, F. Wagner, M. Scheffler, R. Stumpf, R. Watwe, and J. Dumesic. The CO/Pt (111) puzzle. *The Journal of Physical Chemistry B*, 105(18):4018–4025, 2001.

[136] H. Tatewaki, E. Miyoshi, and T. Nakamura. Electronic structure of small copper clusters. I. *The Journal of Chemical Physics*, 76(10):5073–5086, 1982.

[137] E. Miyoshi, H. Tatewaki, and T. Nakamura. Electronic structure of small copper clusters. II. Localized d hole in excited states and ionized states of Cu_2 and Cu_3. *The Journal of Chemical Physics*, 78(2):815–826, 1983.

[138] S. R. Langhoff, C. W. Bauschlicher Jr, S. P. Walch, and B. C. Laskowski. Ab initio study of the ground state surface of Cu_3. *The Journal of chemical physics*, 85(12):7211–7215, 1986.

[139] S. Lecoultre, A. Rydlo, C. Félix, J. Buttet, S. Gilb, and W. Harbich. Optical absorption of small copper clusters in neon: Cu_n,(n= 1–9). *The Journal of chemical physics*, 134(7):074303, 2011.

[140] B.N. Papas and H. F. Schaefer III. Homonuclear transition-metal trimers. *The Journal of chemical physics*, 123(7):074321, 2005.

[141] K. Baishya, J. C. Idrobo, S. Öğüt, M. Yang, K. A. Jackson, and J. Jellinek. First-principles absorption spectra of Cu_n (n=2-20) clusters. *Physical Review B*, 83(24):245402, 2011.

[142] I. S. Parry, A. C. Hermes, A. Kartouzian, and S. R. Mackenzie. Imaging the photodissociation dynamics of neutral metal clusters: copper dimer, Cu_2, and copper oxide, CuO. *Physical Chemistry Chemical Physics*, 16(2):458–466, 2014.

[143] A. T. J. B. Eppink and D. H. Parker. Velocity map imaging of ions and electrons using electrostatic lenses: Application in photoelectron and photofragment ion imaging of molecular oxygen. *Review of Scientific Instruments*, 68(9):3477–3484, 1997.

[144] D. W. Chandler and P. L. Houston. Two-dimensional imaging of state-selected photodissociation products detected by multiphoton ionization. *The Journal of chemical physics*, 87(2):1445–1447, 1987.

[145] D. H. Parker and A. T. J. B. Eppink. Photoelectron and photofragment velocity map imaging of state-selected molecular oxygen dissociation/ionization dynamics. *The Journal of chemical physics*, 107(7):2357–2362, 1997.

[146] P. C. Samartzis, B. L. G. Bakker, D. H. Parker, and T. N. Kitsopoulos. Photoelectron and photofragment velocity imaging following the excitation of CH_3I to the A-band using fs, ps, and ns laser pulses. *The Journal of Physical Chemistry A*, 103(31):6106–6113, 1999.

[147] K. T. Lorenz, M. S. Westley, and D. W. Chandler. Rotational state-to-state differential cross sections for the HCl–Ar collision system using velocity-mapped ion imaging. *Physical Chemistry Chemical Physics*, 2(4):481–494, 2000.

[148] R. Wester. Velocity map imaging of ion-molecule reactions. *Physical Chemistry Chemical Physics*, 16(2):396–405, 2014.

[149] M. Ahmed, D. S. Peterka, and A. G. Suits. H abstraction dynamics by crossed-beam velocity map imaging: Cl+ $CH_3OH \rightarrow CH_2OH$ + HCl. *Chemical Physics Letters*, 317(3):264–268, 2000.

[150] K. Tonokura and T. Suzuki. Slicing photofragment spatial distribution by laser sheet ionization. *Chemical physics letters*, 224(1):1–6, 1994.

[151] C. R. Gebhardt, T. P. Rakitzis, P. C. Samartzis, V. Ladopoulos, and T. N. Kitsopoulos. Slice imaging: A new approach to ion imaging and velocity mapping. *Review of Scientific Instruments*, 72(10):3848–3853, 2001.

[152] B. Baguenard, J. B. Wills, F. Pagliarulo, F. Lépine, B. Climen, M. Barbaire, C. Clavier, M. A. Lebeault, and C. Bordas. Velocity-map imaging electron spectrometer with time resolution. *Review of scientific instruments*, 75(2):324–328, 2004.

[153] D. A. Chestakov, S.-M. Wu, G. Wu, D. H. Parker, A. T. J. B. Eppink, and T. N. Kitsopoulos. Slicing using a conventional velocity map imaging setup: O_2, I_2, and I_2^+ photodissociation. *The Journal of Physical Chemistry A*, 108(39):8100–8105, 2004.

[154] H. Pan, J. Yang, Q. Shuai, D. Zhang, W. Zhang, G. Wu, D. Dai, B. Jiang, D. Zhang, and X. Yang. Velocity map imaging study of the reaction dynamics of the H+ CH_4 → H_2+ CH_3 reaction: the isotope effects. *The Journal of Physical Chemistry A*, 118(13):2426–2430, 2014.

[155] A. J. R. Heck and D. W. Chandler. Imaging techniques for the study of chemical reaction dynamics. *Annual review of physical chemistry*, 46(1):335–372, 1995.

[156] R. N. Bracewell. *The Fourier transform and its applications*. McGraw-Hill New York, 1986.

[157] L. M. Smith, Dennis D. R. Keefer, and S. I. Sudharsanan. Abel inversion using transform techniques. *Journal of Quantitative Spectroscopy & Radiative Transfer*, 39(5):367–373, 1988.

[158] V. Dribinski, A. Ossadtchi, V. A. Mandelshtam, and H. Reisler. Reconstruction of Abel-transformable images: The Gaussian basis-set expansion Abel transform method. *Review of Scientific Instruments*, 73(7):2634–2642, 2002.

[159] G. A. Garcia, L. Nahon, and I. Powis. Two-dimensional charged particle image inversion using a polar basis function expansion. *Review of scientific instruments*, 75(11):4989–4996, 2004.

[160] K. Zhao, T. Colvin, W.T. Hill III, and G. Zhang. Deconvolving two-dimensional images of three-dimensional momentum trajectories. *Review of scientific instruments*, 73(8):3044–3050, 2002.

[161] B. Dick. Inverting ion images without Abel inversion: maximum entropy reconstruction of velocity maps. *Physical Chemistry Chemical Physics*, 16(2):570–580, 2014.

[162] C. Bordas, F. Paulig, H. Helm, and D. L. Huestis. Photoelectron imaging spectrometry: Principle and inversion method. *Review of scientific instruments*, 67(6):2257–2268, 1996.

[163] G. M. Roberts, J. L. Nixon, J. Lecointre, E. Wrede, and J. R. R. Verlet. Toward real-time charged-particle image reconstruction using polar onion-peeling. *Review of Scientific Instruments*, 80(5):053104, 2009.

[164] K. C. Waugh. Methanol synthesis. *Catalysis Today*, 15(1):51–75, 1992.

[165] J. G. Bednorz and K. A. Müller. Possible high T_c superconductivity in the Ba-La-Cu-O system. *Zeitschrift für Physik B Condensed Matter*, 64(2):189–193, 1986.

[166] Z. Z. Sheng and A. M. Hermann. Bulk superconductivity at 120 K in the Tl Ca/Ba Cu O system. *Nature*, 332(6160):138–139, 1988.

[167] M.-K. Wu, J. R. Ashburn, C. Torng, P. H. Hor, R. L. Meng, L. Gao, Z. Huang, Y. Q. Wang, and C. W. Chu. Superconductivity at 93 K in a new mixed-phase Y-Ba-Cu-O compound system at ambient pressure. *Physical Review Letters*, 58(9):908, 1987.

[168] G. Igel, U. Wedig, M. Dolg, P. Fuentealba, H. Preuss, H. Stoll, and R. Frey. Cu and Ag as one-valence-electron atoms: Pseudopotential CI results for CuO and AgO. *The Journal of chemical physics*, 81(6):2737–2740, 1984.

[169] W. Weltner Jr and R. J. Van Zee. Transition metal molecules. *Annual Review of Physical Chemistry*, 35(1):291–327, 1984.

[170] A. J. Merer. Spectroscopy of the diatomic 3d transition metal oxides. *Annual Review of Physical Chemistry*, 40(1):407–438, 1989.

[171] J. F. Harrison. Electronic structure of diatomic molecules composed of a first-row transition metal and main-group element (H-F). *Chemical reviews*, 100(2):679–716, 2000.

[172] Y. Gong, M. Zhou, and L. Andrews. Spectroscopic and theoretical studies of transition metal oxides and dioxygen complexes. *Chemical reviews*, 109(12):6765–6808, 2009.

[173] O. Appelblad, A. Lagerqvist, I. Renhorn, and R. W. Field. The spectrum of CuO: Low lying electronic states observed by laser induced fluorescence. *Physica Scripta*, 22(6):603, 1980.

[174] A. Lagerqvist and U. Uhler. Band spectrum of copper oxide. *Zeitschrift fur Naturforschung Part B*, 22(5):551, 1967.

[175] O. Appelblad and A. Lagerqvist. The spectrum of CuO: Rotational analysis of a blue band system. *Journal of Molecular Spectroscopy*, 48(3):607–608, 1973.

[176] O. Appelblad and A. Lagerqvist. The spectrum of CuO: Rotational analysis of some blue and red bands. *Physica Scripta*, 10(6):307, 1974.

[177] O. Appelblad, A. Lagerqvist, Y. Lefebvre, B. Pinchemel, and J. Schamps. The spectrum of CuO: Rotational analysis of some green bands. *Physica Scripta*, 18(2):125, 1978.

[178] Y. Lefebvre, B. Pinchemel, and J. Schamps. Rotational analysis of a red A' $^2\Sigma^+$-X $^2\Pi_i$ system of CuO. *Journal of Molecular Spectroscopy*, 68(1):81–88, 1977.

[179] B. Pinchemel, Y. Lefebvre, and J. Schamps. Spectrum of CuO: a red $^2\Delta$-X$^2\Pi_i$ transition. *Journal of Physics B: Atomic and Molecular Physics*, 10(16):3215, 1977.

[180] O. Appelblad, I. Renhorn, M. Dulick, M. R. Purnell, and J. M. Brown. The characterisation of the A' $^2\Sigma^-$ state of copper oxide from its nuclear hyperfine structure. *Physica Scripta*, 28(5):539–550, 1983.

[181] Y. Lefebvre, B. Pinchemel, J. M. Delaval, and J. Schamps. Laser induced fluorescence of an infrared Y $^2\Sigma^+$-X $^2\Pi_i$ transition of CuO: Interpretation of the X $^2\Pi_i$ ground state Λ-type doubling. *Physica Scripta*, 25(2):329, 1982.

[182] O. Appelblad and A. Lagerqvist. The spectrum of CuO. rotational analysis of some blue and violet bands. *Physica Scripta*, 13(5):275, 1976.

[183] O. Appelblad, A. Lagerqvist, and M. Lyyra. The spectrum of CuO: Rotational analysis of a $^4\Sigma_{1/2}$-$^2\Pi_{1/2}$ transition. *Physica Scripta*, 18(2):137, 1978.

[184] O. Appelblad, A. Lagerqvist, and M. Lyyra. The spectrum of CuO: Rotational analysis of a band at 4182 Å. *Physica Scripta*, 20(1):93, 1979.

[185] J. Schamps, B. Pinchemel, Y. Lefebvre, and G. Raseev. The electronic valence states of CuO: An energy level diagram. *Journal of Molecular Spectroscopy*, 101(2):344–357, 1983.

[186] M. J. Griffiths and R. F. Barrow. Observations on the electronic spectra of CuO, AgO and AuO isolated in rare gas matrices. *Journal of the Chemical Society, Faraday Transactions 2: Molecular and Chemical Physics*, 73(7):943–951, 1977.

[187] J. S. Shirk and A. M. Bass. Absorption and laser-excited fluorescence of matrix-isolated CuO. *The Journal of Chemical Physics*, 52(4):1894–1901, 1970.

[188] K. R. Thompson, W. C. Easley, and L. B. Knight. Spectra of matrix isolated transition metal monoxides. Manganese (II) and copper (II) oxides. Evidence for a $^2\Pi$ ground state for copper (II) oxide. *The Journal of Physical Chemistry*, 77(1):49–52, 1973.

[189] J. M. Delaval, F. David, Y. Lefebvre, P. Bernage, P. Niay, and J. Schamps. The electronic valence states of CuO: Radiative lifetimes of the A, A', C, and D states. *Journal of Molecular Spectroscopy*, 101(2):358–368, 1983.

[190] T. C. Steimle, D. F. Nachman, and D. A. Fletcher. Laboratory measurement of the permanent electric dipole moment of gas-phase CuO in its X $^2\Pi$ state. *The Journal of chemical physics*, 87(10):5670–5673, 1987.

[191] M. C. L. Gerry, A. J. Merer, U. Sassenberg, and T. C. Steimle. The microwave spectrum of CuO, X $^2\Pi$, measured with optical detection. *The Journal of chemical physics*, 86(9):4754–4761, 1987.

[192] T. C. Steimle, W-L. Chang, and D. F. Nachman. Λ-doubling transitions of metal oxides measured by microwave-optical double resonance: CuO. *Chemical physics letters*, 153(6):534–538, 1988.

[193] T. C. Steimle, K. Namiki, and S. Saito. The millimeter wave spectrum of copper monoxide: CuO. *Journal of Chemical Physics*, 107(16):6109–6113, 1997.

[194] L. C. O'Brien, R. L. Kubicek, S. J. Wall, D. E. Koch, R. J. Friend, and C. R. Brazier. Fourier transform spectroscopy of the $Y^2\Sigma^+$–$X^2\Pi_i$ transition of CuO. *Journal of molecular spectroscopy*, 180(2):365–368, 1996.

[195] M. L. Polak, M. K. Gilles, J. Ho, and W. C. Lineberger. Photoelectron spectroscopy of copper oxide (CuO^-). *The Journal of Physical Chemistry*, 95(9):3460–3463, 1991.

[196] H. Wu, S. R. Desai, and L.-S. Wang. Chemical bonding between Cu and oxygen–copper oxides vs O_2 complexes: A study of CuO_x (x= 0-6) species by anion photoelectron spectroscopy. *The Journal of Physical Chemistry A*, 101(11):2103–2111, 1997.

[197] S. Smoes, F. Mandy, A. V. Auwera-Mahieu, and J. Drowart. Determination by the mass spectrometric Knudsen cell method of the dissociation energies of the group IB chalcogenides. *Bulletin des Societes Chimiques Belges*, 81(1):45–56, 1972.

[198] L. R. Watson, T. L. Thiem, R. A. Dressler, R. H. Salter, and E. Murad. High temperature mass spectrometric studies of the bond energies of gas-phase zinc oxide, nickel oxide, and copper (II) oxide. *The Journal of Physical Chemistry*, 97(21):5577–5580, 1993.

[199] D. E. Clemmer, N. F. Dalleska, and P. B. Armentrout. Reaction of Zn^+ with NO_2. The gas-phase thermochemistry of ZnO. *The Journal of chemical physics*, 95(10):7263–7268, 1991.

[200] C. Vinckier, T. Verhaeghe, and I. Vanhees. Kinetic study in a microwave-induced plasma afterglow of the Cu(4 ^{2}S) atom reaction with N_2O from 458 to 980 K and with NO_2 from 303 to 762 K. *Journal of the Chemical Society-Faraday Transactions*, 90(14):2003–2007, 1994.

[201] M. T. Rodgers, B. Walker, and P. B. Armentrout. Reactions of Cu^+(^{1}S and ^{3}D) with O_2, CO, CO_2, N_2, NO, N_2O, and NO_2 studied by guided ion beam mass spectrometry. *International journal of mass spectrometry*, 182:99–120, 1999.

[202] P. S. Bagus, C. J. Nelin, and C. W. Bauschlicher Jr. On the low-lying states of CuO. *The Journal of chemical physics*, 79(6):2975–2981, 1983.

[203] S. R. Langhoff and C. W. Bauschlicher Jr. Theoretical study of the $X^2\Pi$ and $A^2\Sigma^+$ states of CuO and CuS. *Chemical physics letters*, 124(3):241–247, 1986.

[204] P. V. Madhavan and M. D. Newton. Electronic states of CuO. *The Journal of chemical physics*, 83(5):2337–2347, 1985.

[205] H. Xian, Z. X. Cao, X. Xu, X. Lu, and Q. E. Zhang. Theoretical study of low-lying electronic states of CuO and CuO^-. *Chemical Physics Letters*, 326(5):485–493, 2000.

[206] B. Dai, K. Deng, J. Yang, and Q. Zhu. Excited states of the 3d transition metal monoxides. *The Journal of chemical physics*, 118(21):9608–9613, 2003.

[207] S. Midda, N. C. Bera, I. Bhattacharyya, and A. K. Das. Ab initio and density functional study of spectroscopic properties of CuO and CuS. *Journal of Molecular Structure: THEOCHEM*, 761(1):17–20, 2006.

[208] L. F. A. Ferrão, O. Roberto-Neto, and F. B. C. Machado. Electronic structure of CuX^y (X= B, C, N, O, F; y= 0,+ 1,- 1). *International Journal of Quantum Chemistry*, 108(13):2512–2522, 2008.

[209] R. S. Ram, C. N. Jarman, and P. F. Bernath. Fourier transform emission spectroscopy of the copper dimer. *Journal of Molecular Spectroscopy*, 156(2):468–486, 1992.

[210] A. D. Sappey, J. E. Harrington, and J. C. Weisshaar. Resonant two-photon ionization-photoelectron spectroscopy of Cu_2: Autoionization dynamics and Cu_2^+ vibronic states. *The Journal of chemical physics*, 91(7):3854–3868, 1989.

[211] A. Kramida, Y. Ralchenko, J. Reader, and NIST ASD Team. NIST Atomic Spectra Database (ver. 5.2), [Online]. Available: `http://physics.nist.gov/asd` [2014, October 13]. National Institute of Standards and Technology, Gaithersburg, MD., 2014.

[212] R. B. Metz, C. Nicolas, M. Ahmed, and S. R. Leone. Direct determination of the ionization energies of FeO and CuO with VUV radiation. *The Journal of chemical physics*, 123(11):114313, 2005.

[213] K. B. MacAdam, S. F. Dyubko, V. A. Efremov, V. G. Gerasimov, and A. S. Kutsenko. Laser-microwave spectroscopy of Cu I atoms in S, P, D, F and G Rydberg states. *Journal of Physics B: Atomic, Molecular and Optical Physics*, 42(16):165009, 2009.

[214] E. R. Fisher, J. L. Elkind, D. E. Clemmer, R. Georgiadis, S. K. Loh, N. Aristov, L. S. Sunderlin, and P. B. Armentrout. Reactions of fourth-period metal ions (Ca^+- Zn^+) with O_2: Metal-oxide ion bond energies. *The Journal of Chemical Physics*, 93(4):2676–2691, 1990.

[215] A. G. Shenstone. The first spectrum of copper (Cu I). *Philosophical Transactions of the Royal Society of London. Series A, Mathematical and Physical Sciences*, 241(832):297–322, 1948.

[216] K. L. Reid. Photoelectron angular distributions. *Annual review of physical chemistry*, 54(1):397–424, 2003.

[217] T. P. Rakitzis and R. N. Zare. Photofragment angular momentum distributions in the molecular frame: determination and interpretation. *The Journal of chemical physics*, 110(7):3341–3350, 1999.

[218] J. Ruamps. Spectre d'emission des molecules Cu_2, Ag_2 et Au_2. *Comptes rendus hebdomadaires des seances de l'academie des sciences*, 238(14):1489–1491, 1954.

[219] B. Kleman and S. Lindkvist. The band spectrum of the Cu_2 molecule. *Arkiv For Fysik*, 8(4):333–339, 1954.

[220] N. L. Singh. Emission bands in Cu_2. *Physical Review*, 99(5):1624–1624, 1955.

[221] J. Ruamps. Production et étude du spectre optique de molécules diatomiques de métaux et contribution au calcul théorique des intensités. *Annales de Physique*, 4(9-10):1111–1157, 1959.

[222] N. Aslund, R. F. Barrow, W. G. Richards, and D. N. Travis. Rotational analysis of bands of the B-X system of Cu_2 and of the A-X system of Bi_2. *Arkiv för Fysik*, 30:171, 1965.

[223] D. S. Pesic and S. Weniger. Study of vibration structure of the B-X system of a $^{63}Cu^{65}Cu$ molecule. *Comptes rendus hebdomadaires des seances de l'academie des sciences serie B*, 272(1):46, 1971.

[224] D. S. Pesic and S. Weniger. Rotational analysis of bands of the A-X system of Cu_2 (^{63}Cu). *Comptes rendus hebdomadaires des seances de l'academie des sciences serie B*, 273(14):602, 1971.

[225] J. Lochet. Laser-induced fluorescence of the Cu_2 molecule. *Journal of Physics B: Atomic and Molecular Physics*, 11(3):L55, 1978.

[226] J. G. McCaffrey, R. R. Bennett, M. D. Morse, and W. H. Breckenridge. Laser excitation spectroscopy of the A and B states of jet-cooled copper dimer: Evidence for large electronic isotope shifts. *The Journal of chemical physics*, 91(1):92–103, 1989.

[227] J. L. Gole, J. H. English, and V. E. Bondybey. Laser spectroscopy of cooled metal clusters: Copper dimer. *The Journal of Physical Chemistry*, 86(14):2560–2563, 1982.

[228] T. Okazaki and Y. Ando. New optical absorption spectra of Cu_2 molecules produced by the gas evaporation technique. *Molecular Physics*, 98(7):447–452, 2000.

[229] R. H. Page and C. S. Gudeman. Rotationally resolved dicopper (Cu_2) laser-induced fluorescence spectra. *The Journal of chemical physics*, 94(1):39–51, 1991.

[230] M. Doverstål, B. Lindgren, U. Sassenberg, and H. Yu. The A-X system of the copper dimer studied by resonant two-photon ionization spectroscopy. *Chemical physics letters*, 192(2):283–288, 1992.

[231] V. E. Bondybey, G. P. Schwartz, and J. H. English. Laser vaporization of alloys: Laser induced fluorescence of heteronuclear metal clusters. *The Journal of Chemical Physics*, 78(1):11–15, 1983.

[232] R. E. Steele. Photoluminescence, lifetimes, and discharge excitation of Cu_2. *Journal of Molecular Spectroscopy*, 61(3):477–478, 1976.

[233] J. Drowart and R. E. Honig. Mass spectrometric study of copper, silver, and gold. *The Journal of Chemical Physics*, 25(3):581–582, 1956.

[234] J. Drowart and R. E. Honig. A mass spectrometric method for the determination of dissociation energies of diatomic molecules. *The Journal of Physical Chemistry*, 61(7):980–985, 1957.

[235] P. Schissel. Dissociation energies of Cu_2, Ag_2, and Au_2. *The Journal of Chemical Physics*, 26(5):1276–1280, 1957.

[236] M. Ackerman, F. E. Stafford, and J. Drowart. Mass spectrometric determination of the dissociation energies of the molecules AgAu, AgCu, and AuCu. *The Journal of Chemical Physics*, 33(6):1784–1789, 1960.

[237] K. Hilpert. Mass spectrometric determination of the dissociation energies of CuTb(g), CuDy(g), and CuHo(g). *Berichte der Bunsengesellschaft für physikalische Chemie*, 83(2):161–167, 1979.

[238] E. A. Rohlfing and J. J. Valentini. UV laser excited fluorescence spectroscopy of the jet-cooled copper dimer. *The Journal of chemical physics*, 84(12):6560–6566, 1986.

[239] A. D. Sappey, J. E. Harrington, and J. C. Weisshaar. Cu_2^+ vibronic states at 0–1.4 eV from multiphoton ionization-photoelectron spectroscopy. *The Journal of chemical physics*, 88(8):5243–5245, 1988.

[240] M. Moskovits and J. E. Hulse. Optical spectroscopy of copper clusters: Atom to bulk. *The Journal of Chemical Physics*, 67(9):4271–4278, 1977.

[241] G. A. Ozin, H. Huber, D. McIntosh, S. Mitchell, J. G. Norman Jr, and L. Noodleman. Selective naked-cluster cryophotochemistry and SCF-Xα-SW calculations for copper (Cu_2) and silver (Ag_2). *Journal of the American Chemical Society*, 101(13):3504–3511, 1979.

[242] G. A. Ozin, S. A. Mitchell, and J. Garcia-Prieto. Fluorescence spectroscopy and photoprocesses of copper, Cu and Cu_2 in rare gas matrixes. *The Journal of Physical Chemistry*, 86(4):473–479, 1982.

[243] H. Wiggenhauser, D. M. Kolb, H. H. Rotermund, W. Schrittenlacher, and W. Schroeder. Fluorescence spectroscopy in the nanosecond range for matrix-isolated Cu atoms and dimers. *Chemical physics letters*, 122(1):71–75, 1985.

[244] V. E. Bondybey. The lowest a $^3\Sigma^+_u$ state of Cu_2. *The Journal of Chemical Physics*, 77(7):3771–3772, 1982.

[245] V. E. Bondybey and J. H. English. Observation and characterization of a new electronic state of diatomic copper in solid neon. *The Journal of Physical Chemistry*, 87(23):4647–4650, 1983.

[246] S.-W. Wang. The geometric and electronic structure of small copper clusters Cu_n and Cu_n^+ (n= 1–3) by an effective core potential method. *The Journal of chemical physics*, 82(10):4633–4640, 1985.

[247] T. C. Thompson, D. G. Truhlar, and C. A. Mead. On the form of the adiabatic and diabatic representation and the validity of the adiabatic approximation for X_3 Jahn-Teller systems. *The Journal of chemical physics*, 82(5):2392–2407, 1985.

[248] P. Fuentealba and Y. Simón-Manso. Basis set superposition error in atomic cluster calculations. *Chemical physics letters*, 314(1):108–113, 1999.

[249] S. P. Walch and B. C. Laskowski. Calculated ground state potential surface and excitation energies for the copper trimer. *The Journal of chemical physics*, 84(5):2734–2743, 1986.

[250] A. B. Anderson. Structures and electronic properties of copper clusters and bulk; comments on Mulliken-Walsh diagrams and on criticisms of the extended Hückel procedure. *The Journal of Chemical Physics*, 68(4):1744–1751, 1978.

[251] J. A. Howard, K. F. Preston, R. Sutcliffe, and B. Mile. Electron spin resonance spectrum of matrix isolated Cu_3. *The Journal of Physical Chemistry*, 87(4):536–537, 1983.

[252] D. P. DiLella, K. Taylor, and M. Moskovits. Tricopper. A fluxional molecule. *The Journal of Physical Chemistry*, 87(3):524–527, 1983.

[253] M. Moskovits. Tricopper-revisited. *Chemical physics letters*, 118(2):111–114, 1985.

[254] D. M. Lindsay, G. A. Thompson, and Y. Wang. ESR spectra of $Cu_3(^2A_1)$ in an N_2 matrix. *J. Phys. Chem.;(United States)*, 91(10), 1987.

[255] W. H. Crumley, J. S. Hayden, and J. L. Gole. Laser induced excitation spectroscopy of copper trimer in various stages of supersonic expansion: Observation of fluorescence from dissociative levels. *The Journal of chemical physics*, 84(10):5250–5261, 1986.

[256] E. A. Rohlfing and J. J. Valentini. Laser-excited fluorescence spectroscopy of the jet-cooled copper trimer. *Chemical physics letters*, 126(2):113–118, 1986.

[257] M. B. Knickelbein. Photodissociation spectroscopy of Cu_3, Cu_3Ar, and Cu_3Kr. *The Journal of chemical physics*, 100(7):4729–4737, 1994.

[258] J. W. Zwanziger, R. L. Whetten, and E. R. Grant. Assignment of the vibronic level structure of trimeric copper (Cu_3) ground state. *The Journal of Physical Chemistry*, 90(15):3298–3301, 1986.

[259] D. G. Truhlar, T. C. Thompson, and C. A. Mead. The potential energy surface of the Jahn-Teller-distorted ^{2}E'ground state of copper trimer. *Chemical physics letters*, 127(4):287–291, 1986.

[260] M. D. Morse. Copper trimer: a revised assignment of the upper state of the 5397 å system. *Chemical physics letters*, 133(1):8–13, 1987.

[261] A. Bérces. The structures and vibrational frequencies of small clusters of transition metal and main group elements. A gradient corrected density functional study. *Spectrochimica Acta Part A: Molecular and Biomolecular Spectroscopy*, 53(8):1257–1272, 1997.

[262] K. Hilpert and K. A. Gingerich. Atomization enthalpies of the molecules Cu_3, Ag_3, and Au_3. *Berichte der Bunsengesellschaft für Physikalische Chemie*, 84(8):739–745, 1980.

[263] A. Andrejeva, J. P. Harris, and T. G. Wright. Resonance-enhanced multiphoton ionization spectroscopy of laser-ablated copper atoms. *Chemical Physics Letters*, 2014.

[264] I. S. Parry, A. Kartouzian, S. M. Hamilton, O. P. Balaj, M. K. Beyer, and S. R. Mackenzie. Collisional activation of N_2O decomposition and CO oxidation reactions on isolated rhodium clusters. *The Journal of Physical Chemistry A*, 117(36):8855–8863, 2013.

[265] M. B. Comisarow and A. G. Marshall. Fourier transform ion cyclotron resonance spectroscopy. *Chemical physics letters*, 25(2):282–283, 1974.

[266] F. Xian, C. L. Hendrickson, and A. G. Marshall. High resolution mass spectrometry. *Analytical chemistry*, 84(2):708–719, 2012.

[267] A. G. Marshall. Milestones in Fourier transform ion cyclotron resonance mass spectrometry technique development. *International journal of mass spectrometry*, 200(1):331–356, 2000.

[268] E. O. Lawrence and M. S. Livingston. The production of high speed light ions without the use of high voltages. *Physical Review*, 40(1):19, 1932.

[269] J. A. Hipple, H. Sommer, and H. A. Thomas. A precise method of determining the Faraday by magnetic resonance. *Physical Review*, 76(12):1877, 1949.

[270] H. Sommer, H. A. Thomas, and J. A. Hipple. The measurement of e/M by cyclotron resonance. *Physical Review*, 82(5):697, 1951.

[271] D. Wobschall. Ion cyclotron resonance spectrometer. *Review of Scientific Instruments*, 36(4):466–475, 1965.

[272] J. L. Beauchamp. Ion cyclotron resonance spectroscopy. *Annual Review of Physical Chemistry*, 22(1):527–561, 1971.

[273] R. T. McIver Jr. A trapped ion analyzer cell for ion cyclotron resonance spectroscopy. *Review of Scientific Instruments*, 41(4):555–558, 1970.

[274] P. Genequand. Le résotron, spectromètre de masse cyclotronique à balayage rapide. *Zeitschrift für angewandte Mathematik und Physik ZAMP*, 22(5):951–975, 1971.

[275] A. G. Marshall, C. L. Hendrickson, and G. S. Jackson. Fourier transform ion cyclotron resonance mass spectrometry: a primer. *Mass spectrometry reviews*, 17(1):1–35, 1998.

[276] L. Schweikhard and A. G. Marshall. Excitation modes for Fourier transform-ion cyclotron resonance mass spectrometry. *Journal of the American Society for Mass Spectrometry*, 4(6):433–452, 1993.

[277] A. G. Marshall and C. L. Hendrickson. Fourier transform ion cyclotron resonance detection: principles and experimental configurations. *International Journal of Mass Spectrometry*, 215(1):59–75, 2002.

[278] S. Guan and A. G. Marshall. Stored waveform inverse Fourier transform (SWIFT) ion excitation in trapped-ion mass spectometry: theory and applications. *International Journal of Mass Spectrometry and Ion Processes*, 157:5–37, 1996.

[279] P. Pfändler, G. Bodenhausen, J. Rapin, R. Houriet, and T. Gäumann. Two-dimensional Fourier transform ion cyclotron resonance mass spectrometry. *Chemical physics letters*, 138(2):195–200, 1987.

[280] C. W. Ross III, S. Guan, P. B. Grosshans, T. L. Ricca, and A. G. Marshall. Two-dimensional Fourier transform ion cyclotron resonance mass spectrometry/mass spectrometry with stored-waveform ion radius modulation. *Journal of the American Chemical Society*, 115(17):7854–7861, 1993.

[281] V. H. Vartanian, J. S. Anderson, and D. A. Laude. Advances in trapped ion cells for Fourier transform ion cyclotron resonance mass spectrometry. *Mass Spectrometry Reviews*, 14(1):1–19, 1995.

[282] G. S. Jackson, J. D. Canterbury, S. Guan, and A. G. Marshall. Linearity and quadrupolarity of tetragonal and cylindrical Penning traps of arbitrary length-to-width ratio. *Journal of the American Society for Mass Spectrometry*, 8(3):283–293, 1997.

[283] R. C. Dunbar. The effect of ion position on ICR signal strength. *International journal of mass spectrometry and ion processes*, 56(1):1–9, 1984.

[284] M. Alemann, H. P. Kellerhals, and K.-P. Wanczek. Sidebands in the ICR spectrum and their application for exact mass determination. *Chemical Physics Letters*, 84(3):547–551, 1981.

[285] M. B. Comisarow and A. G. Marshall. Theory of Fourier transform ion cyclotron resonance mass spectroscopy. I. Fundamental equations and low-pressure line shape. *The Journal of Chemical Physics*, 64(1):110–119, 1976.

[286] A. G. Marshall and S. Guan. Advantages of high magnetic field for Fourier transform ion cyclotron resonance mass spectrometry. *Rapid Communications in Mass Spectrometry*, 10(14):1819–1823, 1996.

[287] F. Xian, C. L. Hendrickson, G. T. Blakney, S. C. Beu, and A. G. Marshall. Automated broadband phase correction of Fourier transform ion cyclotron resonance mass spectra. *Analytical chemistry*, 82(21):8807–8812, 2010.

[288] Y. Qi, M. P. Barrow, H. Li, J. E. Meier, S. L. Van Orden, C. J. Thompson, and P. B. O'Connor. Absorption-mode: the next generation of Fourier transform mass spectra. *Analytical chemistry*, 84(6):2923–2929, 2012.

[289] S. Guan, G.-Z. Li, and A. G. Marshall. Effect of ion-neutral collision mechanism on the trapped-ion equation of motion: a new mass spectral line shape for high-mass trapped ions. *International journal of mass spectrometry and ion processes*, 167:185–193, 1997.

[290] A. G. Marshall and C. L. Hendrickson. High-resolution mass spectrometers. *Annu. Rev. Anal. Chem.*, 1:579–599, 2008.

[291] L. Sleno, D. A. Volmer, and A. G. Marshall. Assigning product ions from complex MS/MS spectra: the importance of mass uncertainty and resolving power. *Journal of the American Society for Mass Spectrometry*, 16(2):183–198, 2005.

[292] D. J. Aaserud, Z. Guan, D. P. Little, and F. W. McLafferty. DNA sequencing with blackbody infrared radiative dissociation of electrosprayed ions. *International journal of mass spectrometry and ion processes*, 167:705–712, 1997.

[293] B. A. Parks, L. Jiang, P. M. Thomas, C. D. Wenger, M. J. Roth, M. T. Boyne, P. V. Burke, K. E. Kwast, and N. L. Kelleher. Top-down proteomics on a chromatographic time scale using linear ion trap Fourier transform hybrid mass spectrometers. *Analytical chemistry*, 79(21):7984–7991, 2007.

[294] J. Pól, V. Vidová, T. Hyötyläinen, M. Volnỳ, P. Novák, M. Strohalm, R. Kostiainen, V. Havlíček, S. Wiedmer, and J. Holopainen. Spatial distribution of glycerophospholipids in the ocular lens. *PloS one*, 6(4):e19441, 2011.

[295] A. G. Marshall and R. P. Rodgers. Petroleomics: Chemistry of the underworld. *Proceedings of the National Academy of Sciences*, 105(47):18090–18095, 2008.

[296] S. M. Weidner and S. Trimpin. Mass spectrometry of synthetic polymers. *Analytical chemistry*, 80(12):4349–4361, 2008.

[297] R. C. Dunbar. BIRD (blackbody infrared radiative dissociation): Evolution, principles, and applications. *Mass spectrometry reviews*, 23(2):127–158, 2004.

[298] R. L. Woodin, D. S. Bomse, and J. L. Beauchamp. Multiphoton dissociation of molecules with low power continuous wave infrared laser radiation. *Journal of the American Chemical Society*, 100(10):3248–3250, 1978.

[299] P. Caravatti and M. Allemann. The infinity cell: A new trapped-ion cell with radiofrequency covered trapping electrodes for Fourier transform ion cyclotron resonance mass spectrometry. *Organic Mass Spectrometry*, 26(5):514–518, 1991.

[300] O. P. Balaj, C. B. Berg, S. J. Reitmeier, V. E. Bondybey, and M. K. Beyer. A novel design of a temperature-controlled FT-ICR cell for low-temperature black-body infrared radiative dissociation (BIRD) studies of hydrated ions. *International Journal of Mass Spectrometry*, 279(1):5–9, 2009.

[301] K. C. Taylor. Nitric oxide catalysis in automotive exhaust systems. *Catalysis Reviews: Science and Engineering*, 35(4):457–481, 1993.

[302] K. Koszinowski, M. Schlangen, D. Schröder, and H. Schwarz. C-H- and N-H-activation by gaseous Rh_2^+ and $PtRh^+$ cluster ions. *International Journal of Mass Spectrometry*, 237(1):19–23, 2004.

[303] V. P. Zhdanov and B. Kasemo. Mechanism and kinetics of the NO CO reaction on Rh. *Surface science reports*, 29(2):31–90, 1997.

[304] G. Ertl. Reactions at well-defined surfaces. *Surface Science*, 299:742–754, 1994.

[305] M. B. Knickelbein. Reactions of transition metal clusters with small molecules 1. *Annual review of physical chemistry*, 50(1):79–115, 1999.

[306] J. Evans and M. Tromp. Interaction of small gas phase molecules with alumina supported rhodium nanoparticles: an in situ spectroscopic study. *Journal of Physics: Condensed Matter*, 20(18):184020, 2008.

[307] M. L. Anderson, M. S. Ford, P. J. Derrick, T. Drewello, D. Woodruff, and S. R. Mackenzie. Nitric oxide decomposition on small rhodium clusters, $Rh_n^{+/-}$. *The Journal of Physical Chemistry A*, 110(38):10992–11000, 2006.

[308] I. Balteanu, O. P. Balaj, B. Fox-Beyer, P. Rodrigues, M. T. Barros, A. M. C. Moutinho, M. L. Costa, M. K. Beyer, and V. E. Bondybey. Size- and charge-state-dependent reactivity of azi-

doacetonitrile with anionic and cationic rhodium clusters $Rh_n^{\pm}$. *Organometallics*, 23(9):1978–1985, 2004.

[309] G. Albert, C. Berg, M. Beyer, U. Achatz, S. Joos, G. Niedner-Schatteburg, and V. E. Bondybey. Methane activation by rhodium cluster argon complexes. *Chemical physics letters*, 268(3):235–241, 1997.

[310] S. M. Hamilton, W. S. Hopkins, D. J. Harding, T. R. Walsh, M. Haertelt, C. Kerpal, P. Gruene, G. Meijer, A. Fielicke, and S. R. Mackenzie. Infrared-induced reactivity of N_2O on small gas-phase rhodium clusters. *The Journal of Physical Chemistry A*, 115(12):2489–2497, 2011.

[311] D. J. Harding, T. R. Walsh, S. M. Hamilton, W. S. Hopkins, S. R. Mackenzie, P. Gruene, M. Haertelt, G. Meijer, and A. Fielicke. Communications: The structure of Rh_8^+ in the gas phase. *The Journal of chemical physics*, 132(1):011101, 2010.

[312] A. Fielicke, G. von Helden, G. Meijer, B. Simard, S. Dénommée, and D. M. Rayner. Vibrational spectroscopy of CO in gas-phase rhodium cluster-CO complexes. *Journal of the American Chemical Society*, 125(37):11184–11185, 2003.

[313] S. M. Hamilton, W. S. Hopkins, D. J. Harding, T. R. Walsh, P. Gruene, M. Haertelt, A. Fielicke, G. Meijer, and S. R. Mackenzie. Infrared induced reactivity on the surface of isolated size-selected clusters: Dissociation of N_2O on rhodium clusters. *Journal of the American Chemical Society*, 132(5):1448–1449, 2010.

[314] A. C. Hermes, S. M. Hamilton, W. S. Hopkins, D. J. Harding, C. Kerpal, G. Meijer, A. Fielicke, and S. R. Mackenzie. Effects of coadsorbed oxygen on the infrared driven decomposition of N_2O on isolated Rh_5^+ clusters. *The Journal of Physical Chemistry Letters*, 2(24):3053–3057, 2011.

[315] C. D. Zeinalipour-Yazdi and R. A. van Santen. Coverage-dependent adsorption energy of carbon monoxide on a rhodium nanocluster. *The Journal of Physical Chemistry C*, 116(15):8721–8730, 2012.

[316] H. Xie, M. Ren, Q. Lei, W. Fang, and F. Ying. Explore the catalytic reaction mechanism in the reduction of NO by CO on the Rh_7^+ cluster: A quantum chemical study. *The Journal of Physical Chemistry C*, 116(14):7776–7781, 2012.

[317] S. L. Romo-Ávila and R. A. Guirado-López. Adsorption of nitric oxide on small $Rh_n^{\pm}$ clusters: Role of the local atomic environment on the dissociation of the N–O bond. *The Journal of Physical Chemistry A*, 116(3):1059–1068, 2012.

[318] S. Shetty, R. A. van Santen, P. A. Stevens, and S. Raman. Molecular steps for the syngas conversion on the Rh_6 cluster. *Journal of Molecular Catalysis A: Chemical*, 330(1):73–87, 2010.

[319] M. K. Beyer and V. E. Bondybey. Energy resolved measurement of endothermic reaction and dissociation thresholds: Fourier transform ion cyclotron resonance mass spectrometry meets guided ion beam. *Rapid communications in mass spectrometry*, 11(14):1588–1591, 1997.

[320] K. M. Ervin and P. B. Armentrout. Translational energy dependence of $Ar^+ + XY \rightarrow ArX^+ + Y$ (XY= H_2, D_2, HD) from thermal to 30 eV c.m. *The Journal of chemical physics*, 83(1):166–189, 1985.

[321] F. Muntean and P. B. Armentrout. Guided ion beam study of collision-induced dissociation dynamics: integral and differential cross sections. *The Journal of Chemical Physics*, 115(3):1213–1228, 2001.

[322] J. N. Bass. Translation to vibration energy transfer in O + NH_3 and O + CO_2 collisions. *The Journal of Chemical Physics*, 60(7):2913–2921, 1974.

[323] X. Guo, M. C. Duursma, P. G. Kistemaker, N. Nibbering, K. Vekey, L. Drahos, and R. Heeren. Manipulating internal energy of protonated biomolecules in electrospray ionization Fourier transform ion cyclotron resonance mass spectrometry. *Journal of mass spectrometry*, 38(6):597–606, 2003.

[324] P. de Sainte Claire, G. H. Peslherbe, and W. L. Hase. Energy transfer dynamics in the collision-induced dissociation of Al_6 and Al_{13} clusters. *The Journal of Physical Chemistry*, 99(20):8147–8161, 1995.

[325] P. de Sainte Claire and W. L. Hase. Thresholds for the collision-induced dissociation of clusters by rare gas impact. *The Journal of Physical Chemistry*, 100(20):8190–8196, 1996.

[326] R. Ahlrichs, M. Bär, M. Häser, H. Horn, and C. Kölmel. Electronic structure calculations on workstation computers: The program system turbomole. *Chemical Physics Letters*, 162(3):165–169, 1989.

[327] D. Harding, S. R. Mackenzie, and T. R. Walsh. Structural isomers and reactivity for Rh_6 and Rh_6^+. *The Journal of Physical Chemistry B*, 110(37):18272–18277, 2006.

[328] T. M. Soini, S. Krüger, and N. Rösch. The DFT+Umol method and its application to the adsorption of CO on platinum model clusters. *The Journal of chemical physics*, 140(17):174709, 2014.

[329] M. P. Langevin. Une formule fondamentale de théorie cinétique. *Annales de chimie et de physique*, 5:245–288, 1905.

[330] T. Su and M. T. Bowers. Theory of ion-polar molecule collisions. Comparison with experimental charge transfer reactions of rare gas ions to geometric isomers of difluorobenzene and dichloroethylene. *The Journal of Chemical Physics*, 58(7):3027–3037, 1973.

[331] R. C. Dunbar and T. B. McMahon. Activation of unimolecular reactions by ambient blackbody radiation. *Science*, 279(5348):194–197, 1998.

[332] F. A. Lindemann, S. Arrhenius, I. Langmuir, N. R. Dhar, J. Perrin, and W. C. Lewis. Discussion on the radiation theory of chemical action. *Transactions of the Faraday Society*, 17:598–606, 1922.

[333] D. S. Bomse and J. L. Beauchamp. Slow multiphoton excitation as a probe of bimolecular and unimolecular reaction energetics. Multiphoton dissociation of proton-bound alcohol dimers. *Journal of the American Chemical Society*, 103(12):3292–3296, 1981.

[334] J. M. Jasinski, R. N. Rosenfeld, F. K. Meyer, and J. I. Brauman. Infrared photochemistry of $[(C_2H_5)_2O]_2H^+$ and $C_3F_6^+$. A comparison of pulsed and continuous-wave laser photodissociation methods. *Journal of the American Chemical Society*, 104(3):652–658, 1982.

[335] R. C. Dunbar. Kinetics of low-intensity infrared laser photodissociation. The thermal model and application of the Tolman theorem. *The Journal of chemical physics*, 95(4):2537–2548, 1991.

[336] R. C. Dunbar and R. C. Zaniewski. Infrared multiphoton dissociation of styrene ions by low-power continuous CO_2 laser irradiation. *The Journal of chemical physics*, 96(7):5069–5075, 1992.

[337] D. Thölmann, D. S. Tonner, and T. B. McMahon. Spontaneous unimolecular dissociation of small cluster ions,$(H_3O^+)L_n$ and $Cl^-(H_2O)_n$ (n= 2–4), under Fourier transform ion cyclotron resonance conditions. *The Journal of Physical Chemistry*, 98(8):2002–2004, 1994.

[338] R. C. Dunbar, T. B. McMahon, D. Thölmann, D. S. Tonner, D. R. Salahub, and D. Wei. Zero-pressure thermal-radiation-induced dissociation of gas-phase cluster ions: Comparison of theory and experiment for $(H_2O)_2Cl^-$ and $(H_2O)_3Cl^-$. *Journal of the American Chemical Society*, 117(51):12819–12825, 1995.

[339] D. Scott Tonner, D. Thölmann, and T. B. McMahon. Deuterium isotope effect on the radiatively induced unimolecular dissociation of small cluster ions. *Chemical physics letters*, 233(3):324–330, 1995.

[340] R. C. Dunbar. Kinetics of thermal unimolecular dissociation by ambient infrared radiation. *The Journal of Physical Chemistry*, 98(35):8705–8712, 1994.

[341] G. T. Uechi and R. C. Dunbar. The kinetics of infrared laser photodissociation of n-butylbenzene ions at low pressure. *The Journal of chemical physics*, 96(12):8897–8905, 1992.

[342] C.-Y. Lin and R. C. Dunbar. Zero-pressure thermal-radiation-induced dissociation of tetraethylsilane cation. *The Journal of Physical Chemistry*, 100(2):655–659, 1996.

[343] W. D. Price, P. D. Schnier, and E. R. Williams. Tandem mass spectrometry of large biomolecule ions by blackbody infrared radiative dissociation. *Analytical chemistry*, 68(5):859–866, 1996.

[344] P. D. Schnier, W. D. Price, R. A. Jockusch, and E. R. Williams. Blackbody infrared radiative dissociation of bradykinin and its analogues: Energetics, dynamics, and evidence for salt-bridge structures in the gas phase. *Journal of the American Chemical Society*, 118(30):7178–7189, 1996.

[345] W. D. Price, P. D. Schnier, R. A. Jockusch, E. F. Strittmatter, and E. R. Williams. Unimolecular reaction kinetics in the high-pressure limit without collisions. *Journal of the American Chemical Society*, 118(43):10640–10644, 1996.

[346] W. D. Price and E. R. Williams. Activation of peptide ions by blackbody radiation: Factors that lead to dissociation kinetics in the rapid energy exchange limit. *The Journal of Physical Chemistry A*, 101(47):8844–8852, 1997.

[347] R. A. Jockusch, P. D. Schnier, W. D. Price, E. F. Strittmatter, P. A. Demirev, and E. R. Williams. Effects of charge state on fragmentation pathways, dynamics, and activation energies of ubiquitin ions measured by blackbody infrared radiative dissociation. *Analytical chemistry*, 69(6):1119–1126, 1997.

[348] W. D. Price, P. D. Schnier, and E. R. Williams. Binding energies of the proton-bound amino acid dimers Gly.Gly, Ala.Ala, Gly.Ala, and Lys.Lys measured by blackbody infrared radiative dissociation. *The Journal of Physical Chemistry B*, 101(4):664–673, 1997.

[349] R. L. Wong, E. W. Robinson, and E. R. Williams. Activation of protonated peptides and molecular ions of small molecules using heated filaments in Fourier-transform ion cyclotron resonance mass spectrometry. *International Journal of Mass Spectrometry*, 234(1):1–9, 2004.

[350] M. Sena and J. M. Riveros. Thermal dissociation of acetophenone molecular ions activated by infrared radiation. *The Journal of Physical Chemistry A*, 101(24):4384–4391, 1997.

[351] G. A. Janaway and J. I. Brauman. Negative ion electron photodetachment from a near-blackbody photon source. *The Journal of Physical Chemistry A*, 104(6):1117–1120, 2000.

[352] T. Giroldo and J. M. Riveros. Keto-enol isomerization of gas-phase 2'-methylacetophenone molecular ions probed by high-temperature near-blackbody-induced dissociation, ion-molecule reactions, and ab initio calculations. *The Journal of Physical Chemistry A*, 106(42):9930–9938, 2002.

[353] M. Sena and J. M. Riveros. Ring-hydrogen participation in the keto-enol isomerization of the acetophenone radical cation. *Chemistry-A European Journal*, 6(5):785–793, 2000.

[354] M. Sena and J. M. Riveros. Dissociation of p-cymene molecular ions induced by thermal radiation. *International Journal of Mass Spectrometry*, 227(1):135–145, 2003.

[355] M. A. Freitas, C. L. Hendrickson, and A. G. Marshall. Gas phase activation energy for unimolecular dissociation of biomolecular ions determined by focused radiation for gaseous multiphoton energy transfer (FRAGMENT). *Rapid communications in mass spectrometry*, 13(15):1639–1642, 1999.

[356] R. A. Jockusch, K. Paech, and E. R. Williams. Energetics from slow infrared multiphoton dissociation of biomolecules. *The Journal of Physical Chemistry A*, 104(14):3188–3196, 2000.

[357] M. A. Freitas, C. L. Hendrickson, and A. G. Marshall. Determination of relative ordering of activation energies for gas-phase ion unimolecular dissociation by infrared radiation for gaseous multiphoton energy transfer. *Journal of the American Chemical Society*, 122(32):7768–7775, 2000.

[358] J. C. Hannis and D. C. Muddiman. Tailoring the gas-phase dissociation and determining the relative energy of activation for dissociation of 7-deaza purine modified oligonucleotides containing a repeating motif. *International Journal of Mass Spectrometry*, 219(1):139–150, 2002.

[359] K. Paech, R. A. Jockusch, and E. R. Williams. Slow infrared laser dissociation of molecules in the rapid energy exchange limit. *The Journal of Physical Chemistry A*, 106(42):9761–9766, 2002.

[360] Roger Dodd. Ubiquitin spheres.png. `http://commons.wikimedia.org/wiki/File:Ubiquitin_spheres.png`.

[361] R. A. Jockusch, A. S. Lemoff, and E. R. Williams. Hydration of valine-cation complexes in the gas phase: on the number of water molecules necessary to form a zwitterion. *The Journal of Physical Chemistry A*, 105(48):10929–10942, 2001.

[362] R. G. Gilbert and S. C. Smith. *Theory of unimolecular and recombination reactions*. 1990.

[363] J. M. Hollas. *High resolution spectroscopy*, volume 1. 1998.

[364] T. Beyer and D. F. Swinehart. Algorithm 448: number of multiply-restricted partitions. *Communications of the ACM*, 16(6):379, 1973.

[365] E. F. Strittmatter, P. D. Schnier, J. S. Klassen, and E. R. Williams. Dissociation energies of deoxyribose nucleotide dimer anions measured using blackbody infrared radiative dissociation. *Journal of the American Society for Mass Spectrometry*, 10(11):1095–1104, 1999.

[366] W. D. Price, R. A. Jockusch, and E. R. Williams. Is arginine a zwitterion in the gas phase? *Journal of the American Chemical Society*, 119(49):11988–11989, 1997.

[367] L. Deng, E. N. Kitova, and J. S. Klassen. Mapping protein-ligand interactions in the gas phase using a functional group replacement strategy. Comparison of CID and BIRD activation methods. *Journal of The American Society for Mass Spectrometry*, 24(7):988–996, 2013.

[368] E. N. Kitova, D. R. Bundle, and J. S. Klassen. Thermal dissociation of protein-oligosaccharide complexes in the gas phase: Mapping the intrinsic intermolecular interactions. *Journal of the American Chemical Society*, 124(20):5902–5913, 2002.

[369] E. N. Kitova, W. Wang, D. R. Bundle, and J. S. Klassen. Retention of bioactive ligand conformation in a gaseous protein-trisaccharide complex. *Journal of the American Chemical Society*, 124(47):13980–13981, 2002.

[370] E. N. Kitova, D. R. Bundle, and J. S. Klassen. Evidence for the preservation of specific intermolecular interactions in gaseous protein-oligosaccharide complexes. *Journal of the American Chemical Society*, 124(32):9340–9341, 2002.

[371] Y. Ge, D. M. Horn, and F. W. McLafferty. Blackbody infrared radiative dissociation of larger (42 kDa) multiply charged proteins. *International Journal of Mass Spectrometry*, 210:203–214, 2001.

[372] N. Felitsyn, E. N. Kitova, and J. S. Klassen. Thermal decomposition of a gaseous multiprotein complex studied by blackbody infrared radiative dissociation. Investigating the origin of the asymmetric dissociation behavior. *Analytical chemistry*, 73(19):4647–4661, 2001.

[373] D. S. Gross, Y. Zhao, and E. R. Williams. Dissociation of heme-globin complexes by blackbody infrared radiative dissociation: Molecular specificity in the gas phase? *Journal of the American Society for Mass Spectrometry*, 8(5):519–524, 1997.

[374] P. D. Schnier, W. D. Price, E. F. Strittmatter, and E. R. Williams. Dissociation energetics and mechanisms of leucine enkephalin $(M+ H)^+$ and $(2M+ X)^+$ ions (X= H, Li, Na, K, and Rb) measured by blackbody infrared radiative dissociation. *Journal of the American Society for Mass Spectrometry*, 8(8):771–780, 1997.

[375] R. A. Jockusch and E. R. Williams. Binding energies of proton-bound dimers of imidazole and n-acetylalanine methyl ester obtained by blackbody infrared radiative dissociation. *The Journal of Physical Chemistry A*, 102(24):4543–4550, 1998.

[376] E. F. Strittmatter, R. L. Wong, and E. R. Williams. Effects of gas-phase basicity on the proton transfer between organic bases and trifluoroacetic acid in the gas phase: Energetics of charge solvation and salt bridges. *The Journal of Physical Chemistry A*, 104(45):10271–10279, 2000.

[377] P. D. Schnier, J. S. Klassen, E. F. Strittmatter, and E. R. Williams. Activation energies for dissociation of double strand oligonucleotide anions: evidence for Watson-Crick base pairing in vacuo. *Journal of the American Chemical Society*, 120(37):9605–9613, 1998.

[378] S. M. Stevens, W. D. Price R. C. Dunbar, M. Sena, C. H. Watson, L. S. Nichols, J. M. Riveros, D. E. Richardson, and J. R. Eyler. Blackbody infrared radiative dissociation of partially solvated tris (2, 2'-bipyridine) ruthenium (II) complex ions. *The Journal of Physical Chemistry A*, 106(42):9686–9694, 2002.

[379] S. M. Stevens, R. C. Dunbar, W. D. Price, M. Sena, C. H. Watson, L. S. Nichols, J. M. Riveros, D. E. Richardson, and J. R. Eyler. Blackbody infrared radiative dissociation of partially solvated mixed ligand Ru (II) complex ions. *The Journal of Physical Chemistry A*, 108(45):9892–9900, 2004.

[380] T. Schindler, C. Berg, G. Niedner-Schatteburg, and V. E. Bondybey. Protonated water clusters and their black body radiation induced fragmentation. *Chemical physics letters*, 250(3):301–308, 1996.

[381] M. Beyer, C. Berg, H. W. Görlitzer, T. Schindler, U. Achatz, G. Albert, G. Niedner-Schatteburg, and V. E. Bondybey. Fragmentation and intracluster reactions of hydrated aluminum cations $Al^+(H_2O)_n$, n=3-50. *Journal of the American Chemical Society*, 118(31):7386–7389, 1996.

[382] S. Lee, P. Freivogel, T. Schindler, and J. L. Beauchamp. Freeze-dried biomolecules: FT-ICR studies of the specific solvation of functional groups and clathrate formation observed by the slow evaporation of water from hydrated peptides and model compounds in the gas phase. *Journal of the American Chemical Society*, 120(45):11758–11765, 1998.

[383] R. J. Cooper, T. M. Chang, and E. R. Williams. Hydrated alkali metal ions: Spectroscopic evidence for clathrates. *The Journal of Physical Chemistry A*, 117(30):6571–6579, 2013.

[384] R. F. Höckendorf, O. P. Balaj, C. van der Linde, and M. K. Beyer. Thermochemistry from ion-molecule reactions of hydrated ions in the gas phase: a new variant of nanocalorimetry reveals product energy partitioning. *Physical Chemistry Chemical Physics*, 12(15):3772–3779, 2010.

[385] C. Berg, U. Achatz, M. Beyer, S. Joos, G. Albert, T. Schindler, G. Niedner-Schatteburg, and V. E. Bondybey. Chemistry and charge transfer phenomena in water cluster cations. *International journal of mass spectrometry and ion processes*, 167:723–734, 1997.

[386] C. Berg, M. Beyer, U. Achatz, S. Joos, G. Niedner-Schatteburg, and V. E. Bondybey. Stability and reactivity of hydrated magnesium cations. *Chemical physics*, 239(1):379–392, 1998.

[387] B. S. Fox, I. Balteanu, O. P. Balaj, H. Liu, M. K. Beyer, and V. E. Bondybey. Black body radiation induced hydrogen formation in hydrated vanadium cations $V^+(H_2O)_n$. *Physical Chemistry Chemical Physics*, 4(11):2224–2228, 2002.

[388] B. S. Fox, M. K. Beyer, U. Achatz, S. Joos, G. Niedner-Schatteburg, and V. E. Bondybey. Precipitation reactions in water clusters. *The Journal of Physical Chemistry A*, 104(6):1147–1151, 2000.

[389] B. S. Fox, O. P. Balaj, I. Balteanu, M. K. Beyer, and V. E. Bondybey. Single-molecule precipitation of transition metal (I) chlorides in water clusters. *Journal of the American Chemical Society*, 124(2):172–173, 2002.

[390] R. Heeren and K. Vékey. A novel method to determine collisional energy transfer efficiency by Fourier transform ion cyclotron resonance mass spectrometry. *Rapid communications in mass spectrometry*, 12(17):1175–1181, 1998.

[391] R. L. Wong, K. Paech, and E. R. Williams. Blackbody infrared radiative dissociation at low temperature: hydration of $X^{2+}(H_2O)_n$, for X= Mg, Ca. *International Journal of Mass Spectrometry*, 232(1):59–66, 2004.

[392] O. Chen, S. Groh, A. Liechty, and D. P. Ridge. Binding of nitric oxide to iron (II) porphyrins: Radiative association, blackbody infrared radiative dissociation, and gas-phase association equilibrium. *Journal of the American Chemical Society*, 121(50):11910–11911, 1999.

[393] J. Laskin and J. H. Futrell. Entropy is the major driving force for fragmentation of proteins and protein-ligand complexes in the gas phase. *The Journal of Physical Chemistry A*, 107(30):5836–5839, 2003.

[394] B. S. Fox, M. K. Beyer, and V. E. Bondybey. Black body fragmentation of cationic ammonia clusters. *The Journal of Physical Chemistry A*, 105(26):6386–6392, 2001.

[395] U. Achatz, B. S. Fox, M. K. Beyer, and V. E. Bondybey. Hypoiodous acid as guest molecule in protonated water clusters: A combined FT-ICR/DFT study of $I(H_2O)_n^+$. *Journal of the American Chemical Society*, 123(25):6151–6156, 2001.

[396] Y. Toker, I. Rahinov, D. Schwalm, U. Even, O. Heber, M. L. Rappaport, D. Strasser, and D. Zajfman. Blackbody-induced radiative dissociation of cationic SF_6 clusters. *Physical Review A*, 86(2):023202, 2012.

[397] D. J. Harding, R. D. Davies, S. R. Mackenzie, and T. R. Walsh. Oxides of small rhodium clusters: Theoretical investigation of experimental reactivities. *The Journal of chemical physics*, 129(12):124304–124304, 2008.